THÈSE

En vue de l'obtention du

DOCTORAT DE L'UNIVERSITÉ DE TOULOUSE

Délivré par :

Institut National Polytechnique de Toulouse (Toulouse INP)

Discipline ou spécialité :

Dynamique des fluides

Présentée et soutenue par :

M. ABHIJEET BADHE

le mardi 19 juillet 2022

Titre :

Low-order Thermoacoustic Network Modeling and Simulation of Spray Flame Transfer Function

---

Ecole doctorale :

Mécanique, Energétique, Génie civil, Procédés (MEGeP)

Unité de recherche :

Centre Européen de Recherche et Formation Avancées en Calcul Scientifique (CERFACS)

Directeur(s) de Thèse :

M. FRANCK NICOUD

M. LAURENT GICQUEL

Rapporteurs :

M. JONAS MOECK, NORWEGIAN UNI OF SCE AND TECHN TRONDHEIM

M. SEBASTIEN DUCRUIX, CENTRALESUPELEC GIF SUR YVETTE

Membre(s) du jury :

M. THIERRY SCHULLER, UNIVERSITE PAUL SABATIER, Président

M. FRANCK NICOUD, UNIVERSITE DE MONTPELLIER, Membre

M. LAURENT GICQUEL, CERFACS, Membre

MME TARANEH SAYADI, UNIVERSITE SORBONNE, Membre

ABSTRACT

Thermoacoustic combustion instabilities continue to be a major hurdle in the development of future gas turbine combustion systems. These instabilities are characterized by large-amplitude pressure oscillations in the combustor. They are undesirable as they lead to severe vibrations increasing noise and pollutant emissions, causing excessive thermal and mechanical stresses on combustor components, and even threatening structural integrity. Large Eddy Simulation (LES) has proved to be a powerful tool capable of predicting many unsteady combustor phenomena, including instabilities. However, due to the high computational costs associated with LES, it cannot be a standalone design tool to analyze all possible designs and operating conditions to which instabilities remain extremely sensitive. This is where analytical, reduced- or low-order models (ROM / LOM) tend to be valuable and complement LES well, particularly during the predesign stages of combustor development. While most available LOM tools make some important physical simplifications (e.g., linearization of acoustics, flame response), they also typically use over-simplified geometries. One primary objective is to address the latter limitation and improve existing LOM techniques to be able to handle complex realistic geometries.

A major part of the work revolves around developing and validating this new acoustic network modeling tool based on modal expansions (Galerkin Series) and state-space methods (viz. STORM: State-Space Reduced Order Model) for predicting and analyzing instabilities. In STORM, a complex system to be analyzed is decomposed and represented as a network of simpler geometrical elements (subdomains), connection (coupling), flame, and impedance elements. The unique features of STORM are the recently introduced Overcomplete Frame modal expansion technique for modeling acoustics in the network subdomains and the so-called surface spectral connections methodology that was developed. Together they allow seamless interconnections between subdomains with 1D/2D/3D acoustics and construct networks representing complex industry-relevant configurations. The rational approximation methods are discussed for incorporating realistic flame/acoustic interaction models (i.e., Flame transfer functions (FTFs)) in STORM networks. The importance of a few physical constraints, particularly causality, in algorithms deriving these low-order, time-domain, state-space, data-driven flame response models from experimental or high-order simulation data are highlighted. A special type of

network impedance element, DECBC (Delayed Entropy Coupled Boundary Condition), is also developed that facilitates predicting mixed entropy-acoustic instabilities. Overall, STORM presents a cost-efficient, modular and flexible tool for predicting thermoacoustic instabilities and should aid in determining stability regimes and optimum passive control strategies.

In the second minor part of the thesis, the acoustic forcing of the turbulent swirling spray flame is simulated by employing the Euler-Lagrange (EL) LES approach. The objective was to compute the FTF and assess the suitability of the existing EL-LES two-phase combustion modeling framework for such a system identification problem. Recent work has demonstrated the potential of EL-LES in accurately predicting self-sustained limit-cycle instability. However, forced simulations exhibit some difficulties, as discussed. FTF retrieved numerically deviates from experimental reference values by about 20-30%. Results remain sensitive, in general, to the modeling parameters, and further investigations are required to improve the models and prediction fidelity.

Keywords: Thermoacoustics, Low-order modeling, Acoustic network, Flame Transfer Function (FTF), Spray flame, Large Eddy Simulations (LES).

RÉSUMÉ

Les instabilités thermoacoustiques continuent d'être un obstacle majeur dans le développement des systèmes de combustion des turbines à gaz. Ces instabilités sont caractérisées par des oscillations de pression de grande amplitude dans la chambre de combustion. Elles sont indésirables car elles entraînent de fortes vibrations augmentant le bruit et les émissions de polluants, provoquant des contraintes thermiques et mécaniques excessives sur les composants de la chambre de combustion, voire menaçant l'intégrité structurelle du système complet. La simulation aux grandes échelles (LES) s'est avérée être un outil puissant capable de prédire de nombreux phénomènes de combustion instationnaires, y compris les instabilités. Cependant, les coûts de calcul élevés associés empêchent cette approche d'être utilisée en phase de conception pour analyser toutes les conceptions possibles et les conditions de fonctionnement auxquelles les instabilités restent extrêmement sensibles. C'est pourquoi les modèles de bas ordre (LOM) sont précieux et complètent bien les LES, en particulier pendant les étapes de préconception de la chambre de combustion. Bien que la plupart des outils LOM disponibles effectuent des simplifications physiques importantes (par exemple, linéarisation de l'acoustique, réponse à la flamme), ils utilisent également généralement des géométries trop simplifiées. L'un des principaux objectifs de ce travail est de remédier à cette dernière limitation et d'améliorer les techniques LOM existantes pour pouvoir gérer des géométries réalistes complexes.

Une grande partie du travail s'articule autour du développement et de la validation d'un nouvel outil de modélisation de réseaux acoustiques basé sur des expansions modales (Galerkin Series) et des méthodes d'espace d'états (viz. STORM) pour prédire et analyser les instabilités. Dans STORM, un système complexe à analyser est décomposé et représenté comme un réseau d'éléments géométriques plus simples (sous-domaines), de connexion (couplage), de flamme et d'éléments d'impédance. Les caractéristiques uniques de STORM sont la technique d'expansion modale sur des Frame récemment introduite pour modéliser l'acoustique dans les sous-domaines du réseau et la méthodologie dite des connexions spectrales de surface qui a été développée récemment au CERFACS. Ensemble, ils permettent des interconnexions transparentes entre les sous-domaines avec une acoustique 1D/2D/3D et construisent des réseaux représentant des configurations complexes pertinentes pour l'industrie. Les méthodes d'approximation rationnelle sont discutées pour incorporer des modèles réalistes d'interaction flamme/acoustique (c'est-à-dire, les fonctions de transfert de flamme (FTF) dans les réseaux STORM. L'importance de quelques contraintes physiques, en particulier la causalité, dans les algorithmes dérivant ces modèles de réponse de flamme d'ordre inférieur, dans le domaine temporel,

dans l'espace d'états et basés sur les données à partir de données de simulation expérimentales ou d'ordre élevé, est mise en évidence. Un type spécial d'élément d'impédance de réseau, DECBC (Delayed Entropy Coupled Boundary Condition), est également développé pour faciliter la prédiction des instabilités mixtes entropie-acoustique. Dans l'ensemble, STORM présente un outil efficace, modulaire et flexible pour prédire les instabilités thermoacoustiques et devrait aider à déterminer les régimes de stabilité et les stratégies de contrôle passif optimales.

Dans la deuxième partie mineure de la thèse, le forçage acoustique de la flamme de pulvérisation tourbillonnante turbulente est simulé en utilisant l'approche Euler-Lagrange (EL) LES. L'objectif était de calculer le FTF et d'évaluer la pertinence du cadre de modélisation de la combustion diphasique EL-LES existant pour un tel problème d'identification de système. Des travaux récents ont démontré le potentiel de EL-LES pour prédire avec précision l'instabilité auto-entretenue. Cependant, les simulations forcées présentent certaines difficultés et la FTF obtenue numériquement s'écarte des valeurs de référence expérimentales d'environ 20 à 30%. Les résultats restent sensibles, en général, aux paramètres de modélisation, si bien que d'autres investigations seront nécessaires pour améliorer les modèles et la fidélité des prévisions.

Mots clés: Thermoacoustique, Modélisation de bas ordre, Réseau acoustique, Fonction de transfert de flamme (FTF), Flamme de spray, Simulations aux grandes échelles (LES).

Acknowledgments

I carried out this Ph.D. work as an Early Stage Researcher (ESR) under the Marie-Curie Innovative Training Network (ITN) project ANNULIGhT (https://www.ntnu.edu/annulight), and want to acknowledge the funding received from the European Commission.

Firstly, I would like to thank Dr. Thierry Poinsot for offering me the opportunity to conduct research and pursue a Ph.D. at CERFACS. I am grateful to my thesis advisers, Dr. Franck Nicoud and Dr. Laurent Gicquel, for their continued guidance, support, and patience they have shown with me throughout this work.

I would like to extend my sincere thanks to the reviewers Dr. Jonas Moeck, Dr. Sébastien Ducruix, for carefully evaluating this work; and Dr. Taraneh Sayadi and Dr. Thierry Schuller for agreeing to serve as jury members on my thesis committee.

My deepest gratitude goes to Franck Nicoud and Charlélie Laurent for introducing me to thermoacoustics, concepts associated with reduced-order modeling, and, most importantly, the STORM tool. This work wouldn't have been possible without the initial mentoring of Charlélie Laurent, Fabien Dupuy, and Davide Laera. I greatly appreciate their help and always being available to answer my endless questions!

I also thank all current and former Ph.D. students of CERFACS for their suggestions and assistance throughout. I am grateful to my friends for their encouragement and all the good times spent together during these 3.5 years. Also, a big thank you to all the seniors, CSG, COOP, and Admin staff at CERFACS for making working at CERFACS so smooth and easy.

Lastly, I would like to dedicate this thesis to my late father, whose life has always been a source of inspiration for me; and I can't thank my dear mother enough for always believing in me, motivating me, and being there through thick and thin!

Abhijeet Sanjay Badhe
Toulouse, 19 July 2022.

Contents

1 General Introduction **1**

1.1 Climate Change Crisis versus Energy Challenge 1
1.2 Thermoacoustic Combustion Instabilities in Gas Turbines 4
1.2.1 Combustion Instability Mechanisms 5
1.2.2 About Linear and Nonlinear Instability 10
1.3 Annular Combustors and Azimuthal Modes 12
1.4 Reduced-Order Modeling of Thermoacoustic Combustion Instabilities 14
1.4.1 Reduced- or Low- Order Modeling of Acoustics 15
1.4.2 Low-Order Modeling of Flame Dynamics 24
1.5 PhD Thesis Objectives and Outline 27
1.6 Publications 30

2 STORM: State-Space Reduced-Order Thermoacoustic Network Modeling Tool **31**

2.1 Acoustic Network Representation of Systems 31
2.1.1 Introduction to State-Space Method 32
2.2 Over-complete Frame Modal Expansion of Acoustic Subdomains . . 36
2.2.1 Example 1: 1D-1D Ducts with Section Jump 37
2.2.2 State-space Model of an Acoustic Subdomain 41
2.2.3 State-space Model of the 1D-1D Connection Element 47
2.2.4 State-space Model of the 1D-3D Connection Element 49
2.2.5 Example 2: Coupling 1D-3D Acoustic Cavities 50
2.3 Surface Spectral Connections 52
2.3.1 Illustrative Examples: Coupling 3D-3D Subdomains 53
2.3.2 Curvilinear Helmholtz Equation 55
2.3.3 Embedding Coupling Conditions 56
2.3.4 Surface Modal Expansion 58
2.3.5 SS sub-model for 3D-3D-MLPF Liner Spectral Connection . . 61
2.3.6 Adapted SS sub-model of Acoustic Subdomain for Spectral Connection 63
2.4 Solver Structure, and Numerical Strategies for Spurious Eigenmodes 65
2.5 Conclusions 70

3 STORM Linear Stability Analysis of Annular Configurations **73**

3.1 Simplified Plenum-Burner-Chamber (PBC) Configuration 73
3.2 MICCA-Spray Annular Lab-scale Rig 80

3.3 SAFRAN Engine Combustor . . . 85
3.4 Numerical Efficiency . . . 89
3.5 Conclusions . . . 91

4 Modeling of Linear Flame Dynamics in STORM 93
4.1 Introduction . . . 93
4.2 Three equivalent representations of a flame as an LTI system . . . 95
4.2.1 Frequency-domain Representation (Transfer Function) . . . 96
4.2.2 Time-domain Representation (Impulse Response and State-Space Model) . . . 99
4.3 Generating State-Space model from Frequency Response . . . 102
4.3.1 Rational Approximation of Frequency Response . . . 102
4.3.2 *Douasbin et al.* Algorithm (Algo1) . . . 104
4.3.3 Vector Fitting (VF) Algorithm (Algo2) . . . 106
4.3.4 State-Space Model Realization . . . 107
4.4 Physical Constraints in Fitting a Model on Frequency Response Data 109
4.5 Examples of Flame Frequency Response Fitting . . . 114
4.6 Causality in Frequency Response Data . . . 120
4.6.1 Kramers-Krönig Dispersion Relations . . . 121
4.6.2 Bode's Gain-Phase Relation . . . 121
4.6.3 Detecting Causality Violation in the Frequency Response . . . 124
4.7 Conclusions and Perspectives . . . 127

5 Delayed Entropy Coupled Boundary Condition 131
5.1 About Entropy-Acoustic Feedback Mechanism . . . 132
5.2 Zero-Mach-number Assumption and Physical Modeling Strategy . . . 134
5.2.1 Acoustic Energy Flux Mismatch in Impedance Matching . . . 137
5.2.2 Entropy Waves Modeling in the Helmholtz Domain . . . 140
5.3 State-Space Model of 1D-DECBC Network Element . . . 144
5.3.1 1D Test-Case for Validation . . . 144
5.3.2 Entropy Transfer Function (ETF) and Nozzle Impedance . . . 146
5.3.3 State-Space Model Realizations (SS-R1 and SS-R2) . . . 147
5.4 State-Space Model of real-valued 1D Acoustic Impedance . . . 154
5.5 Results and Validation . . . 154
5.5.1 Test1: Applying Nozzle Impedance without Entropy-Acoustic Feedback . . . 156
5.5.2 Test2: 1D-DECBC Results with SS-R1 . . . 157
5.5.3 Test3: 1D-DECBC Results with SS-R2 . . . 160
5.6 Conclusions and Perspectives . . . 167

6 Euler-Lagrange (EL) LES Modeling of Spray Flames 169
6.1 Physical Processes in Spray Combustion 169
6.2 Spray Combustion LES: Models and Governing Equations 174
6.2.1 Euler-Lagrange LES Formalism 174
6.2.2 FIM-UR Injection Model 177
6.2.3 Liquid-Wall Interaction Model (Slip vs. Film Treatment) . . . 179
6.2.4 Droplet Drag Model 182
6.2.5 Droplet Evaporation Model 183
6.2.6 Chemical Kinetics Modeling 186
6.2.7 Thickened Flame Turbulent Combustion Model (TFLES) . . 188
6.2.8 Numerical Scheme and Boundary Conditions 190

7 Combustion Dynamics in SICCA-spray Burner 191
7.1 Introduction 191
7.2 SICCA-spray Burner, Mesh and Numerical Setup 193
7.3 Self-sustained thermoacoustic instability LES (Summary of key results) 196
7.3.1 Role of the liquid-wall interaction treatment in spray-acoustic-flame coupling 197
7.3.2 Impact of the Injection Angle 202
7.4 Forced SICCA-spray Flame LES: Results and Discussion 204
7.4.1 Reference Experimental FDF measurements 204
7.4.2 Inlet Forcing vs. Outlet Forcing 205
7.4.3 Impact of the Injection angle on FTF 209
7.4.4 FTF at other frequencies 213
7.5 Conclusions and Perspectives 214

8 Thesis Conclusions and Perspectives 217

Bibliography 221

Chapter 1

General Introduction

Contents

1.1 Climate Change Crisis versus Energy Challenge 1
1.2 Thermoacoustic Combustion Instabilities in Gas Turbines . 4
1.2.1 Combustion Instability Mechanisms 5
1.2.2 About Linear and Nonlinear Instability 10
1.3 Annular Combustors and Azimuthal Modes 12
1.4 Reduced-Order Modeling of Thermoacoustic Combustion Instabilities 14
1.4.1 Reduced- or Low- Order Modeling of Acoustics 15
1.4.2 Low-Order Modeling of Flame Dynamics 24
1.5 PhD Thesis Objectives and Outline 27
1.6 Publications 30

1.1 Climate Change Crisis versus Energy Challenge

The United Nations Inter-Governmental Panel on Climate Change (IPCC) Assessment Report 5 (AR5)[1] published in 2014, brought stark warnings about inevitable and irreversible climate change impact and paved the way to the historic 2015 United Nations Climate Change Conference in Paris. It has been a vital milestone where 196 countries reached an agreement and pledged to take concrete actions towards the cause of climate change for saving this planet. The agreement sets an ambitious goal of limiting the rise in global temperature to 2 °C by the year 2100, in reference to the pre-industrial times, with the current level already at 1.2 °C. Without any new policies for mitigating climate change, projections suggest an increase in global mean temperature by 4.0 - 4.8 °C, and current trends are far from consistent with restricting it to 2 °C. What also matters is not just the mean global temperature rise but its distribution on the earth's surface. Figure 1.1(a) shows the projected temperature distributions for two scenarios and clearly highlights the polar regions

[1] https://www.ipcc.ch/report/ar5/syr/

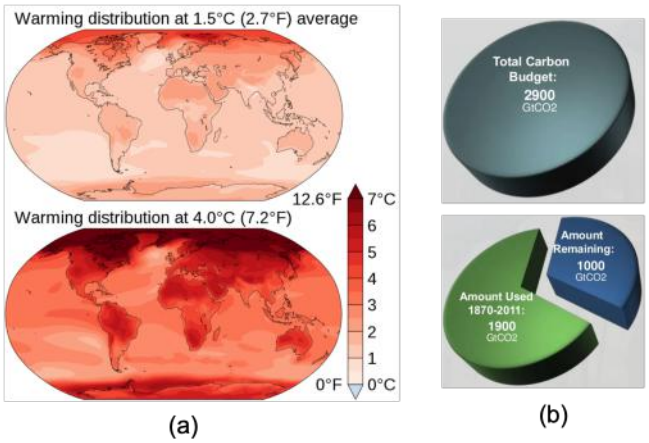

Figure 1.1: (a) Average IPCC AR5 climate model projections for 2081–2100 relative to 1986–2005, under low and high emission scenarios showing the temperature rise distribution. (b) Carbon budget available (only 35%) for the goal of global temperature rise of 2 °C to be achievable by the year 2100.

being the most vulnerable. The melting polar glaciers adversely affect ocean temperatures and currents, disrupting weather patterns and cycles. Besides leading to extreme weather events, already being observed worldwide, global warming poses a severe threat to precipitation, freshwater, and food supply for all living beings in the future.

The IPCC AR5 and World Energy Outlook (WEO) 2021 reports[2] state that currently, about 70% of the total Greenhouse-Gases (GHG) emissions are on account of Energy (35%), Industry (21%) and Transport (14%) sectors, and for the goal of 2 °C to be probable, massive and immediate cuts in GHG emissions are imperative. The urgency for reducing the human carbon footprint is evident from the narrow window for action that is left for the target of 2 °C to be achievable as shown in Fig. 1.1(b).

Key mitigation strategies can be broadly summarized as efficient use of existing energy sources, rapid increase in the proportion of low-carbon, no-carbon fuels, non-conventional and renewable energy sources, maintaining and enhancing the most potent carbon sinks, i.e., the forest cover, and conscious lifestyle, behavioral changes by humans. Transitioning to sustainable energy sources and necessary infrastructure transformation across sectors presents immense economic, technological, and political challenges, with the following few decades being pivotal. This matter is being constantly reviewed, monitored, and tailored by world governments and policymakers.

[2] https://www.iea.org/reports/world-energy-outlook-2021

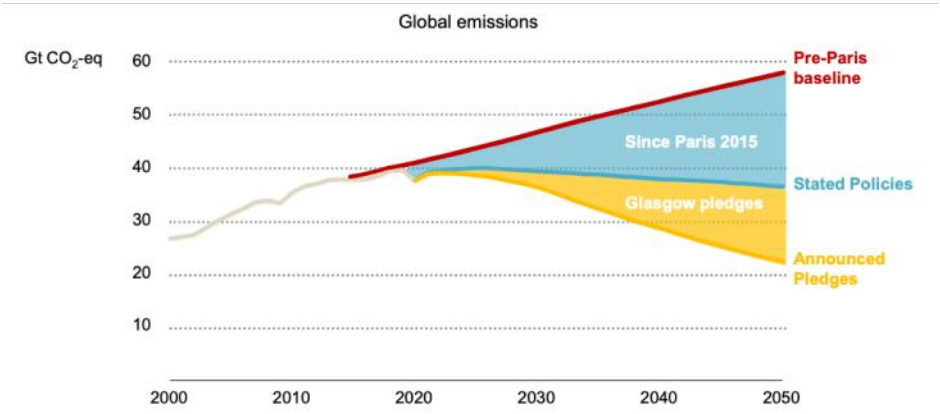

Figure 1.2: Global CO_2 emissions projection as per the International Energy Agency, World Energy Outlook report 2021.

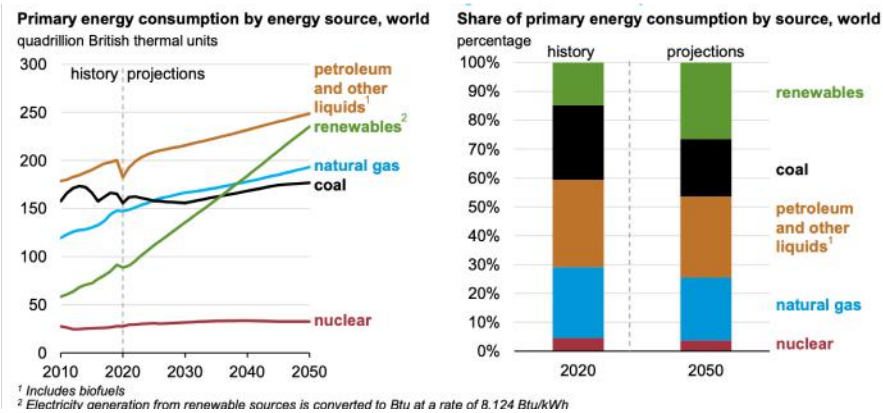

Figure 1.3: World primary energy consumption by source and the energy mix according to U.S. Energy Information Administration (EIA) 2021 outlook.

While climate change is a hard reality, on the other hand, socio-economic development and rising population indicate ever-growing energy demand — expected to double by 2050 as per U.S. Energy Information Administration's (EIA) 2021 outlook,[3] and also as shown in Fig. 1.3. The strong push towards the use of renewables in recent times, and other decarbonization actions, e.g., electrification in transport (evident from the increasing market share of electric vehicles, train locomotives), intense R&D, implementation, and scaling-up of biofuels, and of late green hydrogen combustion technology, is expected to help bend the CO_2 emissions forecast curve to some extent as shown in Fig. 1.2. However, a significant gap in the emissions rate remains for meeting the global warming target. Primary difficulties in ma-

[3] https://www.eia.gov/outlooks/ieo/

terializing the technological shift are also attributed to energy density, production intermittency, storage, transport, and safety issues. The energy challenge in front of humankind is further corroborated by the future (2050) energy mix forecast in Fig. 1.3: despite rapid growth in the proportion of renewables, more than 65% of the humungous energy demand, inevitably, will have to be fulfilled by conventional fuels.

1.2 Thermoacoustic Combustion Instabilities in Gas Turbines

Gas turbines will continue to play a vital role in the electric power generation and air transport sectors for decades to come. Global electricity requirements, expected to be primarily harnessed from natural gas (see Fig. 1.3), and predictions[4] of an annual growth rate of 3.9% and 2.7% in air traffic and air-cargo until the year 2040, respectively, are encouraging prospects.

Figure 1.4: Structural damage of turbine first stage stator, and liner transition piece for a stationary gas turbine engine due to thermoacoustic combustion instabilities. Reproduced from [1].

In line with the responsibility towards climate change, some of the crucial factors driving research and development in the gas turbine industry are compliance with emission regulations, enhancing the range of efficient variable load operation, flexibility in terms of fuel and operating conditions. Technology migration to lean-premixed combustion [2, 3, 4] indeed proved promising in developing modern low-emission engines but have aggravated other problems such as self-excited combustion instabilities and associated hazards of ignition, flashback, and flame blowout when

[4]AIRBUS Global Market Outlook 2021: https://www.airbus.com/en/products-services/commercial-aircraft/market/global-market-forecast

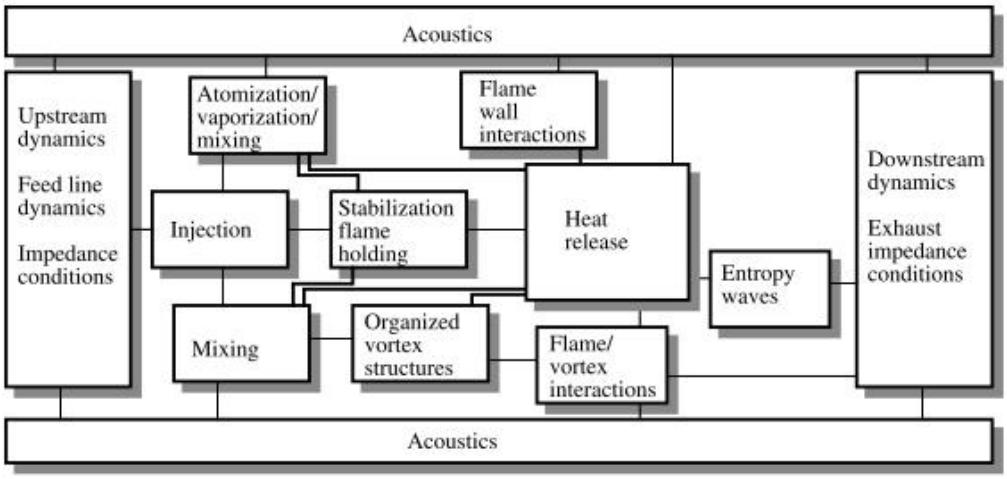

Figure 1.5: An overview of mechanisms that can potentially lead to combustion instabilities in gas turbine engines. Reproduced from [6].

operating very close to the lean limits. Thermoacoustic combustion instabilities are typically characterized by large-amplitude pressure oscillations in the combustor. They are also undesirable as they lead to 1) severe vibrations that interfere with the control-system operation of the engine, 2) enhanced heat transfer and thermal stresses to combustor walls, 3) increased emissions of noise and pollutants such as oxides of nitrogen, soot, and carbon mono-oxides, 4) oscillatory mechanical loads that result in low- or high-cycle fatigue of the components affecting their lifespan or even causing shut-downs and structural damages — for instance, see Fig. 1.4. Self-excited combustion instabilities have posed to be a substantial challenge for many decades, and the amount of research effort gone into understanding this phenomenon and finding ways to predict and control them can be recognized from these excellent reviews [5, 6, 1, 7, 8, 9, 10, 11, 12].

1.2.1 Combustion Instability Mechanisms

While several mechanisms can potentially contribute towards instabilities simultaneously through quite complex interactions (Fig. 1.5), the acoustic-flow-flame coupling due to a closed-loop feedback cycle established between oscillatory combustion (flame heat release) and upstream oscillating flow is found to be the most dominant one. In the confined spaces of the combustion chamber, flames interact with acoustic waves and can amplify one or more natural acoustic eigenmodes of the system when the following Rayleigh criterion is fulfilled [13]:

$$\int p'(\mathbf{x},t)\; q'(\mathbf{x},t)\; dV > 0 \tag{1.1}$$

The Rayleigh criterion states that when unsteady heat release fluctuations $q'(\mathbf{x}, t)$ and acoustic pressure fluctuation $p'(\mathbf{x}, t)$ are in phase, the flame acts like a source feeding the acoustic energy leading to high-amplitude pressure oscillations in the confined volume V of the combustor. See [14, 15] for further discussion about the suitability of the Rayleigh criterion as a necessary and sufficient condition of instability.

Referring to Fig. 1.5, the mechanisms driving instability typically lead to *flame dynamics* i.e., dynamic response of flame shape, position and most importantly *heat release*, which acts as a source of acoustic waves, sitting right in the center of the above diagram. Acoustic waves propagate and interact with the upstream injection system, combustion chamber walls, outlet, and the flame again. Just like there are instability *driving* mechanisms, there also exist *damping* processes that attenuate the growth and limit the amplitude of instability. Some of these key physical driving and damping mechanisms are touched upon next (see the cited publications and references therein for examples and in-depth explanations):

Instability Driving Processes

1. *Thermoacoustic Mechanism:* Arising due to pure flame-acoustics interaction described above [13, 7], this is the fundamental mechanism that is aimed to be modeled in the low-order tool developed in this thesis.

2. *Equivalence Ratio Fluctuations:* The acoustic perturbations modulate the air and fuel supply from the burner, creating inhomogeneities in the fuel-air mixing that are convected to the flame, affecting its flame speed/temperature and thus the heat release [16, 17, 18].

3. *Flame Wrinkling:* Incident acoustic/flow fluctuations modify the flame shape, its surface area, and heat release in corresponding manner, against its tendency of restoring back to its steady state conditions [19, 20, 21, 22, 23, 24].

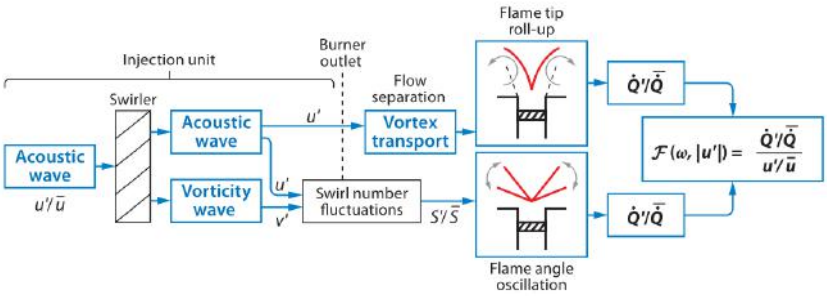

Figure 1.6: Block diagram representation of mechanisms generating heat-release rate fluctuations in swirl stabilized flames. Reproduced from [25].

4. *Inertial/Swirl waves:* As shown in Fig. 1.6, in the case of swirling flames, acoustic waves incident on a swirler generate a vorticity wave (a.k.a inertial wave/swirl wave) that constitute azimuthal velocity perturbations that are convected by the flow in addition to axial acoustic waves. Both waves collectively induce swirl number fluctuations resulting in flame angle oscillations [26, 27, 25, 28].

5. *Flame-vortex interactions and Hydrodynamic Instabilities:* Combustion chamber flows exhibit strong velocity and density gradients, particularly in the shear layers between burner jets and recirculating zones, which are prone to hydrodynamic instabilities forming vortices that interact with the flame front, wrapping and wrinkling them. Besides, vortices are also shed at the edge of sudden expansion between burner and combustor due to flow/acoustic perturbations (see Fig. 1.6). These vortices often trap fresh gases that are convected to the downstream part of the flame where these pockets burn, modulating heat release [29, 30, 31, 32, 33, 34, 35, 36, 37].
   Another global flow instability encountered in strongly swirling flames is the presence of this coherent helical structure, called the *Precessing-Vortex-Core* (PVC). The PVC global mode keeps whirling the vortex core of the swirling flow itself around the central axis (precession). This synchronized oscillation affects overall flame stabilization; and was understood to excite combustion instability as reported in early literature. However, this is not true in general, as reasoned in recent publications, and the converse could be manifested as well. The excitation or suppression of PVC is an outcome of complex nonlinear interaction between flow, flame topology, and acoustic modes - see, e.g., [38, 39, 40, 41, 42, 43].

6. *Entropy-Acoustic Mechanism:* Turbulent swirling flames and flow in combustors produce pockets of hot gases (*hot-spots*), and large-scale eddies, which are convected by the bulk flow from the reaction zone to the combustor outlet — a.k.a entropy waves. One possible origin of these is the strong cold gas dilution jets in the transverse direction near the reaction zone. When these entropy inhomogeneities accelerate through the downstream nozzle and turbine stages, they generate acoustic waves that propagate upstream and may form a feedback loop, perturbing the flame/flow, promoting formation of entropy waves over again. This mechanism can lead to the so-called low-frequency mixed entropy-acoustic instabilities [44, 45, 46]. Part of the generated acoustic waves that propagate downstream constitute the so-called *indirect* combustion noise [10, 47].

7. *Flame-wall interaction:* The overall cooling of the gases due to heat transfer

across the chamber walls (non-adiabaticity) affect the sound-speed, acoustic modes of the configuration, and even flame stabilization topology (V or M shape flame) [48, 49, 50]. Periodic impinging of large parts of the flame front and its quenching on cooled chamber walls can cause global heat-release fluctuations [51, 52]. Besides that, heat transfer characteristics at the flame-holder and its wall-temperature influence flame-root dynamics in the anchoring region, causing significant overall flame movement, heat-release fluctuations, thus generating acoustic waves [53, 54, 55, 56, 57].

8. *Liquid-Fuel Spray Dynamics:* In aero jet engines, liquid fuel is injected by pressure or air-blast atomizers into the combustion chamber [2, 58, 59]. Fuel spray undergoes a series of physical processes before burning, such as filming on injector walls, atomization, evaporation, and mixing that typically results in a complex flame structure, possibly containing premixed, diffusion, droplet-group flame regimes all at the same time. Indeed, these processes are sensitive to and couple with acoustic/flow oscillations, modulating fuel fed to the flame and thus impacting the combustor instability [60, 61, 62, 63, 64, 65, 66, 67].

9. *Intrinsic thermoacoustic modes:* Recently discovered, in this mechanism, a local feedback loop between the flame and acoustics/flow is established within the reaction zone of the combustor. This special type of instability arises independently even when the boundaries of combustor geometry are highly dissipative (nearly non-reflecting) so that all outgoing acoustic waves leave the domain and do not reflect and couple with the flame [68, 69, 70, 71, 72, 73, 74].

Instability Damping/Dissipating Processes:

Acoustic waves, in general, undergo several physical damping/dissipation processes irrespective of whether some acoustic modes of the system are amplified by the flame (unstable) or not (stable). The magnitude of these damping processes typically have a nonlinear dependency on the frequency and amplitude of acoustic perturbations in the combustor, and usually higher frequency modes are rather quickly damped [1, 7]. The damping processes play an essential role in determining the conditions under which the system would become unstable, and they collectively control the oscillation amplitude in case of instability. Some of the key dissipation mechanisms that remove acoustic energy from acoustic waves are:

1. *Viscous and Heat-Transfer Damping Mechanisms*: Acoustics induced flow perturbations near walls in boundary layers dissipate acoustic energy due to viscous effects transforming it into vortical velocity fluctuations. In addition, acoustic energy is converted into entropy fluctuation due to heat transfer in the temperature boundary layer. Flow separation from sharp edges such as

sudden expansion at combustor dump plane, dilution holes, effusion cooling holes on chamber walls, transfer acoustic energy into vortices which are dissipated by standard fluid dynamic processes [1].

2. *Transfer of energy from natural acoustic modes to other frequencies*: In the case of a thermoacoustically unstable combustor, the oscillations, in general, are composed of one or more nearly pure tones at specific frequencies which are close to the natural frequencies (eigenmodes) of the system. Nonlinear processes exist that transfer energy from these amplified/unstable modes to other narrowband, coherent oscillatory modes (higher harmonics or sub-harmonics) that may or may not be amplified. The energy is also transferred to incoherent, broadband fluctuations. Since energy at higher frequencies is usually more rapidly dissipated, these nonlinear processes constitute as *dissipation* mechanisms. See [75, 76] for recent relevant work on prediction and analysis of unstable oscillations comprising of the fundamental mode and its higher harmonics.

3. *Convection and or Radiation of Acoustic Energy*: Some of the acoustic energy can be lost from the system, through the exhaust, by convective transport with the mean flow, and also by propagation and radiation to the environment.

4. *Supplementary Damping devices:* Combustors by design commonly provide very weak damping, and due to enormous rapid heat release (high energy-density conditions), instability driving mechanisms often tend to dominate, making the combustor considerably susceptible to instabilities over a wide range of operating conditions. Therefore, as a countermeasure, external passive control devices are incorporated to artificially enhance acoustic damping and suppress instabilities such as baffles [77, 78], Helmholtz resonators [79, 80, 81], perforated plates [82, 83, 84, 85] etc.

The balance between gain due to driving mechanisms and losses due to damping processes dictates the intensity/amplitude of pressure oscillation inside the combustor. Its commonly observed that when a particular unstable mode is suppressed by suitable action, another mode potentially becomes unstable [11]. Reliable tools are required for the prediction of conditions leading to instabilities and determining passive control methods [1] to deal with it. Passive control methods imply creating inherently stable designs. Some standard techniques used by OEMs include a combination of the following [6]: (1) Modifying of the injection system, distributing or staging fuel/air to change the flame structure and characteristic time-delay between the fuel injection and its consumption, and altering the resonance conditions by minor design changes, (2) deployment of acoustic liners, Helmholtz resonators to augment the energy losses and reduce the level of organized perturbation in the

system, (3) integration of baffles to protect the combustion zone from the oscillating flow, and to eliminate the highly destructive transverse (*screech*) modes that are often encountered in jet engine afterburners, (4) Symmetry breaking [86, 87, 9, 88, 89], especially in the case of annular combustion chambers.

Working out optimal passive control strategies, in practice, to curb instability drivers and or increase the damping until amplitude drops under acceptable levels of mean combustor pressure is certainly not a straightforward task. At the heart of the problem lies the nature of thermoacoustic instabilities, their extra-sensitive behavior to design and operating conditions, and uncertainties in modeling the phenomenon [11, 90].

1.2.2 About Linear and Nonlinear Instability

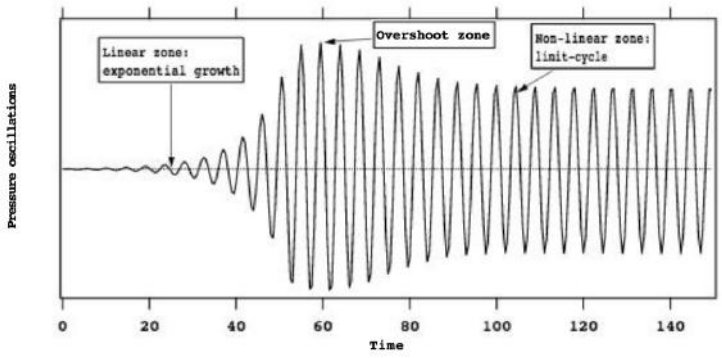

Figure 1.7: Growth of an instability into a limit cycle. Taken from [13].

This sub-section will briefly review the concepts of Linear Stability, Non-Linear Stability, Super-critical and Sub-critical bifurcations. The physical processes that initiate combustion instabilities are in general amplitude-dependent and can exist in two separate regimes - linear and non-linear [1, 91, 90]. A hypothetical dependency of instability driving H(A) and damping D(A) functions is shown in Fig. 1.8, where A is the amplitude of oscillation. The linear regime is characterized by infinitely small-amplitude disturbances in comparison to the mean quantities; and as seen in Fig. 1.8 near the origin, the H(A) and D(A) functions can be approximated to be linearly varying with the amplitude, though at different rates. The $A = 0$ point is *linearly unstable* since the system is overly sensitive to infinitesimal perturbation. In this case, since the rate of driving is higher than damping, the perturbation grows until it reaches an equilibrium point, i.e., the *limit-cycle* amplitude A_{LC}. Fig. 1.7 shows a typical time trace of pressure oscillation in a combustor growing into a limit-cycle. Linear stability analysis is thus often performed to determine whether or not a system is inherently stable.

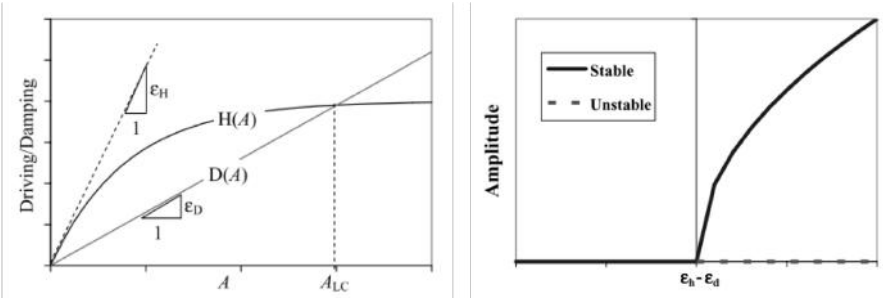

Figure 1.8: Left: Hypothetical dependency of instability driving H(A) and damping D(A) functions respectively. Right: Example of Super-Critical Bifurcation. Adapted from [1]

As the amplitude of perturbation increases and becomes finite-valued, driving and damping processes become non-linearly dependent on the amplitude, and as a result, perturbation does not grow infinitely and saturates at some value — the limit-cycle. At limit-cycle, although the system is oscillating at possibly large and finite amplitude, it is an equilibrium point or fixed point or a stable state from a system dynamics point of view. Any small-amplitude disturbance around this point will bring the system back to that same point.

Super-critical bifurcation [7, 91, 90] occurs at an operating point separating linearly stable and unstable regimes. It is a point across which a linearly stable system becomes linearly unstable, and the system abruptly begins to oscillate with amplitude growing to reach a (limit cycle) equilibrium state. The right side plot in Fig. 1.8 highlights super-critical bifurcation when varying a certain operating parameter of the system, making the driving rate greater than damping.

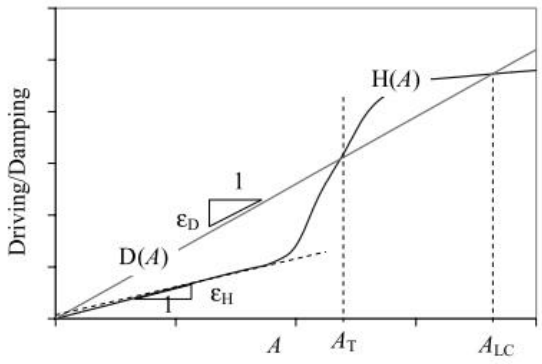

Figure 1.9: Hypothetical dependency of instability driving H(A) and damping D(A) functions respectively. Highlights nonlinear instability or sub-critical bifurcation responsible for triggering of instability. Adapted from [1]

Unlike linear instability, a non-linearly unstable system is as such at an equilibrium state for small-amplitude fluctuations, but it becomes unstable when the amplitude of fluctuation becomes greater than some threshold value A_T as shown in Fig. 1.9. This form of instability is often referred to as sub-critical bifurcation and describe the *triggering* [7, 92, 91] phenomenon of combustion instability when a seemingly stable system is subjected to considerable magnitude disturbances.

1.3 Annular Combustors and Azimuthal Modes

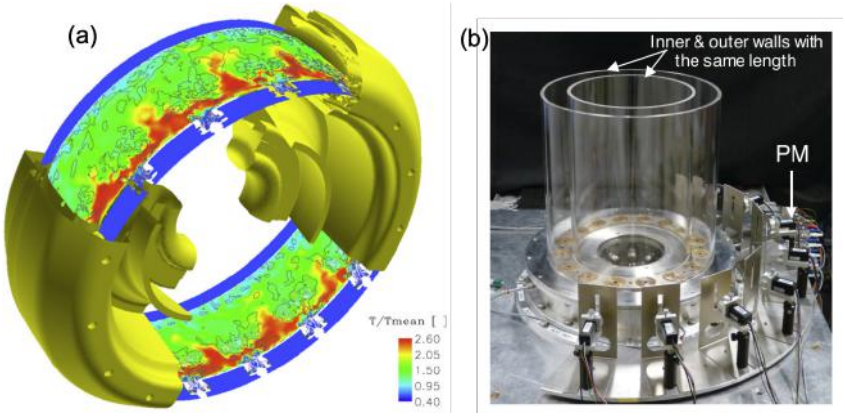

Figure 1.10: (a) A helicopter engine's annular combustor 3D LES computation. Temperature field on a cylindrical plane passing through the injectors with velocity magnitude isocontours. Reproduced from [93]. (b) Lab-scale annular MICCA-Spray rig with 16 swirled spray injectors, operated at EM2C laboratory. Picture taken from [94].

Many engine architectures, especially those of helicopter and aero jet engines, have annular combustion chambers with multiple (16-24) burners (See Fig. 1.10). Unlike longitudinal combustors, analyzing combustion instabilities here is considerably complex. Acoustic waves can travel azimuthally, interacting with these multiple flames. Structure of acoustic eigenmodes [13], assuming only 1D azimuthal propagation, in general, is given by the superposition of two waves - one traveling clockwise (CW) say with amplitude A^+ and other in anti-clockwise (ACW) direction with amplitude A^-. Depending on the values taken by A^+ and A^-, different types of azimuthal modes are possible, as shown in Fig. 1.11. When either of A^+ or A^- is zero, we get a purely CW (clockwise) or ACW (anti-clockwise) *Spinning mode* whose structure is characterized by constant modulus and linearly varying phase. When $A^+ = A^-$ we get *Standing modes* whose pressure modulus depict nodes and anti-nodes and constant phase (0 or π) just as in 1D ducts. When A^+ and A^- each have non-zero values, *Mixed modes* are obtained as shown in Fig. 1.11 for $A^+ = 0.5$

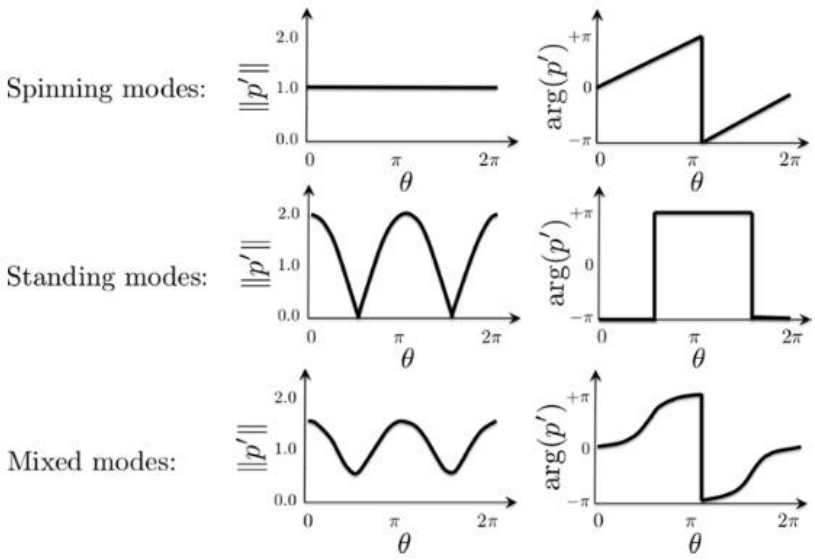

Figure 1.11: Structures of azimuthal acoustic eigenmodes: Spinning (top), standing (middle) and mixed(bottom) shown through the modulus and phase plots of complex acoustic pressure with respect to azimuthal coordinate θ. Reproduced from [13].

and $A^+ = 1$. It should be noted that the circumference of annular chambers is usually greater or comparable to its length. Therefore, combustion instabilities are often manifested as some possible combination of azimuthal and longitudinal acoustic modes becoming unstable and resulting in high-amplitude oscillations [9, 95].

Worth and Dawson [96, 97, 98] investigated the effect of burner spacing and swirl orientation of burners on self-excited azimuthal instabilities — all burners swirling in ACW direction (same-swirl configuration) or with alternate CW and ACW swirl (alternate-swirl configuration). They found the azimuthal instability in general to be *degenerate* (i.e., modes having the same frequencies but different structures). The unstable limit-cycle modes were observed to be varying in amplitude and randomly switching between standing and spinning modes with time (a.k.a. *modal dynamics*). However, statistical analysis of the measured pressure probe signals and global heat release fluctuations suggested a strong correlation between mode nature and burner spacing for same-swirl configuration. The standing mode was statistically preferred to appear for the alternate-swirl configuration irrespective of burner spacing. The statistical probability of a particular nature of the azimuthal mode was attributed to a couple of things: first, the extent of flame-flame interaction (flame merging), which can cause significant re-distribution of global heat-release and formation of large-scale coherent structures along the annulus, and second the bulk circumferential fluid motion induced in the chamber by swirl burners.

Similar modal dynamics were observed and reported in a series of articles by Bourgouin et al. [99, 100, 101] again on swirling gaseous flames, and particularly on the existence of a mixed azimuthal-longitudinal unstable mode (a.k.a. *slanted mode*). Characterization of azimuthal modes and investigation into the prevalence of a particular type (standing/spinning) was conducted for non-swirling bluff-body stabilized flames by Mazur et al. [102], and for spray flames by Prieur et al. [103]. Prieur et al. in [104] also looked into the sensitivity of azimuthal instabilities to two important parameters - the burner fuel equivalence ratio and bulk velocity, and stability maps were generated distinct regions having a strong bias towards spinning or standing unstable modes. Interestingly, there is also an overlap region where both have an equal likelihood; however, a hysteresis phenomenon was observed where the final nature depends on the 'history,' i.e., in other words, the path through which the unstable operating point in the overlap region was reached.

More recently: the impact of mean azimuthal bulk flow in the chamber, mainly how it suppresses one unstable mode and destabilizes another mode [105]; the influence of gaseous fuel and liquid fuels of different volatility on the stability map [94]; variations in azimuthal and or radial symmetry via fuel staging and resulting modal dynamics [106] was examined. The impact of pressurized (2-3 atm) conditions, significant-amplitude presence of higher harmonics in limit-cycles, dynamics between azimuthal-longitudinal unstable modes was investigated as well [107].

Experiments are indeed essential in understanding azimuthal instabilities in general, and the studies cited above highlight the intriguing physics and some of the inherent complexities associated with the phenomenon. However, based on the physical insights acquired, it is also vital to develop reliable numerical modeling tools to aid industry design and development activities. The following section will provide an overview of various modeling approaches for predicting and analyzing thermoacoustic instabilities.

1.4 Reduced-Order Modeling of Thermoacoustic Combustion Instabilities

Complementing experiments quite well has been the considerable progress made in high-fidelity compressible reacting flow Large Eddy Simulations (LES)[108, 13]. By resolving most of the underlying physics by employing sophisticated physical models and advanced numerical methods, it has proved to be a powerful tool in predicting instabilities[93, 109, 51, 110, 57]. However, it is implausible for the high-order LES method to be a standalone design tool due to prohibitive computational costs. Therefore, simplified analytical or theoretical reduced-order (ROM) or low-order (LOM) modeling tools (commonly referred to as *acoustic tools*) are typically

employed in practice [111]. It is owing to the sensitivity of combustion instabilities to configuration geometry and operating conditions [11, 90], methods allowing fast, flexible stability analysis are necessary during pre-design evaluation stages. This is especially true in assessing and determining optimal passive control strategies that require generating stability maps and understanding the system behavior over wide parameter space.

The fundamental principle behind reduced- or low-order models (ROM/LOM) is to reduce the computational complexity of mathematical models in numerical simulations of the physical phenomenon. In other words, it means reducing the degrees-of-freedom (DoF) of the original model obtained from first principles and deriving an approximate yet physically-consistent model. This could be achieved either by making simplifying assumptions in physics (physics-based order reduction) or by exploiting data from experiments/high-order simulations (data-driven model order reduction). All ROMs/LOMs have the following general requirements:

- As small approximation error as possible compared to the full-order model.
- Conservation of the properties and characteristics of the full-order model (e.g., stability, causality)
- Computationally efficient, flexible, and robust.

Combustion instabilities physically are fully described from first-principles by equations governing compressible reacting flow, i.e., the nonlinear Navier-Stokes (NS) equations for reacting flow. A ubiquitous physics-based model-order reduction approach is the *linearizing* of classical flow equations (Navier Stokes or Euler) and solving only for the acoustic perturbations around frozen (zero Mach number) or some mean flow conditions [13, 1, 7, 112]. Flame-dynamics, i.e., the effect of the flame on acoustics and vice-versa is *modeled* through the classical notions of Flame Transfer Function (FTF) or Flame Describing Function (FDF) [113, 25, 12]. FTFs/FDFs define the unsteady flame response (heat release) to acoustic perturbations at some reference location upstream of the flame and are further elaborated in the following Sec. 1.4.2.

Fig. 1.12 provides a broad classification of modeling approaches and tools for analyzing thermoacoustic instabilities, with their *order* (i.e., the cost and complexities) increasing from left to right. Upcoming subsections briefly discuss, first the low-order modeling of acoustics (Sec. 1.4.1), then followed by the low-order representation of flame dynamics (Sec. 1.4.2).

1.4.1 Reduced- or Low- Order Modeling of Acoustics

In full-order methods such as LES, there is no separation of acoustics and flame dynamics as such. Both large and smaller spatiotemporal scales are resolved on a

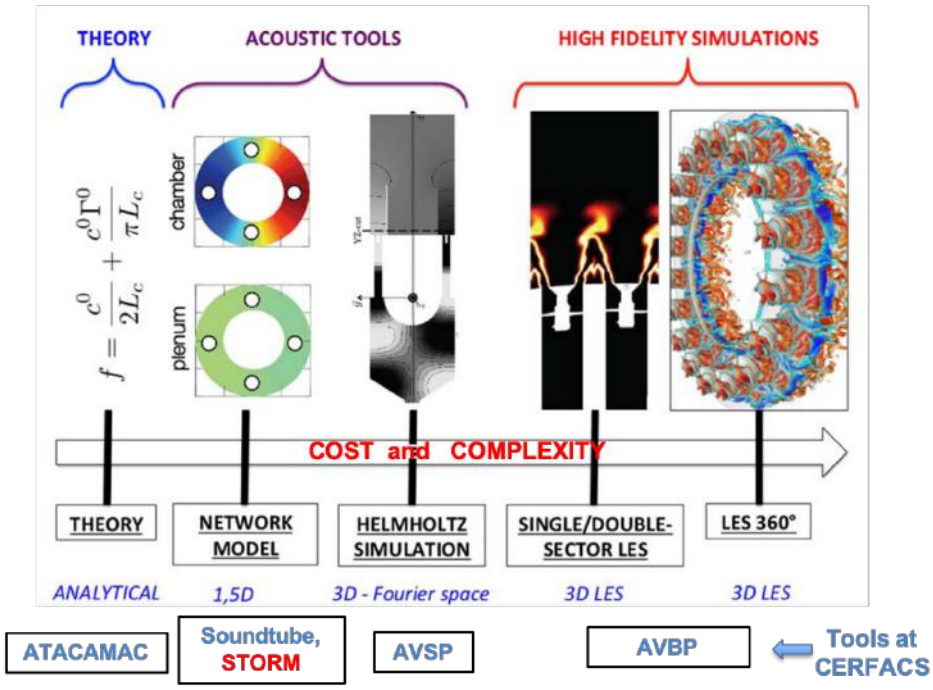

Figure 1.12: An overview of the different classes of tools available for modeling and prediction of combustion instabilities based on their model-order. Development of the thermoacoustic network modeling tool STORM is the Part-1 of this thesis.

finely discretized geometry (mesh): Acoustics, multi-species transport, convective vorticity/entropy waves, hydrodynamic effects (PVC, vortex shedding), heat-fluxes, etc., i.e., most of the physics that plays a role in combustion instabilities is resolved. While the remaining very small (subgrid) scale effects of turbulence, turbulence-chemistry interaction, combustion (species consumption/production) phenomena are suitably modeled [13, 114, 115, 108].

Referring to Fig. 1.12, the *acoustic tools* obtained after linearizing the basic reacting flow governing equations (NS or Euler) can be further classified into several sub-categories, which are reviewed next.

1.4.1.1 Direct 3D FE/FV Discretization Methods: LNSE / LEE / Wave / Helmholtz Equations

One broad family of methods is in which the fundamental flow-equations — Navier-Stokes (NS) or Euler (EE) equations — are linearized (LNSE/LEE) or possibly further reduced to Wave or Helmholtz equations. They can be directly discretized using Finite-Element (FE) or Finite-Volume (FV) methods and solved for any arbitrarily complex geometry. However, unlike LES or RANS, the mesh resolution can

be much coarser since the equations only resolve for the larger-scale acoustic and convected entropy/vorticity waves; and the complex flame dynamics is introduced through low-order FTF/FDF representations.

Linearized Navier-Stokes (LNSE) and Euler (LEE) Equations:

The most general form of Navier-Stokes equations can be reduced to reach the LNSE/LEE equations by making several simplifying physical assumptions to model acoustic propagation. See [13, 7, 112] for details of mathematical development of these equations. In the following, the *key assumptions* are listed, their purpose and implications are discussed, and only the final form of equations is presented.

- **H1:** Multi-species transport, their different molar weights, thermo-fluid-dynamic properties such as heat capacity, conductivity, diffusivity, and chemical reactions are not considered.
- **H2:** Viscous diffusion of heat and momentum are neglected.
- **H3:** Fluid is considered as an ideal gas.

It is owing to **H1** assumption, *air* is typically considered as the working fluid medium along with its physical properties. The large temperature variations in the combustor are crucial for sound speed and are usually accounted for in the mean conditions around which the equations are linearized. **H2** is the most important assumption in obtaining Euler equations from NS and eventually LEE after linearization. It discards any form of viscous acoustic damping due to hydrodynamic interactions. **H3** is usually valid for gas turbines, but for combustion instability studies in rocket engines with cryogenic flames, extreme pressure, temperature conditions makes *real-gas* thermodynamics critical - see for e.g., [116, 117].

The next important step is linearization. Any flow variable is decomposed as $f(\vec{x},t) = f_0(\vec{x}) + f'(\vec{x},t)$, where f_0 is the mean-field, and f' is the coherent oscillating part. Note that here the acoustic-turbulence interactions are not considered. In that case, it would be necessary to introduce a triple decomposition $f = f_0 + f' + f''$, with f'' representing the non-coherent (random) turbulent fluctuations. The coherent acoustic oscillations around mean steady-state is assumed to be linear, meaning:

- **H4 (Linear Acoustics):** For any flow variable f, the oscillating part f' is assumed to be very small in comparison to the mean value f_0, i.e., $f'/f_0 = \varepsilon << 1$

After introducing the $f(\vec{x},t) = f_0(\vec{x}) + f'(\vec{x},t)$ decomposition, only the terms of order ε (first-order) are retained to get the set of LEE equations. For the sake of brevity, the LEE are not shown here, but can be found in Chapter 5, Sec. 5.2 of this

manuscript. (Similarly, in case assumption **H2** is not applied, LNSE are obtained, which will include corresponding linearized viscous terms as well.)

LNSE/LEE solve for pressure, velocity, density, and entropy fluctuations assuming mean reference quantities are known. Mean quantities are usually obtained a prioriiori from high-order CFD such as RANS or time-averaged fields from LES or approximated as presumed uniform fields. In the set of coupled mass, momentum, and energy conservation equations in LNSE/LEE, the energy equation contains the heat release source term that needs closure. It is modeled and achieved through FTFs/FDFs described in the following Sec. 1.4.2. LNSE and LEE have significant applications in areas of aero-acoustics and combustion noise studies [118, 10, 47, 119, 120], since they by construction provide a well-suited reduced-order framework to model the propagation of not only acoustic but also vorticity/entropy perturbations through combustor and turbine stages. Although limited, LNSE/LEE have also been applied to thermoacoustic problems. E.g., to study the effect of zero/non-zero mean flow on the thermoacoustic eigenmodes stability, [112], for analyzing the so-called non-normal effects in the presence of non-zero mean flow [121], prediction of mixed entropy-acoustic instabilities [45]. More recently, the research group of Sattelmayer and Schuermans at TU Munich have published a series of articles on the development and use of FEM LNSE/LEE tools for modeling and prediction of high-frequency transverse (screech) modes [122, 123]. They also proposed methods for modeling physical acoustic damping and getting away (or undoing) the adverse impact of artificial numerical dissipation in LEE [124, 125] — LEE particularly are highly susceptible to numerical instability issues due to lack of physical viscous acoustic dissipation, and therefore introducing artificial damping in numerical schemes generally becomes necessary. Another challenge is that LNSE/LEE are still a set of five coupled transport equations, and numerical discretization of all the correlation terms between mean and fluctuating quantities increases the complexities, and solving them can soon become computationally expensive for large industrial configurations. Therefore, often equations are further simplified by invoking the *zero-Mach number* assumption.

- **H5 (zero-Mach number):** Mean flow is assumed to be at rest ($M = 0$).

H5 is a strong assumption and remains valid for thermoacoustic stability predictions of systems only in very-low-Mach-number limit. Nicoud and Wieczorek [112] demonstrated on simple academic 1D configuration analytically that zero-Mach assumption can lead to significant errors in the prediction of thermoacoustic oscillation frequencies, their growth rates (i.e., stability), especially when the mean flow is not isentropic, a condition which is always met in combustion applications. Besides, the net effect of the non-zero Mach number terms on the stability of thermoacoustic modes also strongly depends on both the boundary conditions and the flame re-

sponse[5] - see [112, 45, 46]. Also, **H5** will eliminate all convective terms $\vec{u}_0 \cdot \vec{\nabla}(\cdot)$ and yield a set of coupled equations governing the fluctuating pressure, velocity, and entropy around the stagnant mean flow - the *zero-Mach linearized Euler Equations*[6].

Linearized Reactive Flow (LRF) Equations

Avdonin et al. [126] present an interesting approach, called *Linearized Reactive Flow* (LRF) solver, which falls somewhere in between the high-order methods (LES) and family of linearized reduced-order methods (LNSE/LEE). The authors linearized compressible Navier-Stokes equations *along with* the species transport equations and reaction source terms, thereby including a model for the dynamic response of the flame to flow perturbations in an inherent manner. For conducting stability analysis, LRF eliminates the need for FTFs, which otherwise have to be externally provided for all the low-order acoustics modeling approaches discussed in this section. Alternatively, the method also proves to be a low-cost option for computing FTFs. While the LRF method was successfully applied to a simple laminar premixed flame, its suitability to turbulent flames remains to be seen as per the authors.

Wave and Helmholtz Equation:

Thanks to the zero-Mach **H5** condition, the LEE equations can be combined and further reduced to just one PDE that governs the propagation of linear acoustic waves in the fluid called as *Wave-Equation* and or its frequency-domain equivalent the *Helmholtz Equation* [127, 13]. The wave equation is written as:

$$\nabla \cdot \left(\frac{1}{\rho_0} \vec{\nabla} p' \right) - \frac{1}{\gamma p_0} \frac{\partial^2 p'}{\partial t^2} = - \frac{\gamma - 1}{\gamma p_0} \frac{\partial q'}{\partial t} \tag{1.2}$$

Wave-equation can be directly solved for thermoacoustic stability analysis - see [128] for example. However, a more widely adopted approach in thermoacoustic community are the Helmholtz equations solvers [127, 129]. Often in linear acoustics harmonic oscillations are assumed and stability analysis is performed in frequency-domain. Therefore, fluctuating quantities in time-domain can be related to their frequency-domain counterpart through Fourier Transform and its inverse:

$$\hat{p}(\vec{x}, \omega) = \int_{-\infty}^{+\infty} e^{-j\omega t} p(\vec{x}, t) dt, \quad p(\vec{x}, t) = \int_{-\infty}^{+\infty} e^{j\omega t} \hat{p}(\vec{x}, \omega) d\omega \tag{1.3}$$

Applying Fourier Transform to the Wave-Equation gives frequency-domain Helmholtz equation as follows:

$$\nabla \cdot \left(\frac{1}{\rho_0} \vec{\nabla} \hat{p} \right) + \frac{\omega^2}{\gamma p_0} \hat{p} = -j\omega \frac{\gamma - 1}{\gamma p_0} \hat{q} \tag{1.4}$$

[5] Further discussion on this in Chapter 5.

[6] Detailed derivation can be found in [112, 7, 13], or their final form in Ch. 5, Sec. 5.2

For homogenous uniform mean fields of sound-speed c_0, density ρ_0, specific heat ratio γ, the following simplified version of Helmholtz equation is realized:

$$c_0^2 \nabla^2 \hat{p}(\vec{x}, \omega) + \omega^2 \hat{p}(\vec{x}, \omega) = -j\omega(\gamma - 1)\hat{q} \tag{1.5}$$

Note that for solving the above Helmholtz equation, additional elements are necessary:

- *zero-Mach linearized momentum equation:* for computing acoustic velocity field from pressure. They are related by following equation in frequency-domain:
$$j\omega\rho_0 \hat{\vec{u}} + \vec{\nabla}\hat{p} = 0 \tag{1.6}$$
- *FTF/FDF:* Source terms on the right-hand side due to flame dynamics, i.e. heat release oscillation, is modeled through FTF/FDFs discussed in the following Sec. 1.4.2.
- *Acoustic Boundary Conditions (BCs)*: Can be (i) simple homogeneous Dirichlet BC $\hat{p} = 0$ for boundary that is open to the atmosphere (pressure-release BC); or (ii) homogeneous Neumann BC $\vec{\nabla}\hat{p} \cdot \vec{n}_s = 0$ (rigid-wall BC), where $\vec{n}_s$ outward surface normal unit vector; or (iii) more generic Robin-type BC: $\hat{p} + Z(j\omega)\rho_0 c_0 \hat{\vec{u}} \cdot \vec{n}_s = 0$, where $Z(j\omega)$ is a frequency-dependent, complex-valued acoustic impedance.

Solutions of the frequency-domain *homogeneous* Helmholtz equation, i.e., without heat release source term or nontrivial Robin's type of BCs, provide the natural acoustic eigenmodes of the system. In the resulting complex-valued eigenvalues (eigenfrequencies) $\omega = \omega_r + j\omega_i$, the real part is the mode's oscillation frequency, and the imaginary part is its growth rate. The modes are neither amplified nor damped, i.e., their ω_i 0. However, solutions to the general *inhomogeneous* Eq. (1.4), the eigenmodes would get stabilized ($\omega_i < 0$) or get unstable ($\omega_i > 0$) in the presence of complex impedances and or active flames feedback.

Helmholtz solvers have undergone significant developments over the past decade and have been successfully employed from laboratory-scale to complex industrial geometries for predicting thermoacoustic eigenmodes and their linear stability[109]. Flame describing function (FDF) too has been coupled with Helmholtz solvers for predicting limit-cycle amplitudes [130, 131]. Acoustic dissipation effects due to multi-perforated liners of combustors and acoustic-hydrodynamic interactions that are quite prominent in geometrically complex components such as swirlers were modeled [132, 133, 134]. Besides that, convective flow effects and coupled entropy-acoustic modes [45, 46] could be accounted for as well.

The in-house Helmholtz solver AVSP [127] has been used in the current work. More details and discussion will follow in upcoming Chapters 3 and 4.

1.4.1.2 Acoustic Network LOMs

Another family of low-order acoustic tools is the so-called "network models." They are much faster than FV/FE-based solvers and are used in practice for fast resolutions and parametric studies, especially during pre-design stages. These tools are based on theoretical, quasi-analytical techniques wherein a complex configuration is decomposed into simpler acoustic sub-domains. They are connected/coupled together to construct a network and are solved using simple numerical methods. Network tools can be categorized based on the spatial description used for the acoustic waves [111] in the sub-domains of the network as *Characteristic Wave-based (Riemann Invariants)* or *Modal expansion (Galerkin Projection)* models. These are briefly discussed here in this sub-section.

Characteristic Wave-based (Riemann Invariants) Network LOMs:

Wave-based methods usually assume quasi-1D acoustic sub-domains wherein planar wave propagation is assumed in the forward (amplitude A_k^+) and backward (amplitude A_k^-) directions as shown in Fig. 1.13. Jump relations [13, 135, 136, 137, 138] are used at connection interfaces to ensure pressure and flow-rate continuity, and across infinitely thin flames if present — flames are usually assumed acoustically compact, i.e., their thickness is negligible in comparison to the acoustic wavelength. The amplitudes of the forward and backward propagating waves are determined by connecting each duct element to satisfy all jump relations and boundary conditions. The resulting system of equations can be recast into a matrix form yielding a frequency-domain scalar dispersion relation $F(j\omega) = 0$ — e.g., [135, 136] from the recent literature for such problem formulation. This linear system can then be solved to get the system eigenfrequencies and mode shapes.

Early works on wave-based low-order network modeling pursued in many re-

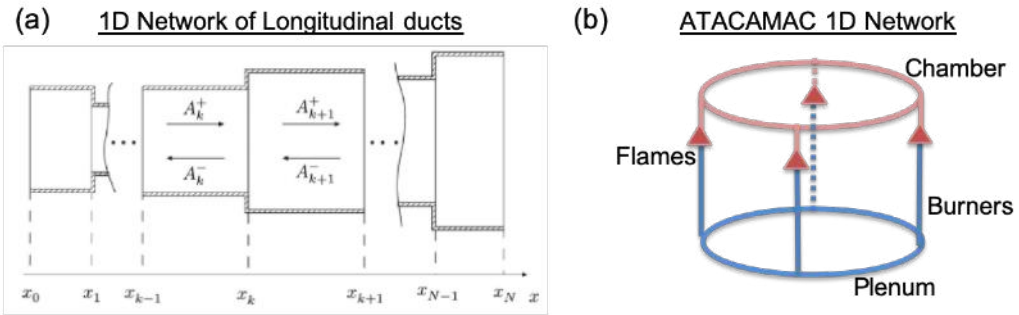

Figure 1.13: (a) Wave-based 1D network made of a series of longitudinal ducts with section area jumps. (b) A wave-based canonical Plenum-Burner-Chamber (PBC) network (adapted from [111]).

search groups can be found in [139, 140, 141]. More recent applications are of Han et al. [142], Li and Morgans [143] who used their wave-based network tool OSCILOS for linear and nonlinear stability analysis for longitudinal configurations and have successfully predicted limit-cycles observed in experiments. Orchini et al. [144] highlight crucial differences between the nonlinear oscillatory response of the system predicted by the frequency-domain and time-domain (state-space based) methods. Schuller et al. [135] examined conditions when coupling/decoupling of the chamber, plenum modes in longitudinal configurations would occur. Since wave-based methods assume planar 1D acoustic wave propagation in the network elements, they cannot capture non-planar modes or multi-dimensional modes in complex configurations. For instance, 1) unstable transverse modes that are often observed in rocket engines, afterburners of military jet engines, despite their combustor geometry being longitudinal; 2) mixed longitudinal and azimuthal modes in annular combustors. However, an advantage of wave-based 1D networks is that it is quite easy to consider non-zero mean-flow - see, e.g., [112, 145, 87]. Bauerheim et al. [136, 87] proposed an Analytical Tool to Analyze and Control Azimuthal Modes in Annular Combustors (ATACAMAC) for examining azimuthal instabilities in a canonical Plenum-Burner-Chamber (PBC) configuration. This wave-based network model, shown in Fig. 1.13 will be used to validate linear stability analysis results from the methodology in STORM (based on modal expansions) presented in Ch. 3 on the same PBC geometry.

Modal Expansion (Galerkin Projection) LOMs

In the Modal Expansions method, the thermoacoustic pressure field (i.e. solution to the Wave equation above) in each sub-domain of the network is sought as a linear combination of (or series expansion) natural acoustic eigenmodes of that sub-domain.

$$p(\vec{x},t) = \sum_{n=1}^{N} \dot{\Gamma}_n(t)\phi_n(\vec{x}) = \dot{\mathbf{\Gamma}}^T(t)\boldsymbol{\phi}(\vec{x}) \tag{1.7}$$

The unknown modal coefficients vary in time under the influence of volumetric forcing due to an active flame if present and boundary forcing imposed due to connections with neighboring sub-domains. The technique originating in the field of theoretical acoustics was first applied for investigating combustion instabilities by Culick [5], and Zinn [146] many decades ago. Since then, many researchers have exploited it for in-depth investigations of nonlinear effects in instabilities for simple Rijke tube-like geometries [147, 148], academic thin annulus-like geometry [149, 150, 151]. Simplified plenum-burner-chamber configurations [152, 153, 154, 155] where burners are modeled as transfer matrices, while modal expansion is used to express the pressure field in plenum and chamber were investigated as well.

Unlike wave-based low-order modeling, this method is not limited to planar

acoustic waves and can resolve both multi-dimensional modes. However, incorporating mean-flow effects is not straightforward, just like conventional Helmholtz solvers [127, 45, 46], due to the inherent zero-Mach assumption.

The eigenfunctions used as the basis in the expansion can be obtained analytically for simple geometries. For complex arbitrary shaped 3D geometries, a basis can be constructed from the natural acoustic eigenmodes calculated a priori from a Helmholtz solver as was shown by Bethke et al. [156] and Laurent et al. [157].

The use of the modal expansion technique for building extensive acoustic or thermoacoustic networks has been rather limited in the past. A notable exception is the work of Schuermans, Bellucci, Noiray, Bothien, and colleagues, who have been developing this so-called *TA*3 tool for two decades. The tool has been successfully applied to realistic 3D combustor geometries, can take complex impedances into account, and has been used for active control, stability analysis, and nonlinear time-domain simulations. It has also been extensively validated with engine test data. Few select publications - [152, 162, 163, 149, 164].

The research group of Candel and Ducruix at EM2C Paris is developing a reduced-order modeling tool called *StaHF*, especially targeting high-frequency instabilities in rocket engines. See works of Méry [158], Gonzalez-Flesca et al. [159], Marchal et al. [160], Fougnie et al. [161].

STORM - **St**ate-space **R**educed **O**rder **M**odeling, is an in-house thermoacoustic network modeling tool based on generalized modal expansion recently proposed by Laurent et al. [157]. It draws inspiration and is conceptually similar to the TA3 tool of Schuermans and colleagues, but there is one fundamental difference too. Laurent et al. [157] improved the classical modal expansion technique to overcome an important limitation relating to the modal basis functions that have critical implications for explicitly constructing networks with multiple, multi-dimensional acoustic subdomains.

The development of STORM is one of the primary subjects of this Ph.D. work, and the modeling principles are detailed in the following Ch. 3 of this manuscript.

Hybrid Network LOMs

Recently, Yang et al. [165], and Orchini et al. [166] employed both wave-based and modal expansion methods together for low-order modeling of canonical plenum-burner-chamber configurations. Burners were modeled with 1D waves, whereas plenum and chamber as 2D acoustic elements with modal expansion. They investigated nonlinear modal interactions to identify conditions favoring a particular mode structure- spinning/standing/slanted or longitudinal mode, and random switching between them due to its sensitivity to nonlinear flame response parameters.

1.4.2 Low-Order Modeling of Flame Dynamics

After presenting an overview of low-order modeling (LOM) of acoustics in the previous sub-section, approaches for low-order representation of flame dynamics are introduced and briefly discussed here.

In Sec. 1.2.1 and Fig. 1.5, it was discussed how unsteady heat release due to flame dynamics (which acts as a source of acoustic waves due to gas dilatation) is at the core of thermoacoustic instability mechanisms. It is vital to recognize the wide spatio-temporal scale separation between acoustic waves and flames in this context. The acoustic wavelengths ($\lambda = c/f$) are typically of the same order as the geometry, and much larger than global flame/reaction-zone length scales (L) in most practical cases. However, the scales of vorticity, equivalence-ratio, entropy waves perturbing the flame are usually smaller, and the local flame-thickness, where most heat-release occurs, furthermore - typically of $O(10^{-5})$ to $O(10^{-3})$ m. Therefore, most practical flames can be considered as *acoustically compact*[7] but *convectively non-compact*. This is respectively characterized by nondimensional Helmholtz (He) and a Strouhal (St) numbers [1, 7] given as

$$He \equiv \frac{fL}{c} << 1 \;\Rightarrow\; \text{Acoustically compact flame} \tag{1.8}$$

$$St \equiv \frac{fL}{\bar{u}} << 1 \;\Rightarrow\; \text{Convectively compact flame} \tag{1.9}$$

where $\bar{u}$ is a characteristic convection velocity.

Modeling flame dynamics from first principles ought to account for chemical kinetics, turbulence-chemistry interaction, hydrodynamic effects, flame-wall interaction, etc., as is done in high-order methods such as LES or RANS. These intricate phenomena actually motivate the idea of separating acoustics and flame dynamics: acoustics is resolved explicitly, while the finer flame dynamics processes are all reduced down and modeled, rather described, through FTFs/FDFs. Normally FTFs/FDFs are then coupled with acoustic solvers to close the thermoacoustic feedback loop and conduct stability analysis. Indeed, modeling flame-dynamics in the context of low-order modeling of combustion instabilities is the most challenging aspect as described in these reviews [25, 12].

Flame-Transfer Function (FTF), defined in frequency domain[8], is the ratio of relative global heat-release rate fluctuations to the relative axial velocity fluctuations

[7] Acoustic compactness typically is not true when there are long flames in the combustor [145] or high-frequency transverse (*screech*) modes are under question (see for eg. [167, 168, 169, 170, 9]). Also, in annular combustion chambers, while an individual flame is compact with respect to an azimuthal mode, the heat-release zone of all flames collectively is not compact [171].

[8] considering Fourier convention $e^{j\omega t}$ for temporal harmonic variation of any fluctuating quantity.

impinging on the flame; calculated for small relative axial velocity fluctuations (cf. **H5:** linear acoustics).

$$\mathcal{F}(\omega) = \frac{\dot{Q}'(\omega)/\bar{\dot{Q}}}{u'/\bar{u}} = G(\omega)\, e^{-j\varphi(\omega)} \tag{1.10}$$

where, $u'/\bar{u}$ is acoustic velocity fluctuation levels at a *reference* location upstream of the flame, and $G = |\mathcal{F}|$, $\varphi(\omega) = \angle(\mathcal{F})$ are respectively the gain and phase of FTF $\mathcal{F}(\omega)$. The phase difference between heat-release and velocity oscillations contains a *time-delay* that denotes the delay between acoustic perturbation at the reference location and the corresponding resulting heat-release fluctuation. This is inspired from the classical the $n-\tau$ model proposed of Crocco [172] in 1950s, where n is the flame-interaction index (gain) and τ is the time-delay such that the phase $\varphi(\omega) = \omega\tau$.

Note that an FTF provides *linear* response of the flame to the incoming acoustic velocity perturbation and is applicable only for small-amplitude fluctuations at the onset of instability. It does not account for nonlinear effects such as saturation of heat-release fluctuations required to model and predict limit cycles.

More advanced formulations of FTFs were also proposed:

1. For some simple flame geometries such as conical or V-shaped flames, closed-form analytical FTFs based on flame-front tracking using level-set methods (a.k.a G-Equation) are available [19, 20, 18, 173].

2. FTFs that take into account effect of different flow-flame-acoustic interaction mechanisms simultaneously by superposition (thanks to linearity) of multiple corresponding individual FTFs, for e.g., effect of flow ($u'/\bar{u}$), pressure ($p'/\bar{p}$), equivalence ratio ($\phi'/\bar{\phi}$) perturbations etc. [174, 175, 176].

3. Furthermore, *global* FTFs of realistic flames are also often characterized by not one or two delay time-scales, but by a distribution of time-delay (a.k.a Distributed Time Delay (DTD) models). For eg., a *presumed* Gaussian distribution around mean delay τ with standard deviation σ, giving rise to the so-called $n-\tau-\sigma$ type of FTFs, can be found in the literature - see [12, 177, 178, 179] and references therein.

4. In case of acoustically noncompact flames, global FTFs become inaccurate representation of the flame response. In such cases, spatio-temporal variations of heat-release fluctuations must be taken into account, and therefore, some authors have also proposed FTF where the gain and time-delay spatial distribution $n(\vec{x})$ and $\tau(\vec{x})$ are characterized in form of *local FTFs* [127, 128, 180, 181]. However, here the $n(\vec{x})$ and $\tau(\vec{x})$ spatial distributions are typically taken to be independent of frequency ω.

Flame-Describing Function (FDF), an extended concept of FTF, is simply a family of transfer functions corresponding to different amplitude levels of incident velocity perturbations, defined as

$$\mathcal{F}\left(\omega,\left|u'\right|\right)=\frac{\dot{Q}'\left(\omega,\left|u'\right|\right)/\overline{\dot{Q}}}{u'/\bar{u}}=G\left(\omega,\left|u'\right|\right)e^{-j\varphi(\omega,|u'|)} \tag{1.11}$$

When coupled with acoustic solvers, FDFs can help predict limit-cycle amplitude, mode-switching, triggering (cf. Sec. 1.2.2) and other such *nonlinear*[9] instability characteristics [113, 182, 130, 143, 183] briefly discussed earlier in Sec. 1.2.2. See [184, 75] for more advanced formulations of FDFs which can predict for example the simultaneous presence of the fundamental unstable mode and its harmonics in a limit-cycle oscillation; and [185, 186] for nonlinear stability analysis with G-equation-based flame dynamics model.

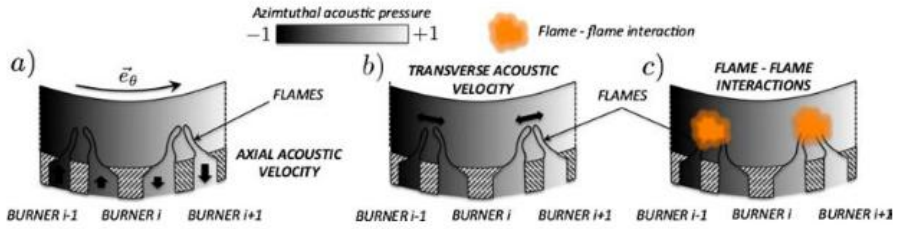

Figure 1.14: Flame dynamics mechanisms involved in azimuthal instabilities. Adapted from [111]

Lastly, before closing this subsection, the modeling of flame dynamics pertinent to the annular combustors is touched upon. It is certainly closely linked to the nature (standing/spinning) of azimuthal instabilities present in the chamber [98, 9, 111], especially the position of flames for the given azimuthal mode structure. Experiments [98], and even LES [93, 109] have revealed few mechanisms as shown in Fig. 1.14: azimuthal mode modulates the axial mass flow rate in the burners but also creates a transverse excitation. Both mechanisms can also generate flame-flame interaction, whose effect on thermo-acoustic instabilities is not well-understood yet. Azimuthal modal dynamics (cf. Sec. 1.3) during self-excited instabilities further complicates the modeling of flame dynamics in annular combustors. Currently, in most studies, the FTFs/FDFs used for stability analysis of annular configurations are obtained by axially forcing single burner setups [187, 188, 183]. Ignoring the influence of transverse excitation and or flame merging (if relevant) is indeed disputable. Therefore, literature investigating flame response to individual and simultaneous transverse+axial forcing experimentally [189, 190, 169, 191], theoretically/numerically

[9]Note that here low-order acoustics model remains in the linear regime (cf. **H5** assumption in Sec. 1.4.1), and it is the (nonlinear) flame response that is the primary source of nonlinearity.)

[192, 193, 194] are emerging in recent times, and is a topic active research. Note that transverse flame forcing is relevant not only for azimuthal instabilities but also in the context of high-frequency screech modes in longitudinal combustors. Nygård et al. [195, 196] applied azimuthal forcing in an annular rig to control, impose and sustain the mode nature (spinning-CW/spinning-ACW/standing), the mode order and analyzed flame dynamics under such conditions. The authors also introduce the so-called *Azimuthal Flame Describing Function (AFDF)* that quantifies the variations in heat release response based on the mode nature and suggest it to be useful in future low-order modeling effort.

1.5 PhD Thesis Objectives and Outline

The author of this Ph.D. manuscript has carried out the work as Early Stage Researcher (ESR) under the Marie-Curie Innovative Training Network (ITN) project ANNULIGhT[10]. The author acknowledges the funding received from the European Commission, and is grateful to CERFACS for the opportunity.

Broadly, there are two parts in this PhD thesis work: The primary and major Part-1 deals with development of **STORM** (**St**ate-**S**pace **R**educed-**O**rder-**M**odeling) - a low-order thermoacoustic network tool under development at CERFACS, and Part-2 will present a brief application study of high-order Euler-Lagrange (EL) LES of turbulent swirling spray flame.

- **Chapter 1 - General Introduction:** This current chapter provided a general introduction to the overarching subject matter of this thesis, i.e., the problem of thermoacoustic combustion instabilities in gas turbine engines. The underlying physical mechanisms were briefly explained. Peculiarities of azimuthal combustion instabilities observed in annular combustors were discussed. The chapter also provided an overview of Reduced-Order (ROM) or Low-Order (LOM) Modeling approaches for predicting and analyzing thermoacoustic combustion instabilities. The development of ROMs/LOMs is ubiquitous and a major research theme in the thermoacoustics community since they provide a low-cost option for modeling a rather complex physical phenomenon. They allow necessary parametric studies for determining strategies for passive control of the instabilities.

PART-1: Development of STORM

STORM is a LOM tool where the modeling of acoustics is based on the idea of modal-expansions, and the state-space framework is employed for building network representation of the systems. Development of STORM was initiated only a few years ago in the preceding Ph.D. of C. Laurent [197].

[10] https://www.ntnu.edu/annulight

- **Chapter 2 - State-Space Reduced-Order Thermoacoustic Network Modeling Tool:** will describe the underlying theory and modeling principles of STORM accompanied with a few canonical examples. The salient features of the tool are discussed. The most distinguishing one is the improved and generalized modal expansion based on the so-called Over-Complete (OC) Frame [157] in contrast to classical Orthogonal-Basis (OB) for low-order modeling of acoustics. Thanks to OC-Frame, it will be shown how it facilitates seamless and full-fledged network construction between subdomains with 1D/2D/3D acoustics and model complex impedances and multi-perforated liners [198].

- **Chapter 3 - STORM Linear Stability Analysis of Annular Configurations:** will apply STORM to build more complex networks of annular configurations. Idealized Plenum-Burner-Chamber (PBC) geometry studied by Bauerheim et al. [136] will be analyzed, and the results from STORM are validated with their 1D wave-based network shown in Fig. 1.13. STORM is also employed to perform the linear stability analysis of lab-scale annular MICCA-spray rig and an actual SAFRAN engine combustor.

It must be acknowledged that most of the foundational work of the methodology, from conceptualization to mathematical formulation and software coding, was carried out by C. Laurent et al. [197, 157]. The objective of Chapters 2 and 3 is to succinctly present and elucidate the essential elements of the modeling approach and provide some complementary results. Complete details, rigorous mathematical derivations, and convergence assessments can be found in C. Laurent's Ph.D. thesis [197]. The author of this manuscript supported the development of the tool through extensive testing and validation studies. The main contribution has been extending the modeling approach to 3D [198, 199], its coding, developing necessary pre-, post-processing tools[11], and successfully demonstrating the stability analysis of complex, realistic configurations, as illustrated in Chapter 3.

- **Chapter 4 - Modeling of Linear Flame Dynamics in STORM:** The previous work of C. Laurent [197], the results presented in preceding chapters, mainly focused on developing and validating the low-order network modeling of acoustics. In almost all the examples, the low-order flame dynamics were represented with simplest, constant $n - \tau$ type FTFs. Therefore, a natural progression was to pursue ways to incorporate more realistic FTFs and develop such modeling capabilities to increase the fidelity of stability analyses. This chapter will focus on this aspect and is a step in that direction. Since

[11] All the pre- and post-processing tools developed are largely based on ANTARES - an in-house python data processing library for CFD (`https://cerfacs.fr/antares/`). Thanks to Dr. Marc Montagnac and the ANTARES development team for helpful discussions and support.

STORM is based on *state-space* (SS) method — a time-domain representation — rational approximation techniques, and a couple of algorithms for fitting SS model on frequency-domain FTF data are reviewed from the literature. Few important physical constraints that must be respected in such data-driven identification of flame-response SS models are described, and some relevant theory, particularly about the causality characteristic of the SS model and FTF data, is discussed as well.

- **Chapter 5 - Delayed Entropy Coupled Boundary Condition (DECBC):** This chapter develops this special impedance boundary condition (DECBC) within the STORM framework that helps predict low-frequency mixed entropy-acoustic instabilities. Modal expansion technique in STORM inherently involves zero-Mach mean flow assumption. DECBC indirectly accounts for mean-flow effects, convected entropy-waves from flame to the combustor outlet. The concept is quite analogous and follows the work of Motheau et al. [45, 46] who developed DECBC for FEM Helmholtz solver AVSP. This chapter presents modeling and validation on a reference 1D case from [45].

PART-2: Euler-Lagrange (EL) LES of SICCA-spray Burner

The minor Part2 of the manuscript is an *application* study where acoustically forced turbulent swirling spray flame has been simulated using the Euler-Lagrange (EL) LES approach in an attempt to predict its Flame-Transfer-Function (FTF) [200]. The objective is to qualify the EL approach, a two-phase combustion modeling framework for such a system identification problem, and at the same time assess the sensitivity of the results to some uncertain modeling parameters.

The work was initiated with the author's wish to develop skills in performing two-phase spray combustion LES. A colleague Ermanno Lo Schiavo - another ESR in the ANNULIGhT project, had built and successfully simulated self-sustained instability in the SICCA-spray burner [60, 201]. Taking E. Lo Schiavo's work as a reference, this complementary task was identified and undertaken with a *limited scope*. Indeed, FTF/FDF is one of the most crucial inputs required to perform thermoacoustic stability analysis with reduced-order (LEE, Helmholtz solvers) or low-order network models such as STORM. Besides experiments, these are usually computed from high-fidelity methods such as LES. The work was carried out in the latter half of the second year (June 2020 - Jan 2021).

- **Chapter 6 - Euler-Lagrange (EL) LES Modeling of Spray Flames**

  Spray combustion is a physical phenomenon characterized by strongly coupled and complex interaction between spray (liquid-phase), flow/turbulence (gas phase), evaporation (phase change), mixing, and of course, chemical reactions. This chapter starts with an overview of relevant spray combustion physics,

followed by a description of the Euler-Lagrange modeling framework. All the specific models employed in the simulations are described while noting the inherent assumptions and known limitations.

- **Chapter 7 - Combustion Dynamics in SICCA-spray Burner**

  This chapter reviews the key results from the work of E. Lo Schiavo et al. [60, 201] and then presents the results of the forced simulations of SICCA-spray flame.

- **Chapter 8 - Thesis Conclusions and Perspectives**

1.6 Publications

This Ph.D. work has led to following journal and conference publications:

1. C. Laurent, A. Badhe, and F. Nicoud, "Representing geometrically complex liners and boundaries in low-order modeling of thermoacoustic instabilities," *Journal of Computational Physics*, vol. 428, 2021.

2. A. Badhe, C. Laurent, C. Lapeyre, and F. Nicoud, "Low-Order Thermoacoustic Analysis of Real Engines," in *Symposium on Thermoacoustics in Combustion (SoTiC): Industry meets Academia, (Munich, Germany)*, 2021.

3. A. Badhe, D. Laera, and L. Gicquel, "High-fidelity Large Eddy Simulations of the Flame Transfer Function of a turbulent swirling spray flame," in *10th European Combustion Meeting, (Napoli, Italy)*, 2021.

Chapter 2

STORM: State-Space Reduced-Order Thermoacoustic Network Modeling Tool

Contents

2.1 Acoustic Network Representation of Systems 31
2.1.1 Introduction to State-Space Method 32
2.2 Over-complete Frame Modal Expansion of Acoustic Subdomains 36
2.2.1 Example 1: 1D-1D Ducts with Section Jump 37
2.2.2 State-space Model of an Acoustic Subdomain 41
2.2.3 State-space Model of the 1D-1D Connection Element 47
2.2.4 State-space Model of the 1D-3D Connection Element 49
2.2.5 Example 2: Coupling 1D-3D Acoustic Cavities 50
2.3 Surface Spectral Connections 52
2.3.1 Illustrative Examples: Coupling 3D-3D Subdomains 53
2.3.2 Curvilinear Helmholtz Equation 55
2.3.3 Embedding Coupling Conditions 56
2.3.4 Surface Modal Expansion 58
2.3.5 SS sub-model for 3D-3D-MLPF Liner Spectral Connection . 61
2.3.6 Adapted SS sub-model of Acoustic Subdomain for Spectral Connection 63
2.4 Solver Structure, and Numerical Strategies for Spurious Eigenmodes 65
2.5 Conclusions 70

2.1 Acoustic Network Representation of Systems

STORM is a new low-order acoustic-network modeling (LOM) tool that is being developed at CERFACS for studying thermoacoustic combustion instabilities in

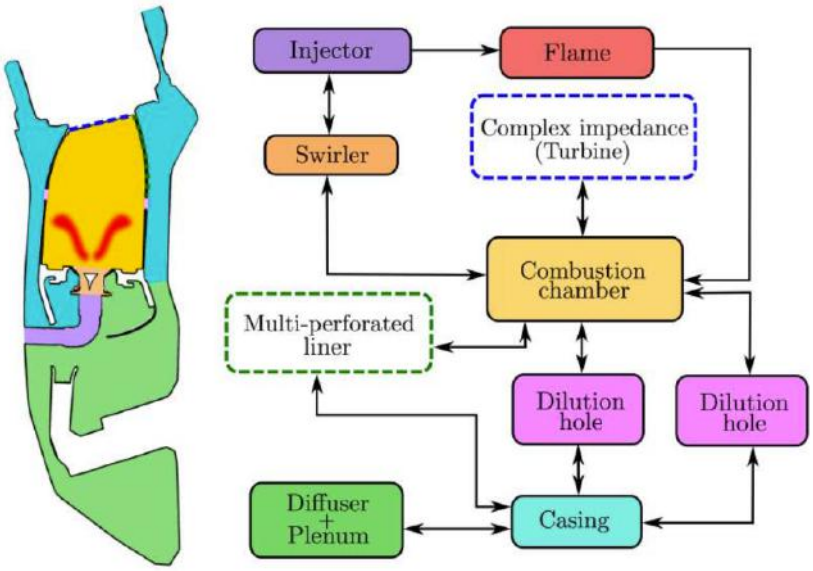

Figure 2.1: Schematic of a gas turbine combustor split into an acoustic network. Arrows indicate coupling between connected subsystems. Each subsystem in the network can be modeled separately. Figure reproduced from [197].

complex realistic configurations, under the assumption of zero-Mach mean flow conditions. It is employs the *state-space* framework, and acoustics modeling is based *generalized modal expansions* [157, 198, 197, 199].

The acoustic network representing a system to be analyzed is built by dividing it into network objects: simpler *geometrical* subdomains, *connection*, *impedance* and *flame* elements. The subdomains can be trivial geometries with 1D/2D acoustics or arbitrary shapes with 3D acoustics. Connection elements are required to couple subdomains in the network by imposing appropriatea physical coupling conditions at the interfaces. A representative example of such decomposition into a network is shown in Fig. 2.1.

The *state-space* framework adopted in thermoacoustics by many research groups in the context of acoustic network modeling [152, 154, 163, 144, 202, 203] has been employed to allow convenient interconnections between different network objects. The state-space (SS) method is briefly introduced in the following subsection.

2.1.1 Introduction to State-Space Method

Dynamical systems are often mathematically modeled from first principles as ordinary differential equations (ODEs) of finite order if the underlying interacting components that make up the system are well characterized, and the physics describing

them is known. A well-known canonical example of a dynamical mechanical system is a spring-mass-damper oscillator governed by a second-order ODE. *State-Space* analysis is a method of representing, solving, and controlling a dynamical system - an approach commonly adopted in modern control engineering [204, 205]. In the state-space method, any finite order ODE governing the system dynamics is recast into a group of first-order ODEs where the variables in each are together known as *state variables*. It is worthwhile to present some key definitions and equations related to state-space methods [204, 205]:

- **State and State Variables:** The state of a dynamic system is the smallest set of variables (called *state variables*) such that the knowledge of these variables at $t = t_0$, along with the inputs for $t \geq t_0$, completely determines the behavior of the system for any time $t \geq t_0$. Note that state variables need not be physically measurable or observable quantities. Such freedom in choosing state variables is an advantage of the state-space methods. Practically, however, it is always convenient to choose easily measurable quantities for the state variables, if possible, to define optimal control laws for the dynamical system.

- **State-Vector and State-Space:** A column vector containing these n state variables is called the *state-vector* $\mathbf{X}(t)$. And the n dimensional space spanned by the state-vector is called the *state-space*.

- **State-Space Equations:** There are three types of variables involved in the modeling of dynamical systems - 1) state variables which are intrinsic to the system under consideration, and 2) input- and 3) output- variables that, as such, are external and independent of the system. The equations relating all these together are the so-called *state-space equations*. As mentioned earlier, the dynamical system is written as a family of first-order ODEs for each state variable in the state-space approach. All these equations are typically written in a compact matrix form given as follows for *linear time-invariant (LTI)* systems.[1]

$$\dot{\mathbf{X}}(t) = \mathbf{A}\mathbf{X}(t) + \mathbf{B}\mathbf{U}(t) \tag{2.1}$$

$$\mathbf{Y}(t) = \mathbf{C}\mathbf{X}(t) + \mathbf{D}\mathbf{U}(t) \tag{2.2}$$

The first equation is called the state-equation that governs the dynamic evolution of system state where $\mathbf{X}(t)$ is the state vector, $\mathbf{A}$ is the system dynamics

[1] State-space analysis, however, applies in general to any dynamical system - linear, nonlinear, time-varying, time-invariant. Nonlinear systems are often linearized around certain operating states called fixed-points, for instance, to carry out linear stability analysis prior to nonlinear prediction and control of system behavior.

matrix, $\mathbf{U}(t)$ is the input vector containing the input variables, and $\mathbf{B}$ is the input matrix. Besides, the second equation above is the state-space output equation that computes the system output vector$\mathbf{Y}(t)$, containing the variables of interest. It is computed from the state vector $\mathbf{X}(t)$, $\mathbf{C}$ the output matrix, and lastly, $\mathbf{D}$ the feedthrough matrix, input vector $\mathbf{U}(t)$, which represents the direct transmission of the input signal to the output, bypassing the system and its intrinsic dynamics.

Coupling multi-input multi-output (MIMO) state-space systems (Redheffer Star product):

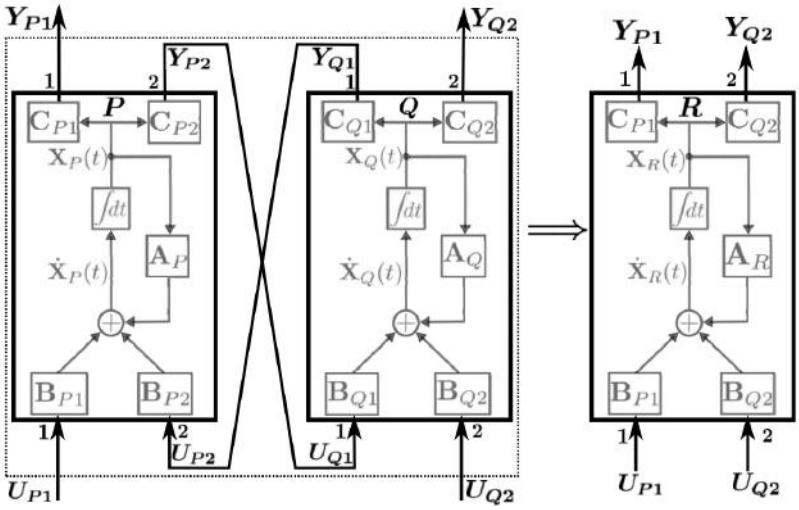

Figure 2.2: Connection of two MIMO systems P and Q. Subscripts P (resp. Q) designate state-space representation matrices and vectors for the subsystem P (resp. Q). Inputs and outputs ports 2 in P are those connected to the subsystem Q, while inputs and outputs ports 1 in P are connected to other systems in the network. Conversely, inputs and outputs ports 1 in Q are those connected to the subsystem P, while inputs and outputs ports 2 in Q are connected to other systems in the network. Figure reproduced from [197].

State-space (SS) models, in general, can have multiple inputs and outputs, i.e., a given subsystem can couple/connect with more than one subsystem to build a network representation of a whole system. There could be multiple connections between the given two subsystems as well. Fig. 2.2 shows a state-space block diagram of two LTI dynamical systems **P** and **Q**. In this hypothetical case, each has two input ports and two output ports, and they are connected as shown. For

clarity, and because it is the case for most of the state-space realizations considered presently, all the feedthrough matrices $\mathbf{D}$ are zero [197].

Then exploiting the so-called *Redheffer star product* [206, 152], the two submodels can be reduced into one resultant state-space model $\mathbf{R}$ by relating their interacting inputs and outputs (actually via matrix product of corresponding port input/output matrices). For example, the SS submodel $\mathbf{P}$ in matrix block-structure is written as (and $\mathbf{Q}$ similarly)

$$\dot{\mathbf{X}}_P(t) = \mathbf{A}_P\mathbf{X}_P(t) + \underbrace{\begin{bmatrix} \mathbf{B}_{P1} & \mathbf{B}_{P2} \end{bmatrix}}_{\mathbf{B}_P} \underbrace{\begin{bmatrix} \mathbf{U}_{P1}(t) \\ \mathbf{U}_{P2}(t) \end{bmatrix}}_{\mathbf{U}_P(t)} \tag{2.3}$$

$$\mathbf{Y}_P(t) = \begin{bmatrix} \mathbf{Y}_{P1}(t) \\ \mathbf{Y}_{P2}(t) \end{bmatrix} = \underbrace{\begin{bmatrix} \mathbf{C}_{P1} \\ \mathbf{C}_{P2} \end{bmatrix}}_{\mathbf{C}_P} \mathbf{X}_P(t) \tag{2.4}$$

then the *Redheffer star product* leads into resultant $\mathbf{R} = \mathbf{P} \star \mathbf{Q}$ state-space model:

$$\underbrace{\begin{bmatrix} \dot{\mathbf{X}}_P(t) \\ \dot{\mathbf{X}}_Q(t) \end{bmatrix}}_{\dot{\mathbf{X}}_R(t)} = \underbrace{\begin{bmatrix} \mathbf{A}_P & \mathbf{B}_{P2}\mathbf{C}_{Q1} \\ \mathbf{B}_{Q1}\mathbf{C}_{P2} & \mathbf{A}_Q \end{bmatrix}}_{\mathbf{A}_R} \begin{bmatrix} \mathbf{X}_P(t) \\ \mathbf{X}_Q(t) \end{bmatrix} + \underbrace{\begin{bmatrix} \mathbf{B}_{P1} \\ \mathbf{B}_{Q2} \end{bmatrix}}_{\mathbf{B}_R} \underbrace{\begin{bmatrix} \mathbf{U}_{P1}(t) \\ \mathbf{U}_{Q2}(t) \end{bmatrix}}_{\mathbf{U}_R(t)} \tag{2.5}$$

$$\underbrace{\begin{bmatrix} \mathbf{Y}_{P1}(t) \\ \mathbf{Y}_{Q2}(t) \end{bmatrix}}_{\mathbf{Y}_R(t)} = \underbrace{\begin{bmatrix} \mathbf{C}_{P1} \\ \mathbf{C}_{Q2} \end{bmatrix}}_{\mathbf{C}_R} \begin{pmatrix} \mathbf{X}_P(t) \\ \mathbf{X}_Q(t) \end{pmatrix} \tag{2.6}$$

In Eq. (2.5), $\mathbf{A}_R$ is the dynamics matrix of the resultant system. The extra-diagonal blocks within it are coupling terms between subsystems $\mathbf{P}$ and $\mathbf{Q}$ [197] — more precisely, $\mathbf{B}_{P2}\mathbf{C}_{Q1}$ represents the effect from $\mathbf{Q}$ onto the dynamics of $\mathbf{P}$, and conversely $\mathbf{B}_{Q1}\mathbf{C}_{P2}$ represents the influence of $\mathbf{P}$ onto the dynamics of $\mathbf{Q}$.

On similar lines, the Redheffer product can be recursively applied to all the SS submodels to couple them and reduce them into one full/global SS model for the entire system as follows:

$$\dot{\mathbf{X}}^f(t) = \mathbf{A}^f\mathbf{X}^f(t) + \mathbf{B}^f\mathbf{U}^f(t) \tag{2.7}$$

Note that for the above global SS equation, the intrinsic dynamical characteristics are all contained inside the global dynamics matrix $\mathbf{A}^f$. The input vector $\mathbf{U}^f(t)$ and matrix $\mathbf{B}^f$ are usually zero unless there is some external forcing applied to the global system. The global SS model can then be solved in one of the following two ways: [197]

1. **Time-domain Resolution:** Eq. 2.7 can be integrated in time to obtain the system-level dynamics starting from an initial condition or temporal evolution under external forcing $\mathbf{U}^f(t)$.

2. **Frequency-domain Resolution:** by finding the eigenvalues and eigenvectors of the global dynamics matrix $\mathbf{A}^f$ so as to obtain the stability information of the eigenmodes of the whole system.

The Redheffer star product is a well-established technique that can couple any number of given state-space network objects as long as the physical quantities communicated between them through multiple inputs/outputs are consistent. In the combustion dynamics community, it was proposed and applied in the state-space LOM by Schuermans et al. [152] as early as 20 years ago. What is rather a more challenging task is to derive state-space models for individual objects.

Therefore, in order to build thermoacoustic networks, the overall objective is to derive appropriate state-space (SS) submodels for all possible types of network objects viz., geometrical (acoustic) subdomains, connection (or coupling) elements, flame, impedance, etc.

2.2 Over-complete Frame Modal Expansion of Acoustic Subdomains

This section will describe the most vital and distinguishing attribute of STORM, i.e., this concept of *generalized modal expansion* that was mentioned earlier.

In the modal-expansion method, the thermoacoustic pressure field in each *geometrical* sub-domain of the network is expressed as a linear combination or series expansion of natural acoustic eigenmodes of that particular subdomain (the basis functions),

$$p(\vec{x},t) = \sum_{n=1}^{N} \dot{\Gamma}_n(t)\phi_n(\vec{x}) = \dot{\mathbf{\Gamma}}^T(t)\boldsymbol{\phi}(\vec{x}) \tag{2.8}$$

where N is a finite number of natural eigenmodes, $\phi_n(\vec{x})$ denote the basis functions and $\dot{\Gamma}_n(t)$ are the corresponding modal amplitudes or coefficients. Note that in the above equation, the natural modes are known a priori as analytical or numerical solutions to homogeneous Helmholtz equation (without flame source term, non-trivial boundary impedances.) for a given subdomain. The modal amplitudes are, therefore, the unknown variables to be determined. They are subject to the influence of boundary conditions imposed by neighboring subdomains and to the volumetric forcing exerted by active flames if present. The modal basis represents the spatial structure of the acoustic pressure field, while the modal amplitudes determine

its temporal evolution. The acoustic velocity field in the subdomain can also be constructed from the gradient of the modal basis as follows:

$$\vec{u}(\vec{x},t) = -\frac{1}{\rho_0}\sum_{n=1}^{N}\Gamma_n(t)\vec{\nabla}\phi_n(\vec{x}) = -\frac{1}{\rho_0}\mathbf{\Gamma}^T(t)\vec{\boldsymbol{\nabla}}\boldsymbol{\phi}(\vec{x}) \tag{2.9}$$

Laurent et al. [157, 197] improved and generalized the classical modal expansions (Galerkin projection) technique. Most previous studies based on modal expansions employed *rigid-wall* natural eigenmodes as an orthogonal[2] basis for seeking the thermoacoustic pressure field solution. However in this recently proposed approach, one can use as the basis functions either an over-complete set of acoustic eigenmodes — called as an ***Over-Complete (OC) Frame*** — or a simple ***Orthogonal Basis (OB)*** as has been the norm so far. The former, where deemed necessary, offers enhanced convergence, correct representation of acoustic variables at the interfaces of interconnecting subdomains, and fixes the issue of Gibbs oscillations in the global network solutions.

In practice, a convenient way to build a frame is by collating rigid-wall ($u' = 0$) and pressure release ($p' = 0$), two families of natural eigenmodes. The second family verifies at least one $p' = 0$ boundary, usually located at the connection boundary between two subdomains. Modal Expansion on an OC-frame eventually relaxes (or unconstrains) the u'=0 (and p'=0) conditions owing to the constituent orthogonal bases, thus facilitating the correct representation of acoustic variables at the interface.

The points made above regarding Overcomplete Frame expansions are elaborated with the help of a simple 1D example in the following Subsec. 2.2.1.

2.2.1 Example 1: 1D-1D Ducts with Section Jump

Consider a pure acoustics problem involving a 1D ducts as shown in Fig. 2.3(a). The physical quantities in the ducts are assumed to be constant and homogenous. The aim is to compute natural acoustic eigenmodes of the system via network decomposition in STORM as depicted in Fig. 2.3(b). The network comprises two geometrical subdomains - long narrow ducts with 1D acoustics, noted as Ω_1, Ω_2, and a connection element Ω_{sc} to impose the right coupling/jump conditions [13, 135] between them, viz., acoustic pressure and flux continuity.

For this network configuration, as shown in Fig. 2.4, a the suitable OC-frame for duct/subdomain Ω_1 is built by concatenating *two families* of OB bases that satisfy different boundary conditions on right hand side connection boundary: (i)

[2] **Orthogonality:** Natural acoustic eigenmodes of any arbirtrary geometry are orthogonal to each other. This can be verified [127], say for set natural eigenmodes $\xi_n(\vec{x},\omega)$, by taking (scalar) inner-product between them: $\langle \xi_n, \xi_m \rangle = 0 \quad \forall m \neq n$. More details to follow in this and Sec. 2.2.2.

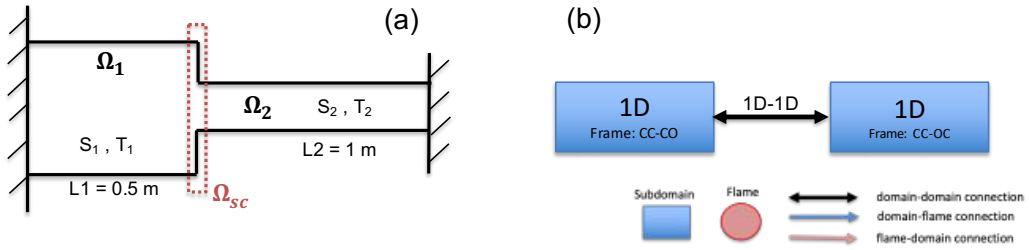

Figure 2.3: (a) An acoustics example of 1D ducts with cross-section area jump, used for illustrating the concept of overcomplete frame modal expansion. The two extreme ends are considered to be closed rigid walls. (b) Network representation of the system. See also Fig. 2.4.

first family[3] CC satisfies $u' = 0$ rigid-wall condition (the blue $\xi_n^{(\Omega_1)}$ modes), and (ii) second family[4] CO verifies $p' = 0$ pressure-release condition (the orange $\zeta_n^{\Omega_2}$ modes). Analogously, for the duct Ω_2 an appropriate choice of frame, with respect to duct Ω_1, will be CC-OC. The natural acoustic eigenmodes for each duct and each family are straightforward to derive analytically as cosine/sine functions - see, e.g., in [13, 207, 135]. Hence, the analytical OC-frames for the two ducts can be mathematically defined as follows:

$$\begin{cases} \left(\phi_n^{(\Omega_1)}(x_1)\right)_{n\leqslant N_1} = \left(\cos\left(\frac{n\pi x_1}{L_1}\right)\right)_{n\leqslant N_1/2} \bigcup \left(\cos\left(\frac{(2n-1)\pi x_1}{2L_1}\right)\right)_{n\leqslant N_1/2} \\ \left(\phi_n^{(\Omega_2)}(x_2)\right)_{n\leqslant N_2} = \left(\cos\left(\frac{n\pi x_2}{L_2}\right)\right)_{n\leqslant N_2/2} \bigcup \left(\sin\left(\frac{(2n-1)\pi x_2}{2L_2}\right)\right)_{n\leqslant N_2/2} \end{cases} \tag{2.10}$$

where N_1, N_2 are total number of modes in the OC frames of subdomains Ω_1, Ω_2 respectively.

The 1D network configuration in Fig. 2.3 is solved with STORM to compute the acoustic eigenmodes of the whole two-duct system, and the first three eigenfrequencies are listed in the Tab. 2.1 along with analytically computed [13, 207, 135] values. The STORM problem is solved in two ways: first employing the classical *rigid-wall OB* (i.e. only $\xi_n^{(\Omega_1)}$ and $\xi_n^{(\Omega_2)}$ orthogonal bases) in both the ducts, and second with the newly proposed *OC-frames* as well. In the following, same number ($N_1 = N_2 = N = 20$) of natural modes are used for the modal expansion in the two subdomains. Note that the eigenfrequencies from both OB and OC modal expansions cases in STORM are correct and in good agreement with analytical solution for this problem, however, there is a major issue with eigenmode shapes between the two as highlighted in Fig. 2.5 and Fig. 2.6.

The rigid-wall OB modal expansion imposes a velocity node at the interface, despite the actual mode shape having non-zero pressure and velocity. In other

[3] CC: Closed-Closed
[4] CO: Closed-Open

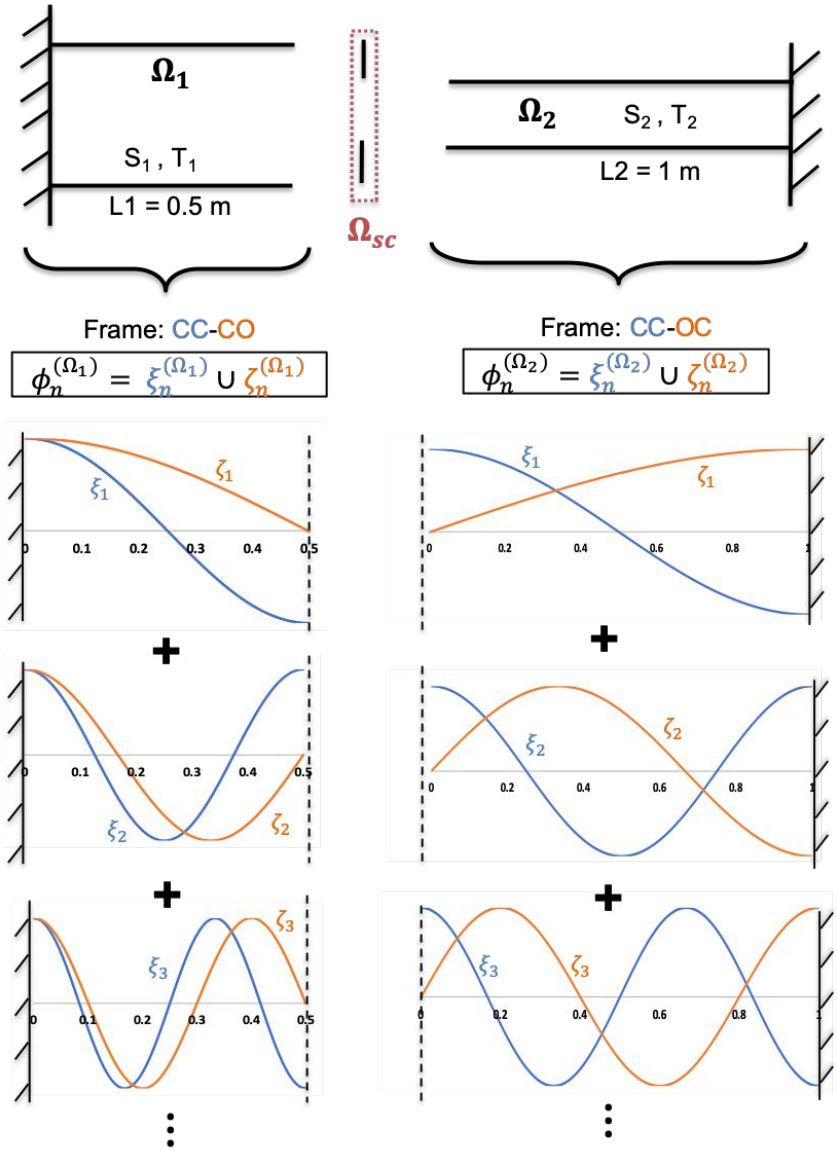

Figure 2.4: Overcomplete (OC) frames for 1D network subdomains Ω_1 and Ω_2 from Fig. 2.3.

words, the OB bases *constrain* the velocity at the junction since they both inherently satisfy rigid-wall (u'=0) boundary condition. In Fig. 2.5 although the full pressure mode shape is predicted reasonably well, minor discrepancies exist locally near the interface. For the more problematic velocity mode shape, characteristic *Gibbs- effect/oscillations/wiggles/fringes* can be observed in the network solution, i.e., in both the ducts, due to the imposed velocity node. Laurent et al. [157, 197] therefore proposed OC-frame modal expansions to deal with this issue. It addresses the following fundamental question associated with OB modal expansion based net-

Parameters	Mode	Analytical	STORM (OB & OC)
$T_1 = T_2, c_0 = 347.0$ m/s	1	105.5	105.5
$P_0 = 1$ atm, $\rho_0 = 1.17$ kg/m^3	2	241.5	241.5
$S_1 = 2S_2 = 0.1$ m^2	3	347.0	347.0

Table 2.1: Frequencies (Hz) of the first three acoustic eigenmodes for the configuration in Fig. 2.3. The eigenfrequencies from STORM are identical from both OB-basis and OC-frame for this example. Physical and geometrical parameters for the specific problem solved are as given in the first column.

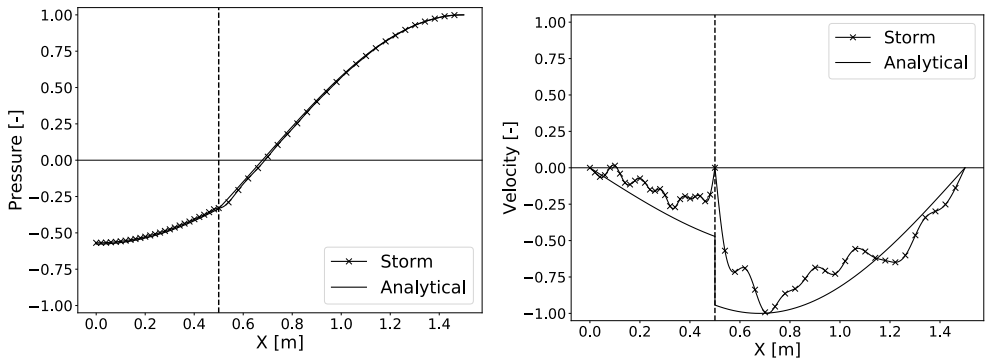

Figure 2.5: First acoustic eigenmode shape (105.5 Hz) of the network in Fig. 2.3, obtained with rigid-wall *Orthogonal Basis (OB)* modal expansions.

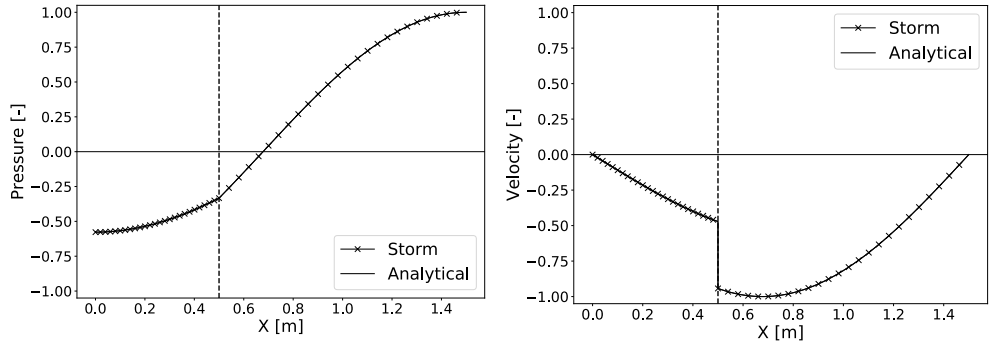

Figure 2.6: First acoustic eigenmode shape (105.5 Hz) of the network in Fig. 2.3, obtained with *Overcomplete (OC)- Frame* modal expansions.

works [157, 197]: *how can a solution expressed as a series expansion of rigid-wall modes converge towards a solution satisfying a non-rigid-wall boundary condition?*

Figure 2.6 depicts how OC-frame expansion improves the mode shapes providing excellent agreement with analytical solution. Referring to Fig. 2.4, in case of OC-

frames, the rigid-wall ($u' = 0$) OB basis of each subdomain (blue ξ_n modes) is augmented with another family of OB basis verifying pressure-release boundary condition ($p' = 0$) at the interface (orange ζ_n modes). As a result, OC-frame provides an additional degree of freedom for acoustic variables at the interface in final network resolution. Both pressure and velocity become unconstrained a priori and can attain their correct actual values. Therefore, OC-frame modal expansions accurately represent acoustic variables or pressure-velocity relation (or impedance in other words)[5]at the interface between two subdomains in the network resolution.

The OB or OC-frame size, i.e., the finite number of natural eigenmodes (N) used in the modal expansion of subdomains, is an important parameter in STORM computations. OC-frame significantly improves the convergence of the modal expansion can provide the first couple of global eigenmodes accurately with very few frame modes ($N < 10$ for this example). On the contrary, for OB, increasing basis size N to order of ~ 100 improves the overall accuracy, but locally near the interface velocity node, and Gibbs fringes are not eliminated. Also, as expected, accurately capturing higher-order modes of the global system will require larger OC-frames of the subdomains. A systematic convergence assessment and error analysis, for the same example above and others, was carried out in the thesis of C. Laurent [197], and will not be repeated here to keep this presentation concise.

Now that the concept of OC-frame is established through the simple acoustics example of 1D ducts in Fig. 2.3, the next subsection will describe the details of state-space (SS) representation of any type of acoustic subdomain. Also, the connection domain/element Ω_{sc} that coupled the two 1D ducts in the example above is essentially quite important and will be presented in the following Sec. 2.2.3.

2.2.2 State-space Model of an Acoustic Subdomain

This section will summarize the state-space representation of a generic acoustic subdomain based on its OC-frame modal expansion - that forms the backbone of STORM tool, as proposed in the previous Ph.D. work of C. Laurent [197].

Consider a general, hypothetical, thermoacoustic network in Fig. 2.7 that contains all elements that are typically found in a gas turbine combustor that must be accounted for comprehensive stability analysis. It contains several different types of network objects as detailed in the accompanying tables in Fig. 2.7.

Focussing on acoustic subdomain Ω_i, the frequency-domain [6] thermoacoustic pressure field $\hat{p}(\vec{x}, \omega)$, under zero-Mach mean-flow assumption (see Ch. 1, Sec. 1.4.1)

[5]Consequently, OC-frame modal expansions become the foundation for: (i) modeling complex boundary impedances (in Chapter 5), and (ii) *surface spectral connections*[198] used to model multi-perforated liner conductivity, or simply couple subdomains with 2D/3D acoustics (described in the forthcoming Sec. 2.3).

[6]Following Fourier Transform defintion in Eq. (1.3) with convention $p'(\vec{x}, t) = \Re\{\hat{p}(\vec{x}, \omega)e^{j\omega t}\}$.

is solution to the following of *inhomogeneous Helmholtz Equation* containing volumetric and boundary surface acoustic source terms:

$$\begin{cases} c_0^2\nabla^2\hat{p}(\vec{x},\omega) - j\omega\alpha\hat{p}(\vec{x},\omega) + \omega^2\hat{p}(\vec{x},\omega) = \hat{h}(\vec{x},\omega) \quad \text{for} \quad \vec{x}\in\Omega_i \\ \nabla_s\hat{p} = 0 \text{ for } \vec{x}_s \in S_{wi}, \\ \hat{p} = 0 \text{ for } \vec{x}_s \in S_{ai}, \\ \nabla_s\hat{p} = \hat{f}\left(\vec{x}_s,\omega\right) \quad \text{or} \quad \hat{p} = \hat{g}\left(\vec{x}_s,\omega\right) \text{ for } \vec{x}_s \in S_{ci} \end{cases} \tag{2.11}$$

where, α is an ad-hoc acoustic loss coefficient for applying homogenous and uniform acoustic damping in the subdomain, $\hat{h}(\vec{x},\omega)$ is a volumetric acoustic source term, $\nabla_s\hat{p}(\vec{x},\omega) = \nabla\hat{p}(\vec{x},\omega)\cdot\vec{n}_s$ is the acoustic surface flux, $\vec{n}_s$ is being the outward pointing surface normal vector at the point $\vec{x}_s$. Note that boundary condition on connection boundaries S_{ci} in general are inhomogeneous of Neumann type or Dirichlet type with $\hat{f}\left(\vec{x}_s,\omega\right)$ and $\hat{g}\left(\vec{x}_s,\omega\right)$ being the surface source terms imposed on subdomain Ω_i by its neighboring subdomains (or by non-trivial global boundary impedances). In other words, S_{ci} connection interfaces are neither $\nabla_s\hat{p} = 0$ (rigid-walls) nor $\hat{p} = 0$ (open-to-atm) and this where OC-frame expansions in subdomains (Ω_i and others) will be instrumental in correct charaterization of acoustic variables on these interfaces. The term $\hat{h}(\vec{x},\omega)$ comprises the contributions of the M_H volumetric heat source network objects/submodels $H_i^{(l)}$ within subdomain Ω_i:

$$\hat{h}(\vec{x},\omega) = -j\omega(\gamma-1)\sum_{l=1}^{M_H}\mathcal{H}_i^{(l)}(\vec{x})\hat{Q}_l(\omega) \tag{2.12}$$

where, $\hat{Q}_l(\omega)$ is the *global* fluctuating heat-release of the flame $H_i^{(l)}$, and $\mathcal{H}_i^{(l)}(\vec{x})$ its spatial distribution.

The part of the thermoacoustic pressure field of the global network solution, in a given subdomain Ω_i, is then sought by projecting the inhomogeneous Helmholtz Eq. (2.11) onto that subdomain's OC-frame/OB-basis $\phi_n(\vec{x})$ through the Galerkin-projection/Modal-expansion process as given by Eq. (2.8).

The OC-frame/OB-basis $\phi_n(\vec{x})$ are natural acoustic eigenmodes of subdomain Ω_i— i.e. solutions of *homogeneous Helmholtz equation*, same as Eq. (2.11) but without source terms. As mentioned earlier, OC/OB can be defined analytically for simple geometries (e.g., 1D-ducts in previous Sec. 2.2.1 - Eq. (2.10)), or can be found numerically using FEM-based Helmholtz solvers [127, 129] (examples to follow).

The Galerkin projection procedure and its rigorous, lengthy mathematical derivation for both cases: the classical modal expansion based on OB, and the new approach of OC-frame, is detailed in the thesis of C. Laurent [197].

In modal expansion based LOMs, a *volume scalar (inner) product* is required that is defined as

$$\langle f,g\rangle = \iiint_{\Omega_i} f(\vec{x})g(\vec{x})d^3\vec{x} \tag{2.13}$$

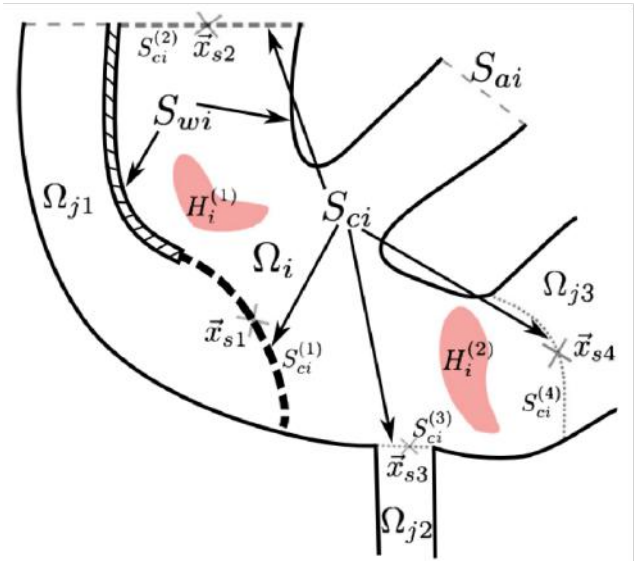

rigid-wall ($u' = 0$)
atmosphere opening ($p' = 0$)
boundary complex impedance (Z)
multi-perforated liner (K_R)
subdomains interface

Symbols/ Notations	Remarks
Ω_i	Acoustic subdomain
Ω_{j1} Ω_{j2} Ω_{j3}	Neighboring subdomains of Ω_i
S_{wi} S_{ai} S_{ci}	Categories of boundaries of Ω_i : rigid-walls, open to atm, connections to other subdomains.
$S_{ci}^{(1)}$	Multi-perforated Liner Connection
$S_{ci}^{(2)}$	Acoustic Impedance Boundary
$S_{ci}^{(3)}$ $S_{ci}^{(4)}$	Domain-domain Connection
$\vec{x}_{sk}$	Surface coordinates on $S_{ci}^{(k)}$
$H_i^{(1)}$ $H_i^{(2)}$	Multiple flames/heat-sources in Ω_i

Figure 2.7: Schematic of a generic STORM thermoacoustic network involving different types of objects: multiple acoustic subdomains and flames, different types of domain-domain connection elements and non-trivial boundary impedance elements. Refer the adjacent tables. Figure adapted from [197].

The basis eigenmodes in OB are orthogonal to each other [127], and can be verified with the above scalar product, which will vanish for any two ϕ_m and ϕ_n $\forall$ $m \neq n$. However, this is not true for an OC-frame. The frame modes of one constituent family may not be orthogonal to modes from the other family. This non-orthogonality has major implications on the OC-frame-based modal expansion and will be described along the way in this chapter. An associated L_2 *norm* can be defined as $||f||_2 = \langle f, f \rangle^{1/2}$.

The Galerkin projection of Eq. (2.11) on an OC-frame yields a system of dynamic ODEs that govern the modal expansion coefficients $\dot{\Gamma}_n(t)$, $\Gamma_n(t)$ in Eq. (2.8) and Eq. (2.9) as follows [197]:

$$\begin{aligned}
&\ddot{\Gamma}_n(t) = -\alpha\dot{\Gamma}_n(t) - \omega_n^2\Gamma_n(t) \\
&+ \sum_{m=1}^{M_S} \iint_{S_{ci}^{(m)}} \rho_0 c_0^2 \left(\varphi^{S_{ci}^{(m)}}(\vec{x}_s, t) \left[\mathbf{\Lambda^{-1}} \boldsymbol{\nabla_s} \boldsymbol{\phi}(\vec{x}_s)\right]_n - u_s^{S_{ci}^{(m)}}(\vec{x}_s, t) \left[\mathbf{\Lambda}^{-1} \boldsymbol{\phi}(\vec{x}_s)\right]_n \right) d^2\vec{x}_s \\
&+ \sum_{l=1}^{M_H} (\gamma - 1) Q_l(t) \left[\mathbf{\Lambda}^{-1} \left\langle \boldsymbol{\phi}, \mathcal{H}_i^{(l)} \right\rangle\right]_n
\end{aligned} \tag{2.14}$$

where terms in the above equation are explained below:

- ω_n is pulsation frequency (rad/s) of the natural acoustic modes in OB/OC-

frame of the subdomain Ω_i.

- Subdomain Ω_i is coupled/connected to $m = 1$ to M_S adjacent subdomains over $S_{c_i}^{(m)}$ connection boundaries.

- In the right hand side, the surface integrals over each $S_{c_i}^{(m)}$, are boundary source terms representing the *acoustic potential* $\varphi^{S_{c_i}^{(m)}}(\vec{x}_s, t)$ and *acoustic velocity* $u_s^{S_{ci}^{(m)}}(\vec{x}_s, t)$ forcing on Ω_i from adjacent subdomains in the network respectively.

  It was necessary to work with acoustic variables - (potential, velocity) instead of what would have been a more natural choice - (pressure, velocity) since potential provided crucial simplification in the derivation of Eq. (2.14), particularly in its inverse Fourier transform from its frequency-domain precursor. The acoustic potential is defined as:

$$\varphi(t) = -\frac{1}{\rho_0}\int p(t')dt' \tag{2.15}$$

- **Gram-Matrix $\mathbf{\Lambda}$** of the OC-frame of Ω_i whose elements are given by

$$\mathbf{\Lambda}_{nm} = \langle \phi_n, \phi_m \rangle = \iiint \phi_n(\vec{x})\phi_m(\vec{x})d^3\vec{x} \tag{2.16}$$

  Note that in the case of OB, $\mathbf{\Lambda}_{nm}$ reduces to a *diagonal matrix* $\mathbf{\Lambda}_n$ due to *orthogonality* of eigenmodes discussed above. However, OC-frames and their non-orthogonality have strong implications: its leads to highly ill-conditioned Gram matrix $\mathbf{\Lambda}$, the apparition of spurious unphysical modes in the global network resolution, their interaction, and other numerical challenges - (covered in Sec. 2.4).

- $\boldsymbol{\nabla_s \phi}(\vec{x}_s)$ is a column vector containing the normal gradients of the OC/OB modes on the connection boundaries $S_{c_i}^{(m)}$.

- $[\ ]_n$ denotes the n^{th} component of the column vector.

- A subdomain Ω_i can also have *none* or $l = 1$ to M_H number of heat sources (or flames) noted $H_i^{(l)}$ within it, and the last term is this volume source term. $\langle \boldsymbol{\phi}, \mathcal{H}_i^l(\vec{x}) \rangle$ a column vector containing the inner products, i.e., *projection of the physical flame shape* $\mathcal{H}_i^l(\vec{x})$ on the OB/OC-frame modes $\phi_n(\vec{x})$, while $Q_l(t)$ is the *global* fluctuating heat release rate of corresponding heat sources.

It is worth emphasizing here that it is not necessary to use an OC-frame modal expansion for all subdomains at all times. The choice is based on geometrical and physical considerations, as will be pointed out in the following examples in this and the subsequent chapter. Under many situations, a simple OB basis is sufficient. In

such a case, the $\phi_n(\vec{x})$ could be replaced by (or would represent) an OB basis, and the above system of equations (Eq. (2.14)) specific to frames are still applicable, thanks to their generality. They simply reduce to the classical Galerkin projection equations due to the orthogonality of OB basis modes. Hence, the proposed OC-frame expansion is referred to as a *generalized modal expansion* method [157, 197].

The dynamical system of ODEs in Eq. (2.14) can be recast into a *State-space (SS) sub-model for the acoustic subdomain*[7] Ω_i which is given as follows:

SS Dynamics Equation

$$\underbrace{\frac{d}{dt}\begin{pmatrix} \Gamma_1(t) \\ \dot{\Gamma}_1(t) \\ \vdots \\ \Gamma_N(t) \\ \dot{\Gamma}_N(t) \end{pmatrix}}_{\mathbf{x}^{\Omega_i}(t)} = \underbrace{\begin{pmatrix} 0 & 1 & & & \\ -\omega_1^2 & -\alpha & & & \\ & & \ddots & & \\ & & & 0 & 1 \\ & & & -\omega_N^2 & -\alpha \end{pmatrix}}_{\mathbf{A}^{\Omega_i}} \begin{pmatrix} \Gamma_1(t) \\ \dot{\Gamma}_1(t) \\ \vdots \\ \Gamma_N(t) \\ \dot{\Gamma}_N(t) \end{pmatrix} + \underbrace{\begin{pmatrix} \mathbf{B}_1^{S_{\text{ci}}^{(1)}} & \dots & \mathbf{B}_1^{S_{\text{ci}}^{(M_S)}} & \mathbf{B}_1^{H_i^{(1)}} & \dots & \mathbf{B}_1^{H_i^{(M_H)}} \\ \vdots & \ddots & \vdots & \vdots & \ddots & \vdots \\ \mathbf{B}_N^{S_{\text{ci}}^{(1)}} & \dots & \mathbf{B}_{N'^i}^{S_{\text{ci}}^{(M_S)}} & \mathbf{B}_N^{H_i^{(1)}} & \dots & \mathbf{B}_N^{H_i^{(M_H)}} \end{pmatrix}}_{\mathbf{B}^{\Omega_i}} \underbrace{\begin{pmatrix} \mathbf{U}^{S_{ci}^{(1)}} \\ \vdots \\ \mathbf{U}^{S_{ci}^{(M_S)}} \\ Q_1(t) \\ \vdots \\ Q_{M_H}(t) \end{pmatrix}}_{\mathbf{U}^{\Omega_i}(t)} \tag{2.17}$$

where *blocks* in the SS input matrix $\mathbf{B}^{\Omega_i}$ and SS input vector $\mathbf{U}^{\Omega_i}(t)$ are

$$\begin{aligned} \mathbf{B}_n^{S_{ci}^{(m)}} &= \rho_0 c_0^2 \Delta S_{ci}^{(m)} \begin{pmatrix} 0 & 0 \\ -\left[\mathbf{\Lambda}^{-1}\boldsymbol{\phi}\left(\vec{x}_{sm}\right)\right]_n & \left[\mathbf{\Lambda}^{-1}\boldsymbol{\nabla}_s\boldsymbol{\phi}\left(\vec{x}_{sm}\right)\right]_n \end{pmatrix} \\ \mathbf{B}_n^{H_i^{(l)}} &= \begin{pmatrix} 0 \\ (\gamma-1)\left[\mathbf{\Lambda}^{-1}\left\langle\boldsymbol{\phi}, \mathcal{H}_i^{(l)}\right\rangle\right]_n \end{pmatrix}, \quad \mathbf{U}^{S_{ci}^{(m)}} = \begin{pmatrix} u^{S_{ci}^{(m)}}\left(\vec{x}_{sm}, t\right) \\ \varphi^{S_{ci}^{(m)}}\left(\vec{x}_{sm}, t\right) \end{pmatrix} \end{aligned} \tag{2.18}$$

Here an **important assumption** is made: that each connection boundary S_{ci} is *spatially very small* of surface area ΔS_{ci}, such that acoustic variables can be approximated to be uniform of on it. This simplifies the boundary surface integral in Eq. (2.14). The assumption is justified for narrow interconnecting ducts with 1D acoustic waves as in the previous example, but is not true in general, especially for

[7] Many state-space (SS) representations, from subdomains to other types of network objects, that are presented in this manuscript, are also described in the Appendix of C. Laurent's thesis [197]. Reproduced here for the ease of readability and explanation of theory and concepts.

the kind of connection boundaries with large surfaces shown in Fig. 2.7. In this latter case, the above equations will have to be adapted by *spatially discretizing* [8] each connection boundary $S_{ci}^{(m)}$ into smaller sub-surfaces (indexed with subscript r) leading to enlarged block structure inside the SS matrices/vectors: for instance, instead of each $\mathbf{B}_n^{S_{ci}^{(m)}}$ (resp. $\mathbf{U}^{S_{ci}^{(m)}}$) there will be $\mathbf{B}_{n,1}^{S_{ci}^{(m)}} \cdots \mathbf{B}_{n,r}^{S_{ci}^{(m)}}$ (resp. $\mathbf{U}_1^{S_{ci}^{(m)}} \cdots \mathbf{U}_r^{S_{ci}^{(m)}}$).

SS Output Equation

Accompanying the SS Dynamics equation is the SS output equation of the subdomain given below. Note that the feedthrough matrix $\mathbf{D}$ is not required and is zero.

$$\underbrace{\begin{pmatrix} \mathbf{Y}^{S_{ci}^{(1)}} \\ \vdots \\ \mathbf{Y}^{S_{ci}^{(M_S)}} \end{pmatrix}}_{\mathbf{Y}^{\Omega_i}(t)} = \underbrace{\begin{pmatrix} \mathbf{C}_1^{S_{ci}^{(1)}} & \dots & \mathbf{C}_N^{S_{ci}^{(1)}} \\ \vdots & \ddots & \vdots \\ \mathbf{C}_1^{S_{ci}^{(M_S)}} & \dots & \mathbf{C}_N^{S_{ci}^{(M_S)}} \end{pmatrix}}_{\mathbf{C}^{\Omega_i}} \underbrace{\begin{pmatrix} \Gamma_1(t) \\ \dot{\Gamma}_1(t) \\ \vdots \\ \Gamma_N(t) \\ \dot{\Gamma}_N(t) \end{pmatrix}}_{\mathbf{X}^{\Omega_i}(t)} \tag{2.19}$$

where the *blocks* inside SS output matrix $\mathbf{C}^{\Omega_i}$ and output vector $Y^{\Omega_i}(t)$ are

$$\mathbf{Y}^{S_{ci}^{(m)}} = \begin{pmatrix} u_s\left(\vec{x}_{sm}\right) \\ p\left(\vec{x}_{sm}\right) \end{pmatrix} \quad , \quad \mathbf{C}_n^{S_{ci}^{(m)}} = \begin{pmatrix} -\frac{1}{\rho_0}\nabla_s\phi_n\left(\vec{x}_{sm}\right) & 0 \\ 0 & \phi_n\left(\vec{x}_{sm}\right) \end{pmatrix} \tag{2.20}$$

SS Dynamics Eq. (2.17) convey how the state-vector, for the subdomain Ω_i under consideration, evolves in time under the influence of inputs: the acoustic potential and velocity boundary forcing from the neighboring subdomains, and volumetric sources, i.e., flames. Simultaneously, the complementary SS Output Eq. (2.19), computes the desired acoustic variables (velocity, pressure) from state-variables at the boundaries of a subdomain as output for the neighboring subdomains. The modal expansion coefficients are the state variables because their values completely describe the acoustic field in the subdomain at any time instant.

Accordingly, the above sets of equations together constitute a multi-input multi-output (MIMO) state-space sub-model for an acoustic subdomain Ω_i, which can then couple with other SS sub-models via Redheffer star product (Sec. 2.1.1) to build a network of the whole system. It must be highlighted here that an acoustic subdomain does not communicate directly with another subdomain, but a connection network element/object in between them facilitates this. The next subsection will elaborate more on connection elements, their purpose, and how they function.

[8] Further elaboration on this assumption in the upcoming examples. Also, an alternative approach employing *spectral discretization* of large connection boundaries of subdomains, instead of *spatial*, is the topic of Sec. 2.3.

2.2.3 State-space Model of the 1D-1D Connection Element

After dividing a complex system into simpler subdomains as in Figs. (2.1, 2.3, 2.7), the acoustic subdomains become independent of each other. Then as expected, special attention is required at the junctions between subdomains for them to be appropriately coupled. The connection elements/objects in the STORM network ensure proper communication between subdomains by imposing expected *physical coupling conditions* at the junction/interface. For example, the pressure continuity and acoustic flux continuity is what is imposed by the 1D-1D connection domain Ω_{sc} in the previous example of Fig. 2.3 - then it is due to sudden section area change that causes a jump in the acoustic velocity at the interface.

Acoustic subdomains in a STORM network, in general, can be of varied dimensions with 1D/2D/3D acoustics. Therefore, different connection elements are required depending upon the subdomains considered in a pair. E.g., the 1D-1D connection element is the most fundamental type of connector that is explained in this section below along with its state-space modeling [197]. Other types of connection elements are presented in the upcoming sections.

Referring to Fig. 2.3, for obtaining a SS submodel for the connection element, a small fictitious subdomain (or control-volume) Ω_{sc} is considered around the section change such that its length $L_{sc} <<< L_1, L_2$, i.e. it is *acoustically compact*. In reality, the acoustics around sudden section-change is 3D locally; however, these 3D perturbations have negligible impact on the overall acoustics of the ducts and eigenmodes of the global system. It is therefore not explicitly resolved in Ω_{sc}. However, instead, an integral approach is employed whereby the acoustics in Ω_{sc} is expressed with *volume-averaged linearized Euler equations (LEE)*, again under zero-Mach mean flow conditions (- being consistent with the acoustic subdomains). Acoustic damping due to conversion into vorticity at the sharp edge is neglected.

Introducing volume-averaged (vol-avg) acoustic pressure ($\bar{p}(t)$), velocity ($\bar{u}(t)$) and potential ($\bar{\varphi}(t)$), the vol-avg-LEE is given as [197, 112]:

$$\begin{cases} \frac{d\bar{u}}{dt} = \frac{1}{\rho_0 L_{sc}} \left(p^{\Omega_1}(t) - p^{\Omega_2}(t) \right) \\ \\ \frac{d\bar{p}}{dt} = \frac{2\rho_0 c_0^2}{L_{sc}(S_1+S_2)} \left(S_1 u_s^{\Omega_1}(t) + S_2 u_s^{\Omega_2}(t) \right) \end{cases} \tag{2.21}$$

where $p^{\Omega_1}(t)$ and $u_s^{\Omega_1}(t)$ (resp. $p^{\Omega_2}(t)$ and $u_s^{\Omega_2}(t)$) are the pressure and the normal acoustic velocity imposed by the subdomain Ω_1 (resp. Ω_2) onto Ω_{sc}. The + sign in the second equation is due to the fact that the outer normals at S_{c1} and S_{c2} (- connection boundaries of Ω_1, Ω_2) are defined with respect to Ω_1 and Ω_2 respectively, and therefore are pointing in opposite directions [197]. For low-frequencies, these conservation equations reduce to the classical quasi-static jump relations $p^{\Omega_1} = p^{\Omega_2}$ and $S_1 u_s^{\Omega_1} = -S_2 u_s^{\Omega_2}$. Vol.avg. acoustic variables then make an appropriate choice

of state-variables for the SS sub-model as they completely express the dynamic state of the connection domain Ω_{sc} under the influence of acoustics from the subdomains on its two sides (and for their geometrical specificities - section areas for this case).

Pressures and normal velocities imposed back by Ω_{sc} onto the two ducts Ω_1 and Ω_2 can then be calculated thanks to 0^{th}-order approximations (i.e. piece-wise constant functions) as:

$$\begin{cases} u_s\left(x_{sc}=0,t\right)=\frac{1}{2}\left(1+\frac{S_2}{S_1}\right)\bar{u}(t), p\left(x_{sc}=0,t\right)=\bar{p}(t) \\ \\ u_s\left(x_{sc}=L_{sc},t\right)=-\frac{1}{2}\left(1+\frac{S_1}{S_2}\right)\bar{u}(t), p\left(x_{sc}=L_{sc},t\right)=\bar{p}(t) \end{cases} \tag{2.22}$$

In other words, satisfying the above equations Eq. (2.21) and Eq. (2.22) ensures appropriate coupling and determines the values of acoustic variables on the respective interfaces of the two subdomains.

The above system can then be recast into a state-space sub-model for coupling 1D-1D subdomains as below:

SS Dynamics:

$$\begin{aligned} \underbrace{\frac{d}{dt}\begin{pmatrix}\bar{u}(t)\\ \bar{p}(t)\\ \bar{\varphi}(t)\end{pmatrix}}_{\mathbf{X}(sc)(t)} &= \underbrace{\begin{pmatrix}0 & 0 & 0\\ 0 & 0 & 0\\ 0 & -1/\rho_0 & 0\end{pmatrix}}_{\mathbf{A}^{(sc)}}\begin{pmatrix}\bar{u}(t)\\ \bar{p}(t)\\ \bar{\varphi}(t)\end{pmatrix} \\ &+ \underbrace{\begin{pmatrix}0 & \frac{1}{\rho_0 L_{sc}} & 0 & -\frac{1}{\rho_0 L_{sc}}\\ \frac{2S_1\rho_0 c_0^2}{L_{sc}(S_1+S_2)} & 0 & \frac{2S_2\rho_0 c_0^2}{L_{sc}(S_1+S_2)} & 0\\ 0 & 0 & 0 & 0\end{pmatrix}}_{\mathbf{B}^{(sc)}}\underbrace{\begin{pmatrix}u_s^{\Omega_1}(t)\\ p^{\Omega_1}(t)\\ u_s^{\Omega_2}(t)\\ p^{\Omega_2}(t)\end{pmatrix}}_{\mathbf{U}^{(sc)}(t)} \end{aligned} \tag{2.23}$$

SS Output:

$$\underbrace{\begin{pmatrix}u_s(0,t)\\ \varphi(0,t)\\ u_s\left(L_{sc},t\right)\\ \varphi\left(L_{sc},t\right)\end{pmatrix}}_{\mathbf{Y}^{(sc)}(t)} = \underbrace{\begin{pmatrix}\frac{1}{2}\left(1+\frac{S_2}{S_1}\right) & 0 & 0\\ 0 & 0 & 1\\ -\frac{1}{2}\left(1+\frac{S_1}{S_2}\right) & 0 & 0\\ 0 & 0 & 1\end{pmatrix}}_{\mathbf{C}^{(sc)}}\begin{pmatrix}\bar{u}(t)\\ \bar{p}(t)\\ \bar{\varphi}(t)\end{pmatrix} \tag{2.24}$$

Note that the SS submodel of Ω_{sc} connection element outputs acoustic (velocity,potential) since the subdomains needs expect these quantities in their inputs - see Eq. (2.17). Similar argument applies to the input vector of Ω_{sc} and output vectors of the subdomains.

In closing, it is worth mentioning that the development of other types of connection, and even impedance objects, is inspired by this fundamental 1D-1D connector and is based on this idea of vol-avg-LEE in a small fictitious domain surrounding the connection interface.

2.2.4 State-space Model of the 1D-3D Connection Element

The connection element described in this section couples a 1D acoustic subdomain with a 3D subdomain.[9] This would typically be the case when long narrow ducts lead to a large cavity. For example, Helmholtz resonators, used as acoustic damping devices in gas turbines, involve a long narrow duct (neck) attached to a large (cavity); or narrow duct-like hypothetical burners feeding into a large combustion chamber. An example calculation of a Helmholtz resonator with STORM is illustrated in the next Sec. 2.2.5.

This connection element is a special adaptation of the previous 1D-1D connector. Using the same notations: let Ω_1 and Ω_2 be the 1D and 3D subdomains, and Ω_{sc} the fictitious subdomain of small thickness L_{sc} enclosing the junction. Unlike 1D-1D case, here the flux conservation equation $S_1 u_s^{\Omega_1} = S_2 u_s^{\Omega_2}$ becomes degenerate because $S_1 << S_2$ and $u_s^{\Omega_2} << u_s^{\Omega_1}$.

In this situation, physically, the acoustic conditions at the junction are such that the pressure from the cavity is imposed on the duct (just like a duct open to an atmosphere), and flux from the duct (due to large velocity) is imposed on the cavity boundary. According to this qualitative explanation, the 1D-1D connector Ω_{sc} state-space submodel is adapted as follows:

SS Dynamics:

$$\frac{d}{dt}\underbrace{(\bar{u}(t))}_{\mathbf{X}^{(sc)}(t)} = \underbrace{(0)}_{\mathbf{A}^{(sc)}}(\bar{u}(t)) + \underbrace{\begin{pmatrix} 0 & \frac{1}{\rho_0 L_{sc}} & 0 & -\frac{1}{\rho_0 L_{sc}} \end{pmatrix}}_{\mathbf{B}^{(sc)}} \underbrace{\begin{pmatrix} u_s^{\Omega_1}(t) \\ p^{\Omega_1}(t) \\ u_s^{\Omega_2}(t) \\ p^{\Omega_2}(t) \end{pmatrix}}_{\mathbf{U}^{(sc)}(t)} \tag{2.25}$$

SS Output:

$$\underbrace{\begin{pmatrix} u_s(0,t) \\ \varphi(0,t) \\ u_s(L_{sc},t) \\ \varphi(L_{sc},t) \end{pmatrix}}_{\mathbf{Y}^{(sc)}(t)} = \underbrace{\begin{pmatrix} 1 \\ 0 \\ 0 \\ 0 \end{pmatrix}}_{\mathbf{C}^{(sc)}}(\bar{u}(t)) + \underbrace{\begin{pmatrix} 0 & 0 & 0 & 0 \\ 0 & 0 & 0 & 0 \\ -1 & 0 & 0 & 0 \\ 0 & 0 & 0 & 0 \end{pmatrix}}_{\mathbf{D}^{(sc)}} \underbrace{\begin{pmatrix} u_s^{\Omega_1}(t) \\ p^{\Omega_1}(t) \\ u_s^{\Omega_2}(t) \\ p^{\Omega_2}(t) \end{pmatrix}}_{\mathbf{U}^{(sc)}(t)} \tag{2.26}$$

[9] Although it is referred to as 1D-3D connector, it can also be used for 1D-2D connections.

Note that the above SS dynamics equation imposes only pressure continuity without influencing velocity. In low-frequency limit, it reduces to quasi-static relation $p^{\Omega_1}(t) = p^{\Omega_2}(t)$. While the correct acoustic flux exchange between the two subdomains is accounted by the SS output equation of Ω_{sc} with the help of a non-zero feedthrough matrix $\mathbf{D}^{(sc)}$. Note here that Ω_{sc} directly transfers velocity $u_s^{\Omega_1}$ in input vector (from Ω_1) to the output vector ($u_s(L_{sc}, t)$, meant for Ω_2) with just a change in the sign.

2.2.5 Example 2: Coupling 1D-3D Acoustic Cavities

This sub-section will demonstrate the calculation of acoustic eigenmodes of a system comprising 1D and 3D acoustic cavities with STORM as shown in Fig. 2.8. In the network, acoustic subdomains are coupled with the 1D-3D connection element described in the previous sub-section. Results are validated with Helmholtz solver AVSP [127] computations of the whole system. As shown in the Fig. 2.8, the geometry consists of a large cavity and a long narrow duct (say *Neck*).

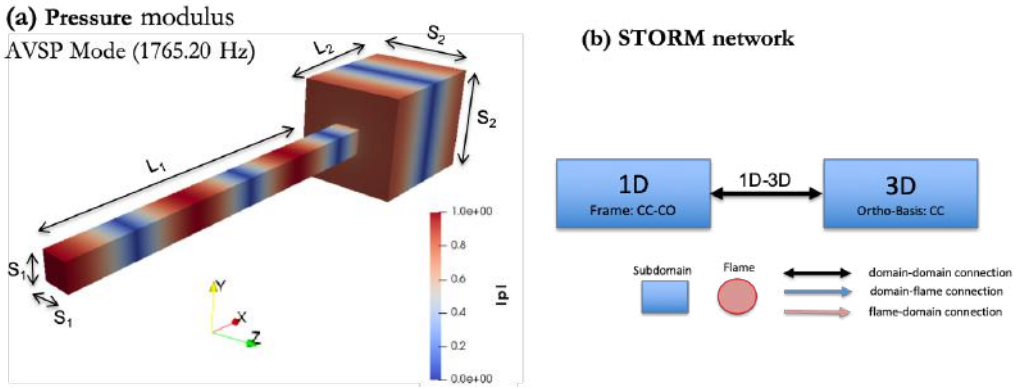

Figure 2.8: (a) System geometry. All global boundaries are presumed rigid walls. Dimensions and physical paramters in Tab. 2.2 below. Contours denote the magnitude $|p|$ of complex-valued pressure Mode-4 (1765.20 Hz) from AVSP. (b) STORM network representation of this case.

Numerical 3D OB basis for cavity subdomain: It is worth noting here that for the 3D acoustic subdomain in the STORM network, a simple rigid-wall OB-basis is sufficient. An OC-frame modal expansion is unnecessary since the Neck is a long, narrow duct with a tiny cross-section compared to the cavity. In other words, 1D duct makes a *point-like connection* with the 3D subdomain. The 2D surface of the 3D cavity acts as a large rigid wall except for the small connection interface with the 1D Neck. The 3D OB-basis for the cavity subdomain is constructed in a separate pre-processing step wherein the rigid-wall eigenmodes of the subdomain

are computed from FEM Helmholtz solver AVSP [127].

Analytical 1D OC-frame for the neck subdomain: On the other hand, for the 1D subdomain, at the junction, the acoustic conditions can be expected to differ from rigid-wall ($u' = 0$) or open-atmosphere ($p' = 0$) and must remain undetermined a priori. Therefore, an overcomplete frame CC-CO (just like the 1D ducts example presented earlier in Sec. 2.2.1) is employed here.

Above geometrical considerations are not valid, of course, when high-frequency transverse *(global system-level)* modes are in focus for this or similar configurations. The 1D subdomain's OC-frame (and the 1D-3D connector) can inherently represent/resolve only global modes having 1D spatial dependence in the Neck. Localized *cavity-level* transverse modes, for which the acoustic perturbation in the Neck is negligible (i.e., decoupled cavity eigenmodes) are, however, correctly predicted by STORM for the current network construction - e.g.: the Mode-5 in Tab. 2.2. This is expected since they are naturally present in the rigid-wall OB basis of the 3D cavity.

Table 2.2 gives results of the first few computed eigenfrequencies of the resonator from AVSP and STORM. An overall good agreement can be observed in the frequencies with less than 1.0 % error.

Parameters	Mode	AVSP	STORM	Nature
$c_0 = 347.0$ m/s	1	332.72	329.571	1L
$P_0 = 1$ atm, $\rho_0 = 1.17$ kg/m^3	2	941.74	932.54	2L
$S_1 = 0.02$, $S_2 = 0.08$ (m^2)	3	1540.00	1525.61	3L
$L_1 = 0.27$, $L_2 = 0.10$ (m)	4	1765.20	1758.05	4L
	5	2174.25	2169.63	1T

Table 2.2: Frequencies (Hz) of the first few acoustic eigenmodes of the system in Fig. 2.8. Physical and geometrical parameters for the specific problem solved are as given in the first column. *L :* Longitudinal, *T :* Transverse.

The pressure magnitude of the fourth mode (1765.20 Hz) computed for the whole geometry in AVSP is depicted in Fig. 2.8(a). It is a higher-order longitudinal mode, and a detailed comparison of its mode structure (pressure and axial velocity) between reference AVSP and STORM network resolution is provided in Fig. 2.9. The mode structure is plotted along a center-line passing through both the neck and the cavity in Fig. 2.9.

In Fig. 2.9, the acoustic Mode-4 overall pressure shape is captured reasonably well by STORM network employing 1D-3D connector, though, at the *point-like* junction, there is a minor discrepancy in the case of STORM. For velocity, in AVSP, the velocity perturbation magnitude drops sharply but continuously at the interface

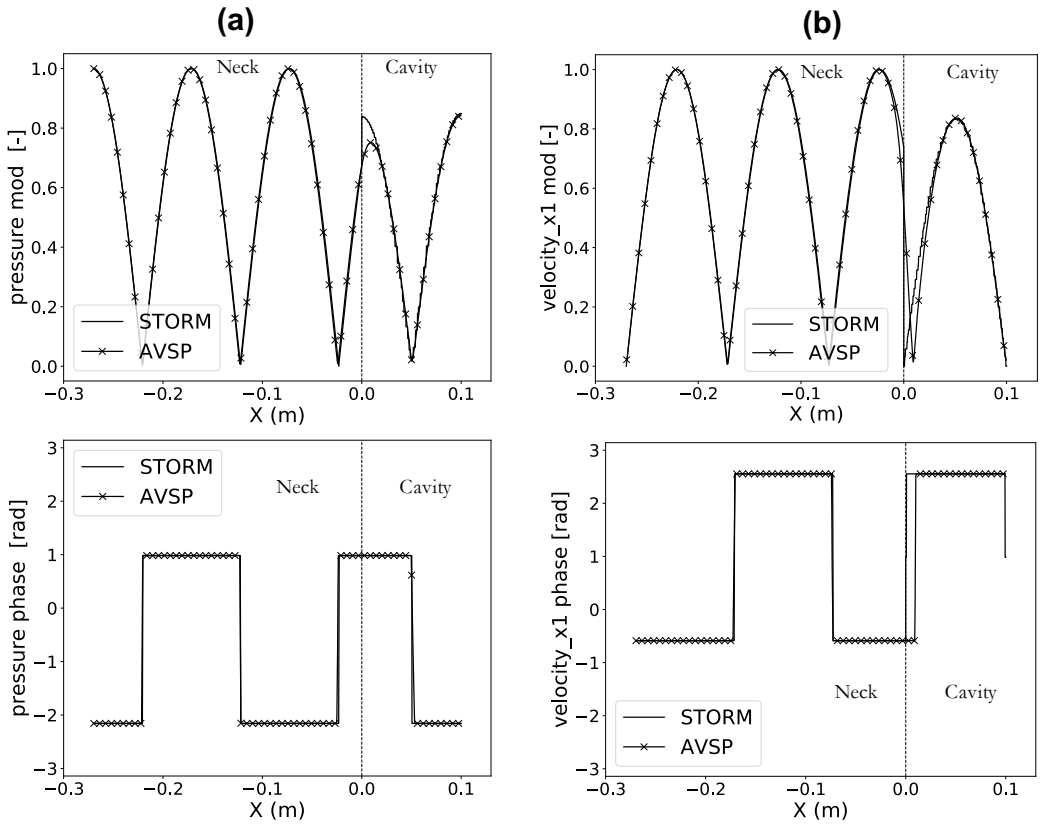

Figure 2.9: Structure of longitudinal Mode-4 in Tab. 2.2 along the center line passing through the system. (a) Pressure magnitude and phase. (b) Axial velocity magnitude and phase.

since it is resolved over a mesh. STORM, however, predicts the velocity jump at sudden expansion notably without the Gibbs effect. Overall, the global system mode structure and frequencies are predicted well.

2.3 Surface Spectral Connections

This section is dedicated to introduce and describe the fundamental working principle of *surface spectral connections* [198, 197, 199]. It is a methodology devised that facilitates coupling between network subdomains with 2D or 3D acoustics over topologically large and curved boundary interfaces. Thanks to OC-frame expansions, these special class of connection elements also provide an opportunity to impose Rayleigh conductivity or complex impedance on the interface/boundary of the subdomain to model it as a multi-perforated liner wall / complex-impedance boundary.

It was mentioned earlier how 1D subdomains make *point connections* with other

subdomains in a network. Acoustic variables, indeed, are uniform in the transverse direction in 1D subdomains by definition, and they only have a longitudinal spatial dependence. However, connections between 2D-2D (or 2D-3D) and 3D-3D subdomains in a network would constitute *line-connection* and *surface-connection* respectively. For any generic subdomain Ω_i, the surface integrals in the boundary acoustic forcing terms in Eq. (2.14) (the system of ODEs governing modal expansion coefficients) simplify for point connections to the variable values at the boundary. Evaluation of these surface integrals in the case of multi-dimensional *surface-(or line-) connections* is the key challenge addressed by this spectral connections methodology [198, 197].

Recall from Sec. 2.2.2, Eq. (2.17) another relevant point, where this assumption was invoked that each connection boundary S_{ci} of any generic acoustic subdomain is *spatially very small* of surface area ΔS_{ci}. Certainly, when multi-dimensional 2D/3D subdomains are to be coupled, this assumption is clearly invalid. One approach to solving this problem that was initially examined was to *spatially discretize* the boundary surface into a smaller number of surface elements such that the variables could be considered uniform over each of them, thus leading to a *piecewise approximation* of the surface integrals. This approach did work in the case of simple subdomains for which OC-frames are prescribed analytically. However, numerical issues and inconsistent results were encountered [197] in cases where subdomain frames were numerically generated from a FEM-based Helmholtz solver. Besides that, deciding on the locations where a complex 3D configuration should be split/decomposed to build a network and the optimum number of discretized subsurfaces on each connection interface is practically not straightforward. To overcome these aforementioned challenges, the current methodology relying on *spectral discretization* was developed.

2.3.1 Illustrative Examples: Coupling 3D-3D Subdomains

The modeling principles underlying surface spectral connections are explained over the following sub-sections with the help of a couple of examples. While *surface*-type connections are considered in these examples, an analogous explanation would apply to *line* spectral connections as well.

Consider the first example (Ex-1) where a simple acoustic network of two 3D subdomains — rectangular Box1 (say subdomain Ω_i) and Box2 (subdomain Ω_j) as shown in Fig. 2.10 (exploded view), that are to be coupled together to compute the natural acoustic eigenmodes of the combined system. For doing so, a *(3D-3D-Conn: 3D-3D surface spectral connection element)* is defined by considering a thin, *fictitious*, shell-like (quasi-2D) connection domain (or control volume) Ω_{sc} as shown in Fig. 2.10, quite analogous to the 1D-1D connector discussed earlier. The Ω_{sc}

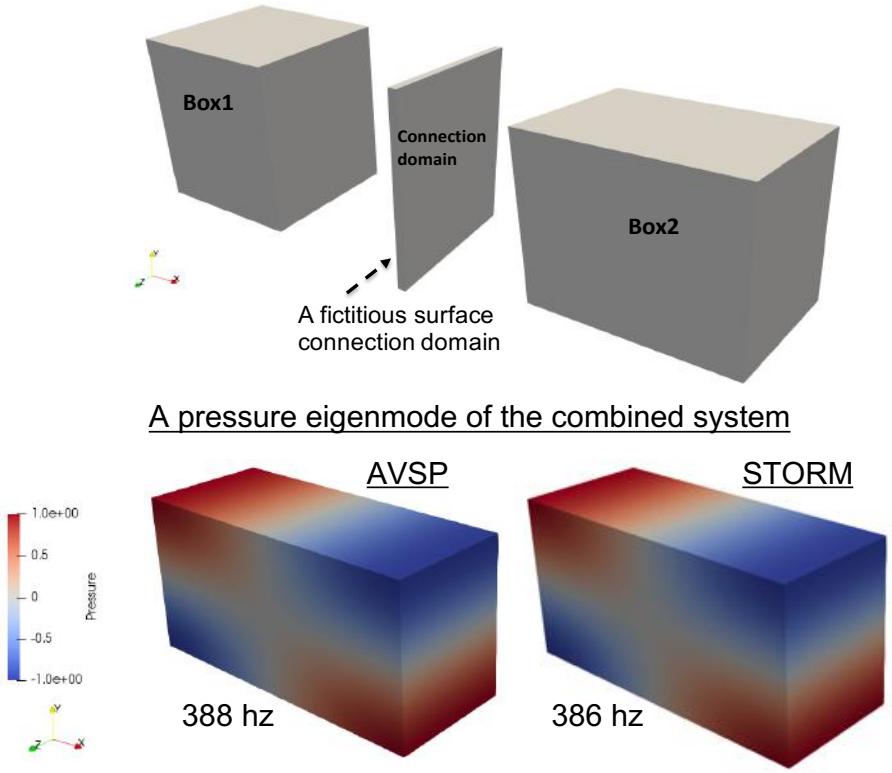

Figure 2.10: Example 1 (Ex-1): Two 3D subdomains coupled to each other via a surface spectral connection in STORM. A multi-dimensional, natural acoustic pressure eigenmode of the combined system compared with that obtained from Helmholtz solver AVSP[127]. Parameters: Box1 length $= 0.4$ **mm, Box2 length** $= 0.6$ **mm, both boxes height** $= 0.5$ **mm, width** $= 0.4$ **mm,** $P_0 = 1$ atm, $c_0 = 347.0$ m/s, $\rho_0 = 1.17$ kg/m^3**.**

domain is topologically identical in shape, enclosing the connection interface i.e. boundaries S_{c_i} and S_{c_j} of subdomains Ω_i and Ω_j respectively. Note that the subdomain connection interfaces, and thus the connection domain, could be arbitrarily curved shaped too.

Another canonical example (Ex-2) to illustrate surface spectral connections is depicted in Fig. 2.11, where the cylindrical and annular cavities are considered being acoustically coupled through multi-perforated (MLPF) liner wall. Let's call the connection element in the following as *3D-3D-MLPF*. Therefore, the aim, in this case, is to model the connection interface as a liner-wall by imposing its characteristic Rayleigh conductivity [83, 132, 208], given by well-known Howe's model [82] as the physical *coupling condition* between the subdomains. STORM results are validated against AVSP [127, 132].

Unlike previous Ex-1 Fig. 2.10, the Howe's model is the physical *coupling con-*

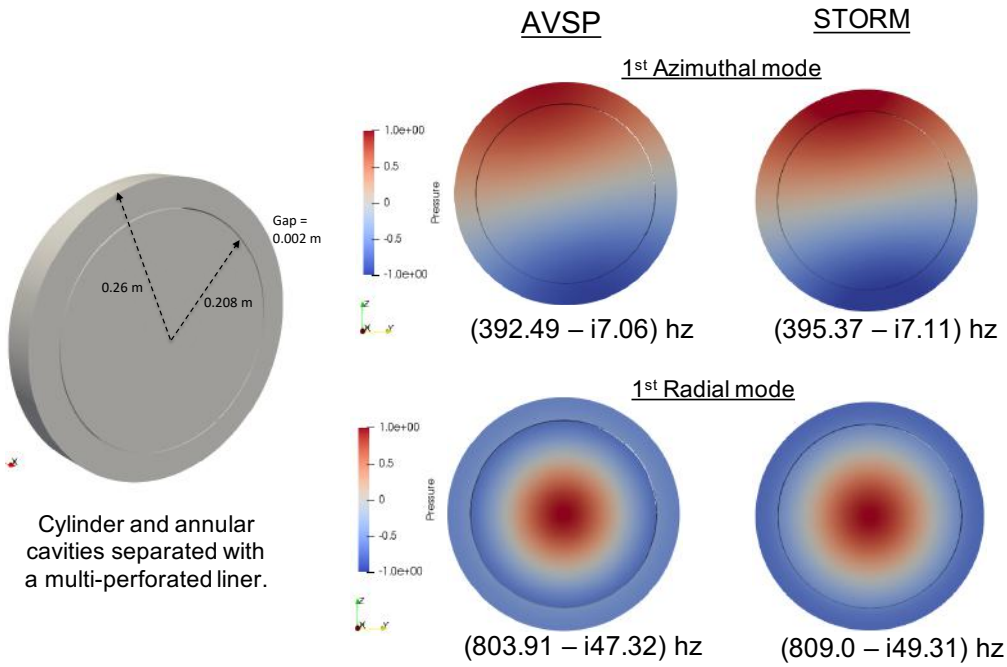

Figure 2.11: Example-2 (Ex-2): Surface spectral connection for modeling multi-perforated liner between the annular (Ω_1) and cylindrical Ω_2 cavities. Two eigenmodes of the system, their frequencies and growth rates noted at the bottom of each. Note that the thin surface connection domain Ω_{sc} in between the two subdomains is not shown.

dition that is enforced by the surface spectral connection domain Ω_{sc} (not shown in Fig. 2.11). The acoustic damping effect induced by the liner is captured fairly well in STORM as highlighted from a couple of system eigenmodes and their negative growth rates.

2.3.2 Curvilinear Helmholtz Equation

First step in developing surface-spectral connections framework is to derive set of equations governing the acoustics over the topologically large, curved connection domain Ω_{sc}. Laurent et al. [198, 197] derived set of linearized Euler Equations (LEE) in a *curvilinear spatial coordinate system*: (α, β, ξ), where (α, β) are two tangential directions and ξ the normal direction of the connection boundaries S_{c_i} and S_{c_j}.

The equations are averaged along the ξ-direction, under the limit that thickness of Ω_{sc}, $L_{\mathfrak{D}} \to 0$, and are expressed in terms of ξ-*averaged* acoustic pressure $\bar{p}(\alpha, \beta, t)$ and normal velocity $\bar{u}_\xi(\alpha, \beta, t)$. In these curvilinear LEE equations, the pressure variable $\bar{p}$ is replaced by acoustic potential $\bar{\varphi}$, to obtain the *curvilinear Helmholtz*

Equation in $\bar{\varphi}$ as below. The accompanying LEE momentum equation in $\bar{u}_\xi(\alpha,\beta,t)$ required later, is also given

$$\begin{cases} \frac{\partial \bar{u}_\xi}{\partial t}(\alpha,\beta,t) = \frac{1}{L_{\mathfrak{D}}\rho_0}\left[p^{\Omega_i}(\alpha,\beta,t) - p^{\Omega_j}(\alpha,\beta,t)\right] \\ \\ c_0^2\nabla_c^2\bar{\varphi}(\alpha,\beta,t) - \frac{\partial^2\bar{\varphi}}{\partial t^2}(\alpha,\beta,t) = \frac{c_0^2}{L_{\mathfrak{D}}}\left[u_\xi^{\Omega_i}(\alpha,\beta,t) - u_\xi^{\Omega_j}(\alpha,\beta,t)\right] \end{cases} \tag{2.27}$$

where ∇_c^2 is the curvilinear Laplacian operator. Note that the superscripts Ω_i (resp. Ω_j) denote the corresponding physical quantities on the connection boundary S_{ci} (resp. S_{cj}), respectively.

The above set of ξ-averaged equations govern the acoustics in Ω_{sc}, i.e. at the connection interface, under the influence of acoustics from neighboring subdomains. Eq. (2.27), meant for developing 3D-3D surface spectral connection element, are analogous to the volume-averaged LEE (Eq. 2.21) for 1D-1D connection discussed earlier but with a major difference: while in case of 1D-1D *point* connection, those Eq. (2.21) could be directly represented into state-space form. However this is not possbile for in the current *surface* connection case, where acoustic variables are varying spatially in transverse directions (α,β). This challenge is addressed with so-called *surface modal expansion* elucidated in the following Sec. 2.3.4.

2.3.3 Embedding Coupling Conditions

For 1D-1D connection, Eq. (2.21) inherently imposes acoustic pressure and flux continuity, and thus also includes jump conditions owing to sudden section change — see Sec. 2.2.3. Likewise, pressure and flux continuity can be imposed by above Eq. (2.27) , as demonstrated in Ex-1 in Fig. 2.10. Besides such basic acoustic coupling of subdomains, thanks to OC-frame modal expansions, the ξ-averaged curvilinear Helmholtz equations (resp. vol. avg. LEE in 1D-1D case) can be embedded with other non-trivial *physical coupling conditions* such as: Complex Acoustic Impedance $Z(j\omega)$ or MLPF-liner Rayleigh Conductivity $K_R(j\omega)$. The Ex-2 in Fig. 2.11 is an example of the latter. In fact, any generic impedance/conductivity models, if are or can be expressed in form of a rational polynomial[10] $Z(j\omega) = \mathcal{N}(j\omega)/\mathcal{D}(j\omega)$, where numerator $\mathcal{N}$ and denominator $\mathcal{D}$ are polynomials in $j\omega$, can be implanted into such ξ-averaged curvilinear Helmholtz equation (resp. 1D vol. avg LEE). An example of acoustic impedance applied to the outlet of a real engine combustor is provided in Sec. 3.3 of following Chapter 3. [11]

[10] Chapter 4 will discuss in detail about generating impedance/FTF models (more precisely, state-space models) from data acquired in experiments or high-order simulations via rational approximations.

[11] Chapter 5 will illustrate 1D case imposing at the outlet a more complex impedance model of supersonic choked nozzle for predicting mixed entropy-acoustic instabilities.

2.3.3.1 State-space sub-model for MLPF-liner Conductivity ($K_R(j\omega)$):

The mathematical formulation of the Surface spectral connection element, specifically for the case of MLPF-liner (3D-3D-MLPF connection), is presented along with key equations over the remaining of the following sub-sections. In continuation of the point made above regarding coupling conditions, an acoustic conductivity model for an MLPF-liner must be included in the curvilinear Eq. (2.27). Similarly, analogous surface spectral connectors can be deduced for other coupling conditions by slightly adapting the equations.

MLPF liner plates/walls usually have some finite thickness (h), innumerous small apertures of radius (a), with inter-aperture spacing (d), and have a bulk bias flow speed U through them. These liners impose the following acoustic jump conditions across them [82, 132]. Thus this infinitesimally thin interface between two 3D subdomains (Ω_i and Ω_j), which is enclosed inside connection domain Ω_{sc}, is expected to model/impose these jump conditions:

$$\begin{cases} \hat{u}_{\xi}^{\Omega_i^{(-)}}(\alpha,\beta,\omega) = \hat{u}_{\xi}^{\Omega_j^{(+)}}(\alpha,\beta,\omega) \\ \left[\hat{p}^{\Omega_j^{(+)}}(\alpha,\beta,\omega) - \hat{p}^{\Omega_i^{(-)}}(\alpha,\beta,\omega)\right] = \frac{-j\omega d^2\rho_u}{K_R(j\omega)}\hat{u}_{\xi}^{\Omega_i^{(-)}}(\alpha,\beta,\omega) \end{cases} \tag{2.28}$$

Note that the above liner coupling/jump conditions are expressed in frequency-domain. The superscripts $\Omega_i^{(-)}$ denote the acoustic variables just upstream of the connecting surface S_{ci}, and $\Omega_j^{(+)}$ are values just downstream of connecting surface S_{cj}. K_R is the Rayleigh conductivity, whose value depends on the geometry of liner plate, physical properties of the fluid, and is given by the well-known analytical Howe's model [82, 132]. Howe's model for K_R is a complex frequency-dependent function involving Bessel's functions and thus is not feasible to be directly inserted into Eq. (2.28) for subsequent mathematical development and state-space formulation. Therefore, Laurent et al. [198, 197] proposed replacing the original model with its simpler 2^{nd}-order polynomial expansion as below:

$$K_R(j\omega) = -K_R^A j\omega - K_R^B(j\omega)^2, \text{ with } K_R^A = -\frac{\pi a^2}{2U}\ ,\ K_R^B = \frac{2a^3}{3U^2} + \frac{\pi a^2 h}{4U^2} \tag{2.29}$$

The above expansion accurately approximates the original model with discrepancies less than 1% for $(a\omega/U) \leq 0.2$, condition that is satisfied for most practicat situations.

For given conductivity K_R, the second row in Eq. (2.28), basically relates pressure-jump across the liner (interface) to upstream velocity. Using inverse Fourier transform, this same equation can be expressed as a single-input single-output (**SISO**) state-space realization $\mathbf{A_{K_R}}, \mathbf{B_{K_R}}, \mathbf{C_{K_R}}$ as follows [198, 197].

SS-Dynamics:

$$\frac{\mathrm{d}}{\mathrm{d}t}\underbrace{(z(t))}_{\mathbf{X}_{K_R}(t)} = \underbrace{\left(-K_R^A/K_R^B\right)}_{\mathbf{A}_{K_R}}(z(t)) + \underbrace{\left(-1/K_R^B\right)}_{\mathbf{B}_{K_R}}\underbrace{\left(s_i\left(u_S^{\Omega_i} \mid \mathscr{K}_k\right)\right)}_{U_{K_R}(t)} \tag{2.30}$$

SS-Output:

$$(Y_{K_R}(t)) = \underbrace{\left(-\rho_u d^2\right)}_{\mathbf{C_{K_R}}}(z(t)) \tag{2.31}$$

Above state-space model, with some abstract state-variable $z(t)$, relates output in time-domain $Y_{K_R}(t)$ (pressure-jump) to input $U_{K_R}(t)$ (velocity). The expression for input $U_{K_R}(t) = s_i\left(u_s^{\Omega_i} \mid \mathscr{K}_k\right)$ will be elaborated in the upcoming sub-sections. It is the projection of velocity $u_s^{\Omega_i}$ on the so-called *surface modal basis* ($\mathscr{K}_k$) introduced in the next subsection.

Finally, the above liner coupling/jump condition, in the form of a SISO state-space representation, can be embedded into the curvilinear Eqs. (2.27) for connection domain Ω_{sc} as follows:

$$\begin{cases} \frac{\partial \bar{u}_\xi}{\partial t}(\alpha,\beta,t) = \frac{1}{L_{\mathfrak{D}}\rho_0}\left[p^{\Omega_i}(\alpha,\beta,t) - p^{\Omega_j}(\alpha,\beta,t) + Y_{K_R}(t)\right] \\ \\ c_0^2\nabla_c^2\bar{\varphi}(\alpha,\beta,t) - \frac{\partial^2\bar{\varphi}}{\partial t^2}(\alpha,\beta,t) = \frac{c_0^2}{L_{\mathfrak{D}}}\left[u_\xi^{\Omega_i}(\alpha,\beta,t) - u_\xi^{\Omega_j}(\alpha,\beta,t)\right] \end{cases} \tag{2.32}$$

For the given conductivity K_R, the SISO state-space model will output the expected pressure jump across the liner, which is then enforced by the $Y_{K_R}(t)$ term in the above curvilinear equation. Eventually, this models the interface between Ω_i and Ω_j as an MLPF-liner. If there is no liner, there is no pressure jump, $Y_{K_R}(t)$ vanishes, and the original curvilinear Eqs. (2.27) is retrieved that enforces acoustic pressure and velocity continuity, as necessary for the basic acoustic coupling between the two 3D subdomains (Fig. 2.10).

2.3.4 Surface Modal Expansion

Previous subsections derived the set of curvilinear Eqs. (2.32) with MLPF-liner coupling conditions implanted, which govern the acoustics in the vicinity of the connection interface as per the acoustic conditions in the neighboring subdomains Ω_i and Ω_j.

The next and final objective is to derive a SS submodel (for the network connection element *3D-3D-MLPF*), that couples with SS submodels of the acoustic subdomains. This is to solve the Eqs. (2.32), determine the appropriate acoustic variables $\bar{\varphi}(\alpha,\beta,t)$ and $\bar{u}_\xi(\alpha,\beta,t)$ on the connection surfaces S_{ci} and S_{cj}, while respecting the coupling conditions, when the global network is resolved. Recall, it was mentioned earlier that Eqs. (2.32) cannot be directly transformed into a SS

submodel due to transverse spatial (α, β) variability of acoustic variables. To deal with this, instead of spatially discretizing the connection surface, another approach based on spectral discretization was developed [198, 197] by introducing *surface modal expansion*.

The idea behind surface modal expansion is that the ξ-averaged acoustic variables $\bar{\varphi}(\alpha, \beta, t)$ and $\bar{u}_\xi(\alpha, \beta, t)$ in the connection domain are sought by expanding them over an *orthogonal basis* $(\mathscr{K}_k(\alpha, \beta))$ of known natural surface eigenmodes of the middle-surface $\mathcal{S}_{sc}$ of thin Ω_{sc} domain, as below:

$$\begin{aligned} \bar{\varphi}(\alpha, \beta, t) &= \sum_{k=1}^{K_s} \nu_k(t)\mathscr{K}_k(\alpha, \beta) = \boldsymbol{\nu}^T(t)\boldsymbol{\mathscr{K}}(\vec{x}_s) \\ \bar{u}_\xi(\alpha, \beta, t) &= \sum_{k=1}^{K_s} \mu_k(t)\mathscr{K}_k(\alpha, \beta) = \boldsymbol{\mu}^T(t)\boldsymbol{\mathscr{K}}(\vec{x}_s) \end{aligned} \tag{2.33}$$

The middle-surface $\mathcal{S}_{sc}$ is thus strictly a curved 2D manifold (α, β) even through Ω_{sc} was considered of infinitesimal thickness, $L_{\mathfrak{D}} \to 0$. The finite number (K_s) of 2D surface eigenmodes in the basis $(\boldsymbol{\mathscr{K}}(\vec{x}_s))$ are determined a priori from analytical or numerical solutions of *homogeneous* curvilinear Helmholtz equation below:

$$\begin{cases} \bar{c_0}^2 \nabla_c^2 \mathscr{K}_k(\alpha, \beta) + \omega_k^2 \mathscr{K}_k(\alpha, \beta) = 0 \quad \text{over } \mathcal{S}_{sc} \\ \\ \mathscr{K}_k = 0 \quad \text{or} \quad \vec{\nabla}_c \mathscr{K}_k = 0 \quad \text{on } \partial\mathcal{S}_{sc} \end{cases} \tag{2.34}$$

where, ∇_c^2 and $\vec{\nabla}_c$ are curvilinear Laplacian and gradient operators [198, 197], $\partial\mathcal{S}_{sc}$ are the 1D contours of peripheral/lateral boundary of the 2D middle-surface $\partial\mathcal{S}_{sc}$, and the above homogeneous Dirichlet or Neumann boundary condtions on $\partial\mathcal{S}_{sc}$ must be chosen to match the lateral BCs of subdomains Ω_i and Ω_j.

The OB basis of natural surface eigenmodes follows the 2D surface inner product:

$$(f|g) = \iint_{\mathcal{S}_{sc}} f(\vec{x}_s) g(\vec{x}_s) d\vec{x}_s \tag{2.35}$$

and the squared L2 norm of the basis surface eignemodes are noted as $\lambda_k = (\mathscr{K}_k|\mathscr{K}_k)$. In practice, the surface OB basis is generated not by directly solving Eq. (2.34), but solving the regular *cartesian* homogeneous Helmholtz equation over a very thin *fictitious* shell-like domain (synonymous to Ω_{sc}) as shown in Fig. 2.10, for example. The quasi-2D modes are then projected onto a 2D-manifold/surface.

Finally, the last step to derive equations governing the unknown surface modal expansion coefficients $\nu_k(t)$ and $\mu_k(t)$ is described next. The classical Galerkin projection procedure [197] is then replicated by substituting the surface modal expansion in Eq. (2.33) into the *inhomogeneous curvilinear Eqs.*(2.32) presented in the previous subsection. In addition, the source terms in those equations — the acoustic

pressure and velocity on connections boundaries S_{c_i} and S_{c_j}— are substituted from *OC-frame modal expansions of subdomains* Ω_i and Ω_j, i.e. Eq. (2.8) and Eq. (2.9). As a result, the following dynamical systems of ODEs are obtained that governs the values of the surface modal expansion coefficients of Eq. (2.33).

$$\ddot{\nu}_k(t) + \omega_k^2 \nu_k(t) = -\frac{\overline{c_0}^2}{\lambda_k L_{\mathscr{D}}} \left[s_i \sum_{n=1}^{N^{(i)}} -\frac{1}{\rho_0^{(i)}} \left(\nabla_s \phi_n^{(i)} \mid \mathscr{K}_k \right) \Gamma_n^{(i)}(t) - s_j \sum_{n=1}^{N^{(j)}} -\frac{1}{\rho_0^{(j)}} \left(\nabla_s \phi_n^{(j)} \mid \mathscr{K}_k \right) \Gamma_n^{(j)}(t) \right] \tag{2.36}$$

$$\dot{\mu}_k(t) = \frac{1}{\lambda_k L_{\mathscr{D}} \overline{\rho_0}} \left[s_i \sum_{n=1}^{N^{(i)}} \left(\phi_n^{(i)} \mid \mathscr{K}_k \right) \dot{\Gamma}_n^{(i)}(t) + s_j \sum_{n=1}^{N^{(j)}} \left(\phi_n^{(j)} \mid \mathscr{K}_k \right) \dot{\Gamma}_n^{(j)}(t) + s_i \sum_{n=1}^{N^{(i)}} -\frac{1}{\rho_0^{(i)}} \left(\nabla_s \phi_n^{(i)} \mid \mathscr{K}_k \right) Y_{K_R} \left\{ \Gamma_n^{(i)}(t) \right\} \right] \tag{2.37}$$

In the above two systems of ODEs, note the subscript k. It refers to the k^{th} component for $k = 1$ to K_s, K_s being the number of modes (dimension) of the surface modal basis. Terms in the above equations are explained further below:

- The superscripts $^{(i)}$ and $^{(j)}$ refer to quantities evaluated in subdomains Ω_i, Ω_j of OC frame sizes $N^{(i)}$, $N^{(j)}$ respectively.
- $s_i = \vec{n}_s^{(i)} \cdot \vec{e}_\xi = \mp 1$ and $s_j = \vec{n}_s^{(i)} \cdot \vec{e}_\xi = \pm 1$ (such that $s_i s_j = -1$) defines the orientation of the subdomains, i.e. their outwards normals $\vec{n}_s^{(i)}$ on S_{ci} with respect to some chosen orientation of the normal $\vec{e}_\xi$ of the middle-surface. (Resp. for S_{cj}).
- In Eq. (2.37), the term $\left(\phi_n^{(i)} \mid \mathscr{K}_k \right)$ is the scalar inner product of profile of n^{th} OC-frame mode of Ω_i on its connection surface S_{ci}, with k^{th} *component* of independently computed surface modal basis $\mathscr{K}_k$. The first term in Eq. (2.37) inside the bracket, from Eq. (2.8), is thus also $\equiv s_i \left(p^{(i)} \mid \mathscr{K}_k \right)$. (Resp. for boundary S_{cj}).
- In Eq. (2.36), the term $\left(\nabla_s \phi_n^{(i)} \mid \mathscr{K}_k \right)$ can be explained same as above point, but for the normal gradient of the frame mode on connection surface S_{ci}. The first term in Eq. (2.36) inside the bracket, from Eq. (2.9), is thus also $\equiv s_i \left(u_s^{(i)} \mid \mathscr{K}_k \right)$. (Resp. for boundary S_{cj}).
- The presence of the time-dependent subdomain modal amplitudes $\Gamma_n^{(i)}(t)$, $\dot{\Gamma}_n^{(i)}(t)$, $\Gamma_n^{(j)}(t)$ and $\dot{\Gamma}_n^{(j)}(t)$ corroborates that the surface connection element indeed couples the acoustics in Ω_i to that in Ω_j, and vice versa.

- The last term in Eq. (2.37) appears from the SISO state-space sub-model for MLPF-liner conductivity coupling condition discussed earlier in Sec. 2.3.3.1. *Note that this term would be absent for Ex-1 in Fig. 2.10 - a case of basic coupling between two 3D subdomains where* $Y_{K_R} = 0$.

Recall the original challenge for which the current spectral connections methodology was developed in the first place: the evaluation of surface integral source terms in the dynamical system of ODEs Eq. (2.14) that governs the modal expansion coefficients of the subdomain. Note that these boundary source terms are exerted by the neighboring subdomain, not directly, but through the relevant connection element. Therefore, ultimately the surface modal expansions of Eq. (2.33) allow these surface integrals to be rewritten as follows (in compact vector/matrix notations):

$$\iint_{S_{ci}^{(m)}} \rho_0 c_0^2 \; \varphi^{S_{ci}^{(m)}}(\vec{x}_s, t) \left[\boldsymbol{\Lambda}^{-1} \boldsymbol{\nabla_s \phi}(\vec{x}_s)\right]_n d^2\vec{x}_s = \rho_0 c_0^2 \left[\boldsymbol{\Lambda}^{-1} \left(\boldsymbol{\nabla_s \phi} | \boldsymbol{\mathscr{K}}^T\right)\right]_{n,*} \boldsymbol{\nu}(t) \quad (2.38)$$

$$\iint_{S_{ci}^{(m)}} \rho_0 c_0^2 \; u_s^{S_{ci}^{(m)}}(\vec{x}_s, t) \left[\boldsymbol{\Lambda}^{-1} \boldsymbol{\phi}(\vec{x}_s)\right]_n d^2\vec{x}_s = s_i \rho_0 c_0^2 \left[\boldsymbol{\Lambda}^{-1} \left(\boldsymbol{\phi} | \boldsymbol{\mathscr{K}}^T\right)\right]_{n,*} \boldsymbol{\mu}(t) \quad (2.39)$$

where $[\mathbf{M}]_{n,*}$ denotes the n^{th} row of the matrix $\mathbf{M}$. The surface source terms in Eq. (2.14) are now evaluated thanks to the surface modal projections $\left(\boldsymbol{\phi} | \boldsymbol{\mathscr{K}}^T\right)$ and $\left(\boldsymbol{\nabla_s \phi} | \boldsymbol{\mathscr{K}}^T\right)$ [198, 197] instead of simple spatial discretization and piecewise approximation.

In Ex-2 depicted in Fig. 2.11, cylindrical and annular cavities separated by a multi-perforated liner are modeled in STORM with 3D-3D-MLPF surface spectral connection. Unlike Ex-1 in Fig. 2.10, where basic coupling (3D-3D-Conn) is employed, Howe's MLPF conductivity model is enforced in Ex-2. The acoustic damping effect induced by the liner is captured fairly well in STORM, as highlighted from a couple of system eigenmodes and their negative growth rates. The STORM results are validated with FEM Helmholtz solver AVSP [127, 132].

2.3.5 SS sub-model for 3D-3D-MLPF Liner Spectral Connection

The systems of ODEs, Eq. (2.36) and Eq. (2.37), can be converted into a MIMO state-space submodel representing the 3D-3D-MLPF surface spectral connector in the network coupling two 3D subdomains. Here this subsection will present the general state-space (SS) representation of this connection element.

To help ease the rigorous notations in the upcoming equations, refer back to Fig. 2.7 as a quick reminder. The following is a SS submodel of the surface spectral

connection element, at boundary $S_{ci}^{(m)}$ of subdomain Ω_i with its neighbor Ω_j, considering it to be an MLPF-liner (3D-3D-MLPF). As discussed earlier, this framework will largely remain the same and would require only small adaptations for other kinds of spectral connections, viz. the basic acoustic coupling (3D-3D-conn) or complex impedance boundary (3D-Z-conn).

Note that the surface spectral connections framework is similar to the 1D-1D connection element in many ways, just that the equations are a bit more involved. It is urged strongly to compare the SS submodel of 1D-1D *point-like* connector discussed in Sec. 2.2.3 with the following, to better appreciate the SS realization of *surface* 3D-3D-MLPF connector.

SS Dynamics:

All the $k = 1$ to K_s components can be put together in a matrix block structure to yield the following realization for SS dynamics equation:

$$\underbrace{\frac{d}{dt}\begin{pmatrix} \mathbf{X}_1^{S_{ci}^{(m)}} \\ \vdots \\ \mathbf{X}_{K_s}^{S_{ci}^{(m)}} \end{pmatrix}}_{\mathbf{X}^{S_{ci}^{(m)}}(t)} = \underbrace{\begin{pmatrix} \mathbf{A}_1^{S_{ci}^{(m)}} & & \\ & \ddots & \\ & & \mathbf{A}_{K_s}^{S_{ci}^{(m)}} \end{pmatrix}}_{\mathbf{A}^{S_{ci}^{(m)}}} \begin{pmatrix} \mathbf{X}_1^{S_{ci}^{(m)}} \\ \vdots \\ \mathbf{X}_{K_s}^{S_{ci}^{(m)}} \end{pmatrix} + \underbrace{\begin{pmatrix} \mathbf{B}_1^{\Omega_{i,j}} & & \\ & \ddots & \\ & & \mathbf{B}_{K_s}^{\Omega_{i,j}} \end{pmatrix}}_{\mathbf{B}^{S_{ci}^{(m)}}} \underbrace{\begin{pmatrix} \mathbf{U}_1^{\Omega_{i,j}} \\ \vdots \\ \mathbf{U}_{K_s}^{\Omega_{i,j}} \end{pmatrix}}_{\mathbf{U}^{S_{ci}^{(m)}}(t)} \tag{2.40}$$

where the k^{th} component block of the state-vector $\mathbf{X}_k^{S_{ci}^{(m)}}$, dynamics-matrix $\mathbf{A}_k^{S_{ci}^{(m)}}$, input-matrix $\mathbf{B}_k^{\Omega_{i,j}}$ and input-vector $\mathbf{U}_k^{\Omega_{i,j}}$ are as given below:

$$\mathbf{X}_k^{S_{ci}^{(m)}} = \begin{pmatrix} \nu_k(t) \\ \dot{\nu}_k(t) \\ \mu_k(t) \\ \mathbf{X}_{\mathbf{K_R},k}(t) \end{pmatrix} \quad , \quad \mathbf{A}_k^{S_{ci}^{(m)}} = \begin{pmatrix} 0 & 1 & 0 & \mathbf{0} \\ -\omega_k^2 & 0 & 0 & \mathbf{0} \\ 0 & 0 & 0 & \frac{1}{\lambda_k L \overline{\rho_0}} \mathbf{C}_{\mathbf{K_R}} \\ 0 & 0 & 0 & \mathbf{A}_{\mathbf{K_R}} \end{pmatrix}$$

$$\mathbf{B}_k^{\Omega_{i,j}} = \begin{pmatrix} 0 & 0 & 0 & 0 \\ -\frac{\overline{c_0}^2}{\lambda_k L_{\mathscr{D}}} & 0 & -\frac{\overline{c_0}^2}{\lambda_k L_{\mathscr{D}}} & 0 \\ 0 & \overline{\rho_0} \lambda_k L_{\mathscr{D}} & 0 & \frac{1}{\overline{\rho_0} \lambda_k L_{\mathscr{D}}} \\ \mathbf{B}_{\mathbf{K_R}} & 0 & 0 & 0 \end{pmatrix} \; , \; \mathbf{U}_k^{\Omega_{i,j}} = \begin{pmatrix} s_i \left(u_s^{\Omega_i} \mid \mathscr{K}_k \right) \\ s_i \left(p^{\Omega_i} \mid \mathscr{K}_k \right) \\ s_j \left(u_s^{\Omega_j} \mid \mathscr{K}_k \right) \\ s_j \left(p^{\Omega_j} \mid \mathscr{K}_k \right) \end{pmatrix} \tag{2.41}$$

In the above equation, note the terms with subscript $\mathbf{K_R}$. It is the SISO state-space submodel for Howe's conductivity $K_R(j\omega)$ — Eqs. (2.30), (2.31), that is embed-

ded in the SS representation of the current 3D-3D-MLPF connector. A natural choice of state-variables are the unknown surface modal expansion coefficients and the state-variable from SISO model stacked together. The SS input vector of 1D-1D connector in Eq. (2.23) had velocity and pressure at *point* interfaces with both the subdomains. In this case, there are K_s component blocks in the input vector, and a k^{th} block has velocity, pressure projections of subdomain boundaries on the k^{th} component (direction) of the surface modal basis — cf. Eqs. (2.37) and (2.36)).

SS Output:

The SS output vector of the 1D-1D connector in Eq. (2.24) had appropriate values of acoustic velocity and potential that respect the coupling conditions, which are imposed back at *point* locations of both the subdomains. Similarly, in this case, the 3D-3D-MLPF connection element should output appropriate acoustic variables back on the *surfaces* of the subdomains. The SS output equation is given as follows:

$$\underbrace{\begin{pmatrix} \mathbf{Y}_1^{\Omega_{i,j}} \\ \vdots \\ \mathbf{Y}_{K_s}^{\Omega_{i,j}} \end{pmatrix}}_{\mathbf{Y}^{S_{ci}^{(m)}(t)}} = \underbrace{\begin{pmatrix} \mathbf{C}_1^{\Omega_{i,j}} & & \\ & \ddots & \\ & & \mathbf{C}_{K_s}^{\Omega_{i,j}} \end{pmatrix}}_{\mathbf{C}^{S_{ci}^{(m)}}} \underbrace{\begin{pmatrix} \mathbf{X}_1^{S_{ci}^{(m)}} \\ \vdots \\ \mathbf{X}_{K_s}^{S_{ci}^{(m)}} \end{pmatrix}}_{\mathbf{X}^{S_{ci}^{(m)}}(t)} \tag{2.42}$$

where the k^{th} component block of output-matrix $\mathbf{C}^{S_{ci}^{(m)}}$ and output-vector $\mathbf{Y}^{S_{ci}^{(m)}}$ is:

$$\mathbf{Y}_k^{\Omega_{i,j}} = \begin{pmatrix} \mu_k(t) \\ \nu_k(t) \\ \mu_k(t) \\ \nu_k(t) \end{pmatrix} \quad , \quad \mathbf{C}_k^{\Omega_{i,j}} = \begin{pmatrix} 0 & 0 & 1 & \mathbf{0} \\ 1 & 0 & 0 & \mathbf{0} \\ 0 & 0 & 1 & \mathbf{0} \\ 1 & 0 & 0 & \mathbf{0} \end{pmatrix} \tag{2.43}$$

Note that the 3D-3D-MLPF connection element simply outputs the surface modal expansion coefficients to both the subdomains so that their surface integral source terms, from this particular connection, can be determined as in Eq. (2.38) and Eq. (2.39). However, the source terms are actually computed in the SS submodel of the subdomain Ω_i (resp. Ω_j) as detailed in the following subsection.

2.3.6 Adapted SS sub-model of Acoustic Subdomain for Spectral Connection

Earlier Sec. 2.2.2 detailed the SS representation of a generic acoustic subdomain in a STORM network — see Eqs.(2.17), (2.19). However that representation assumed point-like connection interfaces. For larger surface connections, it was mentioned how the connection interfaces could be spatially discretized leading to an enlarged block structure of SS input/ouput matrices/vectors.

Similarly, in the case of surface spectral connections too, the aforementioned SS realization needs to be adapted or expanded: over the K_s components of the surface modes (i.e., spectrally discretized) instead of small spatial surface elements. These SS equations for a subdomain Ω_i making surface spectral connection are indicated below. For the sake of conciseness, Ω_i here is assumed to only couple with another subdomain over a 3D-3D-MLPF type surface connection, and there are no other point/surface connections or even any flames within.

SS Dynamics:

$$\underbrace{\frac{d}{dt}\begin{pmatrix} \Gamma_1(t) \\ \dot{\Gamma}_1(t) \\ \vdots \\ \Gamma_N(t) \\ \dot{\Gamma}_N(t) \end{pmatrix}}_{\mathbf{x}^{\Omega_i}(t)} = \underbrace{\begin{pmatrix} 0 & 1 & & & \\ -\omega_1^2 & -\alpha & & & \\ & & \ddots & & \\ & & & 0 & 1 \\ & & & -\omega_N^2 & -\alpha \end{pmatrix}}_{\mathbf{A}^{\Omega_i}} \begin{pmatrix} \Gamma_1(t) \\ \dot{\Gamma}_1(t) \\ \vdots \\ \Gamma_N(t) \\ \dot{\Gamma}_N(t) \end{pmatrix} + \underbrace{\begin{pmatrix} \mathbf{B}_{1,1}^{S_{ci}^{(m)}} & \dots & \mathbf{B}_{1,K_s}^{S_{ci}^{(m)}} \\ \vdots & \ddots & \vdots \\ \mathbf{B}_{N,1}^{S_{ci}^{(m)}} & \dots & \mathbf{B}_{N,K_s}^{S_{ci}^{(m)}} \end{pmatrix}}_{\mathbf{B}^{\Omega_i}} \underbrace{\begin{pmatrix} \mathbf{U}_1^{S_{ci}^{(m)}} \\ \vdots \\ \mathbf{U}_{K_s}^{S_{ci}^{(m)}} \end{pmatrix}}_{\mathbf{U}^{\Omega_i}(t)} \tag{2.44}$$

where the blocks $\mathbf{B}_{n,k}^{S_{ci}^{(m)}}$ and $\mathbf{U}_k^{S_{ci}^{(m)}}$ in the input matrix and input vector are

$$\begin{aligned} \mathbf{B}_{n,k}^{S_{ci}^{(m)}} &= \rho_0 c_0^2 \begin{pmatrix} 0 & 0 \\ -s_i \left[\mathbf{\Lambda}^{-1}\left(\boldsymbol{\phi} \mid \mathscr{K}_k^{(m)}\right)\right]_n & \left[\mathbf{\Lambda}^{-1}\left(\boldsymbol{\nabla}_{\boldsymbol{s}}\boldsymbol{\phi} \mid \mathscr{K}_k^{(m)}\right)\right]_n \end{pmatrix} \\ \mathbf{U}_k^{S_{ci}^{(m)}} &= \begin{pmatrix} \mu_k(t) \\ \nu_k(t) \end{pmatrix} = \frac{1}{\lambda_k} \begin{pmatrix} s_i \left(u_s^{S_{ci}^{(m)}} \mid \mathscr{K}_k\right) \\ \left(\varphi^{S_{ci}^{(m)}} \mid \mathscr{K}_k\right) \end{pmatrix} \end{aligned} \tag{2.45}$$

The input matrix $\mathbf{B}^{\Omega_i}$ along with the input vector $\mathbf{U}^{\Omega_i}(t)$ evaluates the overall boundary surface integral source terms from Eqs. (2.38), (2.39). The input vector in this case have surface modal expansion coefficients from the 3D-3D-MLPF connection element consistent with its SS output vector (Eq. 2.42), unlike point values of acoustic velocity u_s and potential φ in Eqs.(2.17).

SS Output:

$$\underbrace{\begin{pmatrix} \mathbf{Y}_1^{S_{ci}^{(m)}} \\ \vdots \\ \mathbf{Y}_{K_s}^{S_{ci}^{(m)}} \end{pmatrix}}_{\mathbf{Y}^{\Omega_i}(t)} = \underbrace{\begin{pmatrix} \mathbf{C}_{1,1}^{S_{ci}^{(m)}} & \dots & \mathbf{C}_{1,N}^{S_{ci}^{(m)}} \\ \vdots & \ddots & \vdots \\ \mathbf{C}_{K_s,1}^{S_{ci}^{(m)}} & \dots & \mathbf{C}_{K_s,N}^{S_{ci}^{(m)}} \end{pmatrix}}_{\mathbf{C}^{\Omega_i}} \underbrace{\begin{pmatrix} \Gamma_1(t) \\ \dot{\Gamma}_1(t) \\ \vdots \\ \Gamma_N(t) \\ \dot{\Gamma}_N(t) \end{pmatrix}}_{\mathbf{X}^{\Omega_i}(t)} \tag{2.46}$$

where the blocks $\mathbf{C}_{k,n}^{S_{ci}^{(m)}}$ and $\mathbf{Y}_k^{S_{ci}^{(m)}}$ in the output matrix and output vector are

$$\mathbf{Y}_k^{S_{ci}^{(m)}} = s_i \begin{pmatrix} (u_s \mid \mathscr{K}_k) \\ (p \mid \mathscr{K}_k) \end{pmatrix} , \ \mathbf{C}_{k,n}^{S_{ci}^{(m)}} = s_i \begin{pmatrix} -\frac{1}{\rho_0} (\nabla_s \phi_n \mid \mathscr{K}_k) & 0 \\ 0 & (\phi_n \mid \mathscr{K}_k) \end{pmatrix} \tag{2.47}$$

SS output equation of the subdomain Ω_i in this case will compute and output projection components of surface values of acoustic velocity and pressure on the connection boundary consistent with the input vector of 3D-3D-MLPF connector (Eq. 2.40), unlike point-values in Eq. (2.19).

In closing this Sec. 2.3 on *surface spectral connections* methodology, it can be overall summarized as follows: A network including surface spectral connection can be viewed as a nested and coupled modal expansion (Galerkin projection) problem. The acoustic field in a subdomain, expanded onto a modal OC-frame, depends on the boundary forcing from adjacent subdomains through a fictitious 2D connection domain/element imposing coupling conditions; and these boundary source terms are further expanded onto an orthogonal basis of surface eigenmodes. The surface source terms evaluated based on a finite number of surface eigenmodes imply spectral discretization rather than spatial. Hence the name surface spectral connections.

2.4 Solver Structure, and Numerical Strategies for Spurious Eigenmodes

This section will briefly discuss the implications, underlying challenges associated with OC-frame modal expansions compared to classical OB-basis, and numerical strategies/procedures to deal with them. Motivation and fundamental ideas behind these strategies are summarized only qualitatively. Complete mathematical details are not repeated here and can be found in (Ch. 3, Sec. 3.5 of C. Laurent thesis [197]).

Figure 2.12 portrays the internal structure of the core STORM solver and its workflow. The first important step is to build individual state-space submodels of all the network objects. It is followed by assembling all of the MIMO SS submodels together through recursive Redheffer Star Product presented earlier in Sec. 2.1.1.

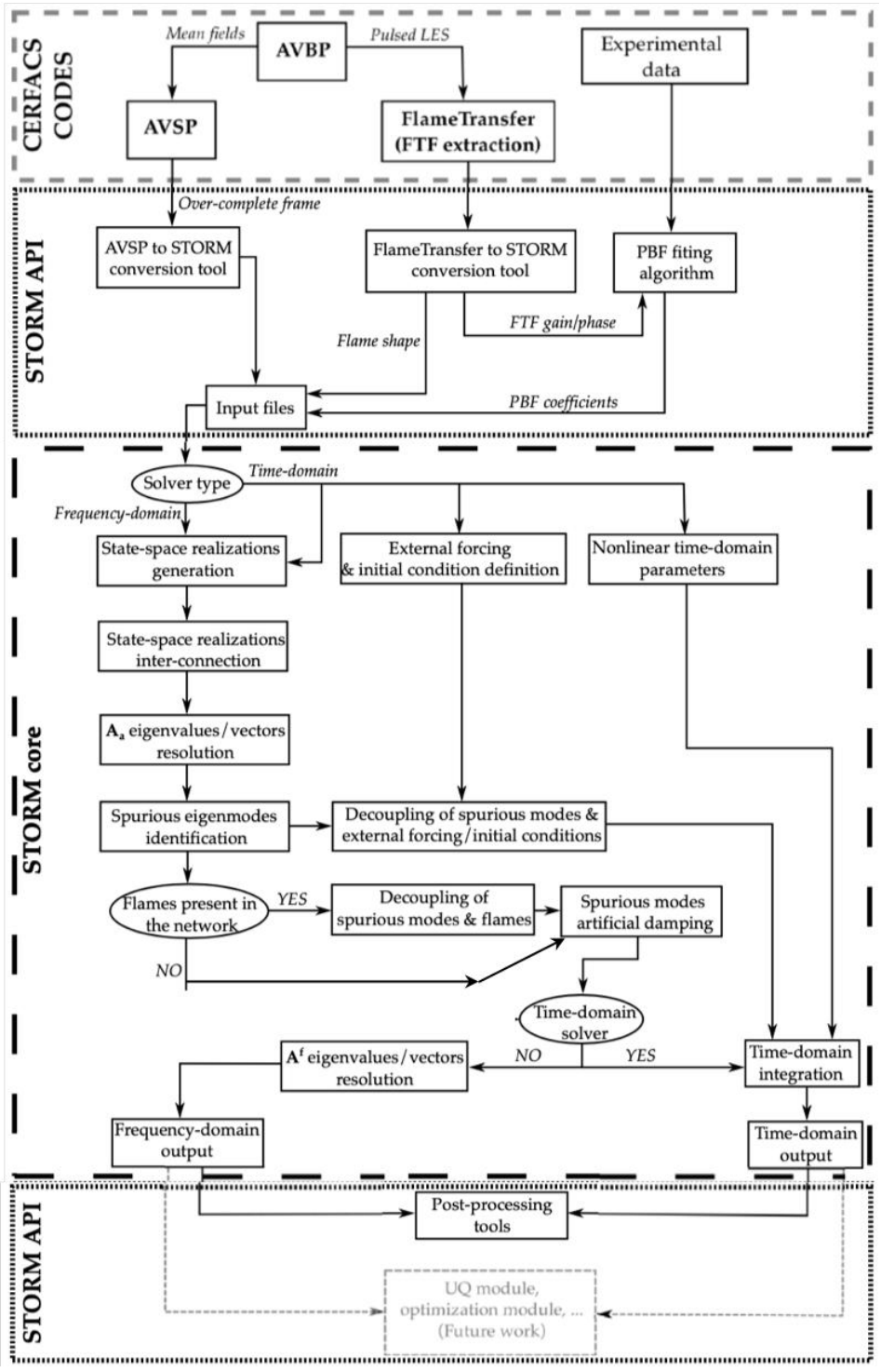

Figure 2.12: Work flowchart of STORM, including the core solver that builds, assembles state-space submodels of network objects, and solves the global system. API hosting the pre- and post-processing tools that interact with other CERFACS codes is also highlighted. Figure adapted from C. Laurent thesis [197].

General Internal Structure of Global SS Dynamics Matrix:

In STORM, all the network objects can be classified into two broad classes: *(i) Passive Elements* that contain acoustic subdomains, connection, and impedance elements; and *(ii) Active Elements* that comprise of flame elements. A *convention* that is followed while assembling SS blocks is that all the passive elements are assembled first, and the active (flame) SS blocks are appended at the last — reason for this will be clarified shortly in the following. After assembling all the network SS subsystems, the matrix block structure of *global SS dynamics* matrix can be represented as follows:

$$\mathbf{A}^f = \begin{pmatrix} \mathbf{A}_a & \boldsymbol{\mathcal{C}}_{fl\to a} \\ \boldsymbol{\mathcal{C}}_{a\to fl} & \mathbf{A}_{fl} \end{pmatrix} \tag{2.48}$$

where $\mathbf{A}_a$ and $\mathbf{A}_{fl}$ are blocks containing SS dynamics matrices of the passive elements and flame elements, respectively. $\boldsymbol{\mathcal{C}}_{fl\to a}$ contains the coupling blocks from flames to acoustic elements (i.e., the heat-release source terms), while $\boldsymbol{\mathcal{C}}_{a\to fl}$ represents the coupling from the acoustic elements to flames (i.e., velocity or pressure fluctuations at the reference points, that are prescribed for FTFs).[12]

In the absence of flames, $\mathbf{A}^f = \mathbf{A}_a$, it represents the passive acoustic network, and its eigensolutions give the natural eigenmodes of the global system. Thermoacoustic modes can then be found after coupling the acoustic network $\mathbf{A}_a$ with the flame elements $\mathbf{A}_{fl}$. Depending upon the number of passive elements, $\mathbf{A}_a$ will have a large matrix block structure internally after SS assembly. For instance, the global SS dynamics equation, depicting the internal block structure of the 1D-ducts example discussed earlier in Sec. 2.2.1, Fig. 2.3 is as follows:

$$\frac{d}{dt}\underbrace{\begin{pmatrix} \mathbf{X}^{(1)}(t) \\ \mathbf{X}^{(sc)}(t) \\ \mathbf{X}^{(2)}(t) \end{pmatrix}}_{\mathbf{X}^f(t)} = \underbrace{\begin{pmatrix} \mathbf{A}^{(1)} & \mathbf{B}^{(1)}\mathbf{C}_1^{(sc)} & \mathbf{0} \\ \mathbf{B}_1^{(sc)}\mathbf{C}^{(1)} & \mathbf{A}^{(sc)} & \mathbf{B}_2^{(sc)}\mathbf{C}^{(2)} \\ \mathbf{0} & \mathbf{B}^{(2)}\mathbf{C}_2^{(sc)} & \mathbf{A}^{(2)} \end{pmatrix}}_{\mathbf{A}^f} \begin{pmatrix} \mathbf{X}^{(1)}(t) \\ \mathbf{X}^{(sc)}(t) \\ \mathbf{X}^{(2)}(t) \end{pmatrix} \tag{2.49}$$

where, $\mathbf{A}, \mathbf{B}, \mathbf{C}$ are SS dynamics, input and output matrices, and the superscripts (1, 2, sc) denote subdomains Ω_1, Ω_2 and 1D1D connector Ω_{sc} respectively.

Energy-based Criterion for Identification of Spurious Modes:

While they have their advantages, OC-frames come at the cost of heightened numerical issues. Over-completeness of frames (i.e., they are a superposition of two OBs), and the non-orthogonality of frame modes - highlighted earlier in Sec. 2.2.2, leads to the following key problems:

[12] Following Ch.3 will present STORM examples with flames, and Ch.4 will dive deep into linear flame response (FTF) modeling in STORM.

1. *Highly ill-conditioned Gram Matrix* $\mathbf{\Lambda}$ *:* The condition number, $\mathcal{C}(\mathbf{\Lambda}) = |\mathbf{\Lambda}||\mathbf{\Lambda}^{-1}|$ (where $|\mathbf{\Lambda}|$ is the Frobenius matrix norm) can typically go as high as 10^{20} to 10^{24}. The set of ODE's governing the modal expansion coefficients of a subdomain - (Eq. (2.14)), involves $\mathbf{\Lambda}^{-1}$. Calculating $\mathbf{\Lambda}^{-1}$ is the first basic numerical difficulty, and it is achieved by employing the Singular-Value-Decomposition (SVD) based Moore-Penrose pseusdo-inverse - (see [197] for more details). During each STORM calculation, the errors stemming from inversion of $\mathbf{\Lambda}$ of each subdomain in the network is typically cross-checked aposteriori to remain low.

2. *Spurious components :* Due to the inherent overcomplete nature of frames, even after accurate inversion of $\mathbf{\Lambda}$, there still exist spurious components in Eq. (2.14) governing the unknown state-variables or the modal expansion coefficients. The components appear in the final global system resolution as unphysical, spurious modes with frequencies comparable to sought-after physical modes. Therefore, a technique for automatically identifying these spurious modes was critical and proposed by Laurent et al. [157, 197]. In this technique, *energy* (to be precise *norms*) of the restrictions of the global pressure mode shapes to each subdomain are evaluated and analyzed. It was found that all spurious system modes have low energies compared to physical modes. This fact is utilized to identify and flag spurious components present in the global state-space passive acoustic network, i.e., in the matrix $\mathbf{A}_a$.

Apparition of spurious modes is linked to OC-frames, and they exist irrespective of whether or not flames are present in a particular STORM network. Besides identification of spurious modes, the convention of the separate grouping of passive and flame elements inside global dynamics matrix $\mathbf{A}^f$ facilitates subsequent application of numerical strategies to mitigate problems arising due to spurious modes. These aspects are described next.

Decoupling of Active Flames from Spurious Modes:

In systems with flames, the spurious modes in the passive acoustic network tend to not only interact/couple with the flame elements but also cause erroneous coupling between pure acoustic physical and spurious modes. This can be observed from the flame heat-release source term on the right side of Eq. (2.14). Flames also respond to spurious modes, just like physical modes, and the resulting heat-release perturbations in turn influence both physical and spurious modes. Consequently, some (otherwise stable) spurious modes are destabilized, and even worse, the physical thermoacoustic modes of interest are adversely impacted. Recall that the Gram matrix Λ is not diagonal in the case where frames are used, so that the modal expansion coefficients are coupled through Λ^{-1} in Eq. (2.14). Especially when the

flame response is non-negligible, the errors induced become significant, corrupting the overall resolution of thermoacoustic modes and their stability.

Therefore, a decoupling operation was implemented [197] to alleviate the interference of spurious acoustic modes between flames and spurious acoustic modes of the network. Before this mitigatory step is applied, the core solver first internally solves a passive eigenvalue problem for the matrix $\mathbf{A}_a$ to identify the spurious modes based on the energy-criterion mentioned above (also indicated in Fig. 2.12). Knowledge of the spurious modes is then exploited to decouple them from flames, whereby, the coupling matrix blocks between passive acoustic network and flames are *corrected*: $\boldsymbol{\mathcal{C}}_{fl\to a}$ to $\tilde{\boldsymbol{\mathcal{C}}}_{fl\to a}$ and $\boldsymbol{\mathcal{C}}_{a\to fl}$ to $\tilde{\boldsymbol{\mathcal{C}}}_{a\to fl}$, $\tilde{(\,)}$ denoting the corrected blocks. The operation, essentially eliminates the receptivity of the spurious eigenmodes to the heat-release fluctuations, and flame receptivity to acoustic fluctuations stemming from spurious eigenmodes, respectively.

Artificial Damping of Spurious modes:

Eventhough the dissociation operation discussed above drastically improves the resolution of thermoacoustic modes, in practice it is observed that a weak coupling still exists between spurious modes and flames. In cases where the flame response is very strong, the previous operation alone does not serve the purpose entirely. Therefore, a supplementary strategy is also implemented where the identified spurious modes in the passive network are selectively and artificially damped with arbitrarily large negative growth rates. Consequently, the energy exchange between flames and spurious modes is forced to be minimum; the spurious modes remain largely damped without affecting physical modes. As a result, the flames then mostly interact with physical acoustic modes as expected, thereby improving the accuracy of the overall thermoacoustic problem. In this operation the passive acoustic matrix is corrected from $\mathbf{A}_a$ to $\tilde{\mathbf{A}}_a$.

Ultimately, the numerical strategies of identifying the spurious modes, decoupling them from flames, and artificially damping them yields the updated global SS dynamics matrix $\tilde{\mathbf{A}}^f$ as below. Solving the eigenvalue problem again for $\tilde{\mathbf{A}}^f$ then furnishes the thermoacoustic modes of the system under investigation.

$$\tilde{\mathbf{A}}^f = \begin{pmatrix} \tilde{\mathbf{A}}_a & \tilde{\boldsymbol{\mathcal{C}}}_{fl\to a} \\ \tilde{\boldsymbol{\mathcal{C}}}_{a\to fl} & \mathbf{A}_{fl} \end{pmatrix} \tag{2.50}$$

Selection algorithm for modes in the surface modal basis:

The finite number of surface modes K_s, i.e., the size of the orthogonal surface modal basis $\mathscr{K}_k$, is obviously the most crucial parameter in surface spectral connections. An SVD-based *selection algorithm* was also designed, where: from a relatively

large set of user-prescribed surface modes for a given network problem, not all but an optimum (i.e., reduced) number of principal components K_s, are used to construct the OB basis $\mathscr{K}_k$ (basically, reducing the dimensions of the surface modal OB basis). The weaker components are ignored and not used. This algorithm was necessary for two reasons: (i) to check that the basis is large enough for accurate surface projections from subdomain boundaries, and (ii) to improve the numerical conditioning and robustness of the method avoiding unnecessarily large basis — another challenge associated with ill-conditioning and spurious components of OC-frame modal expansion of subdomains that was discussed earlier in Sec. 2.4. For a given network, analysis indicates that the optimum K_s is a strong function mainly of the OC-frame size $N^{(i)}, N^{(j)}$ in subdomains Ω_i and Ω_j. The general trend, as expected, is that larger K_s is required as the frame sizes go up. A detailed convergence analysis (for the same case of Ex-2 in Fig. 2.11), and mathematical details of the selection algorithm are not repeated here can be found in [198, 197].

In summary, it is must be reiterated that the substantial advantages offered by OC-frame modal expansion, as highlighted so far and in the upcoming chapter, come with several associated challenges of numerical accuracy and robustness. The strategies presented above to deal with them are critical for the success of the OC-frame modal expansion method.

2.5 Conclusions

This chapter described the recently introduced and under development low-order acoustic-network modeling (LOM) tool STORM based on *generalized modal-expansions* [157, 197, 198, 199] and the *state-space (SS)* framework to study thermoacoustic combustion instabilities in complex realistic configurations. Some of the key observations and conclusions can be compiled as follows:

- Thermoacoustic network modeling, from literature survey in previous Ch. 1, was mostly limited to planar wave-based 1D networks and idealized annular geometries. Although known for a while, the classical modal expansion (Galerkin projection) method has not really been a go-to choice for building full-fledged, extensive acoustic networks. A core impediment has been the reliance on an orthogonal rigid-wall (OB) basis. This shortcoming was resolved with the proposed overcomplete (OC) frame modal expansion technique.

- OC-frame modal expansion method, a *generalization* of the classical approach significantly improves the convergence of expansion and yields correct representation of acoustic variables at the interfaces of subdomains in the network. Also, issues such as Gibbs oscillations/fringes are fixed that arise due to imposed velocity node at the junction due to rigid-wall OB bases of subdomains.

- The state-space method, along with the Redheffer product, renders a powerful framework to represent a variety of network objects as SS submodels and combine them together to build thermoacoustic networks. Stability analysis of the given system can then be performed in frequency-domain, time-domain, or both. However, results in this manuscript are limited to linear, frequency domain analysis. The nonlinear, time-domain analysis will be undertaken in the future.

- OC-frame modal expansions approach provides an opportunity for interconnecting subdomains with 1D/2D/3D acoustics. The *surface spectral connections* methodology [198, 197] makes it possible to not only couple 3D subdomains over topologically large and curved interfaces but also allows imposing multi-perforated (MLPF) liner conductivity at the junction or even complex impedance at the global system boundaries.

- The drawback of OC-frame expansions is the high numerical ill-conditioning of the global system to be solved, inducing some accuracy and robustness issues. Furthermore, the over-complete nature of the frames leads to the presence of spurious unphysical components, which tend to interact with physical components, particularly in the case of systems with flames. Sever numerical strategies developed to systematically deal with these challenges and mitigate their impact were briefly discussed.

Overall, the STORM delivers a very modular, flexible, and computationally fast (low-cost) tool for investigating thermoacoustic stability analysis of complex, realistic gas turbine combustors. While this chapter mainly focused on conveying the modeling concepts for building acoustic networks with the help of simple examples, the next chapter will illustrate larger networks of annular configurations and flames to carry out their linear thermoacoustic stability analysis.

Chapter 3

STORM Linear Stability Analysis of Annular Configurations

Contents

3.1 Simplified Plenum-Burner-Chamber (PBC) Configuration . 73
3.2 MICCA-Spray Annular Lab-scale Rig 80
3.3 SAFRAN Engine Combustor 85
3.4 Numerical Efficiency 89
3.5 Conclusions 91

After describing the low-order thermoacoustic network modeling tool STORM [157, 198, 197, 199] in the previous chapter, to further highlight its current capabilities, a few examples of annular configurations with flames are presented in this chapter. In Sec. 3.1, a network of an academic, simplified Plenum-Burner-Chamber (PBC) gas turbine combustor model is discussed. Subsequent Sec. 3.2 and Sec. 3.3 will demonstrate the application of STORM to carry out linear stability analysis (LSA) of the following complex, real 3D configurations: first is the MICCA-spray lab-scale annular rig from EM2C lab, and second a SAFRAN aeronautical engine combustor.

3.1 Simplified Plenum-Burner-Chamber (PBC) Configuration

Figure 3.1(a) depicts the simplified Plenum-Burner-Chamber (PBC) geometry whose linear stability analysis with STORM is presented in this section. It is the same configuration examined analytically by Bauerheim et al. [136], and their results are used as reference. The geometry consists of two simple annular plenum and chamber cavities connected with four narrow duct-like burners. The end-effects on acoustic modes due to narrow ducts opening into large volumes, are accounted for applying standard lenght corrections [209] on the two ends of the burner tubes: $L_i = L_i^0 + 2 \times 0.4\sqrt{4S_i/\pi}$, where L_i^0 is the length of the i^{th} burner before correction and S_i is the cross-section area.

Four acoustically-compact flames are placed as concentrated heat sources in the four burners at αL_i distance from the plenum junction, where $\alpha = 0.88$ (kept fixed). Although a flame thickness is specified (in Tab. 3.1) , they are modeled as infinitely thin in the ATACAMAC network with jump conditions. Their FTF reference coincides with the flame location. Uniform unburned and burned physical conditions of the gases (pressure, density, temperature, sound speed) are considered upstream and downstream of the flames and are similar to that found typically in a gas turbine engine. The geometrical dimensions and the physical conditions are detailed in Tab. 3.1.

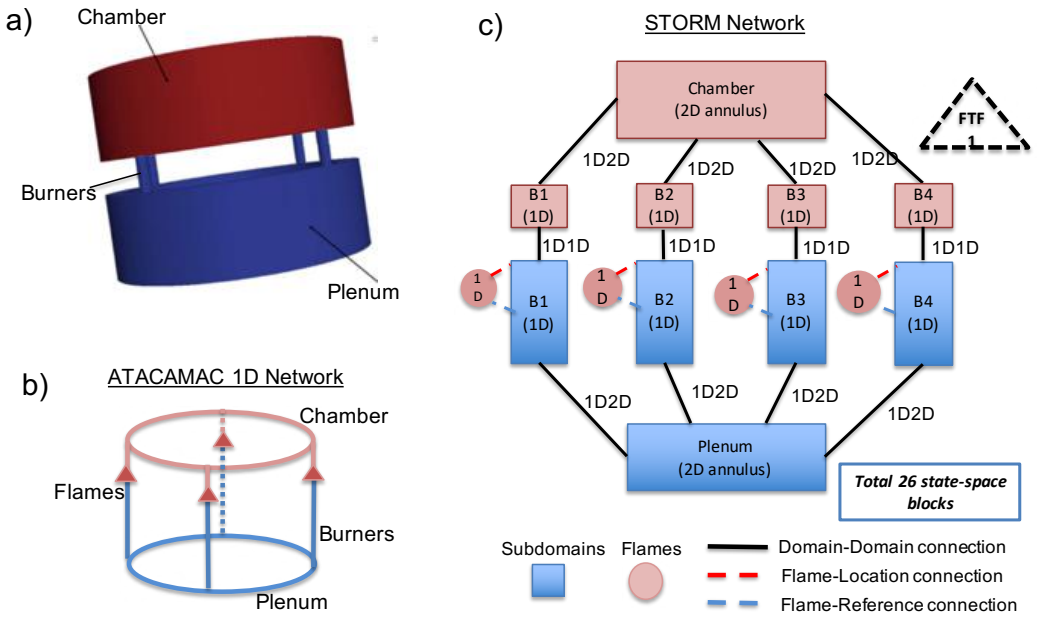

Figure 3.1: (a) Simplified Plenum-Burner-Chamber (PBC) configuration considered for thermoacoustic linear stability analysis with STORM. (b) The reference planar 1D wave-based acoustic network (ATACAMAC) from [136]. (c) Acoustic network representation in STORM.

Bauerheim et al. [136] use the so-called Annular Reduction Network (ANR) strategy to build a 1D network assuming 1D azimuthal wave-propagation in the chamber and plenum, while being longitudinal in the burners, see Fig. 3.1(b). The annular ducts were further split into sectors at the annulus-burner T-junctions, where acoustic jump-relations were utilized. The ANR strategy was advantageous to explicitly study the coupling between the two annular cavities through burners; however, it was not possible to account for axial dependence of the acoustics in the chamber/plenum. This limitation is addressed in STORM's acoustic network.

STORM acoustic network for the PBC configuration contains 26 sub-state-space models: 2 2D annular subdomains representing radially thin plenum and chamber,

Chamber, Plenum Annulus			
Axial Length	L_c , L_p	1.5	m
Mean Radius	R_c , R_p	2.1	m
Radial Thickness	W_c , W_p	0.4	m
Burner Ducts			
Length	$L_{b_i,0}$	0.6	m
Section	S_i	0.03	m^2
Fresh gases			
Mean pressure	p_0	$2 \cdot 10^6$	Pa
Mean temperature	$T_{u,0}$	700	K
Mean density	$\rho_{u,0}$	9.79	kg/m^3
Mean sound speed	$c_{u,0}$	743	m/s
Burnt gases			
Mean pressure	p_0	$2 \cdot 10^6$	Pa
Mean temperature	T_0	1800	K
Mean density	ρ_0	3.81	kg/m^3
Mean sound speed	c_0	1191	m/s
Flame parameters			
Interaction index	n_i	variable	–
Time-delay	τ_i	variable	s
Thickness	e_{fl}	0.03	m

Table 3.1: Above PBC case geometrical and physical parameters [136].

8 1D ducts for the cold and hot parts of the geometrically narrow burners, 4 compact 1D flames, and 12 appropriate connection elements coupling the subdomains. Note that each flame element makes two connections with the subdomains: one corresponds to the FTF reference location just upstream of the flame and the other with the flame heat-release location. Note that unlike domain-domain connection elements (1D-1D, 1D-2D in Fig. 3.1(c)), these flame-subdomain connections do not constitute separate state-space (SS) sub-models. In fact, they communicate with each other directly. While the SS sub-models of acoustic subdomains, 1D1D, 1D-2D connectors, were reviewed previously in Ch. 3, SS sub-model of flame/FTF is a topic briefly described in the upcoming Sec. 3.2, and covered in detail in Ch. 4.

Since the narrow 1D burner ducts make four discrete *point-like* connections with the chamber backplane, it is modeled as a rigid wall (same for the plenum-outlet plane). Yet, note that the acoustic velocity could be non-zero at these connection points after resolving the global system. Besides, the system's external BCs at plenum-inlet and chamber-outlet are presumed as rigid walls initially. Therefore, an analytical orthogonal basis for a 2D annulus that verifies rigid-wall BCs, defined as $\psi_{n,m}$ in Eq. (3.1), is sufficient for the chamber subdomain (note subscript $_c$ and same OB basis also for plenum). For burner 1D ducts, to avoid imposing any a priori

constraints on acoustic variables at connection boundaries, CC-OO overcomplete frames[1] as ϕ_n in Eq. (3.2) are used instead of orthogonal bases.

$$\psi_{n,m}\left(x_c,\theta_c\right) = \left[\cos\left(\frac{n\pi x_c}{L_c}\right)\cos\left(m\theta_c\right) \bigcup \cos\left(\frac{n\pi x_c}{L_c}\right)\sin\left(m\theta_c\right)\right] \tag{3.1}$$

$$\phi_n\left(x_B\right) = \left[\cos\left(\frac{n\pi x_B}{L_B}\right) \bigcup \sin\left(\frac{n\pi x_B}{L_B}\right)\right] \tag{3.2}$$

Following are the sizes of the OB basis / OC-frame employed for the geometrical subdomains in the STORM network (Fig. 3.1(c)) in obtaining the results presented in this secton: (i) For the rigid-wall OB basis of 2D annular chamber/plenum subdomains $N_\psi = 30$ (15 eigenmodes from each set in Eq. 3.1), and (ii) for the CC-OO frame of 1D ducts, $N_\phi = 50$ (25 from each family in Eq. 3.2).

Bauerheim et al. [136] in their ATACAMAC tool (Analytical Tool to Analyze and Control Azimuthal Modes in Annular Chambers), have derived explicit analytical relations for the so-called *coupling parameters* for the PBC configuration shown in Fig. 3.1. These parameters help describe the conditions and, quantitatively to some extent, the degree of coupling between the plenum and chamber through the burners. The values of coupling parameters depend upon geometry, physical conditions, and the FTF parameters. Depending upon the values they take, the thermoacoustic eigenmodes of the system could be classified into Weakly-Coupled (WC) and Strongly-Coupled (SC) modes.

Figure 3.2 compares trajectories of different system eigenmodes from STORM with ATACAMAC on the complex frequency plane, obtained after 50 successive calculations by varying the $n-\tau$ FTF's flame-response delay parameter τ in small increments for different fixed, constant values of flame gain parameter n. For smaller flame interaction indices ($n < 4$ for this configuration), the coupling between the two cavities is weak. The red and green color curves in Fig. 3.2 show the trajectories of Weakly-Coupled-Chamber first azimuthal (WCC1) mode and Weakly-Coupled-Plenum first azimuthal (WCP1) mode. As the time-delay τ/τ_c values vary, both these modes show these characteristic elliptical trajectories where the chamber and plenum modes are almost independent and oscillate at distinct frequencies. Not shown in this Fig. 3.2, but similar and smaller tracks are obtained for values of $n < 3$ (see [136]), and are enclosed inside that of $n = 3$ shrinking in size.

For larger values ($n > 4$), though, the acoustic flame-response is intense enough to meet the criterion favoring strong coupling between plenum and chamber cavities [136]. Trajectories of the first two Strongly-Coupled (SC) *system-modes*, for $n = 8$, are shown as the SC1 and SC2 (blue and magenta) curves in Fig. 3.2. At initial τ/τ_c values, SC1 and SC2 modes are still close to their WC counterparts at lower

[1] CC-OO: a 1D overcomplete frame with one family verifying rigid-wall ($u' = 0$) on both ends *(Closed-Closed)* and other family verifying open ($p' = 0$) conditions *(Open-Open)*.

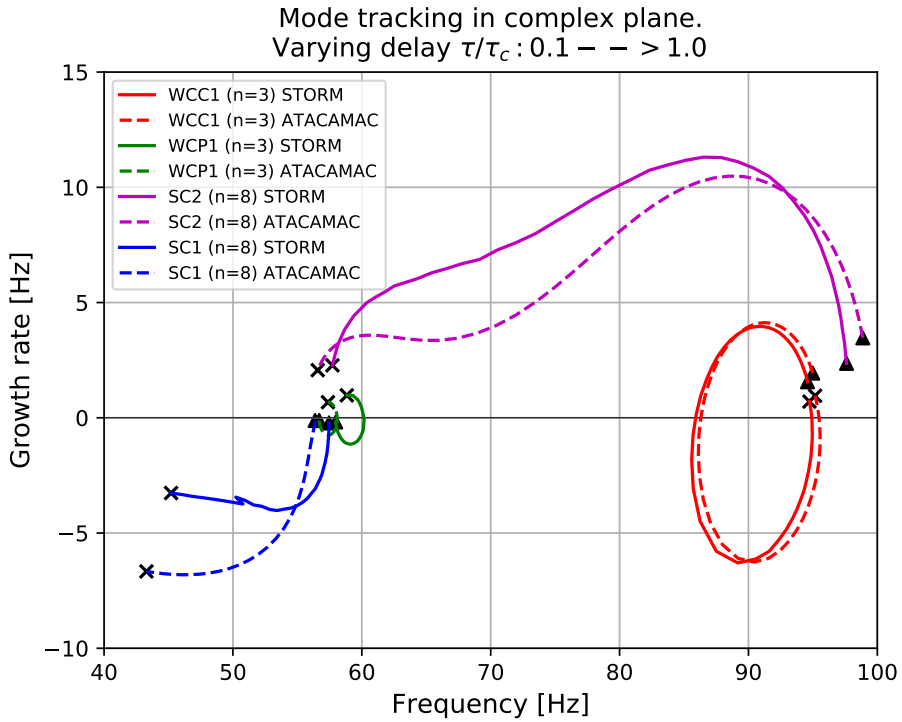

Figure 3.2: Trajectories of different modes in the complex-frequency plane for different flame interaction indices n and varying normalized flame-delay (τ/τ_c). ▲: Starting point, ×: last point of the trajectories. τ_c is the time taken by an acoustic wave to traverse the chamber annulus.

n values in terms of complex frequency and mode shapes. This is confirmed for eg. from the pressure structure of the SC2 mode in Fig. 3.3 at $n = 8$ and $\tau/\tau_c = 0.10$: the mode shows strong acoustic activity only in the chamber. *Note that the pressure in both chamber and plenum is normalized by the max pressure in the system so as to compare their relative amplitudes.*

But as τ/τ_c values increase (for $n = 8$) the modes bifurcate as observed from the drifting frequencies in Fig. 3.2. SC2 mode moves towards the frequency of WCP1, and SC1 is moving towards a longitudinal mode (not shown on the complex plane). Examining the structure of SC2 mode at an intermediate point $\tau/\tau_c = 0.54$ (not shown) reveals apparition of acoustic activity in the plenum, indicating the onset of strong coupling with the entire system resonating at the same frequency. Fig. 3.4 shows the SC2 mode structure at the last point $\tau/\tau_c = 1.0$ with azimuthal acoustic activity in both cavities (relatively stronger in plenum since its close to WCP1 mode).

All of the interesting physics examined with the ATACAMAC model [136] for this Plenum-Burner-Chamber (PBC) configuration is retrieved fairly well by the

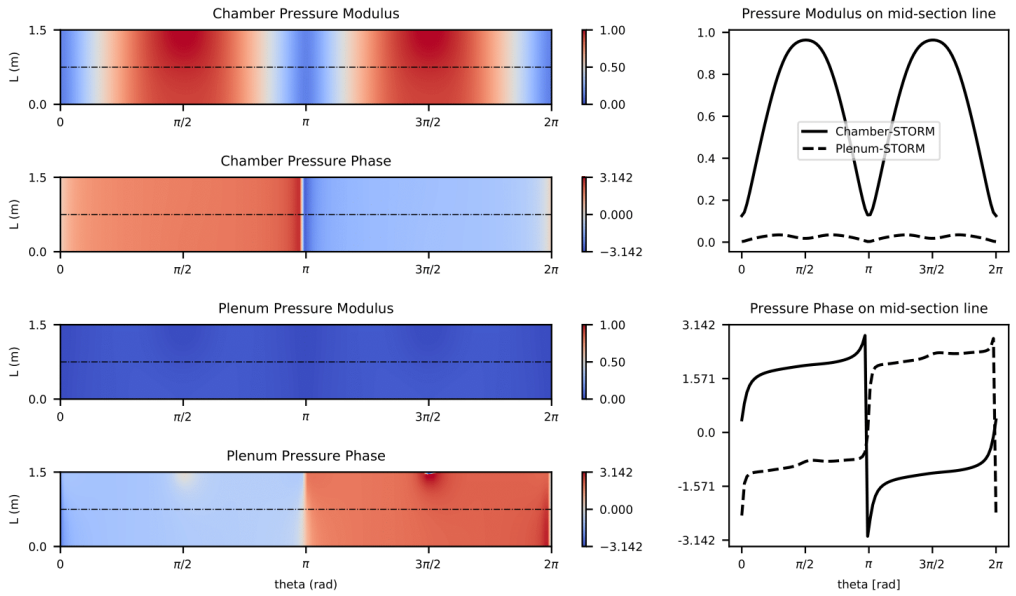

Figure 3.3: SC2 Mode shape for flame-index $n = 8$ and delay $\tau/\tau_c = 0.1$.

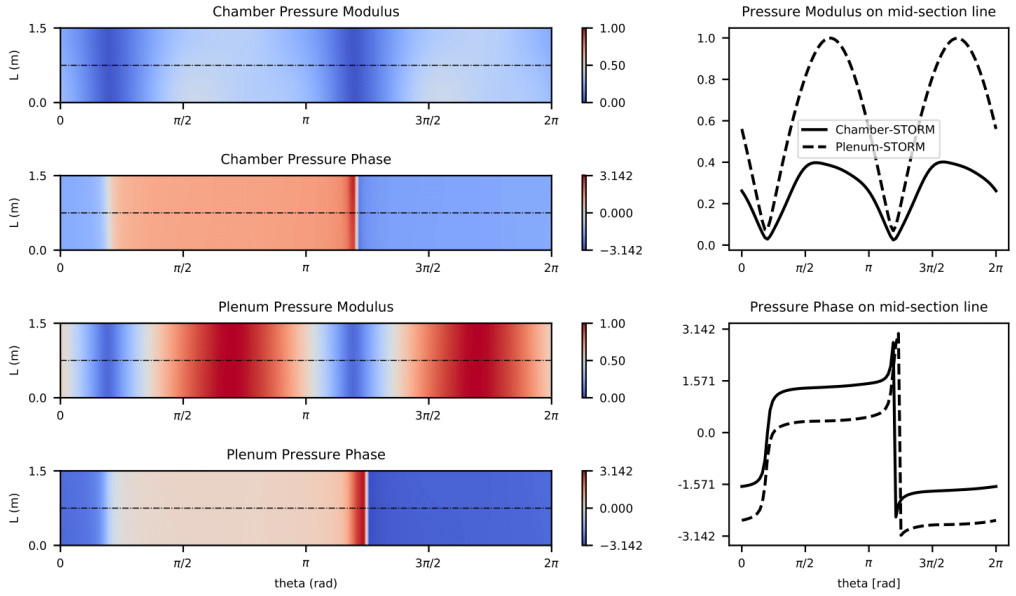

Figure 3.4: SC2 mode shape for flame-index $n = 8$ and delay $\tau/\tau_c = 1.0$.

STORM acoustic network tool. Few discrepancies observed in the mode trajectories in Fig. 3.2 could be attributed to the following deviations:

1. Flames in ATACAMAC network analytical solutions are infinitely thin and modeled with jump conditions. Besides, the FTF flame reference point also

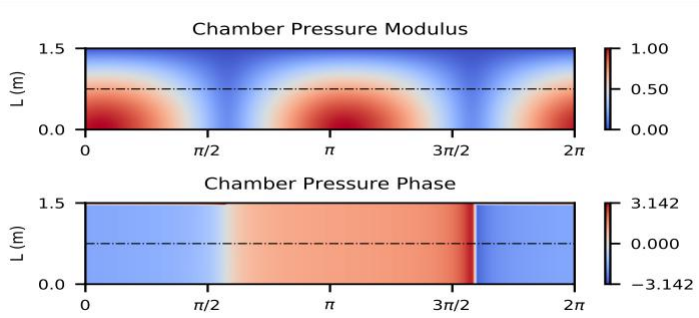

Figure 3.5: PBC: Mixed azimuthal-longitudinal chamber mode in the case of open ($p' = 0$) boundary condition on chamber outlet.

coincides with the flame location. However, in case of STORM, the 1D flame has a finite thickness, within which a Gaussian distribution of heat-release (cf. flame shape $\mathcal{H}_i(x)$ in Eq. 2.14) is presumed. In such academic cases, thin but finite thickness 1D flames are preferred in STORM since infinitely thin flames cause discontinuous velocity jump in thermoacoustic modes, which cannot be accurately captured by finite OB-basis/OC-frame of the modal expansion. It leads to Gibbs fringes in velocity around the flame inside the subdomain. If the velocity at the FTF reference point is affected by these fringes, it can cause spurious flame-response adversely affecting the accuracy of resolution of thermoacoustic modes, particularly their growth rate - see [197] for a demonstration of this point. Secondly, the FTF reference location STORM cannot be inside the flame thickness is approximately considered just upstream (a couple of millimeters) of the flame location.

2. Another major deviation that apparently has a more substantial influence in the discrepancies of mode trajectories in Fig. 3.2 is the fact that plenum and chamber are modeled as 2D annular subdomains, contrary to the fully 1D ATACAMAC network.

As a consequence of point (2) above, the 2D annular subdomains allow accounting for the axial dependence of the acoustics in the chamber/plenum. This PBC configuration can also be analyzed for the case where the chamber is open to the atmosphere by simply modifying the analytical orthogonal basis of the 2D annulus in Eq. (3.1) such that it verifies open ($p' = 0$) boundary conditions at the outlet. Figure 3.5 shows, for example, a mixed azimuthal and longitudinal mode structure correctly represented in the chamber for some arbitrarily chosen $n = 3.0$ and $\tau = 2.0$ milliseconds values. The frequency of this unstable mode is $(216 + 0.282j)$Hz.

3.2 MICCA-Spray Annular Lab-scale Rig

This section reports thermoacoustic linear stability analysis (LSA) of the MICCA-spray configuration using STORM, along with FEM Helmholtz solver AVSP [127] as reference. MICCA-spray is atmospheric pressure annular combustor rig operated at EM2C laboratory [104, 210, 95, 94] as shown in Fig. 1.10(b).

Reference Experimental Data:

Soundararajan et al. [94] experimentally investigated self-sustained azimuthal instabilities in the MICCA-spray rig for three different fuels with distinct volatility. The fuels assessed are liquid heptane, liquid dodecane, and gaseous propane. Indeed in an annular configuration with 16 burners, obtaining a comprehensive understanding of the underlying mechanisms influencing the thermoacoustic instabilities is a rather challenging task. Therefore, a complementary strategy adopted has been to investigate the liquid-spray and flame dynamics in a simpler single injector SICCA-spray burner under similar operating conditions (see Fig. 7.1 in Ch. 7) to understand the prevailing mechanisms. See the following studies, for example [211, 212, 60, 201, 62, 213, 214].

Geometry details: The MICCA-spray rig, shown in Fig. 1.10, consists of [94] an air plenum connected to the combustion chamber through sixteen spray-swirl injectors. The plenum is 80 mm in height with an internal diameter of 280 mm and an outer diameter of 420 mm. The combustion chamber consists of two concentric, cylindrical, and vertical quartz walls of height 400 mm, each with a thickness of 8 mm. The inner quartz wall has an outer diameter of 300 mm, while the outer quartz wall has an inner diameter of 400 mm.

Operating point	$\mathcal{P}$	ϕ	$\dot{m}_{\text{air}}$	u_b
	(kW)	$(-)$	(gs^{-1})	(ms^{-1})
F-1 (Heptane)	6.4	0.85	2.6	43

Table 3.2: SICCA-spray operating condition at which FDF was measured. Note the corresponding F-1 operating point of the annular MICCA-spray on its stability map as black star in Fig. 3.6.

From the experiments performed on MICCA-spray [94], stability maps were plotted for different fuels for varying thermal power-rating and global equivalence ratio. Of these, the map for Heptane fuel is shown in Fig. 3.6. The operating point (F-1) highlighted with $(*)$ corresponds to one of the several operating points at which FDF/FTF measurements were conducted in SICCA-spray — see Tab. 3.2. Since there are 16 burners in MICCA-spray, the thermal power rating of the SICCA-spray is approximately $(1/16)^{th}$ of the MICCA-spray power as marked in Fig. 3.6.

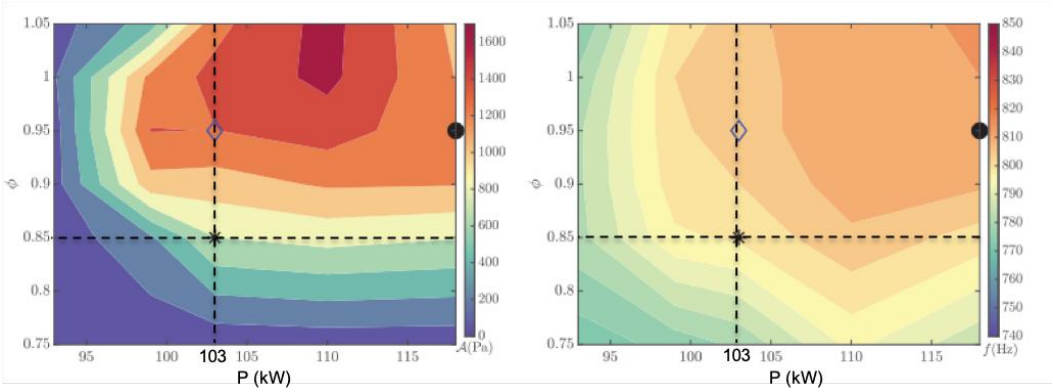

Figure 3.6: MICCA-spray stability map for varying power $\mathcal{P}$, and Heptane fuel equivalence ratio ϕ: color contours indicate oscillation frequency (right) and amplitude (left). Reproduced from [94]. The black star is MICCA-spray operating point, that corresponds to single burner SICCA-spray F-1 conditions at which FDF was measured - see Tab. 3.2. The diamond and black dot are for different fuels [94] and can be ignored.

MICCA-spray LSA discussed in this report is performed at the F-1 operating point employing the measured FTF. Since the combustion chamber outlet is open to the atmosphere, longitudinal and mixed azimuthal-longitudinal instabilities are likely to appear. In the work of [94], only operating conditions leading to unstable 1A1L type chamber azimuthal-longitudinal modes were considered. Note in Fig. 3.6 that a moderate 1A1L type instability is observed at the F-1 operating point at a frequency around 800 Hz with pressure oscillation amplitude 795 Pa.

SICCA-spray FDF measurements published in [94] followed an *indirect* approach wherein the FDF measured with respect to the velocity (measured with hot-wire HW1, see Ch. 7, Fig. 7.1) at a location in plenum was corrected with the swirl-injector response, i.e., an injector describing function. Injector dynamics were characterized under cold flow conditions with the same HW1 in the plenum and HW2 placed in the chamber just above the injector lip. As a result, actual flame dynamics, now for a reference location (HW2) very close to the flame, was isolated from (injector+flame) dynamics. Note that the SICCA-spray FDF/FTF data published in [94] is not used to carry out the MICCA-spray linear stability analysis. Instead, new FDF measurements involving *direct* measurement of velocity with LDV (Laser-Doppler-Velocimetry) under hot-flow conditions at a reference location close to the flame were utilized for MICCA-spray stability analysis.[2]. The FDF reference location precisely is 4mm from the axis and 2.5 mm above the backplane.

[2]Courtesy EM2C laboratory for sharing this FDF data via private communication. It was officially published only recently in Soundararajan et al. [214].

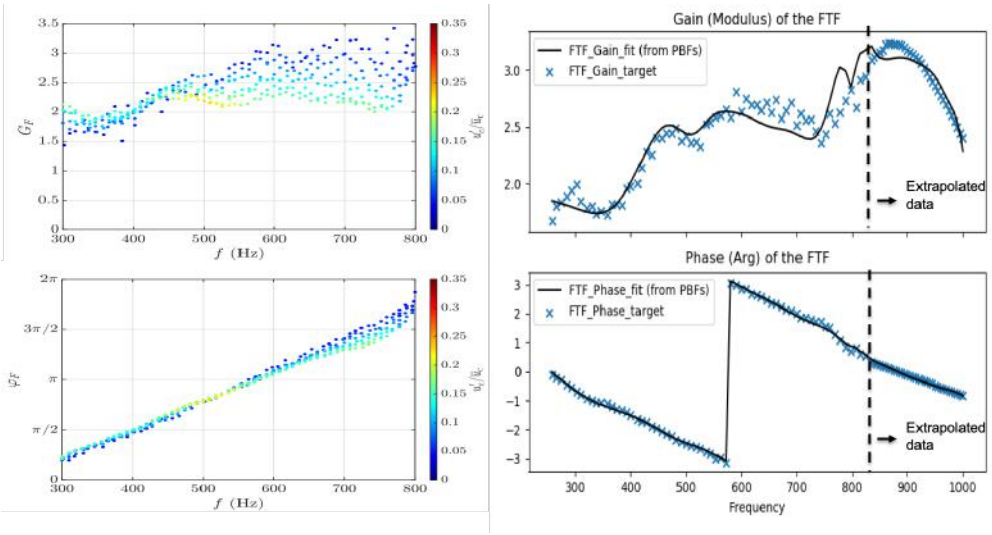

Figure 3.7: (a) Left scatter plot: Experimental FDF measurements for varying loud-speaker voltages and frequency. The color map denotes the $(u'/\bar{u})$ velocity fluctuation amplitude at the FDF reference location. Note that the phase is unwrapped, and the Fourier convention used is not the same as in STORM and the fit in adjacent plot on the right. (b) Right plot: (Blue x) set of data points from FDF measurements at 1500 mV that is treated as FTF. Black curve shows the multi-pole expansion fit of the FTF for STORM computation.

The SICCA-spray flame was pulsed with two loudspeaker driver units upstream of the plenum, and FDF measurements were made for different fixed loudspeaker voltages and frequencies. The loudspeaker voltages applied were from 500 mV to 3000 mV in increments of 500 mV. All the data points are put together on gain and phase scatter plots in Fig. 3.7(a). Note that the velocity fluctuation amplitude $(u'/\bar{u})$ recorded at the reference location (for direct LDV case mentioned above) varies with frequency for a fixed loudspeaker voltage. The velocity perturbation amplitude at each point is thus highlighted with the color contour.

STORM Network and Linear Stability Analysis Results:

While a variety of subdomains 1D/2D/3D could be interconnected to construct an acoustic network in STORM, in this particular case, decomposition of the geometry into subdomains (e.g., combustor, plenum, burners, etc.) is not necessary. The entire geometry with all its intricate details intact is represented as a single, complex *3D subdomain* in the network to which 16 discrete 3D flame elements connect. Since there are no domain-domain coupling or complex boundary impedances, an orthogonal modal basis (OB) is enough; an over-complete (OC) frame is unnecessary for

this 3D complex domain. The modal basis of any 3D arbitrarily shaped geometry is generated numerically from Helmholtz solver [127] by solving computationally faster and cheaper Linear Eigenvalue Problem (LEVP) — more discussion on this in upcoming Sec. 3.4, since its also applicable to the example of engine combustor in subsequent Sec. 3.3. The following STORM computation uses an orthogonal basis of size $N = 60$ natural acoustic eigenmodes and is found to be sufficient.

For the present MICCA-spray case, the acoustic boundary conditions assumed are rigid-wall ($u' = 0$) at the plenum inlet and open to the atmosphere ($p' = 0$) at the chamber outlet. Naturally, the OB basis generated above for the 3D complex subdomain also verifies these boundary conditions.

Mean sound speed field and flame shape are required for AVSP and STORM computations and taken from the time-averaged LES solution of MICCA-spray configuration.[3] Fig. 3.8 depict the mean sound speed field and flame-volume shapes. The color contours of flame volume simply demarcate them (flagged unity) from the rest of the chamber volume (flagged zero).

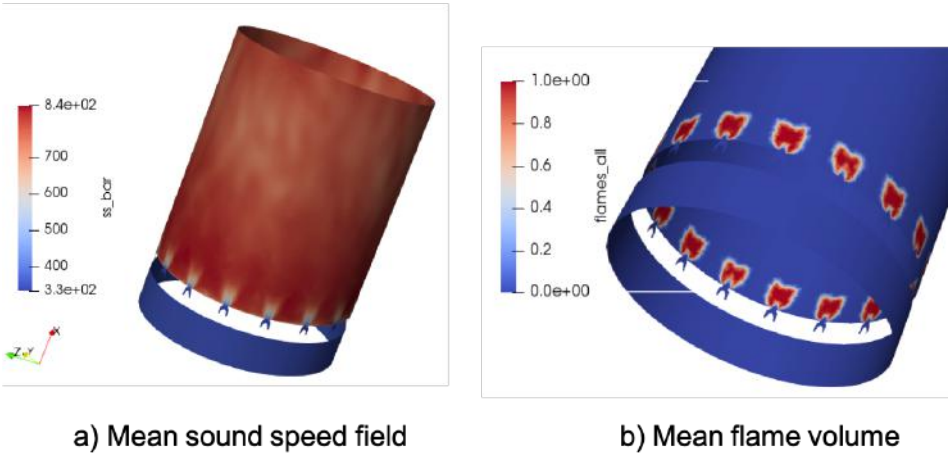

Figure 3.8: Mean sound speed $[m/s]$, and flame shape $\mathcal{H}_i^{(l)}(\vec{x})$ where $l = 1$ to 16. Required both for AVSP and STORM calculations.

As far as flames are considered, all of them are 3D in shape and considered identical. They are assumed to respond only to axial flow perturbations induced in individual injectors by the azimuthal acoustic modes in the plenum/chamber. Flame-flame interaction and flame dynamics to transverse flow-acoustic perturbations are neglected.

From the SICCA-spray FDF measurements described earlier, gain and phase data at a moderate loudspeaker voltage (1500 mV) are considered, and the data is scatter-plotted in Fig. 3.7(b) (blue x). The minimum, max and mean values of

[3] Courtesy Dr. Davide Laera, who is conducting LES of MICCA-spray configuration.

$(u'/\bar{u})$ fluctuation levels over the frequency bandwidth at fixed 1500 mV is 0.033, 0.14 and 0.098 respectively. The mean value is low enough to assume the flame forcing is in a linear regime, and hence this smaller data-set (at 1500 mV) is treated as frequency-dependent, but $(u'/\bar{u})$ amplitude independent FTF. This measured FTF data is extrapolated beyond 800 Hz because chamber 1A1L type modes of interest (investigated in experiments under self-sustained limit-cycle conditions) have a slightly higher frequency in linear eigensolutions from AVSP/STORM, as seen in the following. So while the extrapolation of phase is linear, that of gain is somewhat arbitrary.

The flame response in this example, for each flame in the network, is described by classical FTF that gives unsteady heat release in terms of acoustic velocity perturbation at some upstream reference point — see Eq. (1.10). FTFs are standard flame response models used in linear thermoacoustics. While FTF can be directly introduced in *frequency-domain* Helmholtz solvers (AVSP [127] here) , it ought to be transformed into a *time-domain* state-space (SS) representation before they can be used in a STORM network.

Therefore, SS submodels for flames/FTFs in STORM are obtained through so-called Multi-Pole expansion *(rational approximation)* by fitting a series of rational functions as below to the analytical/experimental FTF data as shown in Fig. 3.7(b).

$$G(\omega)e^{-j\varphi(\omega)} \approx \sum_{k=1}^{M_{PBF}} \frac{-2a_k j\omega}{\omega^2 + 2c_k j\omega - \omega_{0k}^2} \tag{3.3}$$

where $G(j\omega)$ and $\varphi(\omega)$ is the FTF gain and phase respectively. The fit coefficients a_k, c_k, ω_{0k} are determined with the help of rational approximation algorithms. It is then possible to transform the multipole expansion into a SS submodel. See Ch. 4 for more details.

Table 3.3 lists the first few thermoacoustic (TA) modes of the combustor obtained from STORM along with the reference solution from AVSP. The complex frequencies predicted by STORM are in quite good agreement. Growth rates are usually quite sensitive, and some discrepancies exist between STORM and AVSP. Nevertheless, the sign (stability) of the modes, their growth rate magnitudes (whether they are strongly or marginally stable/unstable), and mode structures are predicted reasonably well. As mentioned earlier for Fig. 3.6, an unstable chamber 1A1L type mode was observed in experiments at 800 Hz at limit-cycle conditions, and indeed an unstable mode close to this frequency and structure is predicted by both AVSP and STORM. The pressure mode shape $\Re\{\hat{p}(\vec{x},\omega)\} = |\hat{p}|cos(\angle\hat{p})$ is highlighted in Fig. (3.9). More discussion to follow in Sec. 3.4.

Eigenmodes	AVSP TA modes	STORM TA modes	Nature
352	$351 - 0.76j$	$350 - 1.18j$	(P, 1A, S)
352	$352 - 1.12j$	$352 - 1.72j$	(P, 1A, S)
452	$445 + 20.0j$	$442 + 26.0j$	(C, 1L, –)
652	$653 + 0.42j$	$653 + 0.64j$	(P, 2A, S)
652	$653 - 0.015j$	$653 - 0.017j$	(P, 2A, S)
824	$833 - 10.0j$	$842 - 14.2j$	(C, 1A1L, S)
824	$836 + 0.22j$	$844 + 1.7j$	(C, 1A1L, S)

Table 3.3: MICCA-spray acoustic eigenmodes and thermoacoustic (TA) modes (in Hz) computed from AVSP and STORM. The real and imaginary parts denote the mode frequency and linear growth rates. Modes with +ve growth rates are unstable. (P:Plenum, C:Chamber, A:Azimuthal, L:Longitudinal, S: Spinning, St:Standing)

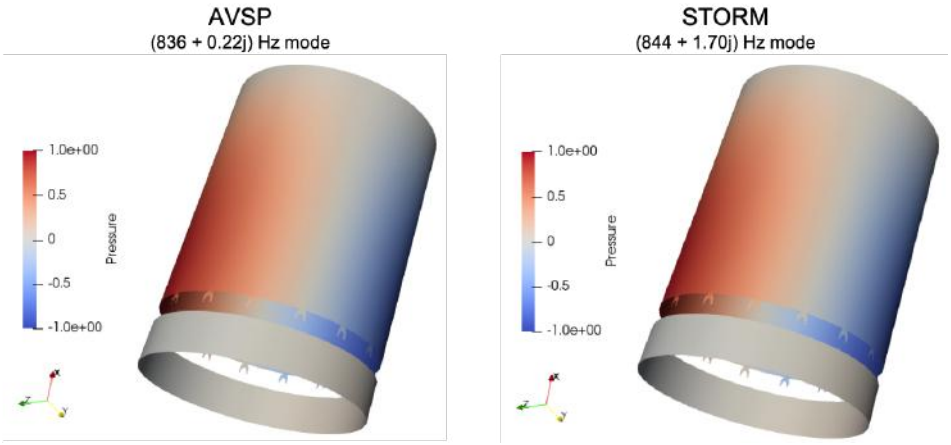

Figure 3.9: Unstable C-1A1L mode structure from AVSP and STORM. This mode was also observed in experiments at 800 Hz (see Fig. 3.6).

3.3 SAFRAN Engine Combustor

One of the main goals behind initiating the development of the tool STORM was to make faster and computationally cheaper thermoacoustic stability analysis of realistic configurations possible. Most low-order network models available in the literature involve drastic simplifications to geometry - for instance, the PBC ATACAMAC case discussed earlier in Sec 3.1. Real engine combustors, on the contrary, include intricate geometrical complexities, multiple cavities, and components such as the chamber, casing, plenum, swirlers, dilution holes, multiperforated liners, upstream compressor diffuser, and downstream turbine stages, all of them interacting acoustically and thus playing a role in the stability of the engine.

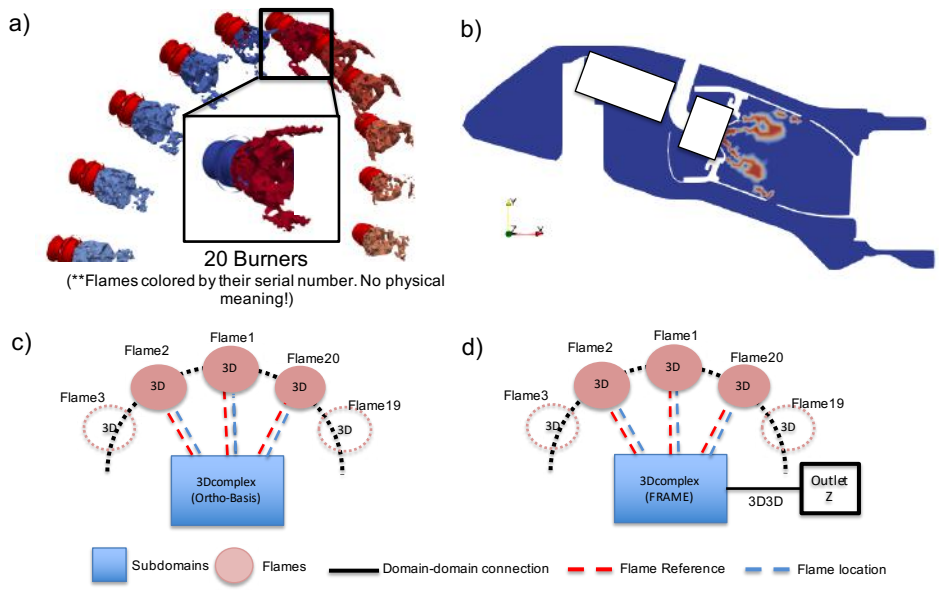

Figure 3.10: Annular Aeronautical Engine Combustor: a) 20 burners and the mean 3D flame shapes, b) cross-sectional cut of the combustor. An illustrative acoustic-network representation in STORM of two different cases based on chamber outlet impedance: c) *Case* $Z{=}\infty$ (i.e. rigid wall) and d) *Case* $Z{=}10$

Some previous works of Schuermans et al. [152, 163], Bellucci et al. [154], Bethke et al. [156], that was based on the state-space framework and classical Galerkin expansions did analyze industrial combustors in the context of low-order modeling. However, the acoustics description was constrained to be based on an orthogonal basis modal expansions, with burners being considered as acoustically compact, lumped elements and were modeled as acoustic transfer matrices. Bethke et al. [156] had demonstrated how arbitrarily complex geometries could be represented as a thermoacoustic LOM by expanding the pressure onto a set of basis functions computed in a preliminary step from a FEM Helmholtz solver.

Linear stability analysis of a SAFRAN aeronautical engine combustor with STORM is presented in this section and validated with classical FEM-based Helmholtz solver (AVSP) [127] predictions. Two cases are considered: ***1) Case-Z∞:*** Chamber Outlet Acoustic Impedance $Z = \infty$ (rigid-wall) and ***2) Case-Z10:*** Outlet Acoustic Impedance Z=10 (arbitrarily chosen for this demonstration). The second case will demonstrate how an over-complete frame in STORM along with the surface spectral connection method helps model non-trivial acoustic boundary conditions at the chamber outlet. Note that the multi-perforated combustion chamber walls are not modeled in this example.

Similar to the MICCA-spray case discussed in the previous section, here as well

the entire geometry, with all its intricate details intact, is represented by a single *3Dcomplex* subdomain in the network Fig. 3.10(c) to which 20 discrete flames connect. The modal basis (or frame as necessary) for the 3Dcomplex domains of arbitrary shapes are generated numerically from AVSP. An advantage of using numerical modal basis/frame is the possibility to account for the inhomogeneous temperature field (or sound speed field) in the combustor.

For the *Case-Z∞*, due to simple rigid-wall ($u' = 0$) boundary condition presumed at the combustor inlet and outlet, and also since there are *no domain-domain connection*, an orthogonal basis made of N=60 modes is chosen and found to be enough.

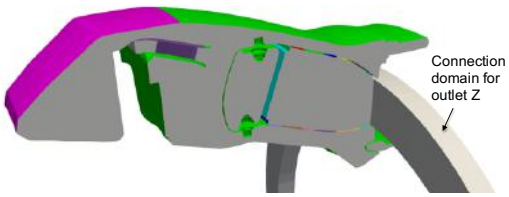

Figure 3.11: Surface spectral connection domain created to model the chamber outlet impedance. Note that in the figure only a sector of the combustor is shown to emphasize the connection domain at the outlet.

However, for the *Case-Z10* (outlet $Z = 10$), an OC-frame is necessary to model the non-trivial resistive impedance considered at the chamber outlet. A frame of the same size $N = 60$ is built from two families of modes: one verifying rigid-wall ($u' = 0$) and the other open ($p' = 0$) at the outlet boundary. The surface spectral connections methodology, described in previous Ch. 2, Sec. 2.3, is employed to impose the impedance on the outlet surface: the combustor 3D subdomain couples with a fictitious connection domain as shown in Fig. 3.11 and as *Outlet-Z* in its network representation in Fig. 3.10(d). The 2D modes required for surface modal expansion are computed in this thin connection domain. The spectral connections modeling framework (i.e., the system of equations) discussed in Sec. 2.3.3 needs to be slightly adapted for embedding the impedance coupling condition in it. It is so because the connection domain couples with only one 3D subdomain instead of two. A simple first-order complex rational function in Eq. (3.4) for the impedance is assumed and fit (with parameters r and ω_c) to get the desired impedance value, $Z = 10$ in this case.

$$Z(j\omega) = \frac{1}{\rho_0 c_0} \frac{\hat{p}(\vec{x}, \omega)}{\hat{u}(\vec{x}, \omega)} = \frac{1}{r + j\omega/\omega_c} \tag{3.4}$$

It can be noted that the above $Z(j\omega)$ impedance function fit will be fair and approximately yield $Z = 10$ only over a certain frequency range. E.g., setting $r = 0.10$ and ω_c to a large value, $Z(j\omega) \to 10$ for a range of low ω values.

Natural Modes (hz)	TA Mode	STORM (Case-Z∞) (hz)	AVSP (Case-Z∞) (hz)	STORM (Case-Z10) (hz)	AVSP (Case-Z10) (hz)
308	1	$(292-7.7j)$	$(292-7.6j)$	$(291-14.9j)$	$(291-11.6j)$
308	2	$(304-17.5j)$	$(304-17.4j)$	$(305-24.9j)$	$(304-21.2j)$
389	3	$(398+28.4j)$	$(398+27.4j)$	$(398+20.3j)$	$(395+21.9j)$
497	4	$(494+13.9j)$	$(494+13.8j)$	$(494+3.7j)$	$(492+7.9j)$
497	5	$(502+15.6j)$	$(501+15.4j)$	$(501+4.0j)$	$(498+8.6j)$

Table 3.4: Natural and Thermoacoustic (TA) modes of the annular engine combustor computed from STORM and Helmholtz solver AVSP. Modes with positive imaginary part (growth rate) are unstable modes.

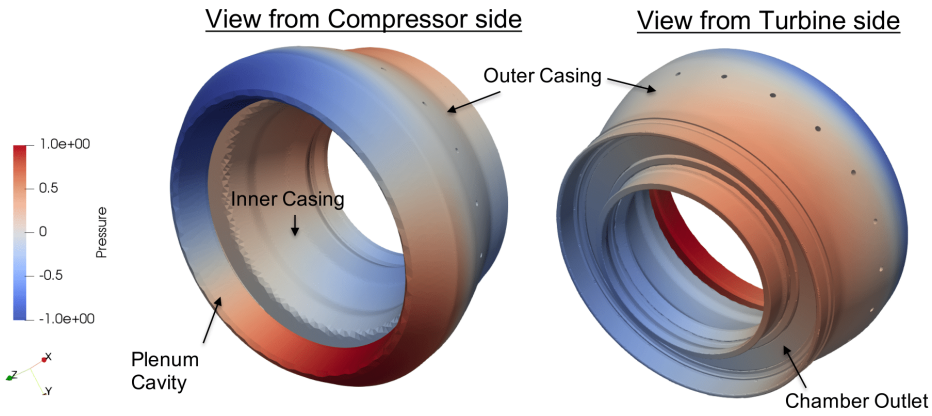

Figure 3.12: *STORM:* unstable TA Mode4 in Tab. 3.4 for Case-Z10.

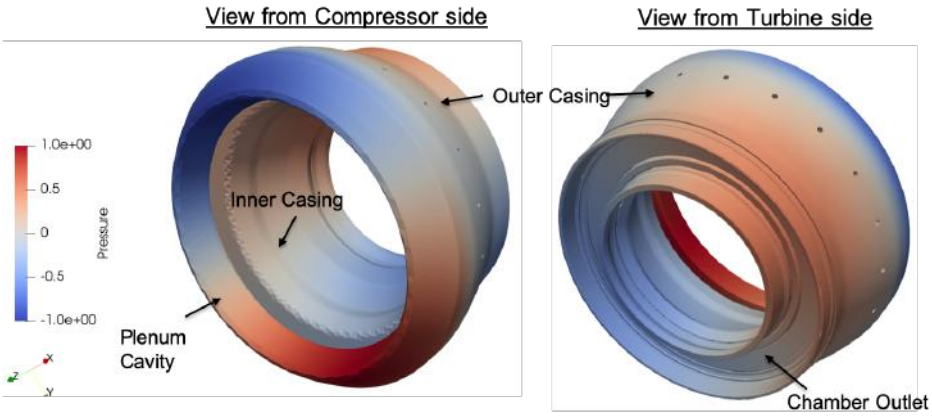

Figure 3.13: *AVSP:* unstable TA Mode4 in Tab. 3.4 for Case-Z10.

The 3D mean flame shape shown in Fig. 3.10 is obtained from combustor sector LES simulations performed in the Ph.D. work of F. Dupuy [215]. Similar to the previous MICCA-spray case, yet again each 3D flame is represented as separate flame-elements in the STORM network shown in Fig. 3.10. This also offers modularity and flexibility to keep the option of studying symmetry-breaking effects open by modifying the flame response (say due to fuel-staging or using different burners along the annulus).

The flames are assumed to respond only to the axial perturbation in the burners induced by azimuthal waves, and the response is taken identical for all of them. It is associated with one *global* constant gain and delay $(n-\tau)$ type FTF transformed into a SS submodel via rational approximation as was described earlier for MICCA-spray.

The results of the first few thermoacoustic (TA) modes computed from STORM and reference FEM AVSP Helmholtz solver are listed in Tab. 3.4. The complex-valued frequencies of TA modes from STORM can be seen to be in very good agreement with the AVSP Helmholtz solver, and so are the mode shapes. For instance, Fig. 3.12 and Fig. 3.13 shows the pressure mode shape of TA Mode 4 (in Tab. 3.4) for Case-Z10 from STORM and AVSP respectively. As one can observe, it is a system mode spanning this complex geometry's computational domain; it is not localized in any particular cavity (chamber/plenum/casing) and has a mixed azimuthal-longitudinal structure. Comparing Case-Z∞ and Case-Z10, the increased damping caused due to the resistive impedance at the outlet surface, modeled via surface spectral connections methodology, is evident in the growth rates of the TA modes in Tab. 3.4.

3.4 Numerical Efficiency

Previous sections demonstrated the capabilities of modal-expansion and state-space-based STORM network tools from academic, simplified Plenum-Burner-Chamber (PBC) configuration to an actual aeronautical engine combustor. What remains is an assessment of the numerical efficiency (or cost) in solving thermoacoustic problems with STORM compared to the reference method - FEM Helmholtz solver AVSP [127].

Recall the general *inhomogeneous* Helmholtz Eq. (1.4) that was discussed in Ch .1, Sec. 1.4.1. Finite-Element Method (FEM) discretization of the frequency-domain, *homogenous* Helmholtz equation (i.e. Eq. (1.4) without non-trivial boundary conditions, and or flame source terms) over a 3D mesh of the geometry, translates into a numerical linear eigenvalue problem **(LEVP)** problem [127, 216], which in

compact matrix notation can be written as

$$\boldsymbol{\mathcal{A}}\mathbf{V} = 0 \tag{3.5}$$

where $\boldsymbol{\mathcal{A}}$ is a constant-valued matrix, and $\mathbf{V}$ its eigenvector. Non-trivial solutions of the above linear system yield the natural acoustic eigenvalues (frequencies) and eigenmodes (spatial shape) of the 3D complex geometry. Since the 3D geometries being dealt with can be big and complex, their mesh sizes of the order of 10^6 to 10^7 (cells), special iterative numerical schemes, and even parallel computations are essential for solving such large eigenvalue problems. Parallel implementation of iterative numerical schemes such as Arnoldi, Jacobi-Davidson, Krylov-Schur, etc., is available in AVSP. Details of these will not be discussed here. See Nicoud et al. [127] and thesis of P. Salas [216] for the formulation of the FEM problem and implementation of the numerical schemes. A broad and in-depth mathematical review on large, linear/nonlinear EVPs and numerical methods for solving them can be found in the seminal literature [217, 218].

On the other hand, FEM discretization of the general inhomogeneous Helmholtz Eq. (1.4), i.e. in presence of active flames and or complex impedance boundaries $Z(j\omega)$, leads to a nonlinear eigenvalue problem **(NLEVP)** which can be represented as follows [127, 216]:

$$\boldsymbol{\mathcal{A}}\mathbf{V} = \boldsymbol{\mathcal{B}}(j\omega)\mathbf{V} \tag{3.6}$$

where $\boldsymbol{\mathcal{B}}(j\omega)$ is a matrix resulting that depends on the frequency (ω). This is due to physical nonlinear dependency of flame-response/FTF (see Eqs. 1.10, 3.3) and impedances $Z(j\omega)$ on frequency ω. Non-trivial solutions of the above Eq. (3.6) then yield the thermoacoustic modes of the system. Solving NLEVP in comparison to LEVP is significantly computationally expensive. Solver techniques, such as *fixed point algorithm*, are required that solve NLEVP by linearizing it with an initial guess of the eigen-solution $(\omega_i, \mathbf{V}_i)$ (typically the natural acoustic modes of the system). The solver then iteratively converges to some true solution (thermoacoustic mode) being sought, and in the due process solving multiple LEVPs.

For both the MICCA-spray annular rig and engine combustor examples discussed earlier, the modal OB-basis/OC-frame, for the 3D complex subdomain were generated numerically by solving computationally fast and cheap linear eigenvalue problems (LEVPs). Such 3D numerical modal basis/frame could be constructed along with other required quantities of interest such as the pressure gradients, the Gram-matrix, etc., (cf. Eq. 2.14) through a one-time pre-processing step. Once done, this creates input files for the core state-space network builder and solver, which can be re-used in any STORM acoustic network as many times as desired. Similarly, in another one-time pre-processing step, the 3D flame shapes are projected onto the 3D modal basis/frame generated, and the projection coefficients associated

with every flame are stored in an input file for the STORM core. With this, the flames can then be re-used in the STORM calculations. Varying their individual response could be easily done since their FTF characteristics (gain and phase) are separately handled and come from the rational approximations (see Fig. 2.12).

In AVSP, unlike LEVPs, which yield a specified number of acoustic eigenmodes in one calculation, TA modes must be individually converged by providing initial guesses. This process can become really cumbersome and computationally expensive, especially for large industrial configurations. Note also that often convergence difficulties are encountered, for instance: 1) cases when there is significant drift in frequencies due to very strong flame response, 2) in case of azimuthal modes which always come in pair, 3) when there are many TA modes of the system clustered on the complex-frequency plane, there is no guarantee that convergence to each of them would be achieved. There are some promising new approaches proposed by other research groups for efficient and faster computations of thermoacoustic NLEVP problems, for example, 1) the approach based on contour integration [219], 2) application of Bloch-Wave theory to configurations with rotational symmetry [220], and very recently 3) sub-space accelerated reduced-order method for NLEVPs [221]. Another new numerical scheme [222], based on rational approximation, was developed recently for NLEVPs.

In comparison to AVSP, STORM performs exceedingly well in this context. Thanks to the rational approximation, the nonlinearity in the EVP due to FTFs (and even $Z(j\omega)$) is transformed in a way into linear state-space flame/impedance submodels (see next Ch.4 for more details). Ultimately, after building the network, what is obtained is a *time-domain global reduced-order linear state-space model* (Eq. 2.7), whose eigenvalues and vectors can be then resolved quite easily. STORM gave the stability of all the TA modes of the annular configurations discussed in this chapter in just one calculation within a *few seconds* of time. The pre-processing steps described above for constructing the numerical basis/frame, and the projection of 20 flames on it, are slightly CPU-intensive calculations than the STORM calculation itself. Still, a comparison of total CPU-time required by AVSP for computing the first few TA modes and STORM (including the preprocessing) gave a factor larger than 10^3. Thermoacoustic calculations of a full-scale annular industrial configuration at such a low cost and speed are indeed worth noting.

3.5 Conclusions

The primary objective of this chapter was to illustrate some of the current capabilities of the STORM tool, complementing examples and conclusions (Sec. 2.5) of previous Ch. 2. Thermoacoustic linear stability analysis of complex, realistic annular configurations along with flame elements was presented.

The simplified Plenum-Burner-Chamber (PBC) configuration was expressed as a relatively large network of 26 state-space submodels involving acoustic 1D/2D subdomains, connection, and flame elements; all put together. The linear stability analysis results with the current modeling methodology of STORM were in reasonably good agreement with the purely 1D wave-based ATACAMAC network. The physical analysis of coupled/decoupled modes described by ATACAMAC theory was consistently retrieved with STORM. An added benefit due to modal-expansion-based acoustics modeling is the possibility of capturing multi-dimensional modes. A simple change in the modal basis of the chamber helped correctly predict the mixed azimuthal-longitudinal chamber modes when the chamber outlet condition is open to the atmosphere ($p' = 0$).

The tool's capabilities were further highlighted by carrying out the linear stability analysis annular MICCA-spray lab-scale rig and SAFRAN engine combustor. The process of generating the numerical basis/frame of arbitrary 3D geometries exploits the cheap, efficient resolution of acoustic eigenmodes with AVSP Helmholtz solver and ultimately resolves the thermoacoustic NLEVP with STORM was described. For the SAFRAN engine combustor, the two cases that were analyzed illustrated the flexibility to use classical OB-basis or OC-frame as required and the strength of the latter, for example, to model the non-trivial outlet impedance with the help of *surface spectral connection* approach. The significant gain in required CPU-time by three orders of magnitude against Helmholtz solver AVSP in solving NLEVP for thermoacoustic modes is worth noting. STORM's network approach's computational speed, modularity, and flexibility suggest the feasibility of conducting extensive parametric studies directly on industrially relevant configurations.

Chapter 4

Modeling of Linear Flame Dynamics in STORM

Contents

4.1 Introduction . . . 93

4.2 Three equivalent representations of a flame as an LTI system 95

4.2.1 Frequency-domain Representation (Transfer Function) 96

4.2.2 Time-domain Representation (Impulse Response and State-Space Model) . . . 99

4.3 Generating State-Space model from Frequency Response . 102

4.3.1 Rational Approximation of Frequency Response . . . 102

4.3.2 *Douasbin et al.* Algorithm (Algo1) . . . 104

4.3.3 Vector Fitting (VF) Algorithm (Algo2) . . . 106

4.3.4 State-Space Model Realization . . . 107

4.4 Physical Constraints in Fitting a Model on Frequency Response Data . . . 109

4.5 Examples of Flame Frequency Response Fitting . . . 114

4.6 Causality in Frequency Response Data . . . 120

4.6.1 Kramers-Krönig Dispersion Relations . . . 121

4.6.2 Bode's Gain-Phase Relation . . . 121

4.6.3 Detecting Causality Violation in the Frequency Response . . 124

4.7 Conclusions and Perspectives . . . 127

4.1 Introduction

The previous chapters elucidated STORM's acoustic network modeling approach based on generalized modal expansions and state-space methods. Several examples, from simple canonical cases to complex industrial configurations, illustrated the application of the tool to perform thermoacoustic linear stability analysis. All the examples in C. Laurent's thesis [197], and in the preceding chapters of this

manuscript, the flames were modeled with the simplest constant $n-\tau$ type flame response model or FTF except for the case of MICCA-spray rig. How the multipole expansion-based rational approximations were employed to obtain the state-space representation of the FTFs was touched upon only briefly. This chapter will cover this topic in more details.

FTFs and acoustic impedances are physical quantities usually expressed in the frequency domain [1, 113, 25, 12], and the state-space models, on the other hand, are defined in the time domain. Barring simple laminar premixed flames, analytical flame models for realistic flames encountered in lab-scale rigs [19, 20, 18], engine combustors (and likewise complex impedances at combustor inlet/outlet boundaries) are often not available. Therefore in practice, data-driven "black-box" flame dynamics models are determined from experimental measurements or high-fidelity LES simulations. It is done by acoustically exciting the flames (or subpart of the geometry whose acoustic impedance is to be characterized)[1] in a well-controlled environment and measuring its response. This process - a.k.a *System Identification*, yields a flame dynamics model usually in the form of the discrete impulse response or frequency-response data. No presumptions are made regarding the functional form of the response model, and it relies only on the input and output data. In the case of frequency-response data, the gain and phase of such FTFs can be typically observed to vary with frequency when represented on Bode plots and showcase peculiar characteristics to be discussed in the next section. Furthermore, as explained by Polifke [12], using such system identification data, "parametric gray-box" (empirical) models can be constructed in terms of a presumed functional form that is fully described by a small number of empirical parameters. The widely used $n-\tau$ model is a classic example of such a parametric model, defining flame response by two parameters. It is possible to assign physical meaning to those parameters, but their values are frequently not determined from the first principles. Instead, they are *tuned*, using phenomenological knowledge of underlying physical mechanisms to match experimental observations, and or are varied over a certain range in order to study parametric sensitivities. In that sense a gray-box model *cannot predict*, but *only describe* flame dynamics.

This chapter takes the linear-time-invariant (LTI) system's view of a flame element in a STORM thermoacoustic network and dives deeper into exploring the methods for generating state-space submodels from flame frequency response datasets (or samples). The chapter will begin by recalling the basic concepts of LTI systems theory, particularly the three equivalent ways of characterizing the dynamics of such systems entirely - viz. transfer functions, impulse responses, and state-space representations. The following sections will describe the rational approximation

[1] Here on, flames are mainly addressed, but the entire discussion in this chapter is applicable for general frequency-dependent acoustic impedances as well.

techniques and algorithms to obtain state-space submodels and elaborate on a few critical physical constraints necessary for the physical admissibility of such time-domain models deduced from FTF/impedance data in frequency-domain. Causality is one property that will be a topic of particular interest in the subsequent parts of this chapter.

4.2 Three equivalent representations of a flame as an LTI system

Linear-time-invariant (LTI) systems theory has far-reaching applications in areas of control engineering, signal processing, system identification, electrical circuit analysis, acoustics, etc. [223, 205, 224, 225, 226, 227, 204], and in general, any technical area where linear ODEs mathematically model the systems. The defining properties of LTI systems are: (i) *Linearity:* the system follows the superposition principle, i.e., if two distinct inputs produce two different outputs, a particular linear combination of these two inputs will give an output that is the same linear combination of the individual outputs, and (ii) *Time-Invariance:* this fundamental property identifies those systems that do not change their behavior with time. If the system yields a specific output when excited with input at one time instant, the system will give the same output when that input is applied at some later time instant.

Many concepts from LTI systems and control theory such as transfer functions, impulse response, state-space models, notions of open-loop or closed-loop feedback systems, Nyquist stability criteria, etc., are drawn and employed by the combustion dynamics community to describe and analyze instabilities in thermoacoustic systems. As discussed earlier in Ch. 1, Sec. 1.4.2, flame dynamics is predominantly modeled/described in terms of the flame transfer function (FTF) or flame describing function (FDF), something which is omnipresent in the literature - see e.g., [1, 113, 25, 228, 12] and references therein. That is, a frequency-domain approach is adopted, quite evidently because it is convenient to carry out linear stability analysis (LSA) of the thermoacoustic system by coupling a flame dynamics model (FTF) with an acoustics solver (e.g., Helmholtz solvers or network models) wherein the eigenmodes are computed. The imaginary part of the complex eigenfrequencies denotes the modes' growth rate (or stability).

The dynamics of LTI systems can be completely described in three equivalent ways: 1) Transfer functions in the frequency domain and 2) Impulse response, 3) State-space models in time-domain. Figure 4.1 denotes a generic open-loop, single-input single-output LTI system that generates an output response $r(t)$ to an input signal $s(t)$. In the context of combustion dynamics, the flame can be viewed as a system whose response is manifested as heat-release-rate fluctuations to an input

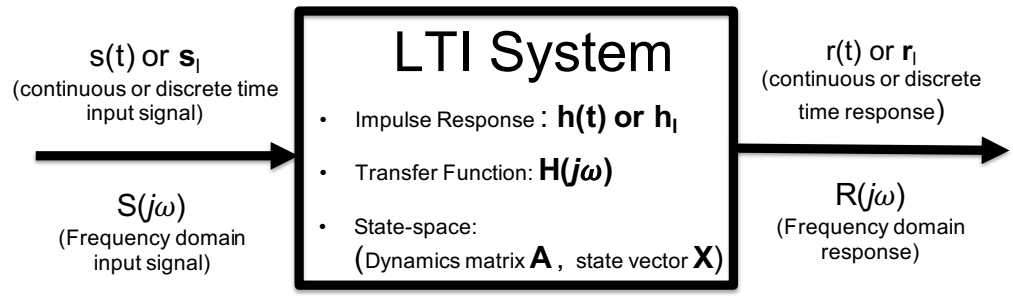

Figure 4.1: Three equivalent representation of an LTI system: 1) Impulse Respose and 2) State-Space Model and 3) Transfer-Fucntion that completely describe its dynamics.

— most commonly the acoustic velocity at some upstream reference location in the case of premixed flames. However, as discussed in Sec. 1.4.2, the flame response could be linked to other perturbations in other quantities as well, such as acoustic pressure or equivalence ratio. Each of these mentioned LTI system representations is briefly discussed next.

4.2.1 Frequency-domain Representation (Transfer Function)

In the frequency domain, it is well established that transfer function $H(s)$ completely describes the linear dynamics of the LTI system in general, defined with complex-valued Laplace variable $s = \sigma + j\omega$, where the real part σ is the growth rate and imaginary part ω the frequency of oscillation (in radians/sec) of the Laplace-transformed signals. Given an input and system transfer function, the output can be directly determined from an algebraic product between $H(s)$ and input signal in s-domain (See Fig. 4.1).

$$R(s) = H(s)S(s) \tag{4.1}$$

Acoustics and combustion dynamics community, equivalently, often adopt a Fourier transform definition that is *extended* over the whole complex plane. It is defined for a *complex-valued* frequency $\tilde{\omega}$, to describe Flame Transfer Function ($\mathcal{F}(\tilde{\omega})$), where the real and imaginary parts denote the frequency of oscillation and its growth rate respectively. [2]

$$\frac{\dot{Q}'}{\bar{\dot{Q}}} = \mathcal{F}(\tilde{\omega})\frac{u'}{\bar{u}} \tag{4.2}$$

An important property of LTI systems is its *frequency response*, which strictly is different from the transfer function though closely related. It is encountered in

[2]Note the difference that arises depending upon whether Laplace or Fourier transform is used: $s = j\tilde{\omega} = j(-j\sigma + \omega)$. That is, when a complex-valued frequency is referred, the oscillation frequency is $\omega = \Re\{\tilde{\omega}\} = \Im\{s\}$ and the growth rate is $\sigma = \Im\{\tilde{\omega}\} = \Re\{s\}$. $H(s)$ and $\mathcal{F}(\tilde{\omega})$ above are equivalent quantities in Laplace and extended-Fourier domains respectively.

thermoacoustics literature that often the terms *Flame Transfer Function (FTF)* and *Flame Frequency Response (FFR)* are used interchangeably. The frequency response of the system is, in fact, the response under steady-state conditions to pure harmonic signals, where both input and resulting output are sinusoidal signals without any transient growth or decay. If the transfer function $H(s)$ is known, the frequency response can be simply obtained by evaluating $H(s)$ along imaginary ω-axis of the complex s-plane i.e., for $s = j\omega$ and $\sigma = 0$ yielding $H(j\omega)$. Conversely, if the FFR is known, estimating approximately the complete *transfer behavior* i.e., transfer function over the complex s-plane is not a trivial task, and there are different methods to approximate it, as discussed in System Identification books [226, 227], and by Schmid et al. [229].

Flame frequency response of realistic flames, contrary to theoretical $n-\tau$ flame models that are characterized with a constant gain and single-time-delay (i.e., linear phase, see Eqs. 1.10, 4.2), when plotted against frequency exhibit peculiar features such as excess gain, i.e., FTF magnitude larger than unity at some frequencies, local maxima, and minima in the gain, and also low-pass filter behavior, i.e., gain at higher frequencies decaying to zero. For the phase, there are deviations from linear variation with frequency, rapid changes, and even inflection at frequencies where the gain maxima/minima are present. All these features can be observed in Fig. 4.2, and can be explained based on the constructive and destructive superposition of the flame responses owing to the underlying physical mechanisms of flame dynamics that were described in Ch. 1 - Sec. 1.2.1, and Sec. 1.4.2.

Flame(s), when considered as an isolated thermoacoustic network element or as an open-loop LTI system, is expected to be a stable system. It is when they are coupled with an acoustic network that the feedback loop between flame(s) and acoustic field is established, leading to some eigenmodes of the whole (closed-loop) system becoming stable or unstable. In most practical cases, FFR at a few discrete points in the frequency bandwidth of interest is the only available data from experiments or simulations. While carrying out quantitative linear stability analysis (LSA), a common practice is to directly and only use the FFR instead of an FTF. It implicitly means extrapolating the FFR along the σ-axis by a constant value (simple extrusion). Schmid et al. [229] elaborate that the accuracy and reliability of such LSA predictions are quite sensitive to how well the FFR-extrusion approximates true-FTF and that care must be taken in interpreting the results. This is especially true for thermoacoustic modes where strong flame feedback leads to relatively large growth rates. To quantify the deviation of FTF-approximation from true-FTF, either by extrusion or other better methods mentioned, the authors [229] recommend determining the so-called *region-of-confidence* based on the number of available FFR data-points in the spectrum and acceptable error bound between the two. It, thus, demarcates a region on the complex-frequency plane around FFR points, and all

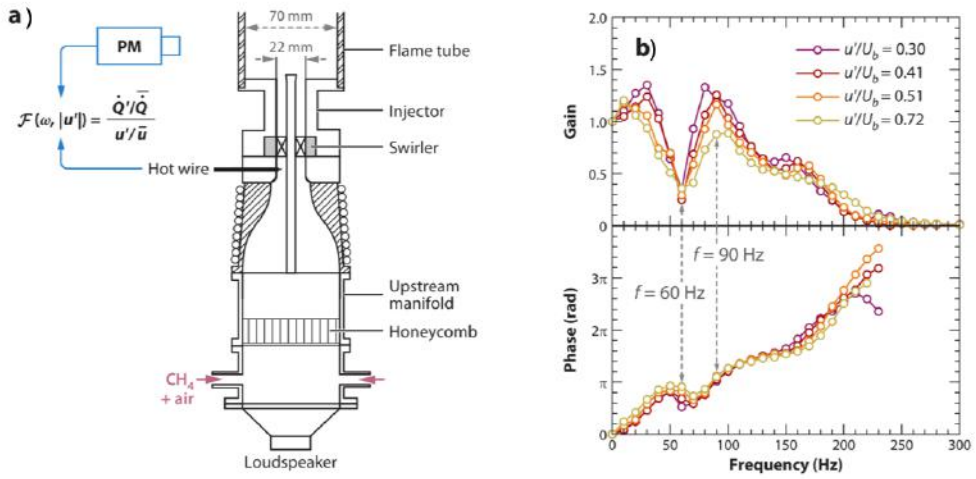

Figure 4.2: a) Lab-scale experimental rig operated at EM2C to determine the adjacent swirling flame describing function. (b) Typical flame describing function (FDF). Figure reproduced from [25], originally adapted from Palies et al. [26].

the eigenmodes falling inside them can be reasoned of being well-predicted.

Flame transfer function (FTFs) can be generalized by parameterizing it with the amplitude of acoustic perturbations the flame is subjected to as an additional variable. The family of flame transfer functions thus obtained is the so-called Flame Describing Function (FDF) that also depends on the oscillation amplitude. In comparison to FTF (see Eq. 4.2), the FDF is given as follows, and an example for a real swirl premixed flame is shown in Fig. 4.2

$$\frac{\dot{Q}'(\tilde{\omega}, |u'|)}{\bar{\dot{Q}}} = \mathcal{F}(\tilde{\omega}, |u'|)\frac{u'}{\bar{u}} \tag{4.3}$$

FDF description helps capture the inherent nonlinear nature of the flame response mainly due to acoustic oscillation amplitude. When coupled with an acoustic solver, it helps model and predict many nonlinear phenomena observed in thermoacoustic combustion instabilities often seen in experiments: limit-cycle amplitudes, frequency-shift during transient growth of oscillations mode switching, instability triggering, hysteresis, etc., e.g., see [113, 182, 130, 143, 183]. It should be noted that this chapter and manuscript mainly deal with the linear FTF form of the flame response model, and FDF representation in STORM will be part of future work.

It is reiterated that the primary objective of this chapter, which is determining the time-domain state-space model for a flame given its sampled frequency response (FFR) data, is covered in the Sec. 4.3 as a continuation of this subsection. However,

before that, the following sub-section will briefly review the time-domain approaches for representing flame response as an LTI system.

4.2.2 Time-domain Representation (Impulse Response and State-Space Model)

4.2.2.1 Impulse Response

In the time-domain, the impulse response function $h(t)$ of an LTI system fully characterizes its dynamics, i.e., knowledge of the impulse response suffices to predict the output for any input signal as depicted in Fig. 4.1. Impulse-response can be defined as a system's response to an ideal impulse, viz., the Dirac-delta function. The time-domain response $r(t)$ is obtained from input signal $s(t)$ through convolution integral, as follows, unlike a simple algebraic product in frequency-domain (Eq. 4.1).

$$r(t) = h(t) * s(t) = \int_{-\infty}^{+\infty} h(\tau)s(t-\tau)d\tau \tag{4.4}$$

The flame transfer function $H(s)$ (in Laplace space), or for stable, steady state harmonic signals frequency response $H(j\omega)$ (in Fourier Space), are direct frequency-domain equivalents of flame impulse response function $h(t)$. They can be converted into each other by Laplace/Fourier transform (and its inverse). The relation above is defined in *continuous-time* sense. However, as detailed by Polifke in [12], when working with *discrete-time* signals, it is rather convenient to use *z-transform* (and its inverse) to define impulse reponse $\mathbf{h}$ as a sequence of coefficients $\mathbf{h} = (h_l)$ (see Fig. 4.1). The discrete convolution sum relating input (s_l) and output (r_l) sequences is then given as follows, where subscript l denotes the time sequence index. For eg. the input signal $\mathbf{s} = (s_l) = (s[l\Delta t])$ for $l = 0, 1...N$ where Δt is the time increment.

$$r_l = \sum_{k=-\infty}^{+\infty} h_k s_{l-k} \tag{4.5}$$

Regarding the point made earlier for the need of *extending* the flame frequency-response (FFR) over entire complex-plane to carry out thermoacoustic stability analysis: one method suggested by Schmid et al. [229] and also demonstrated by Tay-Wo-Chong et al. [230], Macquisten et al. [231] was to utilize the flame impulse response (IR) coefficients h_k, by taking its forward z-transform, to obtain Flame Transfer Function (FTF). Here, the required IR coefficients h_k are determined from an apriori step with inverse z-transform of the FFR data. The resulting FTF can then be evaluated for arbitrary complex-valued frequencies. See the cited references for details and [232, 12] for more theoretical background.

4.2.2.2 About Single- vs. Distributed- time delay in flame dynamics

Time delay plays a crucial role in acoustic flame response and eventually in thermoacoustic combustion instabilities. It is typically associated with the convective transport of flow-flame perturbations, e.g., equivalence-ratio, vorticity waves from the injector towards the flame, wrinkles along the flame front due to upstream velocity perturbations, etc. - see Ch. 1, Sec. 1.2.1, 1.4.2, for a summary of different known physical mechanisms governing flame dynamics. Often not one but several of these physical processes are simultaneously at play, depending on the specificities of the configuration geometry, flow, and operating conditions. It is reasonable to expect that each of these processes, interaction mechanisms, will have different characteristic time scales associated with them. Therefore, ascribing a single constant time delay, as done in simplistic $n - \tau$ type models, is inadequate to describe the flame dynamics of realistic flames.

Flames, when subjected to a perturbation, do not respond instantaneously, but typically the first response is initiated after a certain *dead/propagation* time delay, followed by a dynamic response over a small time interval. In other words, the flame response is not obtained at one later instant but is distributed over multiple time instants. This quite naturally give rise to *Distributed-time-delay* (DTD) flame response models [22, 179, 178, 233, 176], and the aforementioned behavior can be clearly observed in an impulse response of a flame. Polifke in [12] provides a keen review of work on the time-domain approach for describing flame dynamics using impulse response and DTD empirical models, its range of validity and applicability, etc. The author also emphasizes that most of the peculiar features of premixed flames' frequency response can be explained naturally and in a physically intuitive manner with the impulse response DTD approach. It is briefly described next, along with an illustration.

For a simple *single-delay* $n - \tau$ FTF, the impulse response, in discrete-time, would be given by only one non-zero coefficient h_k with one associated time-scale for the delay. On the classic Bode plot, the frequency response of this FTF is constant gain n and a perfectly linear phase $\varphi = \omega\tau$ plot against frequency. Polifke [12] illustrates through a series of contrived examples, by incrementally including elementary complexities in the discrete impulse response, how all the characteristic features observed in frequency response (Bode plots) of swirling premixed flames could be retrieved (see Figs. 3 - 7 in [12]). The accompanying Nyquist plots (a.k.a. phasor diagrams) provide insight into how this is achieved in terms of constructive and destructive superpositions of phasors corresponding to each time-scale or coefficient h_k. *Dual time delays* i.e., only two non-zero coefficients h_k in the impulse response (or only two distinct time-delay scales in the distribution) help reproduce local maxima and minima, excess gain (> 1), and non-linear phase variation in the

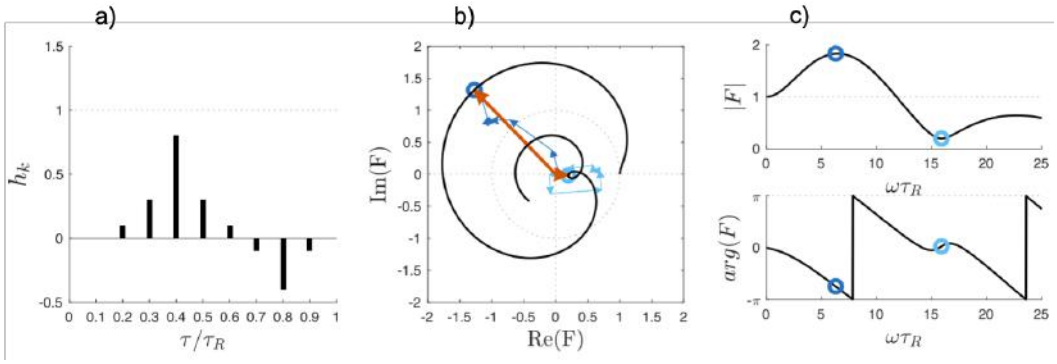

Figure 4.3: a) Example of a discrete-time impulse response h with distributed delays that gives frequency response characteristics of swirling premixed flames - seen in adjacent plots. Time delay $\tau = 3\Delta t$. Times and frequencies are non-dimensionalized with reference time scale τ_R, and the time increment $\Delta t = 0.1\tau_R$. b) Frequency response ($F(\omega)$) representation on Nyquist plot (phasor diagram) and c) Frequency response Gain and Phase (Bode plot). (Replicated from [12])

Bode plots. Further, *distributed delays* with all positive h_k coefficients supplement these features with the low-pass filter behavior. Finally, a distribution with positive and negative coefficients retrieves all the abovementioned features together. This last general case- its impulse-response with distributed delays, Nyquist and Bode plots, are shown in Fig. 4.3.

Preceding discussion leading to Fig. 4.3 makes it evident that the nature of the flame frequency response (FFR) is closely related to the time-delay distribution seen in its impulse response. It also suggests that components of the complex-valued FFR - gain and phase (or the real and imaginary parts) are somehow related. As will be shown in the upcoming sections of this chapter (Sec. 4.4 to 4.6), it is indeed true that the real and imaginary parts of the frequency response of an LTI system are not independent and related to each other by the so-called *Kramers-Krönig dispersion relation* [234, 235]. These relations are the theoretical definition of *causality* in frequency-domain [236, 237, 238] of the response function of LTI systems [239, 240, 241]. Most LTI systems of practical interest are expected to satisfy these conditions.

4.2.2.3 State-Space Models

In the previous two approaches, the flame dynamics is entirely characterized by a functional form of impulse response $h(t)$ in time-domain or transfer function $H(s)$ or $H(j\omega)$ in frequency-domain. Another equivalent time-domain approach for representing LTI systems is the state-space method which was introduced in Sec. 2.1.1.

The state-space model is, however, defined as a dynamical system in terms of *state-variables* as a set of linear ordinary different equations ODEs. As discussed earlier in Sec. 2.1.1, the underlying physics of flame dynamics is quite complicated, and deriving models for it from first principles is a challenging task, especially, for flames of practical interest - turbulent swirling flames. What is typically accessible are flame frequency response measurements from experiments or high-fidelity simulations. Therefore, a technique is needed for obtaining state-space models for linear flame dynamics from FFR measurement data. This is the core subject of this chapter and is discussed in the following section.

4.3 Generating State-Space model from Frequency Response

This section will discuss the main objective of generating a state-space model of flame response from discrete flame frequency response data. The first step towards it is to obtain the frequency response in a functional form from discrete data samples. Two equivalent techniques[3] that are commonly used — Rational Polynomial Function (Padé approximation) and the Pole-Residue Formulation — are presented in the following subsection. Specialty to these mathematical representations is the ease with which they could be transformed into the time domain by inverse Laplace/Fourier transform to obtain impulse response or differential equations for state-space models. A couple of different algorithms to fit this function/formulation on the data-set employed in the current work are introduced in the subsequent subsections. Both these approaches have been utilized in CFD/aeroacoustics/thermoacoustics research for deriving TDIBC (Time-Domain Impedance Boundary Conditions) for compressible LES from frequency-domain acoustic impedance/reflection-coefficient information [242, 243, 244, 245] and also for approximating flame frequency response from measurements as well [246, 163, 179, 186, 202, 88]. Finally, the last subsection will present, of the many possible ways, the approach for state-space model realization from the rational approximation that is employed in STORM.

4.3.1 Rational Approximation of Frequency Response

General problem definition of rational approximation:
Given $\bar{k}$ measurement of the frequency response,

$$H_k = H(j\omega_k) \qquad k = 1, ..., \bar{k} \tag{4.6}$$

[3]Both these techniques are addressed by one general term, *Rational Approximation*, in this chapter and elsewhere in the manuscript.

the idea is to determine a rational function $\tilde{H}(j\omega_k)$ that *approximates* the given measurements

$$\widetilde{H}(j\omega_k) \simeq H_k \qquad \forall k = 1, ..., \bar{k} \tag{4.7}$$

The two techniques used for obtaining $\widetilde{H}(j\omega_k)$ are:

1. **Rational Polynomial Function (Padé approximation):**
   One of the most popular ways of approximating transfer function (actually frequency response to be precise) from frequency response measurement data-samples is to *approximate* it as a rational polynomial function, also known as Padé approximation given as follows. They are universal approximators and can approximate a wide range of functions with arbitrary accuracy [247, 248].

   $$\widetilde{H}(j\omega) = \frac{n(j\omega)}{d(j\omega)} = \frac{\sum_{n=0}^{\bar{n}} a_n (j\omega)^n}{\sum_{n=0}^{\bar{n}} b_n (j\omega)^n} \tag{4.8}$$

   where $a_n, b_n \in \mathbb{R}$ are unknown coefficients, and $\bar{n}$ is the order of the desired model. In Eq. (4.8), note that the numerator and denominators are polynomials in $(j\omega)$ with their degrees $\bar{n}$ taken to be the same as a general case.

2. **Pole-Residue Formulation:**

   An alternative approach to Padé approximation is the so-called *pole-residue* construct wherein the frequency response is modeled as a series of partial fractions as shown in the following general formulation. This approach is also referred to as *Multi-pole expansion*.

   $$\widetilde{H}^{(i)}(j\omega) = R_0^{(i)} + \sum_{n=1}^{\bar{n}_r} \frac{R_n^{(i)}}{j\omega - p_n^{(i-1)}} + \sum_{n=\bar{n}_r+1}^{\bar{n}_r+\bar{n}_c} \left[\frac{R_n^{(i)}}{j\omega - p_n^{(i-1)}} + \frac{\left(R_n^{(i)}\right)^*}{j\omega - \left(p_n^{(i-1)}\right)^*} \right] \tag{4.9}$$

   where the first term $R_0^{(i)} \in \mathbb{R}$ is a constant term, the series in the second term is a real-valued multi-pole expansion for prescribed $\bar{n}_r$ number of real poles p_n, and residues R_n and the series in the third term are $\bar{n}_c$ complex-conjugate pairs of poles (and corresponding residues) on the complex plane. Thus the total order of the model is $\bar{n} = \bar{n}_r + 2\bar{n}_c$. The superscript $(\cdot)^{(i)}$ is the iteration index involved in fitting the above model on the data samples.

Choosing any of the above form, the goal is to fit the model on the discrete frequency response data samples. In other words, the problem is to determine the coefficients a_n and b_n in case of Eq. (4.8) or the poles p_n and residues R_n for Eq. (4.9) by minimizing the error L2 norm between the samples H_k and the model $\widetilde{H}(j\omega_k)$ given as follows

$$e^2 = \frac{1}{\bar{k}} \sum_{k=1}^{\bar{k}} \left| H_k - \widetilde{H}\left(j\omega_k\right) \right|^2 \tag{4.10}$$

It is also worth mentioning that the two rational approximations presented above are mathematically equivalent. In Eq. (4.8), the zeros or roots of the denominator are also poles of the model $\widetilde{H}(j\omega)$. Factorizing the denominator and using partial fraction decomposition techniques, Eq. (4.8) can be recast into a partial fraction series similar to Eq. (4.9). In other words, if a rational polynomial fraction is known, the equivalent pole-residue formulation can be found and vice-versa. This was demonstrated and explicit relations between coefficients a_n, b_n and poles p_n and residues R_n were rigorously derived by Douasbin (Chapter 8 in [249]) for a generic model of order $\bar{n}$.

Minimizing Eq. (4.10) is a *nonlinear* least-squares problem, due to the unknowns b_n in the denominators for Eq. (4.9). Although nonlinear optimization algorithms can be applied directly, it is well-known that they can be quite time-consuming and prone to local minima. The pole-residue formulation relatively leads to much better numerical conditioning of the optimization problem [248].

The following couple of subsections discuss two different algorithms for fitting *pole-residue* form of a model on frequency response data samples, viz. i) *Algo1*: proposed by Douasbin et al. [242, 249] and ii) *Algo2*: Vector Fitting algorithm, the version described by Triverio [248]. The idea is not to present both the methods rigorously here but to highlight the fundamental algorithmic differences. Complete details, including implementation pseudo-codes, can be found in the mentioned references.

4.3.2 *Douasbin et al.* Algorithm (Algo1)

Douasbin et al. [242, 249], in their work proposed a methodology for modeling Delayed Time Domain Impedance Boundary Conditions (D-TDIBC) for compressible Navier-Stokes LES simulations by extending existing TDIBC techniques [245, 244, 243]. One of the motivations behind *delayed* TDIBC technique is the cost-benefit, as it allows computational domains in LES to be clipped and the boundary condition be characterized correctly at the new boundary. D-TDIBC, of course, while retaining the reflection coefficient of the original boundary (before truncation), imposes a *time-delay* on top of it. So, if $R(j\omega)$ is the reflection coefficient in frequency-domain of the original boundary, D-TDIBC imposes the delayed reflection coefficient $R_\tau(j\omega) = R(j\omega)e^{-j\omega\tau}$, in time-domain. τ is the time delay associated with acoustic wave propagation over the truncated domain. For example, long ducts near the inlets/outlets of the geometry could be clipped off for gains in computational cost/time.

With or without delay, the frequency-domain impedance/reflection coefficient ($R_\tau(j\omega)$ or $R(j\omega)$), ought to be transformed in time-domain for LES, as done for TDIBC, or into a state-space model for low-order acoustic network solvers such

as STORM in the current context, or see e.g., [246, 250]. This transformation is achieved thanks to the rational approximation of impedance/reflection-coefficient measurements or sampled data from their complex analytical definitions.

Douasbin et al. [242, 249] proposed an algorithm to get a pole-residue rational approximation of reflection-coefficient data, and it is briefly described in this subsection. The modeling of simple $ne^{-j\omega\tau}$ type flame transfer functions, used for examples presented in previous chapters, was primarily based on this algorithm. In this chapter, attempts are made to use both this and the Vector Fitting (Sec. 4.3.3) algorithms for fitting more general realistic flame frequency responses.

The pole-residue model used by authors in [242, 249] is slightly different from that of Eq. (4.9) since they consider only complex-conjugate pair of poles without real poles and the constant term. A pair of partial fractions due to complex-conjugate poles is also referred to as a *Pole-Base-Function* (PBF). The authors separate real and imaginary parts of a PBF, plot them, evaluate their mathematical properties and identify the relations between unknown coefficients, viz., the real and imaginary parts of conjugate poles and residues. These inter-relations are exploited to obtain a well-calculated *intial guess* before for the subsequent step of optimizing them to minimize the error (cf. Eq. 4.10).

The real part a PBF (say the k^{th} PBF) can typically be observed of being similar to a asymmetric bell curve with following three *properties*: i) $\omega_{0,k}$ the *resonant frequency*, where the real part of the PBF is maximum, ii) $h_{0,k}$ height of the peak at $\omega_{0,k}$, and iii) right-hand-side half-width $\Delta\omega_\varepsilon$, which is defined as, for a given small percentage $\varepsilon \in [0, 1]$, the band-width ($\Delta\omega_\varepsilon = \omega_+ - \omega_{0,k}$) where ω_+ is the frequency where $\Re(PBF_k) = \varepsilon h_{0,k}$. These properties due to characteristic shape of the real part of a PBF are used to identify and derive inter-relations among the unknown coefficients.

The iterative fitting algorithm starts with the user providing a max number of PBFs, and convergence criteria (Eq. 4.10). At each iteration, a PBF is added to the model and is placed at the frequency ($\omega_{0,k}$) where the error between model and target data is max. $h_{0,k}$ of the added PBF is set equal to this max error, and the unknown coefficients are determined using the inter-relations. Finally, a *nonlinear* least-squares problem is solved to optimize all the coefficients of iteratively added PBFs, minimizing the error (Eq. 4.10) between model and the target data. If the convergence criterion is met, the algorithm is terminated. Else, it repeats the process of adding a PBF at each new iteration until the max number of PBFs is reached. The PBF placement in the spectrum is based on the *real part* of the data/model, and the fitting of the imaginary part is left to the last optimization step during each iteration. The algorithm's multi-dimensional nonlinear optimization in STORM uses the gradient-based Levenberg-Marquardt method available in the standard MINPACK library.

For lower model orders, i.e., low number of PBFs, the algorithm works quite efficiently; however, as the order increases, the algorithm struggles a bit, and the convergence takes considerable time compared to the Vector Fitting algorithm discussed next. Several *examples* fitting flame frequency response of realistic burners using both the algorithms are presented in the following Sec. (4.5).

4.3.3 Vector Fitting (VF) Algorithm (Algo2)

Vector Fitting (VF) is a well-established algorithm for the rational approximation of frequency-response data, quite influential and prominent in the area of electrical/electronic circuit analysis and signal integrity simulations of scales from long transmission lines to small integrated-circuit (IC) microchips. VF was originally conceived and proposed by Gustavsen and Semlyen [247] in 1999. Later many research groups have developed it further into advanced and fully-featured algorithms - see the review by Triverio [248].

Combustion dynamics community as well has employed VF for approximating flame frequency responses and acoustic impedances [246, 163, 179, 186, 88, 243, 251, 252] in the context of low-order modeling of aero/thermoacoustics.

VF is inspired from the early works of Levy [253] and Sanathan-Koerner (SK) [254] long back in 1960s for rational approximation. Their prefered approach was to iteratively solve the original nonlinear optimization problem in Eq. (4.10) by *linearizing* it. At each iteration, the resulting linear least-squares can be solved efficiently and robustly with QR decomposition. In the Sanathan-Koerner (SK) method, the error function — rewritten From Eq. (4.8) and Eq. (4.10) — is linearized by replacing $\sum_{n=0}^{\bar{n}} b_n^{(i)}(j\omega)^n$ in denominator with $\sum_{n=0}^{\bar{n}} b_n^{(i-1)}(j\omega)^n$ which known from previous $(i-1)^{th}$ iteration.

$$\left(e_{SK}^{(i)}\right)^2 = \frac{1}{\bar{k}} \sum_{k=1}^{\bar{k}} \left| \frac{H_k \sum_{n=0}^{\bar{n}} b_n^{(i)} \left(j\omega_k\right)^n - \sum_{n=0}^{\bar{n}} a_n^{(i)} \left(j\omega_k\right)^n}{\sum_{n=0}^{\bar{n}} b_n^{(i-1)} \left(j\omega_k\right)^n} \right|^2 \tag{4.11}$$

The SK method for fitting rational polynomial function, in practice, however, is still prone to numerical issues [248] especially when large model order $\bar{n}$ is required and or the data-samples are spread over a wide bandwidth, i.e., are defined for large frequencies ω. The numerical issues are attributed to: i) presence of high powers of $(j\omega)^n$ leading to poor conditioning of the least-squares problem, and ii) the weighting term in the denominator, $\sum_{n=0}^{\bar{n}} b_n^{(i-1)}(j\omega)^n$, typically exhibit large variations over the bandwidth of frequency response data samples.

The VF algorithm, contrary to using Padé approximation type formulation as in SK method (Eq. 4.8), adopts the pole-residue model (Eq. 4.9) that provides much better numerical conditioning addressing above issues to a large extent by a simple yet brilliant solution[247, 248].

The VF algorithm minimizes the following linearized error function that is defined analogously to the SK method's error function in Eq. (4.11). Note that for i^{th} iteration, the poles in the denominator are known quantities from the previous $(i-1)^{th}$ iteration.

$$\left(e_{VF}^{(i)}\right)^2 = \frac{1}{\bar{k}} \sum_{k=1}^{\bar{k}} \left| H_k w^{(i)}(j\omega_k) - \widetilde{H}^{(i)}(j\omega_k) \right|^2 \tag{4.12}$$

where

$$\widetilde{H}^{(i)}(j\omega_k) = r_0^{(i)} + \sum_{n=1}^{\bar{n}} \frac{r_n^{(i)}}{j\omega_k - p_n^{(i-1)}} \tag{4.13}$$

$$w^{(i)}(j\omega_k) = \frac{\prod_{n=1}^{\bar{n}} (j\omega_k - p_n^{(i)})}{\prod_{n=1}^{\bar{n}} (j\omega_k - p_n^{(i-1)})} = 1 + \sum_{n=1}^{\bar{n}} \frac{w_n^{(i)}}{j\omega_k - p_n^{(i-1)}} \tag{4.14}$$

The $\widetilde{H}^{(i)}(j\omega)$ is the approximated model after i^{th} iteration, and the new term $w^{(i)}(j\omega)$, is the so-called *weighting function* that helps deduce updated set of poles $p_n^{(i)}$ from $p_n^{(i-1)}$. See [248] for details.

The user has to provide initial set of poles $p_n^{(0)} \in \mathbb{C}$ as per the model order $\bar{n} = \bar{n}_r + 2\bar{n}_c$ for the fitting process to start $(i = 1)$, and the max number of iterations (i_{max}) to perform before terminating the process unless convergence criteria is met in between. The choice of initial poles could be random for most problems of practical interest, and the algorithm is quite robust and fast to efficiently *relocate* the poles on the complex plane to minimize the error between model and data.

Upon convergence, $p_n^{(i-1)} \rightarrow p_n^{(i)}$, and become poles of the obtained model $\widetilde{H}^{(i)}(j\omega)$. Simultaneously with this, the weighting function $w^{(i)} \rightarrow 1$ as apparent from first equality in Eq. (4.14) and the linearized error function (Eq. 4.12) tends to original error function (Eq. 4.10), as desired.

4.3.4 State-Space Model Realization

Having obtained the model transfer function $\widetilde{H}(j\omega)$ by rational approximation from the frequency response data samples, the ultimate objective to realize a state-space model is described now. There are many ways of state-space model realization from the general pole-residue form (Eq. 4.9) as such [248], and a comprehensive review of different methods is provided in [255]. The one that is employed in STORM is presented here.

Pole-residue formulation with only complex conjugate pairs of poles (cf. Eq. 4.9) are considered for rational approximation in STORM, consistent with the one used by Douasbin et al. [242, 249] for delayed reflection coefficients (Sec. 4.3.2). Further to reach this specific multipole expansion model, substitute for poles $p_n = c_n + jd_n$ and residues $R_n = \alpha_n + j\beta_n$, combine the two partial fractions, and set an additional

term that appears in the numerator of each PBF to zero ($\beta_n d_n + \alpha_n c_n = 0$) — called as *phase parameter* in [242]. The classical flame transfer function $\mathcal{F}(j\omega)$, in Eq. (4.2), is now given by this model $\widetilde{H}(j\omega)$ from multipole expansion as follows.

$$\mathcal{F}(j\omega) \approx \widetilde{H}(j\omega) = \sum_{n=1}^{\bar{n}} \frac{2\alpha_n j\omega}{(j\omega)^2 - 2c_n j\omega + \omega_{0,n}^2} \tag{4.15}$$

where coefficients $\alpha_n, \beta_n, c_n, d_n, \omega_{0,n}$ are real-valued parameters , $\bar{n}$ is the model order or number of PBFs, and $\omega_{0,n}$ is the resonant frequency of pole p_n as mentioned in Douasbin et al. algorithm in Sec. 4.3.2.

Let $\hat{Q} = \sum_1^{\bar{n}} \hat{Q}_n$, so that the FTF (Eq. 4.2) can be expressed in terms of the n^{th} PBF

$$\frac{\hat{Q}_n(j\omega)/\bar{Q}}{\hat{u}(x_{ref}, j\omega)/\bar{u}} = \frac{2\alpha_n j\omega}{(j\omega)^2 - 2c_n j\omega + \omega_{0,n}^2} \tag{4.16}$$

Introducing an intermediate variable $\hat{z}_n(j\omega)$ on the left-hand side, the above equation could be re-written as

$$\left(\frac{\hat{Q}_n(j\omega)/\bar{Q}}{\hat{z}_n(j\omega)}\right)\left(\frac{\hat{z}_n(j\omega)}{\hat{u}(x_{ref}, j\omega)/\bar{u}}\right) = (2\alpha_n j\omega)\left(\frac{1}{(j\omega)^2 - 2c_n j\omega + \omega_{0,n}^2}\right) \tag{4.17}$$

By introducing $\hat{z}_n(j\omega)$, above equation can be split into two sets of equations by equating the terms in left and right parenthesis respectively from both the sides of above equation.

$$\begin{gathered} \hat{Q}_n(j\omega)/\bar{Q} = 2\alpha_n j\omega \hat{z}_n \\ \left[(j\omega)^2 - 2c_n j\omega + \omega_{0,n}^2\right] \hat{z}_n = \hat{u}(x_{ref}, j\omega)/\bar{u} \end{gathered} \tag{4.18}$$

The above two sets of equations can be recast into time-domain by taking inverse Fourier transform, recognizing that the $(j\omega)$ multiplier in a term converts into a time derivative in time-domain.

$$\begin{gathered} Q_n(t)/\bar{Q} = 2\alpha_n \dot{z}_n(t) \\ \tfrac{d^2}{dt^2} z_n(t) - 2c_n \tfrac{d}{dt} z_n(t) + \omega_{0,n}^2 z_n(t) = u(x_{ref}, t)/\bar{u} \end{gathered} \tag{4.19}$$

This dynamical second-order system of ODEs can then be represented in state-space form, assembled together for all the PBFs $n = 1$ to $\bar{n}$, by defining the state vector $\mathbf{X} = [z_1 \quad \dot{z}_1 \quad \cdots \quad z_{\bar{n}} \quad \dot{z}_{\bar{n}}]^T$.

State-space Dynamics Equation:

$$\frac{d}{dt}\mathbf{X} = \mathbf{A}\mathbf{X} + \mathbf{B}\mathbf{U}$$

$$\frac{d}{dt}\begin{bmatrix} z_1 \\ \dot{z}_1 \\ \vdots \\ z_{\bar{n}} \\ \dot{z}_{\bar{n}} \end{bmatrix} = \begin{bmatrix} 0 & 1 & & & \\ -\omega_{0,1}^2 & 2c_1 & & & \\ & & \ddots & & \\ & & & 0 & 1 \\ & & & -\omega_{0,\bar{n}}^2 & 2c_{\bar{n}} \end{bmatrix} \begin{bmatrix} z_1 \\ \dot{z}_1 \\ \vdots \\ z_{\bar{n}} \\ \dot{z}_{\bar{n}} \end{bmatrix} + \begin{bmatrix} 0 \\ 1/\bar{u} \\ \vdots \\ 0 \\ 1/\bar{u} \end{bmatrix} \begin{bmatrix} u(x_{ref}, t) \end{bmatrix} \tag{4.20}$$

State-space Output Equation: (Feedthrough matrix **D** is zero.)

$$\mathbf{Y} = \mathbf{C}\mathbf{X}$$

$$\begin{bmatrix} Q(t) \end{bmatrix} = \begin{bmatrix} 0 & -2\bar{Q}\alpha_1 & \cdots & 0 & -2\bar{Q}\alpha_{\bar{n}} \end{bmatrix} \begin{bmatrix} z_1 \\ \dot{z}_1 \\ \vdots \\ z_{\bar{n}} \\ \dot{z}_{\bar{n}} \end{bmatrix} \tag{4.21}$$

The above equations constitute the state-space model for Flame Transfer Function (FTF) corresponding to a flame object in a STORM acoustic network. Recall that a flame element makes two connections with acoustic subdomains. Eq. (4.20) governs the evolution of these intermediate variables $z_n(t)$ as per the acoustic velocity at reference location in the input vector, and the Eq. (4.21) provides the heat release rate fluctuations output $Q(t)$. The state variables are abstract and act as intermediate variables in the calculation of heat release rate, where $\dot{z}_n(t)$ may be interpreted as the proportion of normalized heat release fluctuating at frequencies contained in the band of width $2c_n$ centered around $\omega_{0,n}$ [157, 197].

4.4 Physical Constraints in Fitting a Model on Frequency Response Data

It is worth emphasizing that the rational approximation discussed in the previous section is not a mere mathematical curve-fitting on the data samples. Instead, the goal is to identify a low-order surrogate model (also called *macromodel*) representing the underlying *physical system dynamics*. The technique fits a model with suitable structure and parameters onto available data, tapping into its inherent correlation. It yields a dynamical model that describes the system behavior and is expected to predict its output reasonably accurately for any given input.

While the fitting accuracy between the macromodel and data is essential, it is not the most important requirement. Few fundamental properties are critical, and must be guaranteed for the physical admissibility of such macromodels for LTI systems, viz., 1) Reality, 2) Causality, 3) Stability and 4) Passivity [239, 248, 255]. Indeed most practical LTI systems, including an isolated (open-loop) flame object

in a STORM acoustic network, are realizable, intrinsically causal, and stable. It is then expected that the frequency response samples and the macromodel structure, by construction, both honor these constraints. As will be shown later, there is a possibility that if either of them fails to meet any of these conditions (as relevant), the entire macromodeling process can be compromised.

Triverio et al. [239] provides a detailed review of these physical conditions that must be respected in generating macromodels for LTI systems. Their mathematical definitions in time-, Laplace, and Fourier domain are highlighted. Analysis and interpretation of how these properties are closely related are also presented. Although the explicatory examples are primarily from electronics engineering, the concepts are generally applicable to all LTI systems.

The motive here is to concisely explain these physical constraints, as a theoretical foundation, before discussing examples of rational approximation of frequency response of realistic flames, failures in obtaining accurate fits, its causes and implications — of particular interest will be the causality condition.

1. **Reality:** The input and output signals of most practical LTI systems are real-valued quantities. Therefore a macromodel generated from complex frequency-domain data, when transformed into time-domain either as an impulse response or a state-space model, ought to be physical, i.e., it should receive and yield real quantities. For this, the system response function must satisfy the following condition in frequency-domain: in case of an acoustic reflection coefficient, for instance, the following should hold valid [239, 256, 242]

$$R(-j\omega) = R^*(j\omega) \tag{4.22}$$

where the $*$ indicates the complex conjugate.

The reality constraint is ensured in a pole-residue macromodel $\widetilde{H}(j\omega)$ by construction. Its structure is such that it contains only real poles (on real axis), or if complex poles are necessary, they must be present in complex-conjugate pairs. See equation (4.9). By taking inverse Fourier transform of Eq. (4.9), one gets the impulse response $\widetilde{h}(t)$ of the macromodel - a time-domain equivalent of the model transfer function $\widetilde{H}(j\omega)$, as follows.

$$\widetilde{h}(t) = R_0 + \sum_{n=1}^{\bar{n}_r} R_n e^{p_n t} + \sum_{n=\bar{n}_r+1}^{\bar{n}_r+\bar{n}_c} \left[2R'_n e^{p'_n t} \cos\left(p''_n t\right) - 2R''_n e^{p'_n t} \sin\left(p''_n t\right) \right] \tag{4.23}$$

for $t \geq 0$, where $p'_n = \Re\{p_n\}$, $p''_n = \Im\{p_n\}$, $R'_n = \Re\{R_n\}$ and $R''_n = \Im\{R_n\}$.

It can be seen that the time-domain impulse response of the macromodel is indeed real-valued.

2. **Causality**: Causality is often intuitively and qualitatively stated as a physical property of all LTI systems that an effect seen on the system cannot precede its cause. For example, if two input signals $s_1(t)$ and $s_2(t)$, equal up to $t = t_0$, are applied to a causal system, their respective outputs are expected to be equal up to $t = t_0$. If this is not the case (see Fig. 4.4), the system is *non-causal* because it anticipates the variation in inputs and responds before the input actually changes.

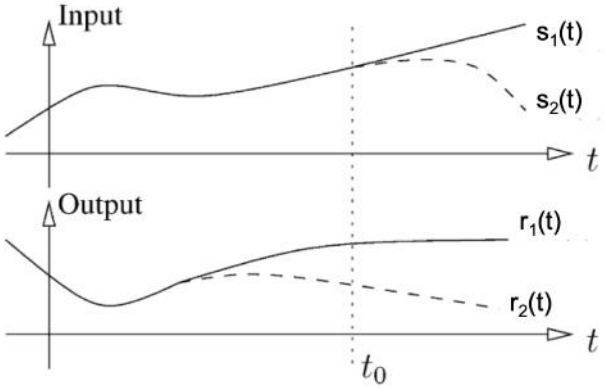

Figure 4.4: Illustration of a noncausal system response: two inputs $s_1(t)$ and $s_2(t)$ are equal upto $t = t_0$, leading to outputs $r_1(t)$ and $r_2(t)$. Response $r_2(t)$ begins to deviate from $r_1(t)$ much earlier than $t = t_0$ when the input actually changes. Adapted from Triverio et al. [239].

Mathematically, the causality principle is defined with help of impulse reponse $h(t)$ in time-domain. An LTI system is causal if and only if its impulse reponse vanishes for $t < 0$, i.e., system response cannot precede the impulse input at $t = 0$,

$$h(t) = 0, \quad t < 0 \tag{4.24}$$

The above definition of causality is general and apply to both lumped and distributed systems [239]. However, for systems responding with finite delay, it may be better to adopt a more stringent definition especially for the latter case. It is given as below by explicitly considering the propagation delay

$$h(t) = 0, \quad t < \tau, \quad \tau > 0 \tag{4.25}$$

where τ is the propagation delay, i.e. as mentioned earlier, the duration after which the first response of the system begins to appear on application of input.

In the current context of generating flame response state-space models, whether or not the original complex-valued frequency-domain data and the macromodel respect causality — better interpreted in time-domain — is a vital question

that arises. Often it is assumed that the flame frequency response data is causal without any guarantee or verification. However, this may not always be the case, as will be shown later, and as also discussed with many theoretical and real-life examples of electronic circuits modeled as LTI systems in [239, 240, 257, 258]. Causality [236, 237, 238] imposes strong condition on the frequency response of an LTI system that is defined by the so-called *Kramers-Krönig (KK) dispersion relations* [234, 235, 241] - introduced in the following Sec. 4.6.

As far as the pole-residue macromodel is concerned (Eq. 4.9), that fits onto the data, it can be shown that it is sufficient to ensure that the real part of the poles are negative for the macromodel to be causal.

$$\Re\{p_n\} \leq 0, \quad \forall n. \tag{4.26}$$

Mathematical proof of the above constraint and theoretical derivation of KK dispersion relations can be found in, for example, in [239, 255, 241] from recent literature.

It is possible to imagine that if the above causality constraint is imposed in the fitting procedure, but the original frequency response data violates causality for some reason, fitting issues would possibly arise. *(How can a causal macromodel fit onto a data-set that is non-causal?)* This aspect is demonstrated and more discussion follows in the upcoming Sec. 4.5 and Sec. 4.6.

3. **Stability**: It is quite important and expected that an LTI system's output remains finite magnitude as long as the incoming signal is finite over time. This is referred to as Bounded-Input bounded-output (BIBO) stability. In time-domain, the BIBO stability is guaranteed when [239]

$$\int_{-\infty}^{+\infty} |h(t)|dt < +\infty \tag{4.27}$$

where $h(t)$ is the impulse response.

In the frequency domain, the usual way to check stability is to analyze the poles of the system transfer function and check if they all fall on the left-hand side of the complex plane [205, 239]. Thus the macromodel (4.9) stability could also be ascertained by enforcing the condition given in Eq. (4.26) during fitting [239, 248, 242, 249]. This is done by simply inverting the sign of the real part of the model poles during fitting iterations. If this is not ensured, any time-domain simulation performed using the macromodel will blow up, diverging exponentially. For example, verify that the model impulse response,

Eq. 4.23, is not bounded if $p'_n = \Re\{p_n\} > 0$). *Overall, the condition in Eq. (4.26) simultaneously enforces causality and stability in the macromodel.*

4. **Passivity**: Passivity is a property that characterizes those physical systems that are unable to generate energy on their own, simply due to the lack of energy sources or gain mechanisms inside them [239, 248, 255]. A circuit made by positive resistors, capacitors, and inductors is an example of a passive system (always energy dissipative), in contrast to an amplifier circuit. In thermoacoustics, boundary impedances/reflection coefficients are passive elements; however, a flame is analogous to an amplifier. An open-loop flame response subjected to acoustic perturbations has intrinsic gain mechanisms that potentially can feed energy into the acoustic field and is thus a non-passive object.

   An acoustic reflection coefficient $R(j\omega)$ is passive when the following condition is true [242, 256]

   $$|R(j\omega)| \leq 1 \tag{4.28}$$

   Indeed in most cases the magnitude of reflected acoustic waves from a boundary cannot be greater than that of incident waves.

   However, regarding flame-response as a non-passive system, the usual input/output quantities of an FTF (velocity and heat-release fluctuations) are not suitable to assess a flame's (non-) passivity. They are inconsistent and do not correspond to (acoustic) energy fluxes, and something more appropriate would be to look at the scattering matrix of the flame or combustor to verify non-passivity. See the following works from a group of Polifke about determining flame/combustor scattering matrices [232, 259, 260].

   To ascertain that a macromodel $\widetilde{H}(j\omega)$ is passive, imposing condition in Eq. (4.28) on macromodel, though necessary, may not be sufficient in a general sense. The conditions that must be satisfied and techniques for enforcing passivity in rational approximation / macromodel require more considerations and are a bit more involved than above. It will not be discussed here, see [239, 255] and references therein for more information.

   Another vital point to note: passivity, if applicable, is the most stringent of all the constraints discussed above, i.e., a macromodel, if passive, implies that it is real, causal, and stable. The converse: i.e., reality, causality, or stability, if any of these conditions are breached, the macromodel is surely not passive [239].

In closing, this section highlights that imposing reality, causality, and stability constraints in rational approximation algorithms discussed earlier is absolutely

necessary for deriving a reliable state-space model for flame response. It is hence enforced by default in both the algorithms. A noncausal flame response macromodel — i.e., presence of even one pole in the right-half of the complex plane and thus also an unstable model — would be a useless flame model in any STORM network, particularly for any kind of time-domain simulation subsequently performed. Its implications on frequency domain linear stability analysis (LSA) may not be that drastic, and LSA could be carried out with a noncasual model without any problems. However, the results obtained may be inaccurate or even unphysical depending upon the degree of causality violation. This point will be investigated in the examples presented in the following section, and the Sec. 4.6 will also make a brief mention about ways for verifying causality violation in frequency samples apriori any fitting attempts.

4.5 Examples of Flame Frequency Response Fitting

This section will employ and evaluate the two algorithms - Algo1: Douasbin et al. [242, 249] and Algo2: Vector Fitting (VF) [248], by attempting to fit different actual turbulent swirling flame frequency response data from the literature. Algo1 is implemented in STORM, while for Algo2, an open-source Matlab implementation from Triverio [248] was utilized. Initially, only the in-house developed Algo1 was considered and employed for rational approximation. However, experiencing issues in fitting led to considering Algo2 and its related literature. It also drew attention towards the importance of physical constraints discussed in the previous section, particularly causality, which often is taken for granted.

Example-1: NoiseDyn Burner

This first example considered is a laboratory scale, NoiseDyn [259, 260, 261] turbulent premixed swirl burner studied by Dupuy et al. [173]. Experimentally measured discrete frequency, gain, and phase data samples are passed to both the fitting algorithms.

Figure 4.5, shows the experimental data and the fits obtained from both algorithms. An excellent fit can be observed between the macromodel and FFR data. The number of PBFs in the macromodel (very low for this particular Example1) and the final best-case L2 error (Eq. 4.10) achieved are indicated in Fig. 4.5 caption.

Example-2: Palies et al. [20] EM2C Burner

This second example is of another lab-scale premixed swirl burner, a variant similar to that shown in Fig. 4.2, that was investigated by Palies et al. [20]. The authors had proposed an analytical, linear flame response model based on

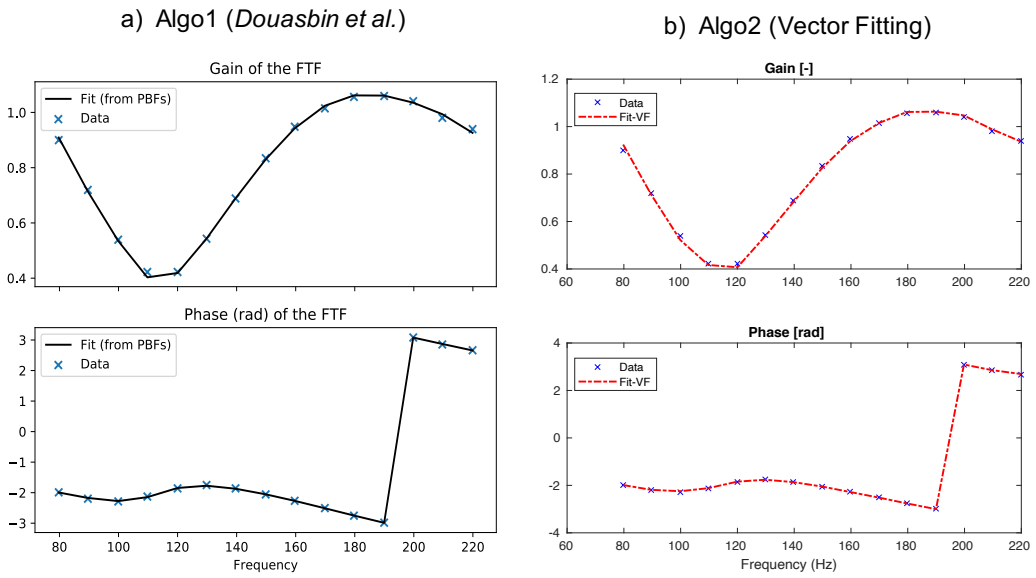

Figure 4.5: Noisedyn Burner experimentally measured frequency response macromodel fitting. No. of PBFs = 4, $e_{Algo1} = 0.041$**,** $e_{Algo2} = 0.017$**.**

perturbed G-equation for a V-shaped flame, whose parameters were determined from experiments. Dupuy et al. [173], cited in the previous example, extended this work and proposed a methodology to determine the same parameters for a similar analytical model with the help of a few LES non-reacting and reacting simulations. Significant gains in computational cost were achieved with the approach; compared to the standard way of computing frequency response by pulsing the flame at discrete frequencies.

For the sake of testing the fitting algorithms, experimentally measured flame frequency response (FFR) data is fetched by digitizing the plots from [20]. Frequency-dependent time-delay is computed ($\tau = \varphi/\omega$) from the original unwrapped phase data in the paper. Figure 4.6 depict the fits achieved. Unlike the preceding NoiseDyn burner example, the target experimental FTF shape is relatively more complicated. The fits fairly capture the target except for the extremities of the data spectrum.

As expected, the general convergence trend of both the algorithms is that starting from a low model order, i.e., number of Pole-Base-Functions (PBFs) ($\bar{n}$ in Eq. 4.9 with $n_r = 0$), the fitting accuracy improves with $\bar{n}$. Even though the data bandwidth (0-250 Hz) is similar to Example-1, and more samples are available, the required model order is higher due to the complexity of the target shape. In this particular case, the model order could not be increased beyond a point because the number of unknown macromodel coefficients exceeds the number of data samples available as the fitting target. Therefore, a larger number of data samples in the spectrum, i.e., better frequency resolution, is always helpful in general.

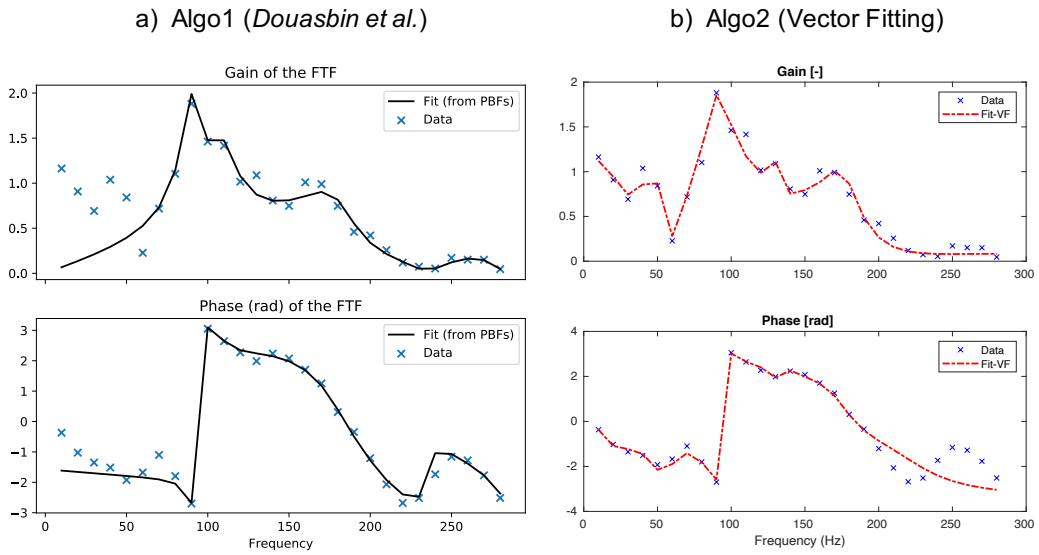

Figure 4.6: Palies et al. [20] burner experimentally measured frequency response fitting. Fewer data samples in the target than in Fig. 4.7. Model number of PBFs = 8. $e_{Algo1} = 1.32$, $e_{Algo2} = 0.14$.

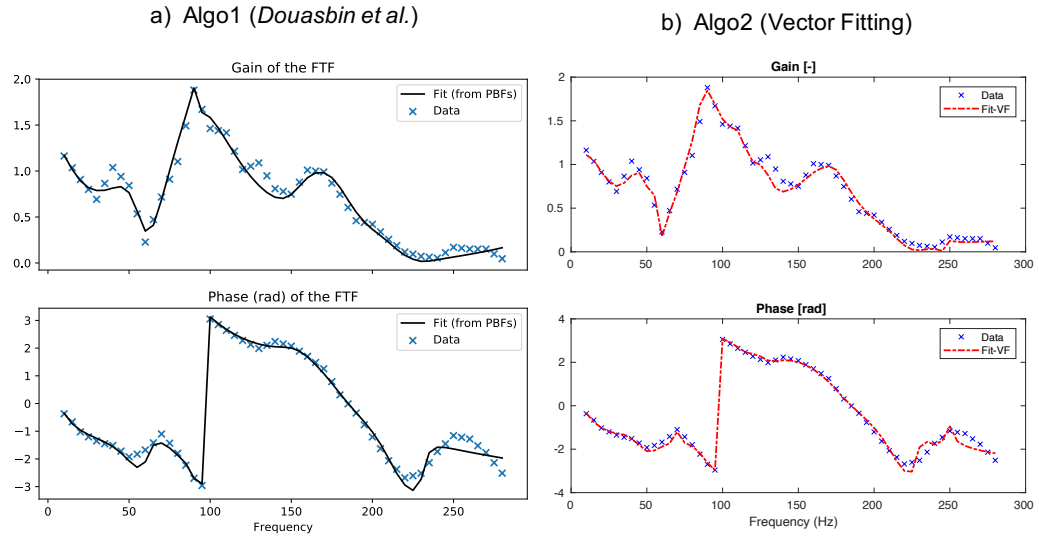

Figure 4.7: Palies et al. [20] burner experimentally measured frequency response fitting. More number of data samples in the target than in Fig. 4.6. Model number of PBFs = 15. $e_{Algo1} = 0.88$, $e_{Algo2} = 0.10$.

The fit with Algo2 in Fig. 4.6 is relatively better than Algo1. This could be attributed to the fact that Algo1 is more constrained than Algo2 due to: firstly, there is no additional constant term in the model structure as R_0 in Eq. (4.9) for

Algo2. Secondly, Algo1 also sets the term in numerator of PBFs (see Sec. 4.3.2, called as *phase parameter* in [242]) to zero.

Another quick test performed is to increase the number of digitized data points in the target, thus providing a wider margin for raising the model order. Figure 4.7 in this case portray how both models provide good fits in this case.

Example-3: SAFRAN Engine Combustor

For this third example, the flame frequency response of a SAFRAN engine combustor computed by Dupuy (Fig. 4.21 in [215] for $p'/\bar{p} = 2.5\%$ outlet forcing case (O25) in the plots) with forced LES of one sector is considered. Linear stability analysis (LSA) of the corresponding annular configuration with STORM was presented in the previous chapter, though a simple constant $n - \tau$ type FTF was employed there.

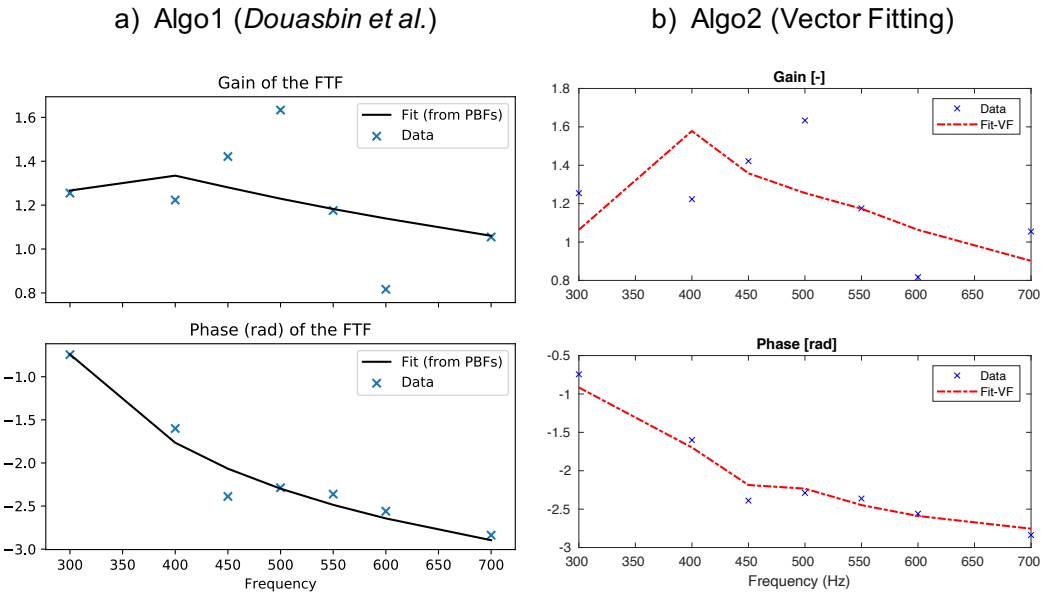

Figure 4.8: SAFRAN engine flame frequency response fitting. Target samples are the actual data points determined from forced LES (Fig. 4.21 in [215], case O25 in the plots). Macromodel number of PBFs = 2. $e_{Algo1} = 0.72$, $e_{Algo2} = 0.38$. **Causality constraint is enforced (by default).**

Figure 4.8 shows the fits achieved from both the algorithms. First of all, there are simply too few data points available in the spectrum to fairly characterize the flame response of this case and or of any realistic flame. This also highlights the conflicting issue of computational cost and complexities in computing FFR for such full-scale real systems. Experimentally determining FFR during test campaigns is

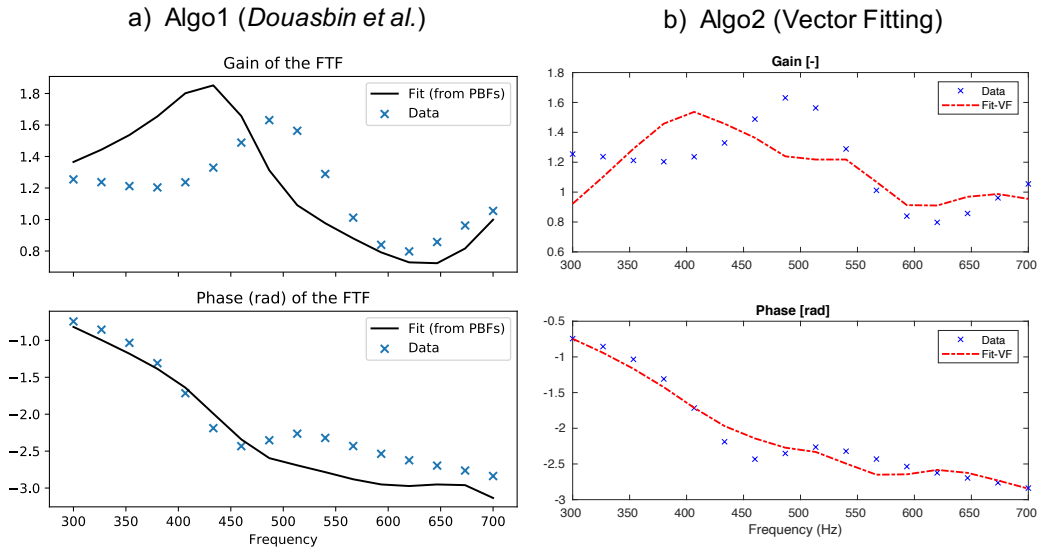

Figure 4.9: SAFRAN engine flame frequency response fitting. Extra points created in the target data samples by interpolation between the actual data points determined from LES (see Fig. 4.8). Macromodel number of PBFs = 5. $e_{Algo1} = 1.68$, $e_{Algo2} = 0.26$. **Causality constraint is enforced (by default).**

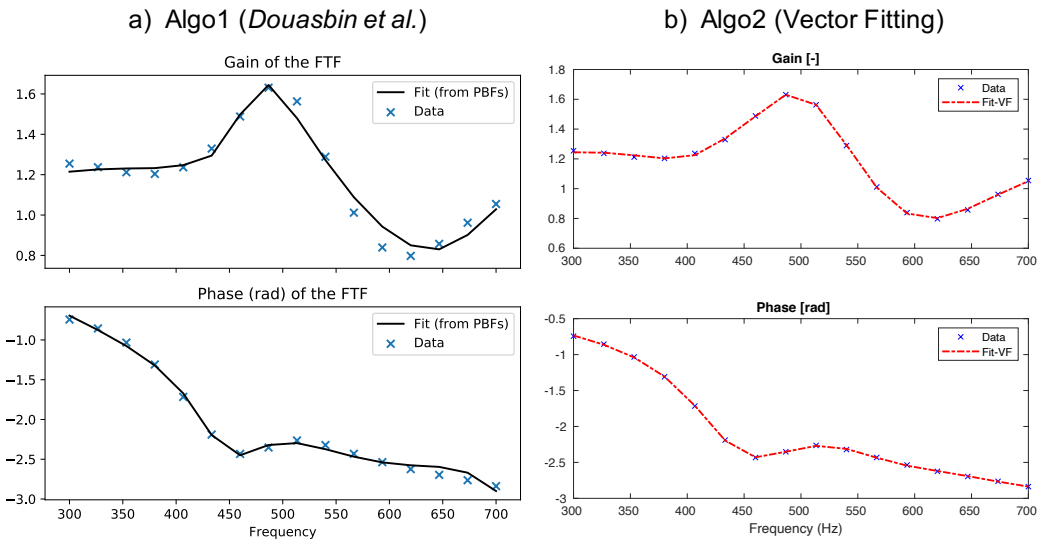

Figure 4.10: SAFRAN engine flame frequency response fitting. Target data samples in this case is exactly same as in Fig. 4.9. Macromodel number of PBFs = 5. $e_{Algo1} = 0.09$, $e_{Algo2} = 0.0096$. **Causality constraint is *not imposed* for this instance.**

expensive and nearly impossible for practical reasons.

The poor fit in Fig. 4.8 could be reasoned to the low model order ($\bar{n} = 2$) due to very few samples. A common practice is to carry out interpolation/extrapolation between known data points in such situations. This, however, is strictly not correct as the interpolated data points may not be causal. Causality condition implies some relationship between the real and imaginary parts of the frequency response function/data (and similarly between gain and phase) of LTI systems which may not be satisfied by the interpolated data points — see the following Sec. 4.6.

Still ignoring the causality aspect for now and interpolating between LES data points, Fig. 4.9 show the new target data samples and the fitting results. Yet again, a gross mismatch between the data and macromodel can be observed, with interpolation not improving the fit quality. This rules out that the poor fit quality in Fig. 4.8 is entirely due to low model order ($\bar{n} = 2$). While working with Algo1 initially, the author spent significant effort figuring out why the fitting was unsuccessful. Several tests, including interpolating and extrapolating the target points, altering the macromodel structure, fitting algorithm, etc., were tried but all in vain. Even Algo2 failed to give acceptable fits in the first attempts. On further investigation, it eventually turned out that the problem lies not in the macromodel structure or algorithm per se but the data.

The problem is that the data samples in this Example-3 violate causality, leading to problems fitting a causal macromodel. An indication of this fact is provided in Fig. 4.10, where causality constraint is relaxed in both algorithms, resulting in near-perfect fits. Even the fitting of the few original data samples (without interpolation) in Fig. 4.8 is successful in this case. Such a noncausal macromodel will have one or more unstable poles in the right half of the complex plane, rendering it useless for time-domain simulations. One way to look at this: the impulse response condition for causality in Eq. (4.25) now no longer holds. In a temporal simulation, the model would respond beforehand in anticipation of input perturbations, leading the flame response into an unbounded runaway oscillatory instability.

Implications of causality violation on frequency-domain linear stability analysis (LSA) are not as stringent as in the time domain. A noncausal macromodel constructed, say from a fit such as in Fig. 4.10, can be used to perform LSA without any difficulty. However, the thermoacoustic modes and their stability predictions would tend to be inaccurate. It is also physically questionable since the lack of causality in the samples means phase advance in the derived model flame response; since the associated time delay is undervalued than its actual value. If the deviation of the noncausal dataset is significant from the valid causal flame frequency response, the LSA results would be indeed unreliable.

As mentioned above, if a time-domain simulation is the aim, a non-causal macromodel is useless as it will lead to a diverging unstable temporal solution. For exam-

ple, a time-domain simulation of a passive acoustic network (without flames), either from some initial condition or forced externally from some boundary, will become unstable if some boundary impedance is described with a non-causal state-space macromodel. However, a temporal simulation of a thermoacoustic network in STORM, say for a limit-cycle calculation, is difficult to perceive with linear FTF since nonlinear effects that depend on oscillation amplitude are not considered. The flame describing function framework (FDF) is typically employed to perform frequency-domain nonlinear stability analysis. Therefore, methods for equivalent time-domain and state-space realization of FDFs will have to be developed in STORM in the future. Ghirardo et al. [262] have proposed one approach for the same. Their state-space realization of FDF is based on the so-called Hammerstein models (a nonlinear dynamical system modeling approach) and the Fourier Bessel series. In the Hammerstein approach, the time-domain nonlinear output $\mathcal{Q}$ (heat release) for input $u(t)$ (velocity at reference location) is expressed as a composition of linear $\mathcal{L}$ and nonlinear $\mathcal{N}$ operators as $\mathcal{Q}[u(t)] = \mathcal{L}[\mathcal{N}[u(t)]]$. Corresponding frequency domain representation is $Q(\omega, A) = L(\omega)N(A)$, where A is the oscillation amplitude. The linear operator is considered independent of oscillation amplitude and only depends on frequency - something quite analogous to a linear FTF. While the nonlinear operator depends only on the amplitude, basically to model nonlinear saturation, and is achieved with the help of the Fourier-Bessel series. Here, the authors have employed the Vector Fitting rational approximation algorithm for fitting the linear operator on the data.

Pinpointing the root cause of why a frequency response data set could be non-causal is not straightforward. It is usually due to errors and noise introduced in experimental measurements, or modeling uncertainties, numerical errors in high fidelity simulations, and or flawed signal/data processing. The errors and noise present in the frequency response data samples are very likely to be noncausal functions themselves [248]. Carefully repeating the measurements while keeping all the known sources of errors to a minimum, unfortunately, is the only recommended option to rectify the noncausal data set [239, 240, 248].

4.6 Causality in Frequency Response Data

The physical condition of causality, in regards to the response of LTI systems, was introduced earlier in Sec. 4.4. While well interpreted in the time domain, the concept imposes strong conditions in the frequency domain. Some theory about causality [237, 238] is discussed in this section, along with a brief mention of techniques that could be employed to verify and ascertain causality violation in frequency response data systematically. For more background, appropriate references are provided.

4.6.1 Kramers-Krönig Dispersion Relations

Causality condition in the frequency domain, theoretically, is defined by the Kramers-Krönig (KK) dispersion relations [234, 235, 236]. They relate the real and imaginary parts of the frequency response function of a causal LTI system, or in other words, they point out that the real and imaginary parts are not independent. See, for example, [239, 241] for the derivation of KK relations. If a causal LTI system frequency response $H(j\omega)$, is separated into its $\Re$ and $\Im$ parts as $H(j\omega) = U(\omega) + jV(\omega)$, then the KK relations are given as

$$\begin{aligned} U(\omega) &= \frac{1}{\pi}\ \mathrm{pv} \int_{-\infty}^{+\infty} \frac{V(\omega')}{\omega - \omega'} d\omega' \\ V(\omega) &= -\frac{1}{\pi}\ \mathrm{pv} \int_{-\infty}^{+\infty} \frac{U(\omega')}{\omega - \omega'} d\omega' \end{aligned} \tag{4.29}$$

where pv denotes the Cauchy's principal value

$$\mathrm{pv} \int_{-\infty}^{+\infty} = \lim_{\varepsilon \to 0^+} \left[\int_{-\infty}^{\omega-\varepsilon} + \int_{\omega+\varepsilon}^{+\infty} \right] \tag{4.30}$$

KK dispersion relations are the necessary and sufficient conditions for causality, and thus, in theory, any frequency response data samples that do not satisfy these are not causal. Mathematically, KK relations are also closely related to the Hilbert transform [240].

4.6.2 Bode's Gain-Phase Relation

Bode [263, 225, 224, 241] derived and showed relation between magnitude (gain) and phase of the frequency response of a causal LTI system, analogous to Kramer-Krönig's dispersion relation. However, there is a *caveat*: Bode's gain-phase relations are valid only for special class of LTI systems called as *minimum-phase systems* (discussed soon in the following Sec. 4.6.2.1). The theorem then is *defined* as follows.

For a stable, causal, minimum-phase system, the phase of a linear frequency response function $\angle H(j\omega)$ is uniquely related to the gain $|H(j\omega)|$ by following relations

$$\angle H(j\omega) = \frac{1}{\pi} \int_{-\infty}^{+\infty} \left(\frac{dM}{du} \right) W(u) du \tag{4.31}$$

where $\angle H(j\omega)$ is in radians and,

$$M = \text{log magnitude} = ln(|H(j\omega)|)$$

$$u = \text{normalized frequency} = ln(\omega/\omega_0)$$

$$W(u) = \text{weighting function} = ln(coth|u|/2)$$

The weighting-function $W(u)$, if plotted, can be observed to resemble a *broadened* Dirac-delta function centered around ω_0[4]. Bode's Eq. (4.31) therefore indicates that the particular phase value ($\angle H(j\omega_0)$) in the spectrum, due to $W(u)$, depends mostly on the local slope of the log-magnitude M and weakly on the same at frequencies in the near vicinity[5].

$W(u)$ can be approximated with exact Dirac-delta (impulse function) [241, 225, 224] as

$$W(u) \approx \frac{\pi^2}{2}\delta(u) \tag{4.32}$$

If the *slope* of log-magnitude ($\frac{dM}{du} \equiv m$) is constant over a frequency decade (e.g., $\omega = 10^2$ to 10^3), then the Bode relations in Eq. (4.31) simplify to (for that frequency decade)

$$\angle H(j\omega) \approx m\frac{\pi}{2} \tag{4.33}$$

The above result, therefore, suggests that the phase lag in the output response of LTI systems over a frequency-decade will be *approximately* equal to the slope of the magnitude curve over that frequency decade times $\pi/2$, as long as the slope is close to constant.

4.6.2.1 Minimum- versus Non-Minimum- Phase Systems

Minimum phase (MP) systems are characterized such that they do not have time-delay between input-output, and their transfer functions do not have any *poles and zeros* in the *right half* of complex plane [225, 224, 241]. If any of these conditions is not satisfied, then the system becomes a *non-minimum phase* (NMP) system.

NMP systems inherently induce an *"extra phase lag"* in their response. For a given response magnitude (gain), the phase lag of the MP system could be uniquely determined from the above Bode relations, but it is not true for NMP systems. The NMP systems exhibit an excess phase lag than that computed from Bode's relation. In this sense, Bode's relations in Eq. (4.31), for the general case of any LTI system, yields only the "minimum" phase for a given magnitude.To further elaborate, a few illustrations drawn from [225]) are discussed next.

It was mentioned above that all systems with time delays are NMP systems. So, consider a simple delay transfer function $H(j\omega) = e^{-j\omega\tau}$, whose gain $|H(j\omega)| = 1$ and phase $\angle H(j\omega) = -\omega\tau$ is known. Here if the phase lag is computed using gain

[4]Bode gain-phase plots, conventionally, are graphed on a log-frequency and log-magnitude (or decibels) scales, as can be found across control theory literature. Accordingly, ω_0 is the particular frequency ($\omega \equiv \omega_0$) at which Bode's relation is being probed/evaluated - for the local slope of the log-magnitude curve and eventually the phase ($\angle H(j\omega_0)$).

[5]a.k.a the *sifting* property of Dirac-delta function

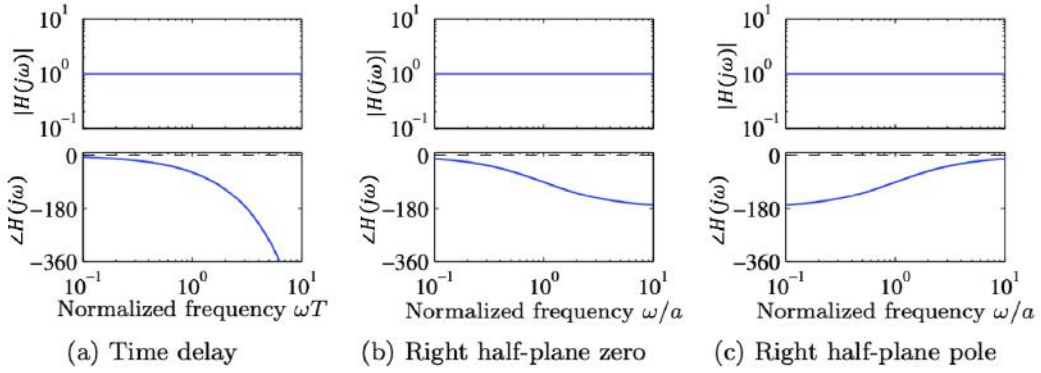

(a) Time delay (b) Right half-plane zero (c) Right half-plane pole

Figure 4.11: Bode plots of non-minimum phase systems that all have same constant unity frequency response magnitude but different phase lag. (a) Time-delay: $H(j\omega) = e^{-j\omega\tau}$, (b) system with right half-plane zero $H(s) = (a-s)/(a+s)$, (c) system with right half-plane pole $H(s) = (s+a)/(s-a)$. The corresponding minimum phase system has the transfer function $G(s) = 1$ in all cases, and the phase curves for that system are shown as dashed lines. Figure reproduced from [225].

$|H(j\omega)| = 1$ and Bode's relation, the result, however, is *zero* — this is the phase lag of a corresponding MP system also having the same unity response magnitude across the spectrum. (This MP system, in fact, is the same transfer function but with zero time delay ($\tau = 0$), i.e., $H(j\omega) = 1$.) Fig. 4.11(a) shows the Bode plot of the delay NMP system along with its MP system. (Note that due to log scale for frequency, the phase is not linear and falls off exponentially in the plot.)

Consider another NMP system with a rational transfer function $H(s) = (a - s)/(a + s)$ with $a > 0$, which has a *zero* $s = a$ *in the right half plane.* Its frequency response gain $|H(j\omega)| = 1$, and its phase $\angle H(j\omega) = -2\arctan(\omega/a)$. The related MP system in this case is again $H(s) = 1$. Fig. 4.11(b) shows the Bode plot of both these NMP and MP systems.

Fig. 4.11(c), shows a similar analysis of NMP system $H(s) = (s + a)/(s - a)$ with $a > 0$, which has a *pole in the right half-plane.* Its phase is $\angle H(j\omega) = -2\arctan(a/\omega)$.

The examples in Fig. 4.11 highlight different NMP systems with the same response magnitude but different phase responses; and the fact that for NMP systems, actual phase lag, unfortunately, cannot be determined by Bode's relation.

Non-minimum phase systems are common and impose severe limitations on the design and performance of robust *feedback (closed-loop)* control systems, as described in [225, 224, 241]. Systems with time delays are infamous for being difficult to control. In poles-zeros representation of the LTI system, poles are more fundamental than zeros and are an intrinsic property of the system dynamics. However, zeros, on

the other hand, depend on external factors such as the actuation system, sensors, and measurement details, i.e., basically how inputs and outputs of the system interact with its state variables. Therefore, an NMP system due to a right half plane zero could be avoided/rectified by redesigning these interfaces/connections, e.g., by making a better choice of input/output variables, rearranging, adding removing actuators/sensors in experiments [225, 224, 241]. These concepts become crucial in the context of *active control* of thermoacoustic (feedback) systems - see, for example, the recent series of articles by Chen et al. [264, 265, 266, 267] from the group of O'Connor at Penn State University.

In the context of causality, note that NMP systems should not be confused with causality violation: they do not imply causality violation in general. NMP systems, due to time-delays and or right half-plane zeros, are physically realizable and can be causal. For instance, consider again the analytical delay response function discussed earlier $H(j\omega) = e^{-j\omega\tau}$. The $\Re\{H(j\omega)\} = cos(\omega\tau)$ and $\Im\{H(j\omega)\} = sin(\omega\tau)$ satisfy Kramer-Krönig dispersion relations, and thus is a valid, causal transfer function.

In conclusion, causality in the frequency response of the system (analytical or sampled data) can be cross-checked with KK dispersion relations; and Bode's relation as well only if the system is warranted of being minimum-phase. Since linear acoustic flame response and many practical LTI systems usually have finite time delays, KK dispersion relations are the appropriate choice to ascertain causality in their frequency response.

4.6.3 Detecting Causality Violation in the Frequency Response

Theory and examples presented over previous sections of this chapter highlighted how causality violation in the frequency response of the LTI system could lead to failures in fitting a physically consistent causal pole-residue macromodel on it. As demonstrated in the example of Fig. 4.10, if relaxing the default causality constraint in fitting algorithms (Eq. 4.26) eliminates substantial macromodel fitting error present otherwise, is an indication of possible lack of causality in the frequency domain data.

Given frequency response analytical model or discrete data of any LTI system, Kramer-Krönig dispersion relations (Eq. 4.29) can be used, in principle, to verify and ascertain causality violation in the model/data. However, there are practical difficulties, especially in the latter case, in numerically evaluating the complex integrals in KK relations. Significant errors are induced:

- *Truncation Errors:* due to limited frequency bandwidth over which the discrete data samples are available - a critical issue!

- *Discretization Errors:* due to the poor spectral resolution of the data.

Therefore, the above errors must be accounted for and rigorously estimated for any causality checks to be trustworthy and meaningful.

Triverio et al. [240, 257, 258, 255] proposed *two robust methods for verifying causality* in frequency response. (1) First one is a *frequency-domain* approach [240, 255] where a direct numerical assessment of KK dispersion relation is carried out. (2) Second is a *time-domain* approach [257, 258], wherein the (filtered) impulse response of the system is estimated via *filtered Inverse Fourier Transform* of the frequency response. Causality is then verified from a variation of its time-domain condition (Eq. 4.24), i.e., (filtered) impulse response. These two methods are briefly and qualitatively described next without venturing into the mathematical details.

1. **Direct assessment of Kramers-Krönig Dispersion Relation [240, 255]:** Given the frequency-response function/data, its real part is reconstructed from the imaginary part (or vice-versa) using KK relations while accounting for the truncation and discretization errors. For example, the real part of an entry in the scattering matrix of an actual high-speed electronic circuit is reconstructed in Fig. 4.12(a), where the blue curve is the actual real part of the data available. The reconstructed real part is not a curve, but the grey band, whose thickness denotes bounds of truncation and discretization errors. If the actual real part does not fall inside this grey band, causality is violated.

   As the bandwidth primarily and the spectral resolution of the data improves, the thickness of the band reduces, and in theory, it should collapse over the actual data if it is causal.

   This frequency-domain method that relies on the so-called *generalized Hilbert transform* is not easy to implement in practice and thus led to the development of the following method that is much easier to implement and physically more intuitive.

2. **Filtered Inverse Fourier Transform [257, 258, 255]:** In this time-domain approach, the fundamental idea is to compute impulse response from the frequency-response to check causality. However, simply applying the standard Inverse Fast Fourier Transform (IFFT) to the band-limited frequency response does not yield an impulse response that can clearly distinguish causal and noncausal data. Both typically will have non-zero, similar or comparable, and diminishing impulse response for $t < 0$ (c.f Eq. 4.24) again due to the truncation and discretization errors mentioned above (see e.g. Fig. 1 in [257]).

   Therefore, to alleviate the impact of missing out-of-band data, the frequency-response $H(j\omega)$ is filtered with a *minimum-phase filter* $F(j\omega)$ — say a low-pass filter, assuming that data is available on the lower end of the spectrum. The filtered frequency response $H_F(j\omega) = F(j\omega)H(j\omega)$ is then inverse Fourier

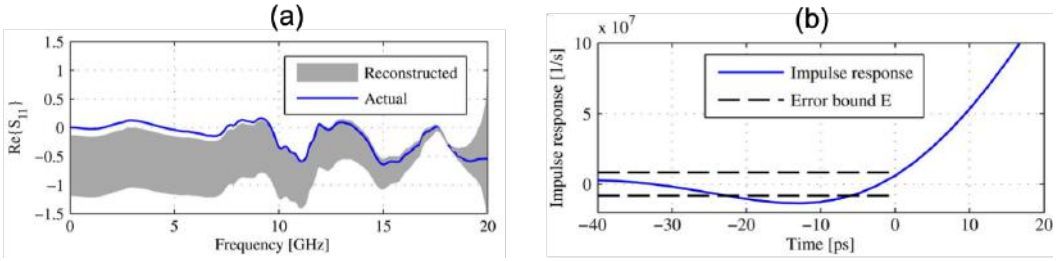

Figure 4.12: Causality check for the frequency-response data. (a) Direct evaluation of Kramer-Krönig dispersion relation. The actual real part of the samples (solid blue line) and its reconstruction assuming causality (grey band). Since the two curves are not compatible below 10 GHz, causality violations are present. (b) For the same example, filtered impulse response $h_F(t)$ obtained from the frequency data samples. Dashed lines are the truncation error bounds. Since the $h_F(t)$ curve cross the bounds, causality is violated. Figure adapted from [257].

transformed to get filtered impulse response $h_F(t)$. Here, the minimum-phase attribute of the filter is critical since it does not alter the causal/noncausal nature of the original data. For example, the general category of filters based on *window functions* that are widely used in practice are not minimum-phase. Recommended options are Chebyshev and Butterworth low-pass filters.

The low-pass filter applied in the frequency domain eventually helps control the truncation error in the computed impulse response. It also facilitates easy determination of a quantitative upper bound of the induced truncation error E - see [258] for details. Consequently, the new adapted impulse response condition condition, in comparison to the original theoretical definition (Eq. 4.24), is now given as

$$|h_F(t)| \leq E \text{ for } t < 0 \tag{4.34}$$

In Fig. 4.12(b), the blue line is the filtered impulse response computed as per the process summarized above for the same example in Fig. 4.12(a). The two dashed lines show the bounds of truncation error. The frequency-response data under scrutiny can be concluded of violating causality (starting from $t = -22.5ps$)) as it fails to satisfy the condition of Eq. (4.34). Note that if the data were causal, it still would have had a non-zero filtered impulse response for $t < 0$ but bounded within the two dashed lines. Even though the time scale and magnitude of violation may seem negligible, it actually makes the extraction of an accurate macromodel, particularly for temporal simulation/analysis, impossible. Generating a macromodel using the Vector Fitting algorithm for this particular example could not bring the fitting error

lower than 73% because the data violates causality. It was mentioned in [257] how adding an artificial delay of 22.5ps into the data nullifies the causality violation bringing the fitting error down substantially to 5.5%.

From the two approaches discussed above, the second time-domain approach is not only easier to implement but also provides information in a more physically intuitive manner for diagnosing causality violation[6]. It also yields information of the *time-extent* of violation — something that is difficult to estimate in frequency-domain. Therefore, in conclusion, the methodology described should be employed for certifying flame frequency response data for causality so that it is physically consistent for subsequent low-order thermoacoustic analysis.

4.7 Conclusions and Perspectives

The capability of STORM to represent complex, practical configurations as a flexible, modular thermoacoustic network was demonstrated in previous chapters, thanks to the OC-frame modal expansion, surface spectral connections, and state-space methodology. All kinds of network objects in STORM are represented as state-space sub-models in the network, including flames.

The rational approximation techniques (Padé approximation or Pole-Residue (Multi-pole) expansion) are an indispensable way to generate a time-domain state-space model from frequency response data samples; not only for linear flame response (FTFs), but also generic frequency-dependent acoustic impedances $Z(j\omega)$. The frequency-domain discrete data could be from experimental measurements or high-order simulations such as LES and even sampled from a closed-form analytical model.

Two different algorithms, Algo1 (from Douasbin et al. [242]) and Algo2 (Vector-Fitting [248]) from the literature were reviewed and employed for fitting a Pole-Residue macromodel onto sampled flame frequency response data actual turbulent swirl burners from literature.

The constraints of reality, causality, stability, and passivity that must be respected in the rational approximation/fitting process for generating physically consistent macromodels were discussed. The author hopes to have convincingly highlighted that causality is one of the most critical of them in the context of flame frequency responses. The most restrictive passivity condition, while may be relevant for acoustic reflection coefficients (or impedances), it is not applicable for FTFs.

The concept of causality is well comprehended in the time domain. However, in the frequency domain, it implies that the real and imaginary parts of the frequency

[6]The method is not available in STORM yet. It will be implemented in near future.

response function/data are not independent but related through the Kramers-Krönig (KK) dispersion relations. Theory about KK relations and other related concepts of Bode's relations, minimum/non-minimum phase systems was briefly reviewed from the literature.

Causality in frequency response data samples is often taken for granted. Occasional failure to get a good rational approximation fit might indicate possible causality violation in the frequency response data samples. This was demonstrated for the third example of the engine combustor, where the data is probably not causal. This is also suggested by the perfect fit obtained after relaxing the causality constraint in the algorithm. The root cause for why the data is not causal is unknown. The engine combustor is undoubtedly an extremely complex configuration to perform forced LES for flame response characterization. One or more factors could potentially be responsible, for instance, spatio-temporal under-resolution of the signals, high noise-to-signal ratio, the choice of reference location used for computing flame response, etc. More investigation is necessary, and the configuration should be reviewed again.

A practical and robust technique from the literature for rigorously characterizing causality violations in data samples was briefly discussed. Implementing it in STORM will be helpful in the future, as a rational approximation will be frequently utilized for generating state-space models. Nevertheless, the data's highly truncated bandwidth and frequency resolution can be a crucial hindrance in such causality assessment.

Ideally, good spectral resolution and a broad bandwidth are desired in the frequency response data samples as they aid the algorithms by providing enough scope to increase the macromodel order (number of Pole-base-functions (PBFs)), if necessary, to achieve accurate fits. However, these requirements are an issue when the frequency response data from expensive high-fidelity LES simulations. It was the case for the third engine combustor example, for which only a countable few frequency response data points were available in the spectrum. Indeed, this suggests the need for continued effort in analytical/theoretical modeling of flame response in the vein of the work carried out by Dupuy et al. [173, 215]. Also, perhaps adopting the more efficient approach of broadband white noise forcing [232, 12], instead of the classical harmonic forcing repeated at distinct frequencies, is an alternative worth considering for identifying flame response in LES.

Not imposing the causality constraint in the fitting algorithm will yield an accurate fit on non-causal data. The resulting non-causal state-space macromodel could also be used without difficulty in linear stability analysis, but depending upon the degree of causality violation, the results will be inaccurate and even unphysical. On the other hand, if a time-domain simulation is the aim, a non-causal macromodel is useless as it will lead to a diverging unstable temporal solution. As discussed

earlier in Sec. 4.5, to perform nonlinear stability analysis in the frequency-domain or time-domain simulations of thermoacoustic networks in STORM, more work is required to develop capabilities for state-space realizations of FDFs or other kinds of nonlinear flame response models.

Chapter 5

Delayed Entropy Coupled Boundary Condition

Contents

5.1 About Entropy-Acoustic Feedback Mechanism 132

5.2 Zero-Mach-number Assumption and Physical Modeling Strategy 134

5.2.1 Acoustic Energy Flux Mismatch in Impedance Matching . . . 137

5.2.2 Entropy Waves Modeling in the Helmholtz Domain 140

5.3 State-Space Model of 1D-DECBC Network Element 144

5.3.1 1D Test-Case for Validation 144

5.3.2 Entropy Transfer Function (ETF) and Nozzle Impedance . . 146

5.3.3 State-Space Model Realizations (SS-R1 and SS-R2) 147

5.4 State-Space Model of real-valued 1D Acoustic Impedance . 154

5.5 Results and Validation 154

5.5.1 Test1: Applying Nozzle Impedance without Entropy-Acoustic Feedback 156

5.5.2 Test2: 1D-DECBC Results with SS-R1 157

5.5.3 Test3: 1D-DECBC Results with SS-R2 160

5.6 Conclusions and Perspectives 167

Acoustic feedback from the exit nozzle or downstream turbine stages to the convected combustor entropy wave was mentioned as one of the potential combustion instability driving mechanisms earlier in Ch. 1, Sec. 1.2.1. Fig. 5.1 depicts a schematic elaborating this mechanism that gives rise to the so-called low-frequency mixed entropy-acoustic combustion instabilities. Its modeling in the low-order STORM's *state-space* network framework is the subject of this chapter. The physical modeling, in principle, closely follows the methodology developed in the previous work at CERFACS by Motheau et al. [45, 46, 268], who formulated this special *Delayed Entropy-Coupled Acoustic Boundary Condition (DECBC)* in FEM Helmholtz solver AVSP [127] to predict these mixed instabilities.

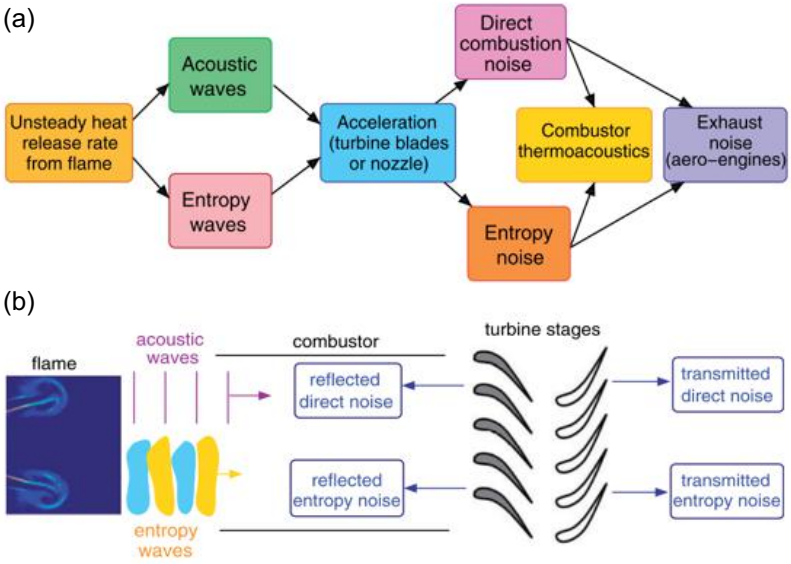

Figure 5.1: Schematic of flow perturbations in a gas turbine combustor. The acoustic (direct) and entropy (indirect) components of combustion noise. Both influence the combustor stability, where the latter is the entropy-acoustic feedback mechanism. Figure reproduced from [47].

5.1 About Entropy-Acoustic Feedback Mechanism

Unsteady heat release of a turbulent flame acts as a source of acoustic waves which propagate at sound speed through the combustor, are partially reflected back to the flame, perturbing it and closing the feedback loop — this is the classical thermoacoustic mechanism described earlier in Ch. 1, Fig. 1.5, and which was also implied in the several examples presented in this manuscript. Part of the acoustic waves that are transmitted further downstream constitute the *direct* combustion noise of the engine. In the primary reaction zone near the flame, the *entropy waves* and large-scale vorticity waves are also generated. The former is nothing but large pockets of considerable temperature *(a.k.a hot spots)* and or gas mixture inhomogeneities. These waves of entropy and vorticity perturbations are *convected* by the mean bulk flow from the combustor to the nozzle/turbine stages; and when accelerated, they produce sound (basically due to volume contraction of fluid regions of variable gas densities and other flow non-uniformities) [44, 269, 270, 271, 272, 273, 274, 275, 276, 119, 120]. Part of this *entropy noise* propagating downstream contribute as the *indirect* component of the combustion noise [10, 47, 277, 278, 279], while the part propagating upstream influence flame/flow in the combustor and can form a closed-loop giving rise to a low-frequency instability [45, 46, 273, 280].

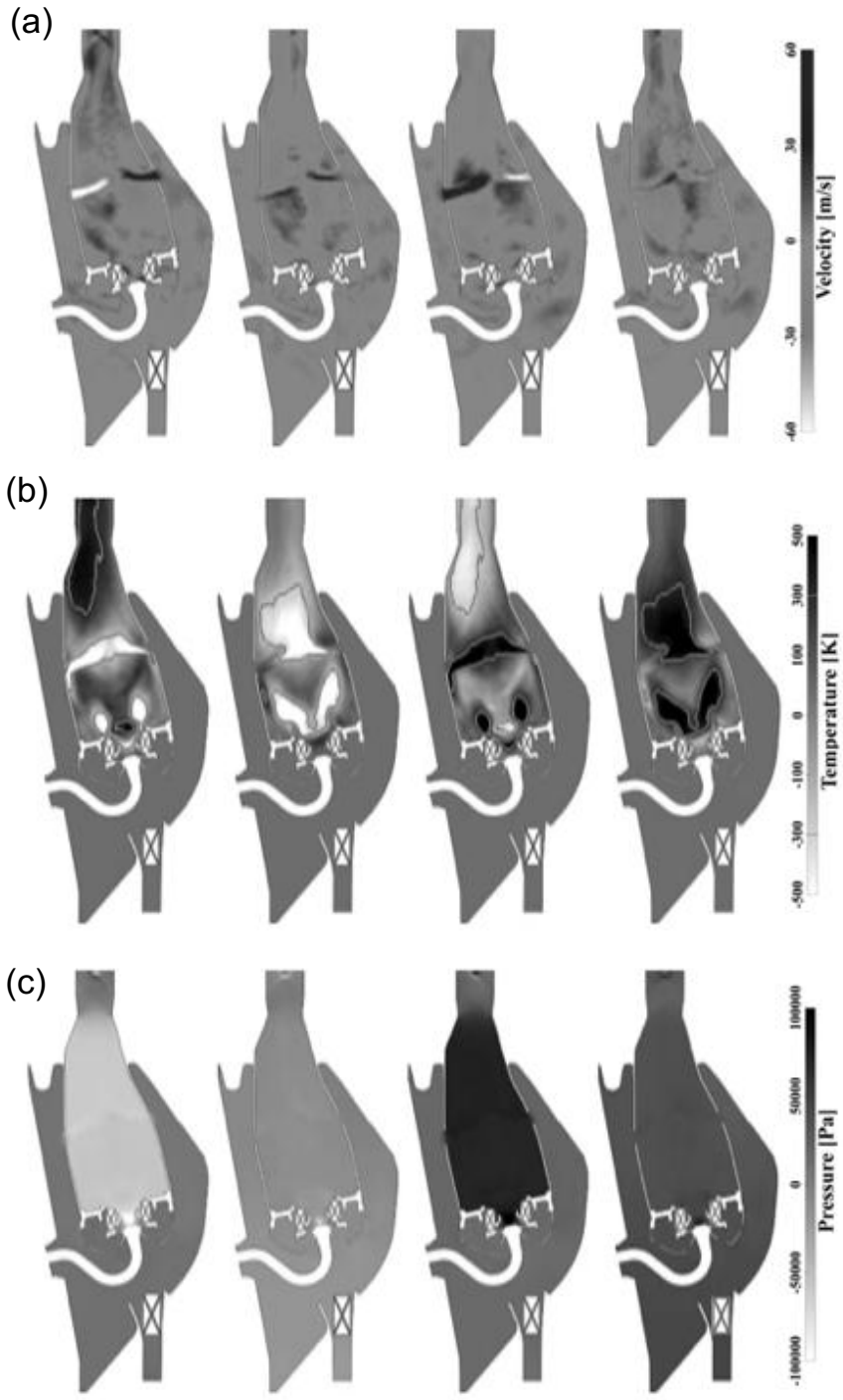

Figure 5.2: (a) Velocity, (b) Temperature and (c) Pressure fluctuating fields obtained from 3D Dynamic Mode Decomposition (DMD) of LES of a real gas turbine engine combustor terminated with a nozzle. Depicts a low-frequency mixed entropy-acoustic instability. Left to Right: instability cycle phases 0, $\pi/2$, π and $3\pi/2$ respectively. (Reproduced from Motheau et al. [46]).

For example, Fig. 5.2 shows a low-frequency, self-sustained, high-amplitude oscillation in an actual SAFRAN aeronautical engine combustor terminated with a nozzle - taken from computations performed by Motheau et al. [46]. The oscillation is depicted as the corresponding 3D DMD mode (Dynamic Mode Decomposition) obtained from LES solution time snap-shots. The frequency of this mode ($\approx$ 320Hz), which was also observed in the engine test campaign, is significantly lower than the first acoustic eigenmode of the combustor ($\approx 750 - 800$Hz). The frequency thus suggests that it is not a pure thermoacoustic mode. Over an instability cycle, the fluctuating temperature field in Fig. 5.2 reveals how a large hot spot is convected downstream into the nozzle, confirming the above-discussed mechanism of mixed entropy-acoustic instability. The entropy-acoustic feedback from the nozzle forms a closed-loop with the flame and flow in the combustor, wherein hot/cold spots are cyclically created — here in this example, predominantly due to interaction between the primary reaction zone of the combustor and strong transverse dilution jets. Note the substantially high amplitude of convected temperature fluctuations ($\pm$ 500K) and pressure oscillation ($\pm$ 100kPa) inside the combustor, suggesting that modeling and predicting such mixed instabilities is equally critical as the thermoacoustic modes.

5.2 Zero-Mach-number Assumption and Physical Modeling Strategy

For analysis of combustion instabilities, besides high-order methods such as LES, Linearized Euler Equations (LEE) is one of the suitable reduced-order modeling approaches for acoustics as discussed in Ch. 1, Sec. 1.4.1. LEE are also omnipresent in the aeroacoustics and combustion-noise research. It constitutes a suitable framework for modeling convected waves of entropy, vorticity fluctuations, in addition to the propagation of acoustic waves. Linearizing the mass, momentum, and energy (in entropy) Euler equations, the complete set of LEE for fluctuating quantities $\rho', p', \mathbf{u}'$ and s' around mean values denoted with subscript $(\,)_0$ are given as follows [112]:

LEE under non-zero Mach number $(M \neq 0)$ **mean flow:**

$$\frac{\partial \rho'}{\partial t} + \mathbf{u}' \cdot \nabla \rho_0 + \rho_0 \nabla \cdot \mathbf{u}' + \mathbf{u}_0 \cdot \nabla \rho' + \rho' \nabla \cdot \mathbf{u_0} = 0, \tag{5.1}$$

$$\rho_0 \frac{\partial \mathbf{u}'}{\partial \mathrm{t}} + \nabla p' + \rho_0 \mathbf{u}' \cdot \nabla \mathbf{u}_0 + \rho_0 \mathbf{u}_0 \cdot \nabla \mathbf{u}' + \rho' \mathbf{u}_0 \cdot \nabla \mathbf{u}_0 = 0, \tag{5.2}$$

$$\frac{\partial s'}{\partial t} + \mathbf{u}' \cdot \nabla s_0 + \mathbf{u}_0 \cdot \nabla s' = \frac{r q'}{p_0} - \frac{r q_0}{p_0^2} p', \tag{5.3}$$

and the accompanying linearized ideal gas state and entropy relations are

$$\frac{p'}{p_0} - \frac{\rho'}{\rho_0} - \frac{T'}{T_0} = 0 \quad \text{and} \quad \frac{s'}{c_v} = \frac{p'}{p_0} - \gamma\frac{\rho'}{\rho_0} \tag{5.4}$$

where c_p and c_v are specific heat capacity at constant pressure and volume respectively, $\gamma = c_p/c_v$, gas constant $r = c_p - c_v$ and q' is the unsteady heat release fluctuation per unit volume. Its straigforward to transform above set of equations into frequency-domain, assuming harmonic oscillations as $g'(\mathbf{x}, t) = \hat{g}(\mathbf{x})e^{j\omega t}$, which can then solved to for eigenmodes and their stability.

The inhomogenuous Wave/Helmholtz equation can be derived from above LEE equations by invoking the *zero-Mach-number* mean flow assumption, i.e., $\mathbf{u_0} = 0$.

LEE under zero-Mach-number ($M = 0$) mean flow:

$$\frac{\partial \rho'}{\partial t} + \mathbf{u}' \cdot \nabla\rho_0 + \rho_0 \nabla \cdot \mathbf{u}' = 0 \tag{5.5}$$

$$\rho_0 \frac{\partial \mathbf{u}'}{\partial t} + \nabla p' = 0 \tag{5.6}$$

$$\frac{\partial s'}{\partial t} + \mathbf{u}' \cdot \nabla s_0 = \frac{rq'}{p_0} \tag{5.7}$$

Taking the time derivative of Eq. (5.5), adding the divergence of Eq. (5.6) divided by ρ_0, and using Eqs. (5.4), (5.7) to eliminate ρ' yield the following: Wave equation for the pressure fluctuations p' discussed earlier in Ch.1, and its frequency-domain counterpart the Helmholtz Equation. (Both are repeated below for easy reference.)

Wave Equation:

$$\nabla \cdot \left(\frac{1}{\rho_0}\vec{\nabla} p'\right) - \frac{1}{\gamma p_0}\frac{\partial^2 p'}{\partial t^2} = -\frac{\gamma - 1}{\gamma p_0}\frac{\partial q'}{\partial t} \tag{5.8}$$

Helmholtz Equation:

$$\nabla \cdot \left(\frac{1}{\rho_0}\vec{\nabla} \hat{p}\right) + \frac{\omega^2}{\gamma p_0}\hat{p} = -j\omega\frac{\gamma - 1}{\gamma p_0}\hat{q} \tag{5.9}$$

Fig. 5.3(a) depicts the SAFRAN engine combustor terminated with a nozzle that was analyzed by Motheau et al. [46, 45, 268] for predicting mixed entropy-acoustic instabilities. Overlaid on it are mean-flow Mach number isolines. Directly solving LEE ($M \neq 0$) on this configuration is a viable option for computing these instabilities; however, the interest in the previous work [46, 45, 268] was to develop capabilities to predict them with the relatively low-cost option of Helmholtz solver AVSP [127].

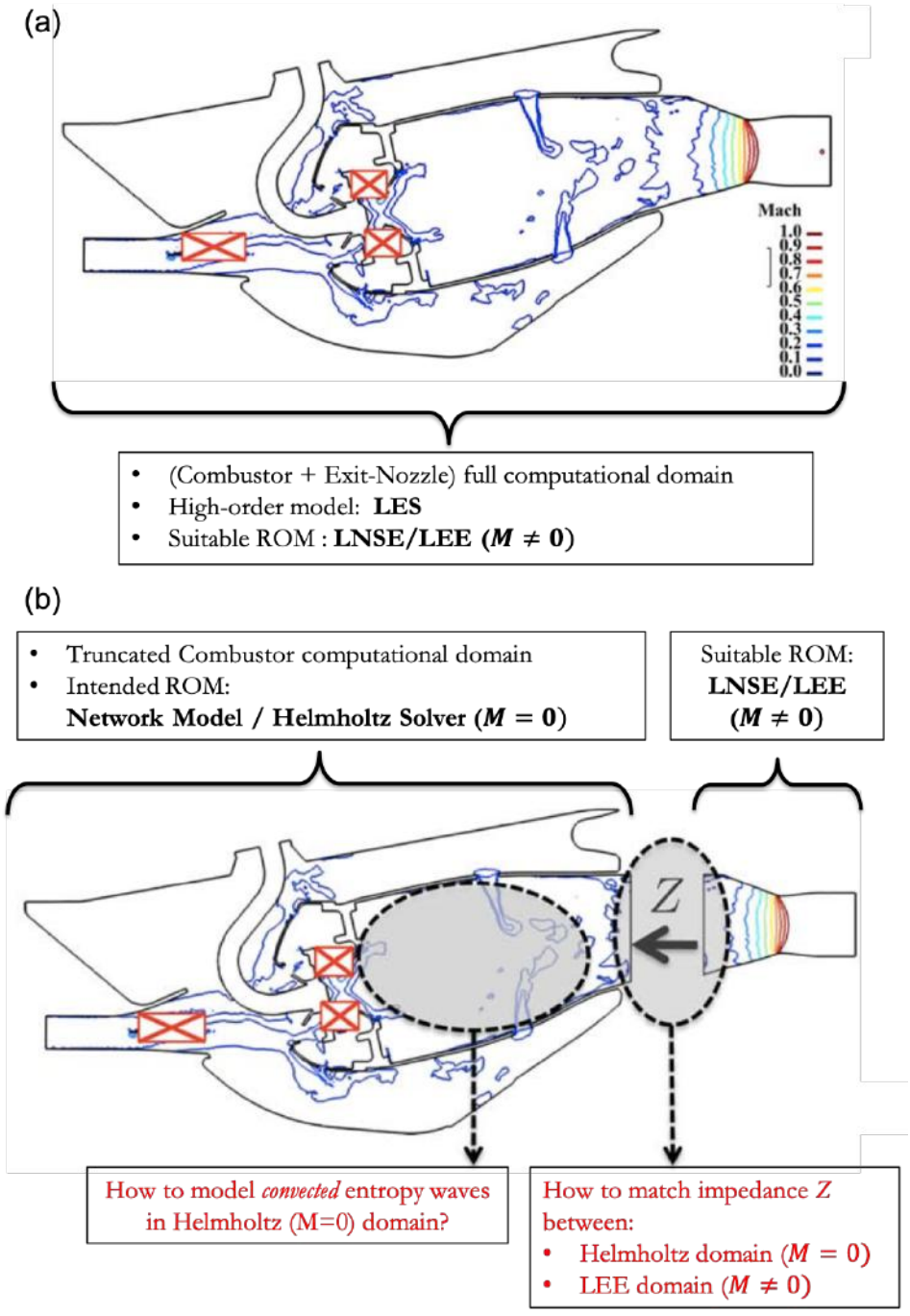

Figure 5.3: (a) SAFRAN Engine (combustor + exit-nozzle) geometry used to investigate mixed entropy-acoustic instabilities with LES, as in Fig. 5.2. Overlaid are the iso-contour lines of the mean-flow Mach number inside the domain. (b) An overview of the reduced-order modeling strategy and challenges owing to the zero-Mach-number (M=0) assumption, leading to the DECBC method. Adapted from [268].

Considering the mean flow Mach number values in the whole computational domain in Fig. 5.3(a), solving Wave/Helmholtz equation on it would not be a correct approach. Nicoud and Wieczorek [112] had investigated the effect of mean flow on thermoacoustic modes for simple academic 1D cases. They have demonstrated that if not in the very-low Mach number regimes (less than 0.1), the results of Helmholtz Eq. ($M = 0$) can significantly deviate from the reference LEE ($M \neq 0$) solution.

Motheau et al. [45] proposed a simple yet effective methodology to account for mean flow effects in the zero-Mach Helmholtz solvers. Exploiting the fact that the mean flow Mach number is substantial only in the constricted downstream nozzle (Fig. 5.3), the computational domain is truncated by clipping off the high-speed element (nozzle) from the combustor. The combustor with a very low Mach number mean-flow is then resolved with the zero-Mach Helmholtz solver. The non-zero Mach number effects originally present (mainly due to the nozzle) are *indirectly* and *partly* modeled by *impedance matching*, i.e., by imposing the equivalent acoustic impedance (Z) of the nozzle on Helmholtz domain boundary as noted in Fig. 5.3(b). Of course, in this case, the acoustic impedance of the nozzle needs to be known a priori; which can be determined from analytical solutions [44, 119, 274], or numerically by solving LEE [281, 120] for the nozzle and or turbine stator/rotor cascade.

However, there are two fundamental issues in the above strategy for modeling mixed entropy-acoustic instabilities and the subsequent derivation of the DECBC. These are highlighted in Fig. 5.3(b) and are discussed over the following two subsections.

5.2.1 Acoustic Energy Flux Mismatch in Impedance Matching

In the impedance matching technique, one fundamental problem is the that of *acoustic energy flux* ($\mathbf{F}$) *mismatch/error* at the boundary of the computational domain. As shown in Fig. 5.4, at the ($M = 0/M \neq 0$) interface between $M = 0$ computational and the $M \neq 0$ external (modelled) domains, $|\mathbf{F}^{M\neq0} - \mathbf{F}^{M=0}| \neq 0$. There always exists this discrepancy in acoustic energy flux crossing the boundary due to absent mean flow, and the magnitude of error clearly depends on the mean-flow Mach number at the interface.

Motheau et al. [45] carried out asymptotic analysis of acoustic energy conservation over a domain under $M \neq 0$, and in the limit of $M = 0$, to estimate the flux error

$$\mathbf{\Delta F} = |\mathbf{F}^{M\neq0} - \mathbf{F}^{M=0}| \tag{5.10}$$

To this purpose, the authors employ following two linearized fluctuating variables: (i) *Total Enthalpy* ($J = c_pT + u^2/2$) and *mass flow rate* ($m = \rho u$) as below (in spatial 1D):

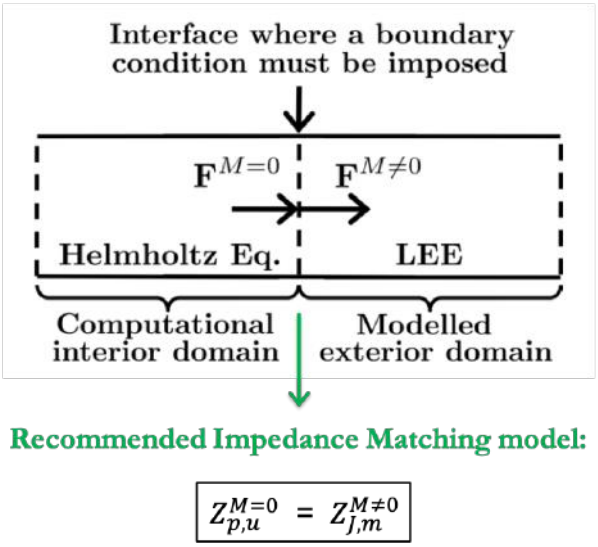

Figure 5.4: Acoustic energy flux mismatch (error) in the impedance matching technique due to the zero-Mach-number mean flow assumption in the computational domain (see also Fig. 5.3). Recommended model is Eq. (5.18) as discussed in Sec. (5.2.1). Adapted from [45].

$$J' = \frac{p'}{\rho_0} + u_0 u' \tag{5.11}$$

$$m' = \rho_0 u' + \frac{u_0}{c_0^2} p' \tag{5.12}$$

It is elucidated in [45] that while fluctuating pressure p' and velocity u' are a natural choice of acoustic variables under $(M = 0)$ conditions, J' and m' as state variables, are more appropriate under $M \neq 0$ conditions. The reasoning given is that (J', m') themselves are independent of the flow when placed in a wave equation, contrary to the (p', u') which are locally dependent on the flow velocity [282]. The former set of variables are also commonly used in aeroacoustic/combustion-noise studies. Under $M \neq 0$ conditions, the acoustic energy flux is given as $\mathbf{F}^{M\neq0} = \int_0^T J'm'dt$; and it reduces to the analogous equation $\mathbf{F}^{M=0} = \int_0^T p'u'dt$ under $M = 0$ condition.

It should, however, be noted that these two sets of independent variables are *strictly equivalent* and one may write LEE/Wave/Helmholtz equations and also impedances/reflection-coefficients with any set. A reduced (non-dimensional) impedance, Z, and reflection coefficient, R, may be defined for each set of variables as follows:

$$Z_{p,u} = \frac{p'}{\rho_0 c_0 u'} \quad \text{and} \quad R_{p,u} = \frac{A^-}{A^+} \tag{5.13}$$

$$Z_{J,m} = \frac{\rho_0 J'}{c_0 m'} \quad \text{and} \quad R_{J,m} = \frac{A^-(1-M)}{A^+(1+M)} \tag{5.14}$$

where A^+, A^- are the forward and backward propagating acoustic waves in the ($M = 0$) computational domain, adjacent to the boundary. The inter-relation between $Z_{p,u}$ and $Z_{J,m}$ can be derived from Eqs. (5.11)-(5.14) as:

$$Z_{j,m} = \frac{Z_{p,u} + M}{MZ_{p,u} + 1} \tag{5.15}$$

$$Z_{p,u} = \frac{M - Z_{J,m}}{MZ_{J,m} - 1} \tag{5.16}$$

The values of the impedances and reflection coefficients for some canonical boundary conditions are enlisted in the Tab. 5.1.

BCs	$Z_{p,u}$	$R_{p,u}$	$Z_{J,m}$	$R_{J,m}$
$\hat{p} = 0$	0	-1	M	$-\frac{1-M}{1+M}$
$\hat{u} = 0$	∞	1	$\frac{1}{M}$	$\frac{1-M}{1+M}$
$\hat{J} = 0$	$-M$	$-\frac{1+M}{1-M}$	0	-1
$\hat{m} = 0$	$-\frac{1}{M}$	$\frac{1+M}{1-M}$	∞	1

Table 5.1: Impedances and reflection coefficients for canonical boundary conditions (BCs): constant pressure ($\hat{p} = 0$), constant velocity ($\hat{u} = 0$), fixed mass flow rate ($\hat{m} = 0$) and fixed total-enthalpy ($\hat{J} = 0$).

Therefore, in the context of acoustic energy flux error in impedance matching (Fig. 5.4), to keep the error $\mathbf{\Delta F}$ to a minimum, the first and foremost requirement is that the mean flow Mach number at the boundary should be very low. The choice of *the location* of the boundary where the external high-speed element's impedance is imposed is thus crucial in accounting for the mean flow effects in the Helmholtz domain. Secondly, there are two possibilities in prescribing the boundary impedance of the Helmholtz ($M = 0$) domain ($Z_{p,u}^{M=0}$) as follows:
(Impedance Matching Model options)

$$Z_{p,u}^{M=0} = Z_{p,u}^{M\neq 0} \tag{5.17}$$

or,

$$Z_{p,u}^{M=0} = Z_{J,m}^{M\neq 0} \tag{5.18}$$

where $Z_{p,u}^{M\neq 0}$ and $Z_{J,m}^{M\neq 0}$ are equivalent impedances of the external LEE domain, defined in terms of fluctuating variables (p', u') and (J', m'), respectively. Although equivalent, $Z_{p,u}^{M\neq 0}$ and $Z_{J,m}^{M\neq 0}$ impedance have numerically different values for LEE ($M \neq 0$) domain by defintion from Eqs. (5.13) and (5.14). Both the above options

can be used, however the model in Eq. (5.18) is *better*. This claim is based on the theoretical asymptotic analysis of Motheau et al. [45], which shows that the acoustic energy flux mismatch (error) for Eq. (5.18) model is

$$\Delta \mathbf{F} = |\mathbf{F}^{M\neq 0} - \mathbf{F}^{M=0}| \sim \mathcal{O}\left(M^2\right) \tag{5.19}$$

smaller compared to model given by Eq. (5.17), for which

$$\Delta \mathbf{F} = |\mathbf{F}^{M\neq 0} - \mathbf{F}^{M=0}| \sim \mathcal{O}\left(M\right) \tag{5.20}$$

where, M is the local mean flow Mach number at the interface (see Fig. 5.4). Thus modes computed with model Eq. (5.18) are expected to be more accurate in capturing mean-flow effects.

The impedance matching technique described in this subsection is only *part of the solution* for modeling mixed entropy-acoustic instabilities. It is enough to account for the mean flow effects in the case of pure acoustic or thermoacoustic problems, where the imposed impedance (Eq. 5.17 or 5.18) on the boundary implies or represents only *pure acoustic* response (or impedance) of the external high-speed element. For predicting mixed entropy-acoustic instabilities, the modeling of entropy fluctuations and its coupling with the acoustic field in the $M = 0$ computational domain is nowhere considered yet. This is the second hurdle in derivation of DECBC [45, 46], as indicated in Fig. 5.3(b), and is described next.

5.2.2 Entropy Waves Modeling in the Helmholtz Domain

FEM Helmholtz solvers, e.g., AVSP [127] at CERFACS, that essentially solve Eq. (5.9) for pressure $\hat{p}$, do not have fluctuating entropy $\hat{s}$ variable in the solution. However, physically for reacting flows, the thermodynamic conditions are *non-isentropic* due to unsteady heat release, causing entropy (or enthalpy, or temperature) to fluctuate in addition to pressure $\hat{p}$ and velocity $\hat{u}$. For example, the generation of entropy perturbation can be confirmed from LEE under the zero-Mach assumption Eqs. (5.5)-(5.7). Note the last entropy equation, where unsteady heat release q' source term forces entropy fluctuations. Compared with the LEE entropy equation under $M \neq 0$ condition (Eq. 5.3), another critical issue becomes evident: the entropy disturbances generated in the primary reaction zone of the combustor near the flame are *not convected by the mean flow* because of zero-Mach assumption. Therefore, in a way, the entropy fluctuations and entropy-acoustic coupling is neglected in the Helmholtz solver; and only flame-acoustic coupling due to unsteady heat release is taken into account.

Besides the mixed instabilities that are in focus in this chapter, entropy fluctuations are also quite relevant to instabilities due to standard thermoacoustic mechanism, as briefly noted in the following couple of points:

- *Disturbance Energy Balance:* In thermoacoustic analysis, acoustic energy balance is commonly carried out to corroborate whether or not a given system is stable. From such balance, stability criterion (e.g., classical Rayleigh criterion and its extensions - see Ch. 7 in [13]) are also derived. If the integral evolution of acoustic energy inside the system and its flux across the boundaries result in a net energy accumulation, the system becomes unstable. The classical acoustic energy is defined only by fluctuating p' and u' variables. However, for the reacting flows, the argument made above applies here again that an additional fluctuating thermodynamic variable (say entropy) must be considered in defining *a proper disturbance/fluctuating energy*. Building upon the early theoretical works of Chu [283], Myers [284], Nicoud and Poinsot [14] later demonstrated how entropy changes must be factored in for a more physically consistent definition of fluctuating energy. It also leads to a different stability criterion than the classical Rayleigh correlation Eq. (1.1) stating that temperature and heat release fluctuations must be in phase for the flame-acoustics coupling to cause instability. See more pertinent work in regards to disturbance energy from Brear et al. [285], George and Sujith [286, 287] and Magri et al. [15].

- *Production of Entropy Fluctuations near Flame:* The following couple of classical paradoxes in thermoacoustic modeling are discussed in literature when jump conditions are derived for acoustic waves propagating through a *flat, infinitesimally thin flame, assumed at rest in a 1D duct*, under zero and non-zero Mach number mean flow: (1) Dowling [270, 140], Nicoud et al. [112, 127] discuss that the linearized thermoacoustic relations (Eq. 5.3) indicate that in general unsteady heat-release of any *active flame* ($Q' \neq 0$) should cause entropy fluctuations. However, Strobio-Chen et al. [138] raise a physical argument that how can a perfectly-premixed flame, under the assumptions of complete combustion, adiabaticity, etc. can produce non-negligible temperature inhomogeneities (i.e., entropy waves) downstream of the flame. (2) Bauerheim et al. [137], for a *passive flame* ($Q' = 0$), conclude from their analysis with a somewhat counter-intuitive outcome that volume-flow-rate conservation (continuity of $v' = u'A$) must be used for perturbations at zero-Mach-number ($M = 0$) while mass conservation (continuity of $m' = \rho_0 u' A + \rho' u_0 A$) at non-zero Mach numbers ($M \neq 0$). This result is again closely related to generation of entropy disturbances near the flame and singularity associated with it.

  Strobio-Chen et al. [138] in their 1D theoretical study, also link the generation of entropy disturbances to the following two aspects. (i)*Movement of the flame discontinuity*, relaxing the hypothesis that the flame is at rest, and (ii) entropy perturbations present upstream of the flame (equivalence-ratio

waves), if any. The paper demonstrates how the above paradoxes could be satisfactorily explained when it is taken into account that a thin flat flame front, in a kinematic balance with the approach flow, will change not only its heat release rate but also its position in response to velocity perturbations.

Returning to the DECBC modeling, because zero-Mach Helmholtz / network solvers do not solve or account for the entropy perturbations, the variable $\hat{s}$ is not available, and they are neither able to advect entropy disturbances generated at the flame. Therefore, the entire entropy-acoustic coupling mechanism needs to be modeled. It is achieved in a way analogous to the low-order flame-acoustic coupling model, i.e., with the help of *transfer functions*. This concept was adopted by Motheau et al. [45, 46] and is utilized here for STORM as well.

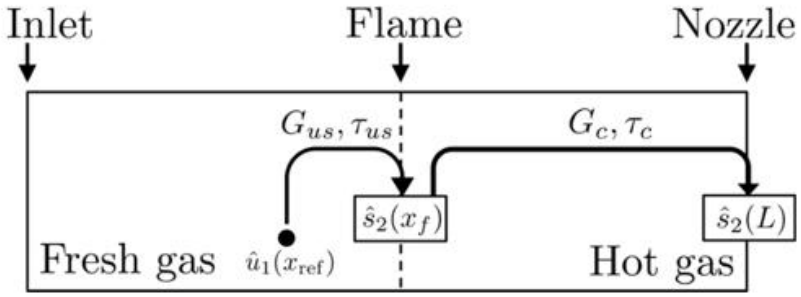

Figure 5.5: Schematic representation of the transfer functions that models the generation of entropy fluctuations at the flame, and their convection to the combustor exit boundary condition.

To elaborate the idea further refer to Fig. 5.5. Assuming that the entropy fluctuations leaving the combustor (or entering the nozzle) at $x = L$ have first been generated in the flame region before being convected by the mean flow, one obtains:

$$\hat{s}_2(L) = G_c \; e^{-j\omega\tau_c} \; \hat{s}_2\left(x_f\right) \tag{5.21}$$

The above equation models the *convection* of entropy perturbations generated at flame to the end of the combustor with a transfer function, where τ_c is the propagation time-scale and G_c is the gain, whose value typically should be smaller than unity denoting the dissipation and dispersion of entropy waves.
The entropy-acoustic coupling is the DECBC methodology is realized in two steps:

1. Production of model entropy fluctuations at the flame region is tied with some acoustic variable available in the Helmholtz/network solver. As indicated in the Fig. 5.5, $\hat{s}_2(x_f)$, is modeled with another transfer function with acoustic velocity $\hat{u}_1(x_{ref})$ at some reference location upstream of the flame.

$$\hat{s}_2\left(x_f\right) = G_{us} \; e^{-j\omega\tau_{us}} \hat{u}_1\left(x_{\text{ref}}\right) \tag{5.22}$$

where G_{us} and τ_{us} are the gain and the time delay of the transfer function for the entropy generation due to an acoustic perturbation at a reference location x_{ref}.

2. The acoustic feedback from the downstream nozzle to the combustor (the computational domain), due to indirect entropy noise, is what remains to be modeled to complete the entropy-acoustic coupling. It is done through the *impedance matching* process discussed in the previous section and Figs. 5.3, 5.4. Note here that the imposed equivalent impedance should represent the acoustic response of the high-speed downstream element to *both* incident acoustic and convected entropy waves. Thus it is important to ensure that entropy waves are considered in the a priori step of determining the impedance of the downstream element.

Lastly, a remark that the following additional sources of indirect noise, their interaction with combustor acoustics, and their influence on combustion stability are not considered in the current study:

- *Vorticity Waves:* Vorticity fluctuations, ς', is defined as the curl of the fluctuating velocity vector field, $\varsigma' = \vec{\nabla} \times \vec{u}'$. The advected vorticity disturbances on acceleration through the nozzle or turbine-rotor stages generate indirect vorticity noise [272, 273, 274, 120]. Since only a theoretical 1D test case with planar fluctuating variables has been employed to validate the DECBC methodology in this chapter, vorticity waves are not applicable. However, in the case of multi-dimensional cases, they could be accounted for through transfer functions, just like entropy waves.

- *Compositional inhomogeneities:* Magri et al. [275, 288, 289] report that local gas mixture inhomogeneities entering into a nozzle too can act as a source of indirect noise.

In summary, due to the inherent zero-Mach number assumption in Helmholtz / network solvers, the modeling of entropy-acoustic feedback and resulting mixed instabilities with the DECBC method thus reduces to (a) prescribing the above *Entropy Transfer Functions* (ETFs) for production, propagation of entropy waves to the combustor exit, and (b) matching the impedance of the downstream nozzle on the boundary. Following Sec. 5.3 will implement the DECBC in the STORM's state-space network framework and for an analytically tractable 1D test case. For simple cases and under important assumptions, ETFs could be determined analytically. But for more realistic complex cases, e.g., the real engine combustor analysed by Motheau et al. [46] in Fig. 5.2, determining the ETF models is still a challenge, and for now rely on high-order methods such as LES [46] or experimental measurements [280, 276, 289], just like flame transfer functions (FTFs).

5.3 State-Space Model of 1D-DECBC Network Element

This section aims to implement the DECBC methodology in STORM and derive a *state-space (SS) model* for it as a network element.

5.3.1 1D Test-Case for Validation

Figure 5.6 shows the simple 1D test case, taken from Motheau et al. [45], that is used for validation of the DECBC formulation. It is a simple 1D duct terminated with a compact, supersonic choked nozzle. The duct has an infinitely thin *passive flame* ($Q' = 0$) at x_f. Homogeneous mean cold/hot gas conditions are presumed on the two sides of the flame. Entropy perturbations are absent upstream of the flame, and those generated at the flame, are convected towards the nozzle as indicated in Fig. 5.6.

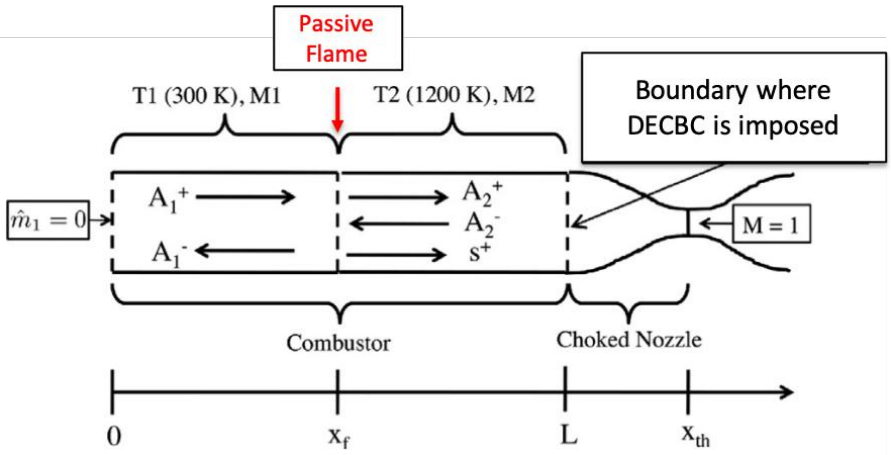

Figure 5.6: 1D test configuration from [45] for validating the DECBC methodology in STORM.

The modeling strategy employed is as discussed in previous Sec. 5.2: the geometry is truncated by removing the high-speed nozzle, and its equivalent impedance is applied at the boundary of the computational domain as highlighted in Fig. 5.6. The zero-Mach-number mean flow assumption prevails in the computational domain since it is intended to be solved with a STORM network. Production and propagation of the entropy waves are modeled with entropy transfer functions as detailed in the upcoming Sec. 5.3.2.

Unlike the wave-based (Riemann Invariants) approach for the spatial description of the acoustics adopted by Motheau et al. [45] for the 1D problem (see Fig. 5.6), the acoustic network modeling in STORM is based on generalized modal expansions and the state-space methods.

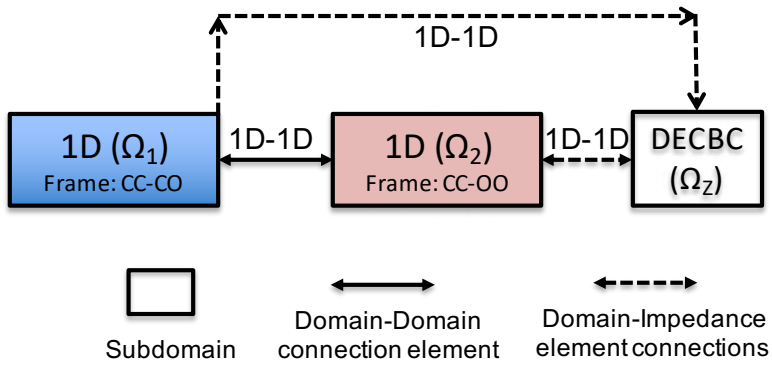

Figure 5.7: STORM network representation of the 1D test config in Fig. 5.6. The DECBC (impedance) element connects with both the 1D subdomains. It models the entropy transfer function (ETF) and the nozzle impedance to be imposed back onto the Ω_2 (combustor) boundary.

In STORM, the network representation of the 1D configuration will be as shown in Fig. 5.7, where the two 1D duct elements represent the cold and hot parts of the computational domain coupled with a 1D1D connection element. A few important points worth noting in building the STORM network:

- *Inlet BC* is $\hat{m}_1 = 0$ as shown in Fig. 5.6, i.e., a constant mass-flow-rate without fluctuations is imposed on the left end of Ω_1 subdomain. Refering to canonical impedances in Tab. 5.1, $Z_{J,m}^{M\neq 0} = \infty$ in this case. Therefore, using the impedance matching model in Eq. (5.18), $Z_{pu}^{M=0} = \infty$ impedance value is imposed on the inlet, which is same as $\hat{u} = 0$.

- Appropriate over-complete (OC) frames are mandatory in the 1D ducts as highlighted in Fig. 5.7 to avoid the acoustic variables from being a priori constrained at the junction between 1D subdomains and the outlet of duct Ω_2. E.g., the frame CC-CO (Closed-Closed and Closed-Open) of subdomain Ω_1 is made of two orthogonal basis families: CC that verifies $u' = 0$ on both ends of Ω_1; and CO that verifies $u' = 0$ and $p' = 0$ on the left and right ends of Ω_1 respectively. Thus CC-CO frame a priori imposes $u' = 0$ on the inlet.

- The DECBC network element (Ω_Z) in Fig. 5.7 is meant to indirectly model the production of entropy fluctuations at the flame as per acoustic perturbations at an upstream reference point in Ω_1, and its propagation to the outlet of Ω_2. In addition to this entropy transfer function (ETF), the Ω_Z element will also model the nozzle impedance and accordingly determine and fix the acoustic variables at the combustor exit. Thus the objective now is to derive an appropriate state-space (SS) model for this DECBC element that will connect

with SS models of acoustic subdomains Ω_1 and Ω_2 both. It is expected that resolving the whole network in Fig. 5.7 will model the entropy-acoustic feedback mechanism and help predict the low-frequency mixed entropy-acoustic mode.

5.3.2 Entropy Transfer Function (ETF) and Nozzle Impedance

As mentioned above, one task of the DECBC network element is to model the entropy transfer functions (ETFs). The production of entropy perturbations at the passive ($\hat{Q} = 0$), flat, infinitely thin flame, in the limit of low Mach ($M \to 0$) mean flow (and noting that the product $u_2\hat{s}$ remains finite, even when $u_2 \to 0$), was proposed in theoretical work of Dowling [270] as:

$$\hat{s}_2(x_f, \omega) = \frac{-c_p^2(T_{02} - T_{01})(\gamma - 1)}{u_2 c_2^2} \frac{\rho_1}{\rho_2}\ \hat{u}_1(x_f, \omega) \tag{5.23}$$

where $T_{0,i} = T_i + \frac{1}{2c_p}u_i^2$ is the mean stagnation temperature. Subscripts 1 and 2 denote mean quantities in upstream (cold) and downstream (hot) parts of the duct and other notations have their usual meaning. ($\hat{}$) denote frequency-domain quantities assuming harmonic oscillations with following Fourier convention $f'(x,t) = \Re\{\hat{f}(x,\omega)e^{j\omega t}\}$. This entropy production model was utilized by Motheau et al. [45] and is used in the current study as well. Therefore, comparing Eq. (5.23) with entropy production transfer function Eq. (5.22) implies that

$$G_{us} = \frac{-c_p^2(T_{02} - T_{01})(\gamma - 1)}{u_2 c_2^2} \frac{\rho_1}{\rho_2} \quad and \quad \tau_{us} = 0 \tag{5.24}$$

Here $\tau_{us} = 0$ because the flame (passive) was modeled as infinitely thin discontinuity, and the reference location was taken exactly at the flame location ($x_{ref} = x_f$) [270, 45]. However, in the case of the STORM network in Fig. 5.7, the reference location is taken in Ω_1 subdomain slightly upstream of the junction that represents the thin passive flame discontinuity.

Propagation of entropy waves and thus the entropy fluctuations at the outlet $x = L$ (or nozzle entrance), can be related to $\hat{u}_1(x_{ref}, \omega)$ from Eqs. (5.21) and (5.22) as:

$$\hat{s}_2(L, \omega) = G_{us}G_c\ e^{-j\omega(\tau_c)}\ \hat{u}_1\left(x_f, \omega\right) \tag{5.25}$$

where propagation gain and delay are given as:

$$G_c = 1 \quad and \quad \tau_c = \frac{L - x_f}{u_2} \tag{5.26}$$

Note that in reality, the propagating entropy waves undergo some dissipation and dispersion due to diffusion, turbulent mixing, etc. [290, 291, 292]. These effects could be accounted for by employing more sophisticated transfer functions like distributed

time-delay (DTD) models discussed in the context of FTFs in Ch. 4. However, dissipation and dispersion effects were neglected in [45] and so is the case in this first study with STORM.

The second task of the DECBC network element is to impose nozzle impedance. The impedance of a compact supersonic choked nozzle to incident acoustic and entropy waves was derived by Marble and Candel [44], inter-relating the fluctuating pressure ($\hat{p}$), acoustic velocity $\hat{u}$ and entropy ($\hat{s}$) at the combustor exit $x = L$ (or nozzle entrance). It essentially represents the boundary condition that is required to be imposed with $\hat{s}(L, \omega)$ given from the above ETF.

$$\left(\frac{\gamma - 1}{2}\right) M_2 \frac{\hat{p}_2(L,\omega)}{\gamma p_2} = \frac{\hat{u}_2(L,\omega)}{c_2} - \frac{1}{2} M_2 \frac{\hat{s}_2(L,\omega)}{c_p} \tag{5.27}$$

On inserting ETF Eq. (5.25), the above equation is re-written as:

$$\hat{p}_2(L,\omega) = A_0 \hat{u}_2(L,\omega) + A_1 \hat{u}(x_f,\omega)\ e^{-j\omega\tau_c} \tag{5.28}$$

where the coefficients are,

$$\begin{aligned} A_0 &= \left(\frac{2\gamma}{\gamma - 1}\right) \frac{p_2}{M_2 c_2} \\ A_1 &= \frac{-\gamma p_2}{(\gamma - 1) c_p} G_{us} G_c \ = \ \frac{\rho_1 c_p \left(T_{02} - T_{01}\right)}{M_2 c_2} \end{aligned} \tag{5.29}$$

Eq. (5.28), when enforced in the zero-Mach-number STORM network (by DECBC element), now analogously inter-relates the acoustic pressure $\hat{p}$ and velocity $\hat{u}$ at $x = L$ with acoustic velocity $\hat{u}(x_f)$ thereby modeling and accounting the entropy-acoustic-feedback mechanism.

5.3.3 State-Space Model Realizations (SS-R1 and SS-R2)

This section will finally derive the *state-space (SS) model* of the DECBC element in STORM network Fig. 5.7 that basically enforces the nozzle impedance condition in Eq. (5.28). Two different but mathematically equivalent SS realizations (SS-R1 and SS-R2) are considered and detailed in the next subsections.

The SS model formulation is largely based on that of 1D-1D connection element (Ω_{sc}) that was detailed in Ch. 2, Sec. 2.2.3 so as to derive a dynamical equation (ODE) that could be transformed into state-space. The technique employs a rather global treatment utilizing volume-averaged LEE in a thin, acoustically compact control volume enclosing the junction — here, the boundary interface between Ω_2 outlet and (modeled) nozzle (Ω_3) as shown in Fig. 5.8. The Ω_Z domain of length L_b represents the boundary DECBC element in the network. Similar to Ω_{sc} of the 1D-1D connector, the local resolution of acoustics in the Ω_Z domain is not necessary.

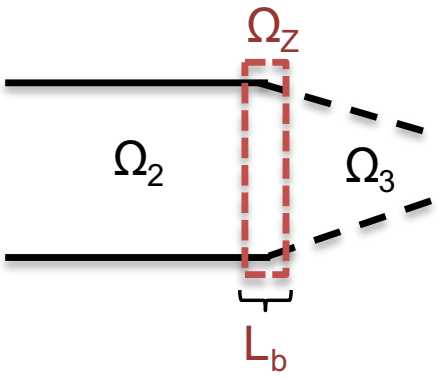

Figure 5.8: A infinitesimally thin ($L_b \to 0$) control volume Ω_Z enclosing the interface between the combustor (Ω_2) and nozzle (Ω_3). The Ω_Z domain is used to derive the state-space model of the DECBC network element highlighted in Fig. 5.7.

The two volume-averaged mass and momentum LEE governed the *dynamics* of acoustic pressure ($\bar{p}(t)$) and velocity ($\bar{u}(t)$) respectively in Ω_{sc}, where ($\bar{}$) denote vol. avg. quantities. They enforced the coupling condition and helped set appropriate values of acoustic variables at the junction. However, in the current case of Ω_Z, only one mass volume-averaged LEE equation is utilized that describes the dynamics of $\bar{p}(t)$; and instead of LEE momentum equation, the nozzle impedance condition given by Eq. (5.28) is used. From Eq. (2.21) in Sec. 2.2.3 the volume-averaged LEE mass equation is rewritten for Ω_Z as

$$\frac{d}{dt}\bar{p}_{\Omega_Z}(t) = \frac{\rho_0 c_0^2}{L_b} u_{\Omega_2}(t) + \frac{\rho_0 c_0^2}{L_b} u_{\Omega_3}(t) \tag{5.30}$$

where, u_{Ω_2} and u_{Ω_3} are the normal acoustic velocity imposed by subdomains Ω_2 and Ω_3 respectively on the interfaces with domain Ω_Z. Also ρ_0 and c_0 are mean quantities in domain Ω_Z that are taken equal to that in Ω_2, i.e., ρ_2 and c_2.

Going into the frequency-space by taking Fourier transform of the above equation; and using the fact that in the limit $L_b \to 0$, $\hat{u}_{\Omega_3}(\omega) \to -\hat{u}_{\Omega_2}(\omega)$, and by substituting for $\hat{u}_{\Omega_3}(\omega)$ from the impedance condition Eq. (5.28) the following equation is obtained

$$j\omega\hat{\bar{p}}(\omega) = \frac{\rho_0 c_0^2}{L_b}\hat{u}_{\Omega_2}(L,\omega) - \frac{\rho_0 c_0^2}{L_b}\frac{1}{A_0}\hat{p}_{\Omega_2}(L,\omega) + \frac{\rho_0 c_0^2}{L_b}\frac{A_1}{A_0}\hat{u}_{\Omega_1}(x_f,\omega)\, e^{-j\omega\tau_c} \tag{5.31}$$

Now that the impedance condition Eq. (5.28) is embedded into the LEE equation governing $\hat{p}(\omega)$ in Ω_Z, it must be taken back into the time-domain for state-space representation of the DECBC element. For this purpose, the nonlinear delay term

$e^{-j\omega\tau_c}$ is an issue. Therefore, it is approximated with the following Multi-pole expansion (or rational approximation), similar to how FTFs were modeled in previous chapters.

$$e^{-j\omega\tau_c} = \sum_{k=1}^{N_{PBFs}} \frac{2a_k j\omega}{(j\omega)^2 - 2c_k j\omega + \omega_{0,k}^2} \tag{5.32}$$

Each term in the above equation is called a Pole-Base-Function (PBF). The coefficient's $a_k, c_k, \omega_{0,k}$ are determined from the fitting algorithm developed by Douasbin et al. [242] (see previous Ch. 4).

5.3.3.1 SS Model Realization-1 (SS-R1)

Eq. (5.31) can be decomposed into N_{PBFs} number of equations, such that

$$\hat{\bar{p}}(\omega) = \sum_{k=1}^{N_{PBFs}} \hat{\bar{p}}_k(\omega) \tag{5.33}$$

and along with Eq. (5.32) it yields

$$j\omega\hat{\bar{p}}_k(\omega) = \frac{\rho_0 c_0^2}{L_b N_{PBFs}} \hat{u}_{\Omega_2}(L,\omega) - \frac{\rho_0 c_0^2}{L_b N_{PBFs}} \frac{1}{A_0} \hat{p}_{\Omega_2}(L,\omega) +$$

$$\frac{\rho_0 c_0^2}{L_b} \frac{A_1}{A_0} \hat{u}_{\Omega_1}(x_f,\omega) \left[\frac{2a_k j\omega}{(j\omega)^2 - 2c_k j\omega + \omega_{0,k}^2} \right] \tag{5.34}$$

Note that the subscript 'k' is not used for $\hat{u}_{\Omega_2}(L,\omega)$ and $\hat{p}_{\Omega_2}(L,\omega)$, but rather their constant coefficients are divided with N_{PBFs}. This simple manipulation provides an important simplification later on for the state-space (SS) representation. Due to this, more specifically, the components of the input vector of the SS dynamics equation of the Ω_Z domain (or the DECBC network element) will be consistent with the components of the SS output vector of the acoustic subdomain Ω_2 it connects with. The SS output equation of Ω_2 simply cannot output $\hat{u}_{\Omega_2,k}(L,\omega)$ and $\hat{p}_{\Omega_2,k}(L,\omega)$, where $k = 1$ to N_{PBFs}.

Equation (5.34), expressed in frequency-domain, needs to be taken back into physical space i.e. time-domain before it could be converted into state-space equations. For doing so, all the terms in Eq. (5.34) are taken to the LHS expect the k^{th} PBF. The coefficient of the PBF is also moved to the LHS in the denominator so as to give a fraction of the form $N(\omega)/D(\omega)$. Next an intermediate variable $\hat{z}_k(\omega)$ is introduced on the LHS as follows, where $k = 1$ to N_{PBFs}

$$\left(\frac{N(\omega)}{\hat{z}_k(\omega)}\right)\left(\frac{\hat{z}_k(\omega)}{D(\omega)}\right) = (2a_k j\omega)\left(\frac{1}{(j\omega)^2 - 2c_k j\omega + \omega_{0,k}^2}\right) \tag{5.35}$$

where,

$$N(\omega) = j\omega\hat{\bar{p}}_k(\omega) - \frac{\rho_0 c_0^2}{L_b N_{PBFs}}\hat{u}_{\Omega_2}(L,\omega) + \frac{\rho_0 c_0^2}{L_b N_{PBFs}}\frac{1}{A_0}\hat{p}_{\Omega_2}(L,\omega) \tag{5.36}$$

and

$$D(\omega) = \frac{\rho_0 c_0^2}{L_b}\frac{A_1}{A_0}\hat{u}_{\Omega_1}(x_f,\omega) \tag{5.37}$$

By introducing $\hat{z}_k(\omega)$, above Eq. (5.35) is split into two sets of equations by equating the terms in left and right parenthesis respectively from both the sides. The two sets of equations are then recast into the time-domain by taking inverse Fourier transform to obtain a system of coupled differential equations (ODEs) (the first two equations in the following group). A third ODE is appended to the group, which is nothing but the definition of k^{th} component of the acoustic potential, $\bar{\varphi}_k^{\Omega_z}$, corresponding to $\bar{p}_k^{\Omega_z}$.

$$\begin{aligned}
\frac{d}{dt}\dot{z}_k(t) &= 2c_k\dot{z}_k(t) - \omega_{0,k}^2 z_k(t) + \frac{\rho_0 c_0^2}{L_b}\frac{A_1}{A_0}u^{\Omega_1}(x_f,t) \\
\frac{d}{dt}\bar{p}_k^{\Omega_Z}(t) &= 2a_k\dot{z}_k(t) + \frac{\rho_0 c_0^2}{L_b N_{PBFs}}u^{\Omega_2}(L,t) - \frac{\rho_0 c_0^2}{L_b N_{PBFs}}\frac{1}{A_0}p^{\Omega_2}(L,t) \\
\frac{d}{dt}\bar{\varphi}_k^{\Omega_Z}(t) &= \frac{-1}{\rho_0}\bar{p}_k^{\Omega_Z}(t)
\end{aligned} \tag{5.38}$$

The intermediate variable $z_k(t)$ is abstract, and ascribing any tangible physical meaning to it may not be possible. The first equation in the above group governs the dynamics of the variable $\dot{z}_k(t)$ under the influence of input - the acoustic velocity at the reference location in subdomain Ω_1. The other equation governs $\bar{p}_k(t)$ in Ω_Z under the influence of velocity and pressure at the exit of the subdomain Ω_2. In addition, it is also coupled to the first equation through the $2a_k\dot{z}_k(t)$ term.

The k^{th} block of the state-space (SS) dynamics equation of the DECBC element can then be finally written from Eq. (5.38) as follows, where $k = 1$ to N_{PBFs}:

$$\underbrace{\frac{d}{dt}\begin{bmatrix} z_k(t) \\ \dot{z}_k(t) \\ \bar{p}_k(t) \\ \bar{\varphi}_k(t) \end{bmatrix}}_{\mathbf{X}_k^{\Omega_z}(t)} = \underbrace{\begin{bmatrix} 0 & 1 & 0 & 0 \\ -\omega_{0,k}^2 & 2c_k & 0 & 0 \\ 0 & 2a_k & 0 & 0 \\ 0 & 0 & -1/\rho_0 & 0 \end{bmatrix}}_{\mathbf{A}_k^{\Omega_z}} \begin{bmatrix} z_k(t) \\ \dot{z}_k(t) \\ \bar{p}_k(t) \\ \bar{\varphi}_k(t) \end{bmatrix} +$$

$$\underbrace{\begin{bmatrix} 0 & 0 & 0 & 0 \\ \frac{\rho_0 c_0^2}{L_b}\frac{A_1}{A_0} & 0 & 0 & 0 \\ 0 & 0 & \frac{\rho_0 c_0^2}{L_b N_{PBFs}} & \frac{-\rho_0 c_0^2}{A_0 L_b N_{PBFs}} \\ 0 & 0 & 0 & 0 \end{bmatrix}}_{\mathbf{B}_k^{\Omega_z}} \underbrace{\begin{bmatrix} u^{\Omega_1}(x_f,t) \\ p^{\Omega_1}(x_f,t) \\ u^{\Omega_2}(L,t) \\ p^{\Omega_2}(L,t) \end{bmatrix}}_{\mathbf{U}_k^{\Omega_z}(t)} \tag{5.39}$$

Assembling all the above blocks together for $k = 1$ to N_{PBFs}, yields as below the full **state-space dynamics** equation of the DECBC element:

$$\underbrace{\frac{d}{dt}\begin{bmatrix} \mathbf{X}_1 \\ \mathbf{X}_2 \\ \vdots \\ \mathbf{X}_{N_{PBFs}} \end{bmatrix}}_{\mathbf{X}^{\Omega_z}(t)} = \underbrace{\begin{bmatrix} \mathbf{A}_1 & & & \\ & \mathbf{A}_2 & & \\ & & \ddots & \\ & & & \mathbf{A}_{N_{PBFs}} \end{bmatrix}}_{\mathbf{A}^{\Omega_z}} \begin{bmatrix} \mathbf{X}_1 \\ \mathbf{X}_2 \\ \vdots \\ \mathbf{X}_{N_{PBFs}} \end{bmatrix} + \underbrace{\begin{bmatrix} \mathbf{B}_1 \\ \mathbf{B}_2 \\ \vdots \\ \mathbf{B}_{N_{PBFs}} \end{bmatrix}}_{\mathbf{B}^{\Omega_z}} \underbrace{\begin{bmatrix} u^{\Omega_1}(x_f,t) \\ p^{\Omega_1}(x_f,t) \\ u^{\Omega_2}(L,t) \\ p^{\Omega_2}(L,t) \end{bmatrix}}_{\mathbf{U}^{\Omega_z}(t)} \tag{5.40}$$

The model representation of the DECBC element is completed with the following **state-space output** equation:

$$\underbrace{\begin{bmatrix} u^{\Omega_z}(t) \\ \varphi^{\Omega_z}(t) \end{bmatrix}}_{\mathbf{Y}^{\Omega_z}(t)} = \underbrace{\begin{bmatrix} \mathbf{C}_1 & \mathbf{C}_2 & \cdots & \mathbf{C}_{N_{PBFs}} \end{bmatrix}}_{\mathbf{C}^{\Omega_z}} \underbrace{\begin{bmatrix} \mathbf{X}_1 \\ \mathbf{X}_2 \\ \vdots \\ \mathbf{X}_{N_{PBFs}} \end{bmatrix}}_{\mathbf{X}^{\Omega_z}(t)} \tag{5.41}$$

where,

$$\mathbf{C}_k = \begin{bmatrix} 0 & 0 & 0 & 0 \\ 0 & 0 & 0 & 1 \end{bmatrix} \tag{5.42}$$

and $u^{\Omega_z}(t)$ and $\varphi^{\Omega_z}(t)$ in the SS output vector is nothing but the volume-averaged acoustic velocity $\bar{u}(t)$ and potential $\bar{\varphi}(t)$ in Ω_Z meant to go to the acoustic subdomain Ω_2. The output is consistent with the SS input vector of Ω_2 that indeed

expects velocity and potential in it (see the SS dynamics equation of a general acoustic subdomain in Ch.2 Eq. 2.17). However, note that the output of velocity $u^{\Omega_z}(t)$ is *nullified* (due to first row of matrix $\mathbf{C}$), and only $\varphi^{\Omega_z}(t)$ is imposed back at the end of Ω_2. This is further elaborated as follows:

- Firstly, $\bar{u}(t)$ is neither available nor can be computed directly from the state-vector - see Eq. (5.39). Recall that for Ω_Z domain, only volume-averaged LEE mass Eq. (5.30) was solved governing the dynamics for $\bar{p}(t)$.
- Thus effectively, the SS dynamics equation of DECBC element (Eq. 5.40) takes acoustic velocity and pressure from the end of Ω_2 in its input vector along with the velocity from reference location in Ω_1. It then determines the appropriate pressure $\bar{p}(t)$ in Ω_Z *as per the nozzle impedance condition* (Eq. 5.28). Only this pressure is then imposed back onto the end of Ω_2, not directly, but as corresponding acoustic potential ($\bar{\varphi} = \sum \bar{\varphi}_k$), while the prevailing acoustic velocity at the end of Ω_2 remains unmodified.

This completes the first state-space realization (SS-R1) of the DECBC model.

5.3.3.2 SS Model Realization-2 (SS-R2)

The previous SS-R1 model of the DECBC element was the model developed initially. On testing it, some *numerical issues* were encountered, particularly with correctly predicting the low-frequency mixed entropy-acoustic mode of interest. The problems are discussed in the upcoming results in Sec. 5.5. After some struggle with SS-R1, another equivalent state-space formulation was deduced, and it apparently worked as expected. Recall that state-space realizations are not unique. This second SS-R2 realization is described in this section.

The first DECBC model (SS-R1) was derived from the dynamical coupled system of ODEs in Eq. (5.38). Note the choice of state-variables in state-space (SS) dynamics equation Eq. (5.39). It is comprised of these components $\bar{p}_k(t)$, $\bar{\varphi}_k(t)$ for $k = 1$ to N_{PBFs}.

The second DECBC model (SS-R2) is also derived from the ODEs in Eq. (5.38) after slightly modifying the second (and thus the third) equation in the group, such that, the state-vector now contains only $\bar{p}(t)$ and $\bar{\varphi}(t)$. Since $\bar{p}(t) = \sum \bar{p}_k(t)$, all the components are combined and the second ODE from Eq. (5.38) can be re-written for $\bar{p}(t)$ as below.

$$\frac{d}{dt}\bar{p}^{\Omega_Z}(t) = \sum_{k=1}^{N_{PBFs}} 2a_k\dot{z}_k(t) + \frac{\rho_0 c_0^2}{L_b}u^{\Omega_2}(L,t) - \frac{\rho_0 c_0^2}{L_b}\frac{1}{A_0}p^{\Omega_2}(L,t) \tag{5.43}$$

The first ODE in Eq. (5.38) remains unchanged and the acoustic potential $\bar{\varphi}(t)$ can similarly defined from $\bar{p}(t)$. So finally from this new system of ODEs, the second

(SS-R2) DECBC model is given as follows:

SS Dynamics Equation:

$$\underbrace{\frac{d}{dt}\begin{bmatrix} z_1(t) \\ \dot{z}_1(t) \\ \vdots \\ z_k(t) \\ \dot{z}_k(t) \\ \bar{p}(t) \\ \bar{\varphi}(t) \end{bmatrix}}_{\mathbf{X}^{\Omega_z}(t)} = \underbrace{\begin{bmatrix} 0 & 1 & & & & & \\ -\omega_{0,1}^2 & 2c_1 & & & & & \\ & & \ddots & & & & \\ & & & 0 & 1 & & \\ & & & -\omega_{0,N_{PBFs}}^2 & 2c_{N_{PBFs}} & & \\ 0 & 2a_1 & \dots & 0 & 2a_{N_{PBFs}} & 0 & 0 \\ 0 & 0 & \dots & 0 & 0 & -1/\rho_0 & 0 \end{bmatrix}}_{\mathbf{A}^{\Omega_z}} \begin{bmatrix} z_1(t) \\ \dot{z}_1(t) \\ \vdots \\ z_k(t) \\ \dot{z}_k(t) \\ \bar{p}(t) \\ \bar{\varphi}(t) \end{bmatrix} +$$

$$\underbrace{\begin{bmatrix} 0 & 0 & & \\ \frac{\rho_0 c_0^2}{L_b}\frac{A_1}{A_0} & 0 & & \\ \vdots & \vdots & & \\ 0 & 0 & & \\ \frac{\rho_0 c_0^2}{L_b}\frac{A_1}{A_0} & 0 & & \\ & & \frac{\rho_0 c_0^2}{L_b} & \frac{-\rho_0 c_0^2}{A_0 L_b} \\ & & 0 & 0 \end{bmatrix}}_{\mathbf{B}^{\Omega_z}} \underbrace{\begin{bmatrix} u^{\Omega_1}(x_f,t) \\ p^{\Omega_1}(x_f,t) \\ u^{\Omega_2}(L,t) \\ p^{\Omega_2}(L,t) \end{bmatrix}}_{\mathbf{U}^{\Omega_z}(t)} \tag{5.44}$$

SS Output Equation:

$$\underbrace{\begin{bmatrix} u^{\Omega_z}(t) \\ \varphi^{\Omega_z}(t) \end{bmatrix}}_{\mathbf{Y}^{\Omega_z}(t)} = \underbrace{\begin{bmatrix} 0 & 0 & \dots & 0 & 0 & 0 & 0 \\ 0 & 0 & \dots & 0 & 0 & 0 & 1 \end{bmatrix}}_{\mathbf{C}^{\Omega_z}} \underbrace{\begin{bmatrix} z_1(t) \\ \dot{z}_1(t) \\ \vdots \\ z_k(t) \\ \dot{z}_k(t) \\ \bar{p}(t) \\ \bar{\varphi}(t) \end{bmatrix}}_{\mathbf{X}^{\Omega_z}(t)} \tag{5.45}$$

This completes the state-space (SS) model derivation of DECBC network element. Two realizations (SS-R1 and SS-R2) have been described in this section.

5.4 State-Space Model of real-valued 1D Acoustic Impedance

Before presenting the results of 1D DECBC test case (Fig. 5.7) in subsequent Sec. 5.5, this section derives a state-space (SS) model of a simple, real-valued, pure acoustic impedance. It is used later for cross-verification of some results in the following Sec. 5.5.1.

The steps are analogous to the derivation of the DECBC SS model detailed in the previous section. Starting with the volume-averaged mass LEE equation (Eq. 5.30), the equation is transformed into frequency-space, the $\hat{u}_{\Omega_3}(\omega)$ is replaced from impedance relation $\mathrm{Z} = \frac{\hat{p}(\omega)}{\rho_0 c_0 \hat{u}(\omega)}$, where Z is real and constant. The equation is transformed back into the time domain. The resulting ODE governing $\bar{p}(t)$ in Ω_Z can be directly written in a state-space form. This equation is accompanied by acoustic potential $\bar{\varphi}(t)$ definition.

SS Dynamics Equation:

$$\underbrace{\frac{d}{dt}\begin{bmatrix} \bar{p}(t) \\ \bar{\varphi}(t) \end{bmatrix}}_{\mathbf{X}^{\Omega_z}(t)} = \underbrace{\begin{bmatrix} 0 & 0 \\ -1/\rho_0 & 0 \end{bmatrix}}_{\mathbf{A}^{\Omega_z}} \begin{bmatrix} \bar{p}(t) \\ \bar{\varphi}(t) \end{bmatrix} + \underbrace{\begin{bmatrix} \frac{\rho_0 c_0^2}{L_b} & \frac{-c_0}{ZL_b} \\ 0 & 0 \end{bmatrix}}_{\mathbf{B}^{\Omega_z}} \underbrace{\begin{bmatrix} u^{\Omega_2}(L,t) \\ p^{\Omega_2}(L,t) \end{bmatrix}}_{\mathbf{U}^{\Omega_z}(t)} \tag{5.46}$$

SS Output Equation:

$$\underbrace{\begin{bmatrix} u^{\Omega_Z}(t) \\ \varphi^{\Omega_Z}(t) \end{bmatrix}}_{\mathbf{Y}^{\Omega_z}(t)} = \underbrace{\begin{bmatrix} 0 & 0 \\ 0 & 1 \end{bmatrix}}_{\mathbf{C}^{\Omega_z}} \underbrace{\begin{bmatrix} \bar{p}(t) \\ \bar{\varphi}(t) \end{bmatrix}}_{\mathbf{X}^{\Omega_z}(t)} \tag{5.47}$$

5.5 Results and Validation

This section will discuss the results of the 1D STORM test network (Fig. 5.7) using state-space DECBC element developed. The aim is to predict the low-frequency mixed entropy-acoustic mode and evaluate the influence of entropy-acoustic feedback on the thermoacoustic modes. The effect of the mean-flow Mach number, due to the DECBC submodel combined with an otherwise zero-Mach-number acoustic network, will also be assessed.

Both state-space (SS) DECBC formulations in STORM (SS-R1 and SS-R2) will examined in subsequent Sec. 5.5.2 and 5.5.3 respectively. The STORM results are validated with reference, 1D wave-based (Riemann invariants), quasi-analytical solutions of the configuration (Fig. 5.6) as detailed in Motheau et al. [45]. Following two reference methods are considered:

1. **LEE:** Solves the frequency-domain 1D linearized Euler equations wherein the mean-flow Mach number in the computational domain is non-zero. The nozzle impedance Eq. (5.27) (with both acoustic and entropic response) is applied at the combustor exit. This method inherently contains the mean-flow effects.

2. **Helm+DECBC:** Solves 1D Helmholtz equation, where *zero-Mach-number* assumption applies. The entropy-acoustic feedback mechanism is modeled with the DECBC approach.

The geometrical and thermodynamic parameters used for solving the 1D configuration in Fig. 5.6 are given in Tab. 5.2 below. Different inlet mean flow Mach numbers (M_1) that are considered are tabulated in Tab. 5.3 alongwith required DECBC submodel input parameters - specifically the entropy transfer function (ETF) gain and propagation delays. As was mentioned earlier, the ETFs, in STORM are modeled via rational approximation (Eq. 5.32). The fitting is carried out for a frequency bandwidth of $0-450Hz$ and thus only eigenmodes falling under the cut-off frequency of 450 Hz are expected to be correctly predicted. Note that as the mean-flow Mach number increases, the advection time of entropy waves τ_c reduces, and so does the corresponding number of Pole-Base-Functions (PBFs) required to fit the ETF as listed in the last column. Indeed, the number of PBFs modifies the sizes of state-space matrices of the DECBC submodel (cf. Eqs. 5.40 and 5.44), and eventually the *global* state-space model of the network (Fig. 5.7) after assembling all the submodels together by Redheffer star product (see Eq. 2.7, from Ch. 2, Sec. 2.1.1).

T_1 [K]	p_1 [Pa]	T_2 [K]	γ	r [SI]	L [m]	x_f [m]	x_{th} [m]	δ_f [m]
300	101325	1200	1.4	287	1	0.75	1.0087	0.005

Table 5.2: Thermodynamic and geometrical parameters for which the configuration in Fig. 5.6 is solved.

M_1	M_2	G_{us}	τ_{us} [ms]	G_c	τ_c [ms]	N_{PBFs}
0.00625	0.0125	-347.2	0	1	28.78	30
0.0125	0.025	-173.6	0	1	14.4	25
0.025	0.05	-86.8	0	1	7.18	20
0.05	0.10	-43.4	0	1	3.56	12

Table 5.3: DECBC model parameters for which the configuration in Fig. 5.6 is solved. M_1, M_2 **are the mean flow Mach number upstream and downstream of the passive flame in subdomain** Ω_1**. Last column indicates the number of PBFs in rational approximation of the ETF (Eq. 5.32).**

5.5.1 Test1: Applying Nozzle Impedance without Entropy-Acoustic Feedback

Here, the motivation is to conduct a quick and straightforward test to cross-check the 1D-DECBC SS formulation when the entropy waves are absent. The idea is to verify a hypothetical situation that when there are no entropy fluctuations propagated to the combustor exit or that they are almost entirely dissipated, will, in that case, the DECBC element correctly apply the pure acoustic impedance of the nozzle or not. For this purpose, the pure acoustic impedance of the nozzle is applied in a separate network problem with the help impedance element derived earlier in Sec. 5.4. Consistent results are expected from both approaches.

Returning to the Marble and Candel [44] relation (Eq. 5.27) and the impedance condition (Eq. 5.28) derived from it after including the entropy transfer function (ETF). Now, suppose entropy perturbations are nullified by setting entropy transfer function (ETF) gain $G_c = 0$, then from Eq. (5.28). In that case, the A_0 coefficient gives the relation between acoustic pressure and velocity that should be verified at the combustor exit, i.e., the pure acoustic impedance of the nozzle. On dividing A_0 with $\rho_2 c_2$ the non-dimensional impedance Z_{nozz} is obtained as

$$Z_{nozz} = \frac{\hat{p}(L,\omega)}{\rho_2 c_2 \hat{u}(L,\omega)} = \frac{A_0}{\rho_2 c_2} = \frac{2}{(\gamma-1)M_2} \tag{5.48}$$

where, ρ_2, c_2 are mean density, sound speed in subdomain Ω_2, and M_2 is the mean flow Mach number. Note that the compact nozzle acoustic impedance above is real-valued and constant (independent of frequency ω).

Therefore now, the network in Fig. 5.7 is solved with DECBC (SS-R1) element with ETF gain $G_c = 0$. The same problem is solved with the DECBC replaced with the acoustic impedance element from Sec. 5.4 imposing the above Z_{nozz} acoustic impedance. Fig. 5.9 highlights that consistent results are obtained from both approaches. Eigen-frequencies of the first three eigenmodes are listed, whose negative growth rates indicate damping induced by the resistive acoustic impedance of the nozzle. Mode shapes are observed to be correct (not shown here).

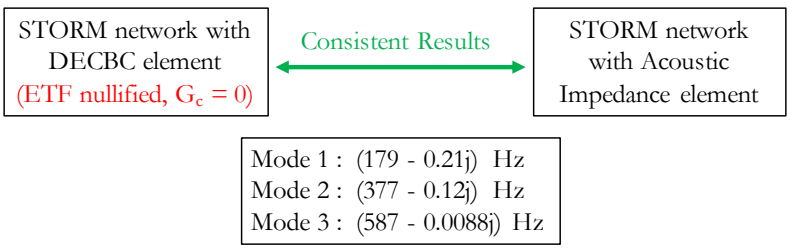

Figure 5.9: Acoustic Eigenmodes of the network in Fig. 5.7 without entropy-acoustic feedback.

5.5.2 Test2: 1D-DECBC Results with SS-R1

Results of the network (Fig. 5.7) resolution with DECBC SS-R1 model, with entropy transfer function (ETF) applied, are presented in this subsection. Very low inlet Mach number, $M_1 = 0.00625$ is considered and thus corresponding ETF parameters mentioned in Tab. 5.3 are administered.

Computed eigenmodes are listed in Tab. 5.4 for varying OC-frame sizes in the 1D acoustic subdomains Ω_1 and Ω_2 of the network. $N_{\Omega_1} = N_{\Omega_2} = N$.

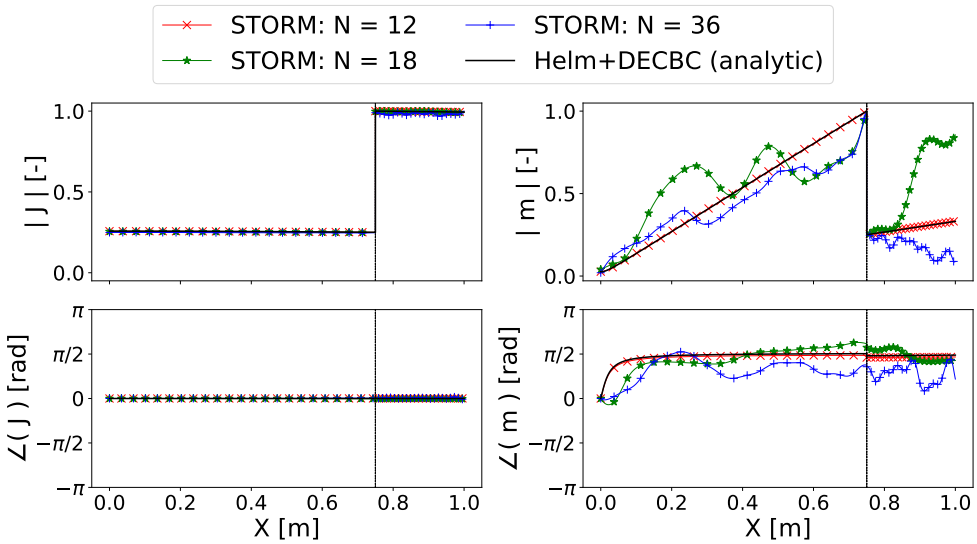

Figure 5.10: Mode 1 shape from Tab. 5.4 with SS-R1 DECBC model.

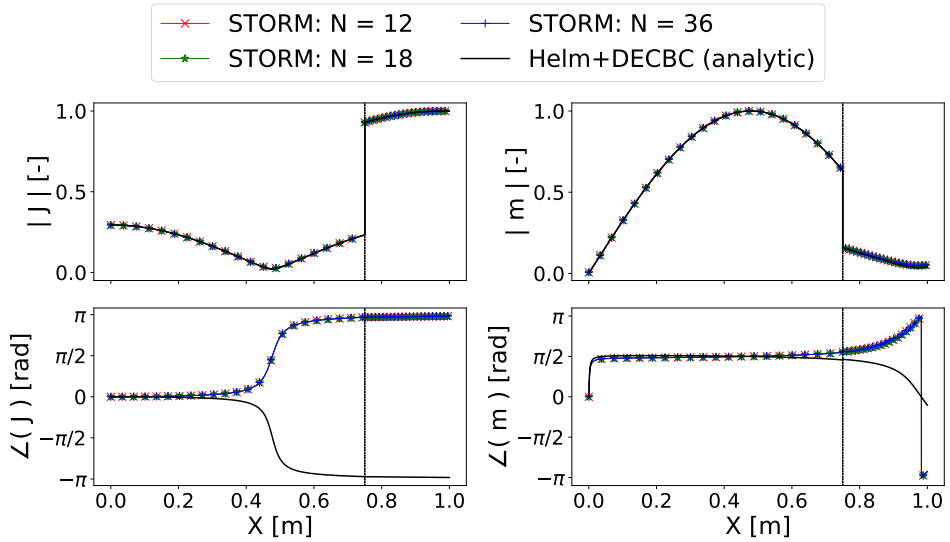

Figure 5.11: Mode 2 shape from Tab. 5.4 with SS-R1 DECBC model.

	STORM+DECBC			(Ref:) Helm+DECBC
	$N = 12$	$N = 18$	$N = 36$	
Mode 1	$17 + 0.7j$	$\mathbf{19 - 4.0j}$	$\mathbf{19 + 8.0j}$	$17 + 0.7j$
Mode 2	$181 + 8.9j$	$181 + 9.0j$	$181 + 8.7j$	$181 + 8.6j$
Mode 3	$386 + 7.9j$	$386 + 8.0j$	$386 + 7.9j$	$386 + 7.9j$

Table 5.4: Eigenmodes with SS-R1 DECBC model for varying frame size N of the 1D acoustic subdomains (Fig. 5.7).

Mode 1 is the low-frequency, mixed, entropy-acoustic mode that was not captured when ETF was not modeled in the previous Sec. 5.5.1, Fig. 5.9. Interestingly, note that the first two acoustic modes that were stable in that case are now destabilized due to entropy-acoustic feedback.

However, a numerical issue can be observed from Tab. 5.4. All the modes are expected to converge with increasing OC-frame size N, and acoustic Mode 2 and 3 indeed do. However, the entropy mode shows this strange sensitivity to N. The growth rate keeps changing drastically in magnitude and sign with increasing N; and only for certain specific frame sizes the entropic mode was predicted correctly, for instance, $N = 12$.

Figures 5.10 and 5.11 depict Mode1 and Mode2 shapes respectively for different N along with the reference Helm+DECBC analytical solution. Note that the mode shapes are plotted in terms of magnitude and phase of fluctuating total enthalpy (J) and mass-flow-rate (m). Again, while the acoustic mode shapes are accurate, the problem is evident with the entropic mode, particularly in the mass-flow-rate mode shape. As mentioned above, for the particular $N = 12$ case, note that the mode shapes are in excellent agreement with the reference solution.

It is suspected that the erratic behavior of the entropy mode could be due to some unwanted interaction with spurious components/modes present in the matrix $\mathbf{A}^f$ — the global state-space (SS) dynamics matrix resulting after assembling all the SS submodels. Recall from Sec. 2.4 and Fig. 2.12 the various numerical treatments carried out to deal with spurious/unphysical components arising due over-complete nature of OC-frames used for modal expansion of the acoustic subdomains. In the current case, there is no active flame, therefore, $\mathbf{A}_f = \mathbf{A}_a$. After identifying the spurious components with the energy criterion, the solver goes to the step of *artificial damping* of these spurious components (see Fig. 2.12 in Ch. 2). In this treatment, briefly, the $\mathbf{A}_a$ matrix is taken into its spectral space with the help of eigenvalue decomposition, and the a priori flagged spurious modes are artificially damped by setting their growth rates to some arbitrarily chosen large negative rate, D in $(1/s)$. See Sec. 3.5 in C. Laurent thesis [197] for exact implementation details.

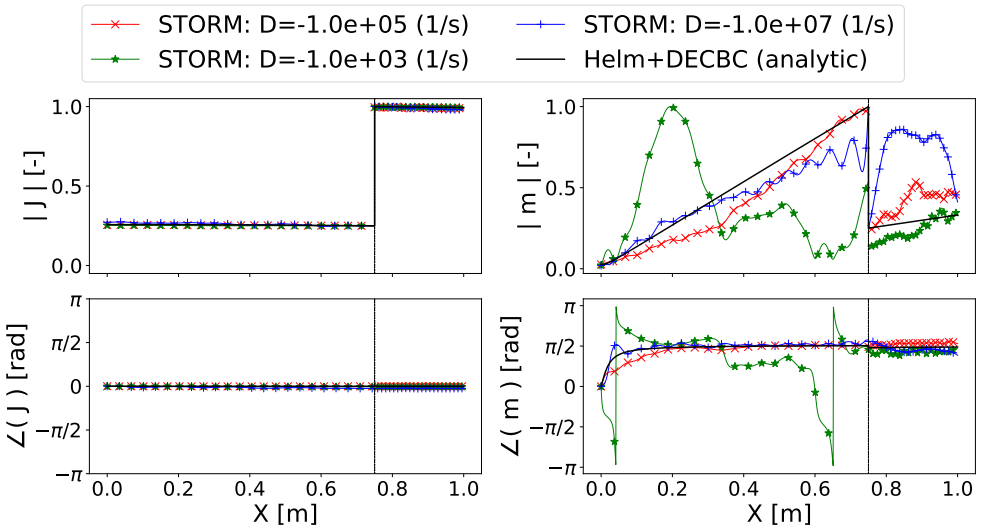

Figure 5.12: Entropy mode with DECBC SS-R1 model for different artificial damping rate of spurious modes.

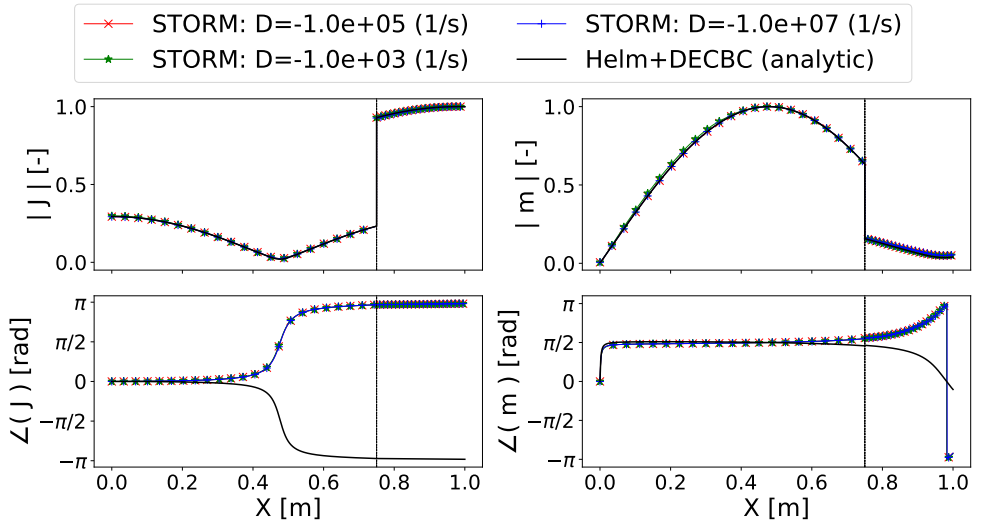

Figure 5.13: Acoustic mode with DECBC SS-R1 model for different artificial damping rate of spurious modes.

The default value set for this numerical parameter is $D = -10^5$ $(1/s)$. From several tests performed in the past, this value worked well for almost all problems. Also, in general, the results were robust to variations of D by a couple of orders of magnitude. An indication of the guess that entropy mode is affected by spurious components is given from the following result. For fixed OC-frame size $N = 50$, the artificial damping rate D is varied. Similar results are obtained yet again. The entropy mode's eigenfrequency and mode shape tend to change drastically with D (Fig.

5.12), however, the result of acoustic modes remain robust (Fig. 5.13).

Several additional tests were performed to determine the root cause of partly correct/incorrect results with SS-R1 and possible ways to rectify the issue. For example:

1. Treating the DECBC network element as *active*, analogous to a flame element, wherein they go through this additional *decoupling (from spurious modes) process* discussed in Sec. 2.4.

2. Splitting the DECBC element into two state-space blocks, where one models the entropy transfer function (ETF), and the other imposes the pure acoustic part of the nozzle impedance condition (Eq. 5.28). (Just another way of implementing the DECBC methodology). Furthermore, the option of treating the ETF block as passive or active (see Sec. 2.4) was also looked at.

The above tests are not detailed further because none of them gave satisfactory results. Overall the results were similar, where the entropy mode continued to be evasive.

Later, the alternate DECBC SS-R2 formulation (Sec. 5.3.3.2) was conceived and tested. This formulation gives good results, as presented in the next subsection.

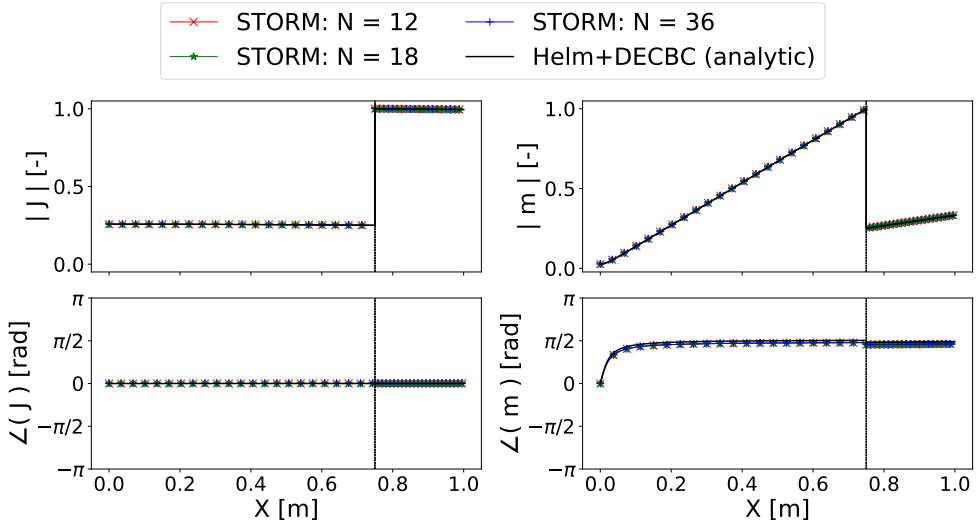

Figure 5.14: Entropy mode $(17 + 0.7j)$ Hz shape with DECBC *SS-R2* model. (Corresponds to the same problem in Fig. 5.10 that was solved with DECBC SS-R1 model.)

5.5.3 Test3: 1D-DECBC Results with SS-R2

The results obtained with DECBC SS-R2 formulation are discussed here. In this case, both entropy and acoustic modes are correctly and consistently predicted in

comparison to reference solution. They are observed to be robust against both, increasing OC-frame sizes of the subdomain and varying artificial damping rate of the spurious modes. For example, the problematic entropy mode obtained with SS-R2 DECBC model for varying OC-frame sizes is shown in Fig. 5.14.

5.5.3.1 Effect of mean-flow Mach number

All the previous results discussed were for very low inlet mean Mach number $M_1 = 0.00625$. Therefore, the next set of results would assess the solutions for increasing mean-flow Mach numbers, modeled *indirectly and partly* by DECBC approach in otherwise *zero-Mach-number* ($M = 0$) STORM network. This subsection will also make use of the LEE reference quasi-analytical solutions [45] (along with Helm + DECBC) for verifying the effect of Mach number. The 1D network configuration (Fig. 5.7) is thus solved for the inlet Mach numbers listed in Tab. 5.3 with DECBC SS-R2 model.

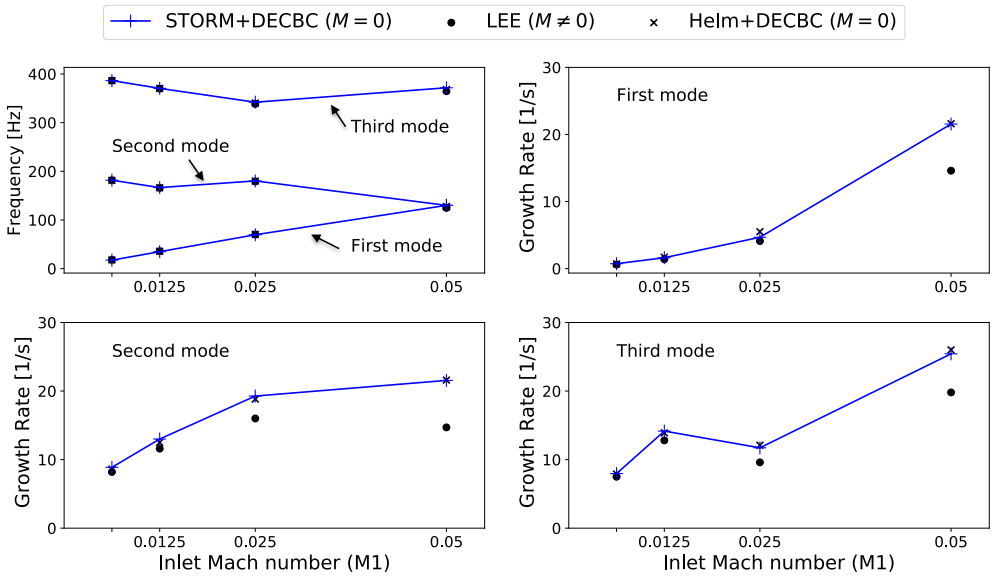

Figure 5.15: First three eigenmodes computed for different inlet mean-flow Mach numbers (M_1) with DECBC *SS-R2* model.

Eigen-frequency results are presented in Fig. 5.15 for various inlet Mach numbers $M1$. The upper left graph show the frequency of the first three eigenmodes, while the other three subplots indicate their respective growth rates.

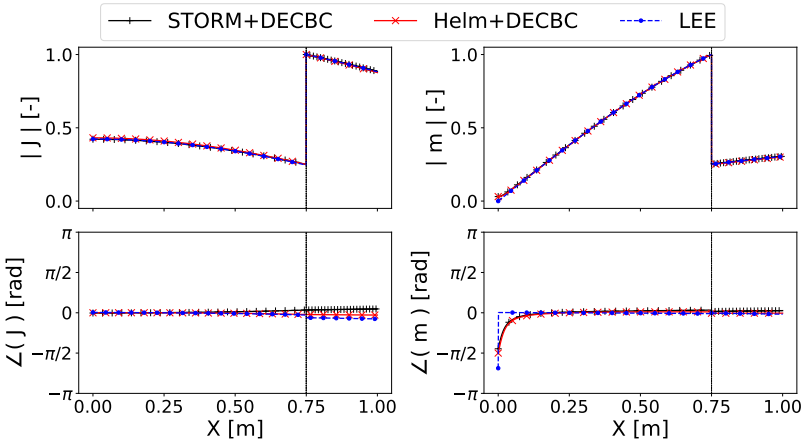

Figure 5.16: First mode shape for $M_1 = 0.025$ from Fig. 5.15.

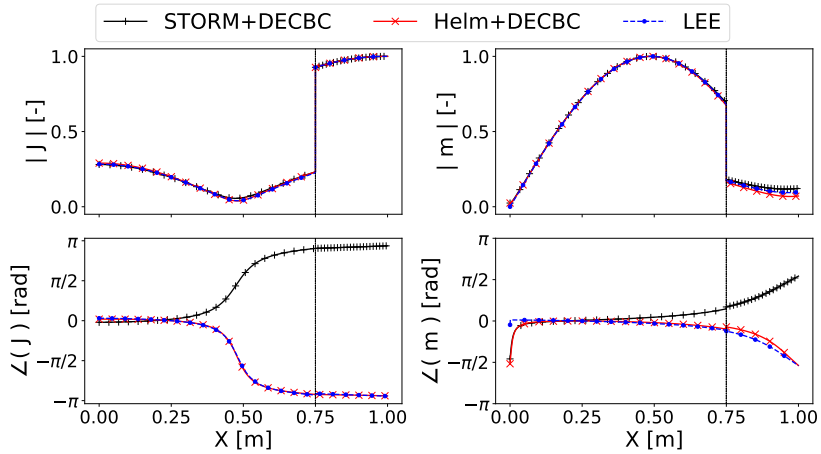

Figure 5.17: Second mode shape for $M_1 = 0.025$ from Fig. 5.15.

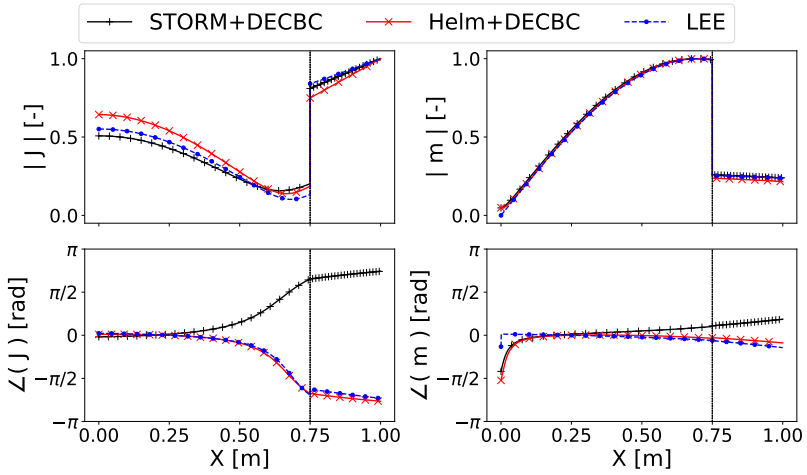

Figure 5.18: First mode shape for $M_1 = 0.05$ from Fig. 5.15.

Since the first low-frequency mode is coupled with convected entropy waves, its frequency in Fig. 5.15 shows a direct correlation and scales according to the mean-flow Mach number (M_1). The second and third mode are mostly of acoustic origin. Their frequency is only slightly modified due to mean-flow effects and also entropy-acoustic feedback, but they do not show a clear trend against increasing Mach number. $M_1 = 0.05$, the first and second modes tend to merge into one mode. Such behavior has also been observed in previous works by Dowling and Stow [140], and Goh and Morgans [292].

The first three modes, all of them are unstable and their growth rate are further increasing with Mach number. For $M1 > 0.025$, unlike frequency, growth rates from STORM, Helm+DECBC methods (with $M = 0$ assumption) start to deviate from reference LEE ($M \neq 0$) as expected at higher Mach numbers. However, the eigenmodes (frequency, growth-rate, mode shape) between (STORM+DECBC) and reference zero-Mach (Helm+DECBC) agree well. See the mode shapes in Figs. (5.14), (5.16)-(5.18). The latter three figures also correspond to mode1 and mode2 at $M_1 = 0.025$ merging into one mode for $M_1 = 0.05$. At $M_1 = 0.05$, the deviation of zero-Mach methods from LEE seems to become evident. It can be anticipated, that at M_1 values beyond the range considered in Fig. 5.15, the discrepancy in results is likely to become significant. This is the inherent limitation of the DECBC methodology. In fact, it stems from the *impedance matching* approach that *indirectly*, and only *partly*, models the mean-flow effect — recall that the Mach number in the computational domain requires to stay in the very-low regime.

5.5.3.2 SS-R1 vs. SS-R2: Non-normality assessment of eigenvalues and eigenvectors of global dynamics matrix $\mathbf{A}^f$

This subsection attempts to diagnose the cause for partially correct/incorrect results observed with the SS-R1 DECBC submodel discussed above (compared to SS-R2) by analyzing the global dynamics matrix $\mathbf{A}^f$. Note that state-space dynamics matrix $\mathbf{A}^{\Omega_z}$ of the DECBC submodel SS-R1 is of size $[4N_{PBFs} \times 4N_{PBFs}]$ and SS-R2 $[(2N_{PBFs} + 2) \times (2N_{PBFs} + 2)]$. Thus, after assembling all the submodels, the $\mathbf{A}^f$ matrix will be larger in the case of SS-R1; for all other parameters taken identical. Whatever the difference in the global state-space model that is influencing the entropy mode for SS-R1 is contained inside the $\mathbf{A}^f$ matrix. Therefore analyzing this matrix should give some information regarding the observed issue.

Specifically, a simple assessment of the *non-normal* character of the matrix $\mathbf{A}^f$, particularly the condition number of eigenvalues and eigenvectors, is carried out. It was suspected that maybe SS-R1 causes $\mathbf{A}^f$ to be more non-normal than SS-R1.

Eigenvalue (Modal) analysis is ubiquitous and a powerful tool in physical sciences (various applications), engineering, and fundamental/applied mathematics. It

works well when the matrices/linear-operators governing the system are normal (or near-normal), i.e., they have a complete set of orthogonal eigenvectors. However, as highlighted by Trefethen and Embree [293], a certain class of problems where systems are governed by *non-normal* matrices/linear-operators could exhibit unexpected behaviors. The authors highlight that conclusions based on eigenvalues alone could be misleading for non-normal matrices / linear operators. See the introductory chapters in [293] for further elaboration on implications of non-normal problems in, e.g., resonance, transient and or asymptotic dynamics, convergence, stability, iterative mathematical algorithms/schemes, etc. Sujith et al. [91] provide a comprehensive and insightful review of non-normal and nonlinear effects specific to thermoacoustic combustion instabilities.

A given matrix $\mathbf{A} \in \mathbb{C}^{n\times n}$, is *normal* if it has a complete set of orthogonal eigenvectors, that is, if it is unitarily diagonalizable: $\mathbf{A} = \mathbf{U}\mathbf{\Lambda}\mathbf{U}^*$. Here, $\mathbf{U}$ is unitary, and $\mathbf{\Lambda}$ is the diagonal matrix of eigenvalues. An equivalent characterization is that $\mathbf{A}$ is normal if it commutes with its adjoint: $\mathbf{A}\mathbf{A}^* = \mathbf{A}^*\mathbf{A}$. Note that in our case, all state-space matrices of sub-models, and thus $\mathbf{A}^f$ are real-valued. However, the eigenvalues and eigenvectors of $\mathbf{A}^f$, of course, can be complex-valued. However, for the discussion of non-normality in this subsection, the subsequent definitions are general and valid for complex matrices.

Now supposing a given matrix $\mathbf{A}$ is diagonalizable but not necessarily normal, and let $\mathbf{V} \in \mathbb{C}^{n\times n}$ denote its *matrix of eigenvectors* of $\mathbf{A}$ such that: $\mathbf{A}\mathbf{V} = \mathbf{V}\mathbf{\Lambda}$ or $\mathbf{A} = \mathbf{V}\mathbf{\Lambda}\mathbf{V}^{-1}$. One common scalar measure of the non-normality of a given matrix is the *condition number* of is its eigenbasis matrix $\mathbf{V}$. For *2-norm* of matrices, the condition number is then defined as [293]:

$$C(\mathbf{V}) = ||\mathbf{V}||_2 \; ||\mathbf{V}^{-1}||_2 = \frac{s_{max}(\mathbf{V})}{s_{min}(\mathbf{V})} \tag{5.49}$$

where, $s_{max}(\mathbf{V})$ and $s_{min}(\mathbf{V})$ are the maximum and minimum singular values of $\mathbf{V}$. In general, $C(\mathbf{V})$ may be any number in the range $1 \leq C(\mathbf{V}) < \infty$, and the value $C(\mathbf{V}) = 1$ when the given matrix $\mathbf{A}$ is exactly normal. The other extreme $C(\mathbf{V}) = \infty$ denotes a $\mathbf{A}$ as *non-diagonalizable or defective* matrix.

However, the condition number of matrix $\mathbf{V}$ only provides an *upper bound* of the condition numbers of the individual eigenvalues of $\mathbf{A}$ (according to Bauer-Fike theorem) [293]. There are several eigenvalues of $\mathbf{A}^f$, many of them spurious/unphysical. Therefore as suggested in [293], a better and more descriptive *scalar measure* is to verify the condition numbers of individual eigenvalues and eigenvectors.

For defining condition number of eigenvalues, the most simple case of a given matrix $\mathbf{A}$ whose eigenvalues $\lambda_1, \lambda_2 \cdots \lambda_n$ are distinct (i.e., simple eigenvalues) is considered. This assumption implies the existence of a full set of left and right

eigenvectors as follows:

$$\mathbf{u}_j^* \mathbf{A} = \lambda_j \mathbf{u}_j^*, \qquad \mathbf{A}\mathbf{v}_j = \lambda_j \mathbf{v}_j \tag{5.50}$$

for $j = 1, 2, \cdots, n$. From principles of perturbation theory (see Chapter 52, in [293]) the condition number definition of an eigenvalue λ_j can be defined as:

$$C(\lambda_j) = \frac{\|\mathbf{u}_j\| \, \|\mathbf{v}_j\|}{\left|\mathbf{u}_j^* \mathbf{v}_j\right|} \tag{5.51}$$

Cauchy-Schwarz inequality $\left|\mathbf{u}_j^* \mathbf{v}_j\right| \leq \|\mathbf{u}_j\| \, \|\mathbf{v}_j\|$ tells that $C(\lambda_j) \geq 1$. Therefore when $C(\lambda_j) = 1$ when the left $\mathbf{u}^*{}_j$ and right eigenvectors are same or colinear and the λ_j is a *normal* eigenvalue.

Previous subsections described how the results with SS-R1 DECBC formulation, particularly the entropy mode, showed sensitivity to the frame size N of the subdomains and the artificial damping rate parameter D (for spurious modes). Since artificial damping treatment alters the $\mathbf{A}^f$ matrix entries, the idea here is to check the eigenvalue condition numbers of individual entropy and acoustic modes before and after the treatment for given frame sizes. The motivation for this assessment is described in the following two points:

- *SS-R1 case:* Irrespective of frame size, in general, the complex frequency and mode shape of entropy (17 Hz) and acoustic modes are both observed to be not accurate before artificial damping. It is only after applying the artificial damping treatment that the acoustic eigenmode result is correct, but entropy mode remains an issue. An exception to this general observation is the $N = 12$ case — for this frame size, both the entropy/acoustic modes are correct before/after artificial damping.

- *SS-R2 case:* For this formulation, irrespective of frame size, the eigenmodes are observed to be correct before/after artificial damping. In other words, the physical modes are robust to any favorable/unfavorable influence of artificial damping treatment and the value of D itself.

Next, in Tab. 5.5, the *reciprocal of eigenvalue condition numbers* (RCONDE) of entropy mode (∼17 Hz) and first acoustic mode (∼181 Hz) are computed (before/after) artificial damping treatment. While RCONDE is a measure of non-normality of the specific eigenvalue, from the perturbation theory point of view, it also represents the sensitivity of eigenvalues to "small" matrix perturbations.

Similarly, corresponding *reciprocal condition number* (or sensitivity) *of right-eigenvector* $\mathbf{v}_j$ (RCONDV) are computed and listed in Tab. 5.6. It is interesting

Frame Size (N)	Eigenmode	RCONDE SS-R1	RCONDE SS-R2
N = 12	Mode1 ∼17 Hz	(6.38E-11 / 1.16E-07)	(3.42E-04 / 3.10E-02)
	Mode2 ∼181 Hz	(8.57E-10 / 2.02E-06)	(5.44E-05 / 4.60E-03)
N = 36	Mode1 ∼17 Hz	(7.28E-13 / 7.10E-10)	(2.20E-04 / 6.70E-03)
	Mode2 ∼181 Hz	(1.24E-11 / 1.40E-08)	(4.96E-05 / 1.80E-03)

Table 5.5: Reciprocal condition number (or sensitivity) of *eigenvalues*, RCONDE, of global dynamics matrix $\mathbf{A}^f$ (before / after) the numerical treatment of artificial damping of spurious modes.

Frame Size (N)	Eigenmode	RCONDV SS-R1	RCONDV SS-R2
N = 12	Mode1 ∼17 Hz	(7.13E-09 / 1.92E-05)	(3.38E-02 / 3.88)
	Mode2 ∼181 Hz	(1.84E-07 / 7.36E-04)	(1.81E-02 / 8.90E-01)
N = 36	Mode1 ∼17 Hz	(1.30E-10 / 1.90E-07)	(6.95E-03 / 4.21E-01)
	Mode2 ∼181 Hz	(3.14E-09 / 2.21E-06)	(1.54E-02 / 3.44E-01)

Table 5.6: Reciprocal condition number (or sensitivity) of *right-eigenvectors*, RCONDV, of global dynamics matrix $\mathbf{A}^f$ (before / after) the numerical treatment of artificial damping of spurious modes.

to look at RCONDV as well because the OC-frame *modal expansion coefficients* [1]of all the acoustic subdomains are contained inside the eigenvector. The final global system mode shape is obtained by reconstructing its part in each subdomain from their respective OC-frame and coefficients. Therefore, the RCONDV number, in a way, is a scalar measure of ill-conditioning of these coefficients depending upon factors such as: state-space formulation SS-R1 or SS-R2, OC-frame-size N, mode type (acoustic or mixed entropic-acoustic), artificial damping treatment; and might throw some light on the strange mode-shapes observed in Figs. 5.10, 5.12.

[1] $\dot{\Gamma}_n(t), \Gamma_n(t)$ respectively in pressure and velocity modal expansion on OC-frame - see Eqs. 2.8, 2.9 from Ch. 2. Recall that the global state-space dynamics equation is defined in physical space (or time-domain): $\dot{\mathbf{X}} = \mathbf{A^f X}$, where $\mathbf{X}$ is the state-vector containing $(\dot{\Gamma}_n(t), \Gamma(t))$ coefficients. In frequency-domain, when eigenvalues and eigenvectors of $\mathbf{A}^f$ are determined, a eigenvector then contains frequency-domain counterparts of the modal expansion coefficients $(\gamma_n(\omega), \gamma_n(\omega)/j\omega)$ for pressure and velocity expansions respectively. The pressure mode in a subdomain then would reconstructed as $\hat{p}(\vec{x}, \omega) = \sum_n \gamma_n(\omega)\phi_n(\vec{x})$, where $\phi_n(\vec{x})$ is the OC-frame of the subdomain. See Sec. 3.2 of C. Laurent thesis [197] for frequency-domain equivalent or predecessor of ODE (Eq. 2.14) governing these coefficients.

Following inferences can be drawn from both the RCOND numbers in the above tables:

- Overall, comparing SS-R1 to SS-R2, it is quite clear that SS-R1 formulation leads to significantly ill-conditioned eigenvalues and eigenvectors. This probably is not good news considering that from two equivalent state-space representations (for a given problem), one can be significantly ill-conditioned than the other. If it is due to choice and number of the state variables, then obviously, *minimal* state-space realizations should be sought.

- Artificial damping treatment improves the conditioning of eigenvalues and vectors for this problem. It may explain the observed improvement in the accuracy of SS-R1 results post-treatment (as discussed in the bullet points above). However, it needs to be seen from other problems if such better conditioning is always attained.

- *Comparing exceptional N=12 case to N=36 for SS-R1:* The correct entropic mode1 observed for N=12 could be linked to both better (/ after) RCOND values (about two orders of magnitude) than N=36. Nevertheless, note that this is the case for acoustic mode2 as well. Also, both RCOND values of mode2 are more or less comparable to mode1; and are not significantly different for mode2 to be always predicted correctly. Hence, concluding that the issue with entropy mode1 predictions is entirely due to poor conditioning may not be justified.

In summary, the above scalar metrics (condition numbers) of eigenvalues and eigenvectors investigated provide some insights but do not clearly distinguish or help reason the strange results from one DECBC state-space compared to another equivalent submodel. A more systematic and comprehensive matrix analysis could help figure out the root cause of the problem with the SS-R1 formulation. Also, one clear difference is the choice and number of state variables. Maybe surveying the state-space theory from controls and dynamical systems literature to investigate whether or not the choice of state variables and their number (from multiple equivalent possibilities) should affect results shall be interesting and useful. The question that needs to be addressed is whether a minimal state-space realization is always necessary.

5.6 Conclusions and Perspectives

The chapter recalled and briefly described the entropy-acoustic feedback mechanism arising from indirect entropy combustion noise generated from the acceleration of

convected entropy perturbation waves (hot-spots) through nozzle or turbine stages downstream of the combustor. The acoustic waves generated can form a closed-loop feedback cycle with flow/flame in the combustor leading to self-sustained low-frequency mixed entropy-acoustic instabilities.

STORM low-order network tool inherently involves zero-Mach-number mean flow assumption just like FEM Helmholtz solvers in the description of the acoustics. Consequently, neither the mean flow effects are modeled, nor the convected entropy waves are present (contrary to what would have been in a domain whose acoustics is described with Linearized-Euler-Equations (LEE)).

A physical modeling strategy to indirectly account for mean-flow effects, the entropy waves, and entropy-acoustic coupling was proposed and employed by Motheau et al. [45, 46] in the context of Helmholtz solvers. The idea was to truncate the domain by removing the high-mean-speed downstream element (nozzle) and matching its equivalent impedance on the boundary of the low-mean-speed computational domain approximated as a zero-Mach domain. At the same time, the production of entropy fluctuations, its propagation by convection, and coupling with the acoustic field are realized with the help of entropy-transfer-functions (ETF). Together this methodology yields a special type of acoustic boundary condition *Delayed Entropy-coupled Boundary Condition* (DECBC). When applied, DECBC helps predict the low-frequency mixed stable/unstable modes and the influence of entropy-acoustic feedback on classic thermoacoustic modes.

This chapter implemented the DECBC methodology in the STORM's modal-expansion, state-space (SS) network framework. A state-space submodel for DECBC representing an impedance network element was developed that modeled the entire entropy-acoustic feedback mechanism. A simple analytically tractable 1D test case from [45] was tested with STORM. Results were validated with analytical solution from two reference methods: LEE ($M \neq 0$) and Helmholtz equation ($M = 0$) along with DECBC (Helm+DECBC).

Two slightly different but equivalent state-space realizations of DECBC (SS-R1 and SS-R2) were detailed and discussed. The SS-R1 formulation gave only partially correct results. The standard thermoacoustic modes (frequency, growth rates, and mode shapes) were correctly predicted, but not the low-frequency mixed entropy-acoustic mode was in general. On the other hand, the SS-R2 DECBC formulation yielded expected results. A basic numerical analysis/assessment of condition numbers of the eigenvalues and eigenvectors of the global state-space dynamics matrix $\mathbf{A}^f$ shed some light on the strange results observed with SS-R1. Since state-space models for a given problem need not be unique, another question that surfaces from the results observed is whether seeking a minimal state-space realization is always necessary. This aspect needs further investigation and should be noted in future modeling efforts.

Chapter 6

Euler-Lagrange (EL) LES Modeling of Spray Flames

Contents

6.1 Physical Processes in Spray Combustion 169
6.2 Spray Combustion LES: Models and Governing Equations 174
6.2.1 Euler-Lagrange LES Formalism 174
6.2.2 FIM-UR Injection Model 177
6.2.3 Liquid-Wall Interaction Model (Slip vs. Film Treatment) . . 179
6.2.4 Droplet Drag Model 182
6.2.5 Droplet Evaporation Model 183
6.2.6 Chemical Kinetics Modeling 186
6.2.7 Thickened Flame Turbulent Combustion Model (TFLES) . . 188
6.2.8 Numerical Scheme and Boundary Conditions 190

Part-2 of the manuscript begins with this chapter introducing two-phase spray combustion physics and the modeling challenges it poses. The specific models employed for the simulations performed in this work are presented.

6.1 Physical Processes in Spray Combustion

Modeling and simulation of two-phase reacting flow present a challenging multi-physics, multi-scale problem on top of already complex enough turbulent flow. Excellent and seminal literature, particularly on the subject of spray combustion modeling is available: Sirignano [59, 295], Lefebvre et al. [58, 2], Aggarwal [296, 297], Jenny et al. [298], Masri [299], in addition to other references cited in the chapter. A few selected research entries reviewing/developing the modeling and simulation of turbulent multi-phase flows more generally with or without reactions that are worth mentioning: Crowe et al. [300], Fox [301], Gorokhovski and Herrmann [302], Subramaniam [303], Desjardins, Le Chenadec, Pitsch and others [304, 305, 306, 307, 308, 309].

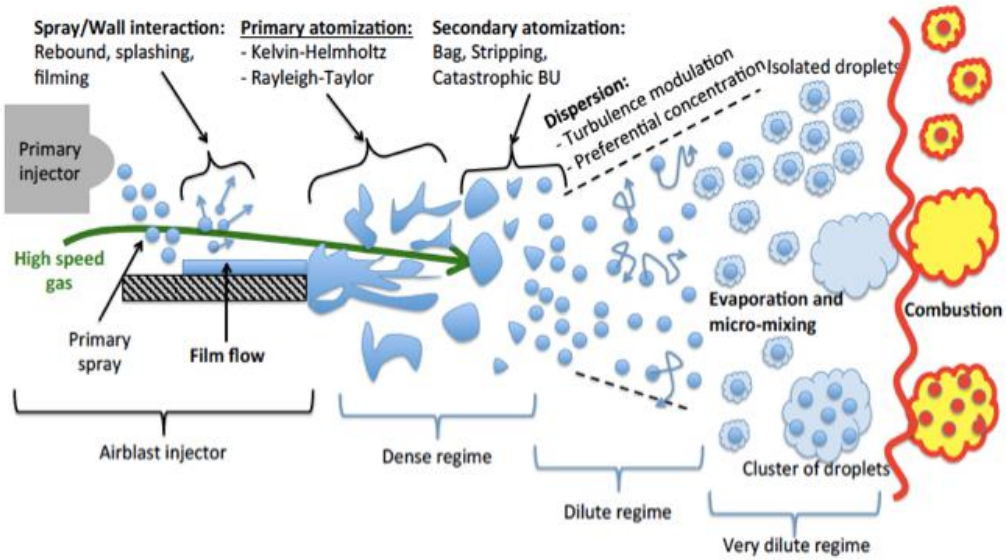

Figure 6.1: An overview of physical processes in spray combustion. Figure reproduced from [294]

This section aims to give a brief introduction and phenomenological description of several physical processes involved in spray combustion accompanied by a representative schematic in Fig. 6.1. More in-depth background on the physics, details of relevant theories, a survey of modeling state-of-the-art, AVBP code implementations, etc., can be found in the latest Ph.D. theses at CERFACS (cited below) dedicated to the specific aspects of spray combustion as listed below.

- *Injection:* Many gas turbine combustors employ air-blast pressure-swirled atomizers that inject liquid fuel under high-pressure as a swirling hollow cone spray [2, 58]. The FIM-UR approach [310], detailed in the following Sec. 6.2.2, will explain a methodology that models the injection of liquid fuel in the computational domain.

  (CERFACS theses: Senoner J. M. (2010) [311], Sanjosé (2009) [312])

- *Liquid-Wall Interaction:* As soon as the liquid is injected into a strongly swirling airflow under pressure, the atomization process is initiated. To make it compact and to enhance the quality of atomization and subsequent fuel-air mixing, the aero-engine air-blast injectors typically consist of a *pre-filming* surface as depicted in Fig. 6.1. The liquid fuel impinges on this surface and, depending upon the wall temperature, liquid-jet speed, and direction, leads to the following phenomena: (i) *Filming:* Majority of the liquid sticks, accumulating on the surface as a thin film, and moves along it with the bulk flow. (ii) *Splash:* A larger droplet bounces back from the surface but is also

split into several smaller droplets. (iii) *Rebound:* The droplets bounce back without disintegrating.

Modeling of this complex liquid-wall interaction, particularly the filming on the wall and its dynamic behavior in response to acoustic oscillations, is at the core of thermoacoustic instability prediction as demonstrated by Lo Schiavo et al. [60] and reviewed in the following chapter. Sec. 6.2.3 will explain a model that tackles the formation of a film on a wall.

(CERFACS theses: Chaussonnet G. (2014) [294], Lafrate M. N., (2016) [313])

- *Atomization:* On the prefilmer edge (or the injector lip), the liquid fragments undergo primary/edge atomization [314]. The high strain between the injected liquid/gas interface cause Kelvin-Helmholtz, Rayleigh-Taylor type of hydrodynamic instabilities, leading to liquid breakup into smaller pockets. In secondary atomization, the fuel pockets/ligaments further break down into a cloud of fine droplets due to aerodynamic forces. Breakup continues until counter-balanced by surface tension that upholds the droplets from further disintegration sustaining its shape and surface.

  (CERFACS theses: Carmona J. (2021) [315], Chaussonnet G. (2014) [294])

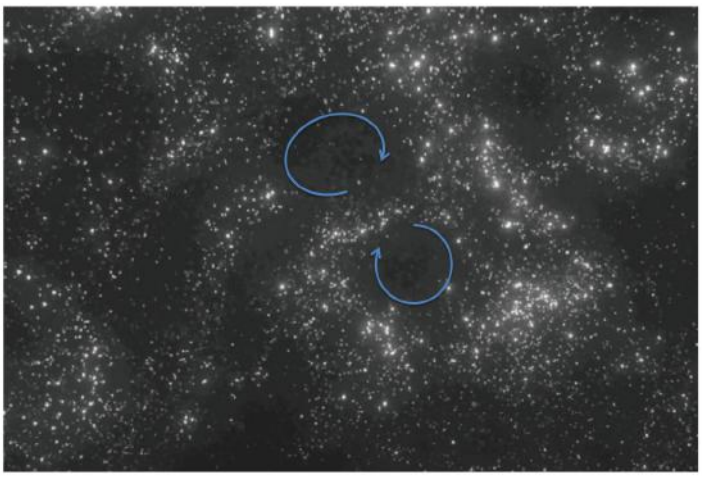

Figure 6.2: Laser-sheet image of particles in homogenous turbulence illustrating inertial clustering. From [316].

- *Dispersion:* The liquid fuel atomization into fine droplets (the dispersed phase) occurs while being simultaneously transported by the bulk turbulent gaseous flow (carrier phase). Thus, turbulence-spray interaction is an essential physical phenomenon that must be modeled. It is achieved with the Euler-Lagrange LES (EL-LES) method (a.k.a. Discrete Particle Simulation: LES-DPS) in

the current work. Here, the Lagrangian droplets/particles are tracked and coupled with the resolved Eulerian gaseous flow field for which they act as point sources. Upcoming Sec. 6.2.1 will detail the Euler-Lagrange formalism.

Depending upon the droplet inertia (mass and size) and turbulence scales, *preferential segregation/inertial clustering* of particles is usually observed as illustrated in the experimental image in Fig. 6.2. Most droplets tend to concentrate in the shear layers between eddies (or regions of low vorticity and high strain). A consequence of this is the heterogeneous distribution of fuel as it approaches the flame's preheating zone and starts to vaporize simultaneously.

(CERFACS thesis: Senoner J. M. (2010) [311], Jaegle F. (2009) [317])

- *Evaporation and Thermo-chemistry:* All fuel droplets are vaporized before they can undergo combustion. This is true either when the bulk of the fuel is vaporized upstream of the reaction zone, forming a vapor cloud reaching the reaction zone while mixing with the air (partially premixed), or even when it is at the level of individual droplet burning via diffusion (non-premixed). In addition to the droplet size distribution and density in the flow (e.g., dilute/very-dilute regimes - Fig. 6.1), the evaporation process is further complicated by the thermo-chemistry of fuel. Kerosene, a heavy hydrocarbon fuel, comprises several components of considerably varying volatility, i.e., vaporization time scales. Therefore, developing multi-component evaporation models and reduced, computationally efficient, yet reliable surrogate chemical kinetic mechanisms is essential: for accurate combustion simulations, predictions of pollutant emissions, transient simulations of ignition, extinction, etc.

  (CERFACS theses: Sierra Sànchez P. (2012) [318], Shastry V. (2022) [319], Cazeres Q. (2021) [320].)

- *Spray Combustion:* The above points suggest a complex and strongly coupled spray, turbulence, and chemistry interaction. Governed by droplet size distribution, density, time scales of evaporation, mixing, chemistry, and the distance to the reaction zone, different types of combustion regimes are possible, as described below and indicated in Fig. 6.3 [61, 321, 322]:

  (i) *Prevaporized Regime 1 :* In this case, the droplets evaporate completely before the vapor-air mixture reaches the reaction zone. The resulting flame acts as a gaseous flame and is uncorrelated to the liquid phase.

  (ii) *Homogeneous Regime 2:* This case is observed when the pre-vaporizing levels are not high as in the previous case, the liquid concentration is dense, then a thick reaction zone is observed (Fig. 6.3). Most droplets evaporate and

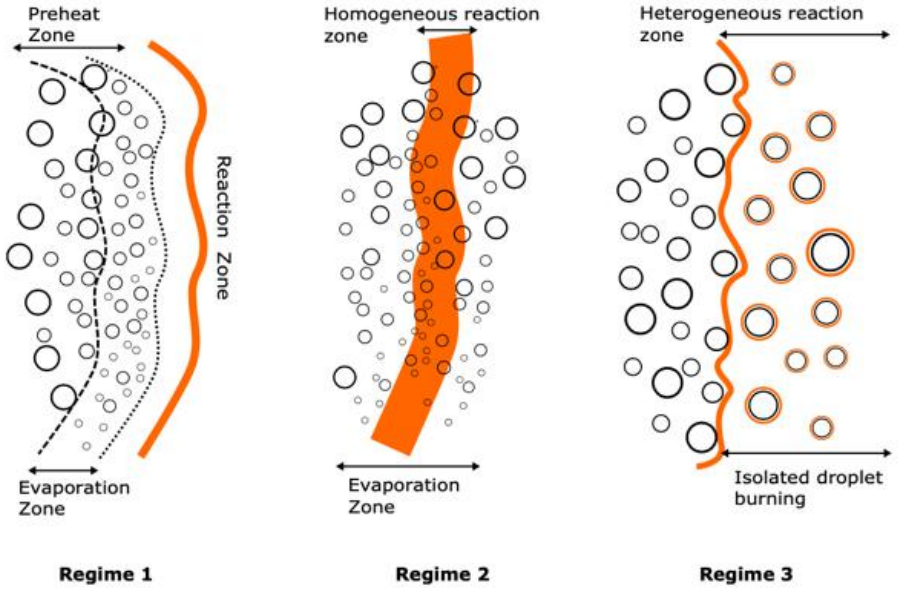

Figure 6.3: Two-phase combustion regimes. Adapted from [324]. See also Reveillon and Vervisch [67] for other ways on defining spray combustion regimes.

provide fuel vapor before and or inside the flame zone to sustain the gaseous reactions.

(iii) *Heterogenous Regime 3:* Is characterized by a strong interaction between the liquid spray and flame. The flame is located in between the spray. Many fuel droplets cross the flame front and burn in groups (clusters) of droplets with a flame envelope around them or even as individual droplets.

Complete pre-vaporization and perfect premixing, though desired, is rarely achieved in reality. Due to the fuel-air mixture stratification, combustion occurs in a partially-premixed regime. Lean/rich, premixed/diffusion regions co-exist locally in the reaction zone of the combustion chamber. Identification of these regimes is critical for high-fidelity modeling and simulation of spray flames that exhibit such complex structure - further discussion in following Sec. 6.2.7 on combustion modeling.

(CERFACS theses: Paulhiac D. (2015) [323], Rochette B. (2019) [324].)

- *Flame Ignition and Stabilization:* Besides thermoacoustic oscillations, unsteady combustion behavior of flame blowout, flashback, and ignition are serious operational hazards [1, 7, 325]. Indeed if a combustor is extinguished, fast ignition, light-around, and stabilization of the flames in a multi-burner annular combustor is a critical design requirement for aero-engines. Devel-

oping capabilities of two-phase combustion LES to simulate these transient behaviors are therefore essential.

(CERFACS theses: Collin-Bastiani F. (2019) [326], Rochette B. (2019) [324])

6.2 Spray Combustion LES: Models and Governing Equations

This section will detail the specific models employed in the current work, highlighting the inherent assumptions, hypotheses, and known limitations. Combustion LES of gaseous fuel is relatively mature whether it is premixed/non-premixed/partially-premixed. From tackling turbulence-chemistry interaction, prediction of pollutant emissions to simulations of unsteady phenomena such as instabilities, ignition, blowout, and is well documented - see [13, 108, 115, 327, 114, 11, 328] and references therein. The modeling of multi-species, reacting, gaseous carrier phase is only briefly mentioned to keep this presentation concise. At the same time, the emphasis is put on summarizing the *two-phase* coupling/interaction models in the following subsections.

6.2.1 Euler-Lagrange LES Formalism

LES of the SICCA-spray burner configuration is performed using the AVBP code, which has been under continuous development at CERFACS[1] for over two decades now. It is a massively parallel code and solves the three-dimensional filtered, fully compressible, reacting multi-species Navier-Stokes equations on unstructured/hybrid grids.

6.2.1.1 Eulerian Gas-Phase

The gas-phase flow and turbulence modeling is based on Large-Eddy-Simulation technique [13, 115, 329, 330], where the main idea is to resolve the large scale eddies in the flow which contain most of the energy, while the very small scales are represented by *subgrid-scale* (SGS) model. The conservation equations of mass (along with multi-species transport equations), momementum and energy [13] are *spatially filtered* - an operation that is directly related to the mesh resolution. As the density is variable in reacting flow, to avoid additional terms, mass-weighted *Favre*-filtered quantities are introduced as $\tilde{g} = \overline{\rho g}/\bar{\rho}$, where $\bar{\rho}$ is the resolved (filtered) density. For any physical quantity g (density, velocity components, scalars etc.), the Favre- filtered component $\tilde{g}$ is resolved in the numerical simulation while the *subgrid scales* $g' = g - \tilde{g}$ are modeled.

[1] AVBP website: www.cerfacs.fr/avbp7x

The core difficulty arising in LES is that the spatial filtering of the equations leads to unresolved subgrid-scale (SGS) terms such as the *Reynolds stresses*, the turbulent diffusion of species, and energy. These terms need to be modeled as detailed in [13] by employing a subgrid-scale (SGS) model for closure of Reynolds stresses by introducing *turbulent kinematic viscosity* ν_t. The latter two unresolved turbulent (SGS) species and heat fluxes are closed by invoking gradient transport assumption, where turbulent Schmidt Sc_t and Prandtl Pr_t number are introduced, respectively. These dimensionless numbers correlate turbulent (SGS) species and thermal diffusivity to turbulent momentum diffusion given by ν_t. In this work, the ν_t is determined by employing the SGS model proposed by Nicoud et al. [331].

In summary, for the Eulerian gas phase, AVBP solves the set of compressible, Navier-Stokes filtered equations as follows [13, 60]:

- **Mass:**

$$\frac{D}{Dt}(\bar{\rho}) = 0 \tag{6.1}$$

- **Species:**

$$\frac{D}{Dt}\left(\bar{\rho}\tilde{Y}_k\right) = -\nabla\cdot\left(\bar{\mathbf{j}}_k + \bar{\mathbf{j}}_k^{\text{sgs}}\right) + \bar{\dot{S}}_{Y_k} \quad , \; k = 1, N_S \tag{6.2}$$

- **Momentum:**

$$\frac{D}{Dt}(\bar{\rho}\tilde{\mathbf{u}}) = -\nabla\cdot\left(\bar{p}\mathbf{I} - \overline{\mathbf{T}} - \overline{\mathbf{T}}^{\text{sgs}}\right) + \bar{\dot{\mathbf{S}}}_M \tag{6.3}$$

- **Energy:**

$$\frac{D}{Dt}(\bar{\rho}E) = -\nabla\cdot\left(\overline{\mathbf{u}\cdot\bar{p}\mathbf{I} - \overline{\mathbf{T}}} + \overline{\mathbf{q}} + \overline{\mathbf{q}}^{\text{sgs}}\right) + \bar{\dot{S}}_E \tag{6.4}$$

where, $\frac{D}{Dt} = \frac{\partial}{\partial t} + \tilde{\mathbf{u}}\cdot\nabla$ is the total derivative, E is the total energy (internal + kinetic), $\mathbf{I}$ is identity matrix, $\bar{\dot{S}}_{Y_k}$, $\bar{\dot{\mathbf{S}}}_M$, $\bar{\dot{S}}_E$ are source-terms appearing due to coupling with liquid-phase Lagrangian particles (discussed in next Sec. 6.2.1.2). $\bar{\mathbf{T}}$ is the filtered (or resolved) stress tensor, $\bar{\mathbf{j}}_k$ is the species mass-diffusion flux, while $\bar{\mathbf{q}}$ denotes the energy fluxes due to differential diffusion of species and temperature. The unresolved turbulent (SGS) terms are closed as:

$$\overline{\mathbf{T}}^{\text{sgs}} = \bar{\rho}(\widetilde{\mathbf{u}:\mathbf{u}} - \tilde{\mathbf{u}}:\tilde{\mathbf{u}}) \simeq 2\bar{\rho}\nu_t\left(\tilde{\mathbf{S}} - \frac{1}{3}\,\mathrm{tr}(\tilde{\mathbf{S}})\mathbf{I}\right) \tag{6.5}$$

$$\bar{\mathbf{j}}_k^{\text{sgs}} = \bar{\rho}\left(\widetilde{Y_k\mathbf{u}} - \tilde{Y}_k\tilde{\mathbf{u}}\right) \simeq 2\bar{\rho}\left(D_t\frac{W_k}{W}\nabla\tilde{X}_k - \tilde{Y}_k\mathbf{V}^{\mathbf{c}}\right) \tag{6.6}$$

$$\overline{\mathbf{q}}^{\text{sgs}} = \bar{\rho}(\widetilde{E\mathbf{u}} - \tilde{E}\tilde{\mathbf{u}}) \simeq -\lambda_t\nabla\tilde{T} + \sum_{k=1}^{N_s}\bar{\mathbf{j}}_k^{\text{sgs}}\tilde{h}_{s,k} \tag{6.7}$$

Turbulent Schmidt Sc_t and Prandtl Pr_t numbers are imposed to be 0.6. D_t and λ_t in above relations then come from Sc_t and Pr_t definitions as: $D_t = \nu_t/\mathsf{Sc}_t$ and $\lambda_t = \bar{\rho}\nu_t\bar{c}_p/\mathsf{Pr}_t$.

6.2.1.2 Lagrangian Liquid-Phase

The previous subsection described the LES equations of multi-species reactive gaseous flow - the carrier phase. When a liquid phase is introduced in the form of a spray, additional equations that track its evolution are presented here.

The fuel spray is modeled as a cloud of discrete, rigid, tiny (less than Kolmogorov's length scale) Lagrangian droplets/particles - the dispersed phase, that are transported by the carrier phase. The evolution of the position, velocity, and temperature of droplets is tracked through a *two-way coupling* between the dispersed and carrier phase. The droplets act as spatial point sources that appear in the gas LES species, momentum, and energy equations above (detailed in the following Sec. 6.2.1.3). On the other hand, it is *presumed* that *only drag force* is exerted by the gas on the particles that is responsible for their motion [311]. Thus, the basic set of equations governing the evolution of Lagrangian particles are given as follows [311, 60]:

$$\frac{d}{dt}\mathbf{x}_p = \mathbf{u}_p \tag{6.8}$$

$$\frac{d}{dt}(m_p\mathbf{u}_p) = \mathbf{F}_p \tag{6.9}$$

$$\frac{d}{dt}m_p = \dot{m}_p \tag{6.10}$$

$$\frac{d(m_p h_{s,p})}{dt} = \dot{\Phi}_p \tag{6.11}$$

where, $\mathbf{x}_p$, $\mathbf{u}_p$ is the particle's position and velocity in the computational domain. $\mathbf{F}_p$ is the *drag force* on the particle (presented in following Sec. 6.2.4). m_p is the mass of the particle, that evolves in Eq. (6.10) *only due to evaporation*, and other effects such as inter-particle collisions, splitting/coalescence of droplets [300] are neglected [311, 60]. $\dot{\Phi}_p$ is the total heat transfer from the gas to the particle, part of which increases the liquid particle's sensible enthalpy (or temperature T_p in other words) and part of it overcomes latent heat of vaporization (L_v) for phase change. Evaporation process and model discussed in following Sec. 6.2.5.

6.2.1.3 Coupling between gas and liquid phase

In the two-way coupling between Eulerian and Lagrangian phases, the coupling from liquid to gas is achieved through the source terms in mass, momentum, and energy Eqs. (6.2)-(6.4) above. There can be multiple Lagrangian particles inside a cell of a computational grid. Each of these point sources is individually accounted for by distributing their contribution to the nearest Eulerian nodes after assigning proper weight, as shown in Fig. 6.4.

For a particle inside a cell with N_v vertices, the projection weights for each vertex, represented by ψ_{p,v_k}, are inversely proportional to the distance d_k from the

droplet as depicted in Fig. 6.4, and is given as:

$$\psi_{p,v_k} = \frac{1/d_k}{\sum_{N_v}^{k=1} 1/d_k} \tag{6.12}$$

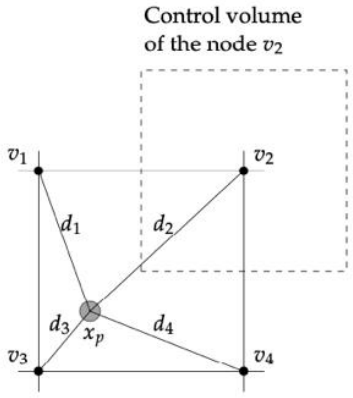

Figure 6.4: Projection of source terms from a Lagrangian particle inside a cell to nearest Eulerian grid vertices [324].

For $p = 1, N_p$ particles inside a cell of volume ΔV, the species, momentum and energy source terms in the gas-phase at each vertex is then obtained by weighted contribution from each particle:

$$\overline{\dot{S}}_{Y_F} = -\frac{1}{\Delta V}\sum_{p=1}^{N_p} \psi_p \left(\dot{m}_p\right) \tag{6.13}$$

$$\overline{\dot{\mathbf{S}}}_M = -\frac{1}{\Delta V}\sum_{p=1}^{N_p} \psi_p \left(\dot{m}_p \mathbf{u}_p + \mathbf{F}_p\right) \tag{6.14}$$

$$\overline{\dot{S}}_E = -\frac{1}{\Delta V}\sum_{p=1}^{N_p} \psi_p \left(\dot{\Phi}_p - \dot{m}_p h_{s.F}\left(T_p\right) + \frac{1}{2}\dot{m}_p \mathbf{u}_p^2 + \mathbf{f}_p \cdot \mathbf{u}_p\right) \tag{6.15}$$

The source terms in above equations are obtained from *macro-scopic models* detailed in following subsections: drag force on the particle $\mathbf{F_p}$ in Sec. 6.2.4 and $\dot{m}_p$ and $\dot{\Phi}_p$ from the evaporation model in Sec. 6.2.5.

6.2.2 FIM-UR Injection Model

Resolving fuel atomization explicitly in highly parallel LES is quite complex from modeling, implementation standpoint; is computationally expensive, and is a topic of active research and development in general. For instance, see these recent works by: CERFACS (Carmona et al. [332, 315], Chaussonnet et al. [314, 333]), CORIA

(Janodet et al. [334], Mukundan et al. [335], Palanti et al. [336], Ahmed et al. [337], Anez et al. [338]), Kurose group (Wen et al. [339, 340], Pillai et al. [63]), and Shinjo et al. [341].

In the current work, in line with Lo Schiavo et al. [60, 201], the atomization process is not resolved explicitly but a *semi-empirical* injection model FIM-UR [310] (*Fuel Injection Method by Upstream Reconstruction*) for pressure-swirled atomizer is used. It is applied as a Lagrangian liquid-phase boundary condition on the atomizer orifice surface of the injector. The working principle of the methodology is briefly described (qualitatively) here in this subsection. Complete details can be found in Sanjosé et al. [310].

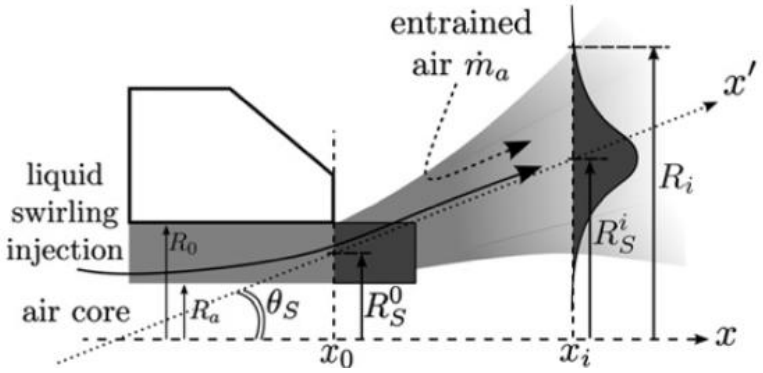

Figure 6.5: The FIM-UR methodology schematic for pressure-swirled atomizers. The model directly injects the Lagrangian fuel particles with prescribed spray properties from the orifice boundary. Adapted from[310].

Fig. 6.5 highlights a part of the pressure-swirl atomizer geometry, particularly its discharge orifice and the liquid injection, undergoing atomization and forming a spray. The grey shaded area is the swirling liquid around an air core inside the atomizer and denotes the hollow-cone spray formed downstream. The spray formed at the exit of the atomizer is supposed to be axisymmetric around the (Ox) axis. A local cylindrical coordinate system (r, θ, x) is considered here. The discharge orifice at $x = x_0$ is the injection plane and the computational boundary.

The *half-spray angle* θ_S is defined as the angle between the main spray direction, along (Ox′) axis, and the symmetry axis (Ox). The radial position along the main spray direction at the abscissa x is written as $R_S(x) = R_S^0 + (x - x_0)tan(\theta_S)$ where R_S^0 is the mean radial position of the cylindrical liquid film at $x = x_0$ plane. Entrainment of the air in the hollow-cone spray causes the liquid-volume fraction α_l to evolve along the spray direction, and it is assumed to be in the form of a Gaussian distribution around (Ox′) axis as indicated.

In the Euler-Lagrange (EL) formalism, the FIM-UR model directly injects La-

grangian droplets into the computational domain, considering that the liquid is already atomized and the spray is fully developed and is in the dilute regime (Fig. 6.1). A single mean droplet diameter of the spray d_p (for mono-disperse sprays) or a statistical droplet size distribution in form probability density function (pdf) (for polydisperse spray), with a characteristic, mean d_p^m and Sauter-Mean-Diameter (SMD) d_p^{SMD}, is prescribed in the model. This droplet size distribution, in a resultant spray for a given atomizer/injector design, can be determined based on some available specific, non-general, empirical correlations [58, 2], or is also commonly characterized through experimental measurements at some far-downstream location. It is then shifted and imposed at the orifice boundary in the simulations - hence the term *upstream reconstruction* in the FIM-UR nomenclature. The natural evolution of the liquid phase, from the liquid breakup, formation of droplets, inter-droplet collisions, coalescence, etc., to a fully atomized spray, all of these physical processes in the immediate downstream vicinity of the atomizer/injector are not explicitly resolved. In other words, the size of the droplets does not change in the simulation downstream from the injection boundary before the preheating and vaporization process kicks in.

The FIM-UR model [310] determines and sets the velocity of Lagrangian particles ($\mathbf{u}_p$) injected at the orifice boundary based on the following input parameters:

1. Liquid fuel mass flow rate, $\dot{m}_l$
2. Atomizer (geometry) orifice radius, R_0.
3. Droplet size distribution (PDF), $f(d_p)$
4. Half-spray angle (or half-cone injection angle), θ_S

6.2.3 Liquid-Wall Interaction Model (Slip vs. Film Treatment)

As discussed earlier and indicated in Fig . 6.1, many injectors have this *prefilming* surface on which the liquid fuel jet from the atomizer impinges and forms a thin film. Even in the SICCA-spray injector simulated in the current work, the liquid fuel films on the conical injector surface as shown in Fig. 7.3 in the following Chapter 7. This subsection will present the model treating interaction between Lagrangian droplets injected by FIM-UR and the injector wall. Two approaches, *SLIP* and *FILM* treatments were tested in the work of Lo Schiavo et al. [60]; and the latter FILM treatment was found crucial in the triggering and predicting self-sustained thermoacoustic oscillation in SICCA-spray burner simulations. More discussion to follow in subsequent Chapter 7. Here, the distinctions are drawn between the two modeling approaches.

SLIP Treatment: As indicated in Fig. 6.6(a), the normal component of the velocity is set to zero as soon as the droplet reaches the wall, and owing to its inertia,

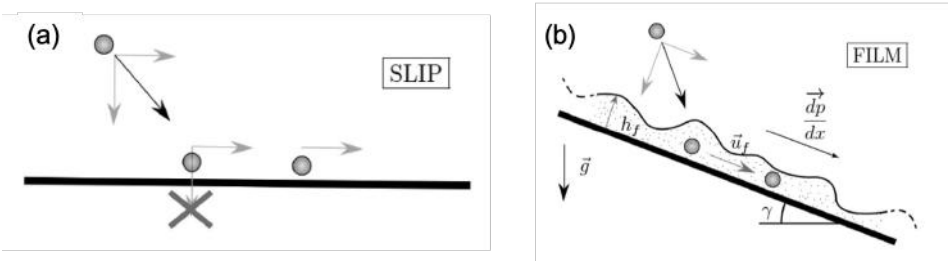

Figure 6.6: Lagrangian droplets and wall interaction treatments: (a) SLIP: Particles impinging on the walls slip along the wall at their initial speed (tangential component). (b) FILM: Particles accumulate on the wall to form a film. Film height h_f and speed $\vec{u}_f$ as per the FILM model developed by Chaussonnet et al. [294, 314]. Figure reproduced from [60].

the droplet slips along the wall at its actual tangential speed.

FILM Treatment:

Chaussonnet et al. [294, 314] developed the FILM model in the context of prefilming airblast edge atomization and implemented it in AVBP Euler-Lagrangian framework - see (Ch.3, 6 in [294]) for complete details).

Physically, the film motion/dynamics is primarily driven by shear stresses exerted by the external gaseous flow on the liquid film. Physical equations governing a *thin* liquid-phase film on a wall were derived from the general incompressible Navier-Stokes (NS) equation in 2D inspired from classical Saint-Venant's [342] analysis (also described by Thual [343]). Fundamental assumptions applicable here are: (a) incompressibility of the fluid, (b) negligible longitudinal gradients (tangential to the wall, along x-direction) compared to normal y-direction, (c) homogeneous exterior/ambient pressure P_{ext}. (d) *steady-state assumption* is invoked that considers the film flow as uniform along the x-direction with temporal derivative vanishing. This implies that the thin film flow adapts instantaneously to external gas flow or wall-geometry changes. Thus the set of incompressible 2D NS equations under the above assumptions governing the liquid film is given as follows:

$$\begin{aligned} \frac{dv}{dy} &= 0 \\ v\frac{du}{dy} &= -\frac{1}{\rho}\frac{\partial p}{\partial x} + \nu\frac{d^2u}{dy^2} + g\sin\gamma \\ \frac{\partial p}{\partial y} &= 0 \end{aligned} \tag{6.16}$$

Mass continuity (first row in Eq. 6.16) states that the wall-normal velocity is constant over the film thickness. As non-porous walls impose that v is zero at the wall

surface, this leads to:

$$v = 0 \tag{6.17}$$

Third row in Eq. (6.16) implies that pressure varies only along x-direction. Finally, the film motion is described by the longitudinal momentum equation (second row in Eq. 6.16), which now becomes:

$$\nu \frac{d^2u}{dy^2} = \frac{1}{\rho}\frac{dp}{dx} - g\sin\gamma \tag{6.18}$$

A bulk velocity of the film can be eventually calculated by integrating above differential momentum equation along *wall-normal* y-direction over film thickness (h_f), and applying boundary conditions $u(0) = 0$ and $\mu\frac{\partial u(h_f)}{\partial y} = \tau_{fg}$, where τ_{fg} is the shear stress at film/gas interface yields following equation for film velocity $u(y)$:

$$u(y) = \left[\left(\frac{dp}{dx} - \rho g\sin\gamma\right)\left(\frac{y}{2} - h\right) + \tau_{fg}\right]\frac{y}{\mu} \tag{6.19}$$

Neglecting the internal velocity variations in the *thin* film, the above equation is averaged along the thickness h_f to yield a average film velocity ($\bar{u}_f$):

$$\bar{u}_f = \frac{1}{h}\int_0^h u(y)\mathrm{d}y = \tau_{fg}\cdot\frac{h}{2\mu} + \left(\rho g\sin\gamma - \frac{dp}{dx}\right)\cdot\frac{h^2}{3\mu} \tag{6.20}$$

In the context of numerical implementation in AVBP, the liquid-phase and liquid/gas interface is not resolved explicitly but is instead represented by discrete, dispersed Lagrangian particles - see Fig. 6.7. Two important quantities that still need closure or need to be modeled are: (i) τ_{fg} the shear stress and (ii) estimation of film height, h_f.

For (i), since the film is considered *thin*, a simple first approximation that is used is to use *wall shear stress* (τ_w) for τ_{fg}. τ_w is calculated from the gas-phase LES solver (either directly if the simulation is wall-resolved or through the law-of-the-wall technique). A *one-way coupling* hypothesis is made here, wherein reverse momentum coupling from liquid-film to gas is not considered. With this approximation, the above physical model for averaged film velocity Eq. (6.20), in terms of τ_w is then given as [294]:

$$\bar{u}_f = \frac{h}{2\mu}\cdot\tau_w + \frac{h^2}{3\mu}\cdot\left(\rho g\sin\gamma - \frac{dp}{dx}\right) \tag{6.21}$$

The estimation of (ii) film height (h_f), is summarized in a representative scheme depicted in Fig. 6.7, wherein local film height is estimated at each boundary node, based on the *in-cell* liquid(particles) volume. However, many more practical implementation subtleties need to be accounted for than what is illustrated in Fig. 6.7 - see [294] for complete details. A direct consequence of film velocity averaging along wall-normal discussed above, and the numerical method of estimating h_f is: the

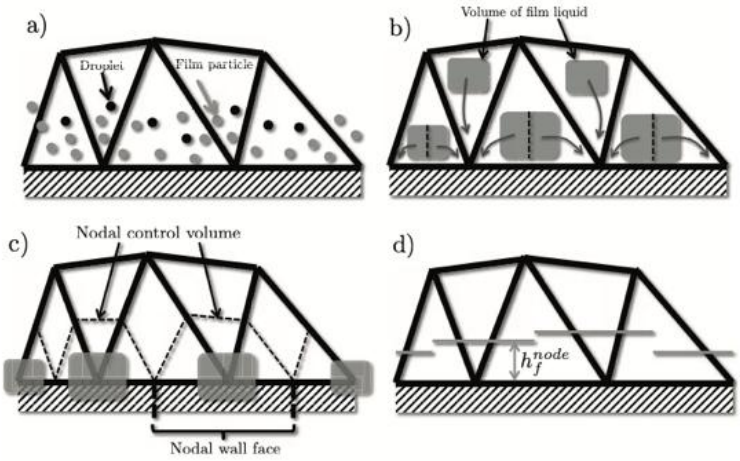

Figure 6.7: Illustration of film thickness/height (h_f) estimation in AVBP. a) Only film particles are accounted for the film liquid volume. b) Film liquid volume calculated in a) is equally distributed to surface nodes. c) Film volume at surface node (calculated in b)) is divided by the nodal wall surface. d) Resulting film thickness value is attributed to the surface node. Figure reproduced from Chaussonnet [294].

velocity of all the particles present locally in a boundary cell is then set to $\bar{u}_f$ from Eq. (6.21), based on local film height and τ_w.

Also note that from Eq. (6.21), when pressure-gradient and gravity effects two terms are negligible or ignored, the film velocity is governed by (or scales with) the shear stress. From a systematic order-of-magnitude analysis [294], to first-order, a *characteristic* film velocity-scale ($U_{f,0}$) can be defined as:

$$U_{f,0} \sim \frac{h_0 \tau_{w,0}}{\mu_0} \tag{6.22}$$

In summary, the FILM treatment causes the Lagrangian particles accumulated in a thin layer (film) on a wall to move at a locally averaged speed equal to the film's speed that depends on the wall shear stress and local liquid volume (or film height, in other words).s

6.2.4 Droplet Drag Model

Considering that the liquid droplets are transported by drag force exerted by the gas phase, this subsection will determine this drag force $\vec{F}_D$ ($= \mathbf{F_p}$) in the above equations. The effect of heterogeneous evaporation around the droplet surface on drag forces is neglected. The force $\vec{F}_D$ is determined based on the relative velocity

between gas and the particle as:

$$\vec{F}_D = \frac{1}{2}\rho_g C_D A \left\|\vec{u}_g - \vec{u}_p\right\| \left(\vec{u}_g - \vec{u}_p\right) \tag{6.23}$$

where ρ_g is the gas density, $\vec{u}_g$ and $\vec{u}_p$ are gas and particle velocity at the particle position, respectively. A is the projected surface area in the direction of the relative velocity vector. The term C_D represents the drag coefficient that needs to be modeled. C_D is a complex function of flow parameters like particle Reynolds number ($\mathsf{Re_p}$), turbulence levels, the orientation of the particle, etc., and is determined from empirical correlation given by Schiller and Nauman [344, 300] as follows:

$$\begin{aligned} C_D &= \frac{24}{\mathsf{Re_p}}\left[1 + 0.15\mathsf{Re_p}^{0.687}\right] \\ \mathsf{Re_p} &= \frac{\rho_g d_p \left\|\vec{u}_g - \vec{u}_p\right\|}{\mu_g} \end{aligned} \tag{6.24}$$

where d_p is the particle diameter and μ_g is the dynamic viscosity of the gas.

6.2.5 Droplet Evaporation Model

Abramzon and Sirignano [345, 59] (AS) droplet evaporation model is utilized in this work. It is based on the vaporization model initially proposed by Spalding [346, 59] for a droplet in a quiescent/stagnant medium. Abramzon and Sirignano extended it for droplets having a relative motion with respect to the carrier gas phase. So, this subsection will begin with a brief description of the Spalding model followed by the AS model. Only key equations are given in the following; detailed theory and derivation of the model is not repeated here and can be found in the cited references.

6.2.5.1 Spalding Evaporation Model

As shown in Fig. 6.8, a single-component pure fuel droplet is considered, and the gas phase is assumed to behave as an ideal gas. A spherically symmetric gas film exists around the liquid droplet and far-field, which is a mixture of fuel vapor and carrier gas. Heat transfer from the gas-film Q_g to the liquid particle surface causes the heating up of droplet (increase in its sensible enthalpy) and eventually vaporization at the gas/liquid interface. This creation of fuel vapor $\dot{m}_F$ induces a radial flow (Stefan's convection [59]) in the gas film in addition to molecular (Fick's) diffusion. Since droplet absorbs heat and emanates fuel vapor, the fuel vapor mass fraction Y_F decreases, and the temperature increases asymptotically from the (liquid/gas) interface to the far-field in the gas film. Therefore from a modeling point of view, the two physical quantities of interest that must be determined/quantified is the rate at which fuel is vaporized $\dot{m}_F$ that in turn depends on the rate at which heat

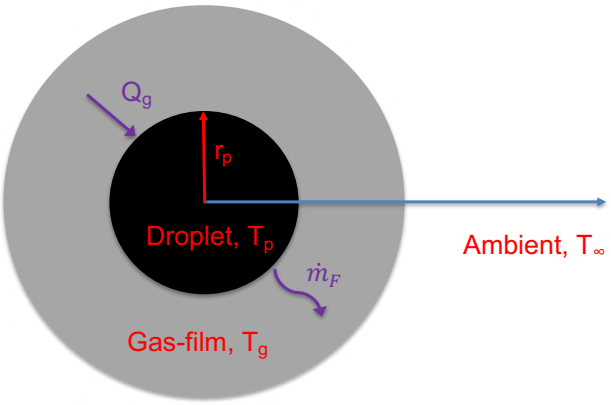

Figure 6.8: Single droplet vaporization

is absorbed by the droplet Q_g. Both these operations are coupled. Spalding derived analytical expressions for them based on mass and energy conservation between liquid and gas phases, as described next.

Assuming there is no relative motion between liquid particle and gas phase (i.e., particle Reynolds number $\mathsf{Re}_p = 0$) and the temperature inside the particle is uniform. Then the temporal evolution of the particle mass $\dot{m}_p$, (or equivalently its radius r_p), and temperature T_p is given by mass and energy conservation on the liquid side as:

$$\frac{d}{dt}m_p = \frac{d}{dt}\left(\frac{4}{3}\rho_l \pi r_p^3\right) = -\dot{m}_F \tag{6.25}$$

and,

$$m_p c_{p,l}\frac{dT_p}{dt} = Q_L \tag{6.26}$$

where, ρ_l, $c_{p,l}$ are the liquid density and specific heat capacity. $\dot{m}_F$ is the rate of fuel evaporation, and Q_L is the part of the heat from the gas film that increases the droplet's temperature (sensible enthalpy). Thus,

$$Q_g = Q_L + \dot{m}_F L_v \tag{6.27}$$

where, L_v is the *latent heat of vaporization* of the fuel.

Similarly, in the gas phase (or the gas film), conservation of mass, fuel-vapor mass-fraction, and energy (enthalpy) are applied considering a spherical coordinate system [59]. It is assumed that the gas film's heat and mass transfer processes are in a quasi-steady state, and the thermophysical properties are constant. The analysis results in the following differential equation for fuel-vapor mass fraction $Y_F(r)$ in the gas film:

$$4\pi r^2 \rho_g \mathcal{D}\frac{\mathrm{d}Y_F(r)}{\mathrm{d}r} = \dot{m}_F\left(Y_F(r) - 1\right) \tag{6.28}$$

where, ρ_g is the density in gas-film and $\mathcal{D}$ is the mass diffusivity. Integrating the above equation in the gas film from liquid surface ($r = r_p$) to far-field ($r = \infty$) with

$Y_{F,s}$ and $Y_{F,\infty}$ being the fuel-vapor mass fractions at the respective locations. The following analytical expression for *evaporation rate* of fuel droplet was derived by Spalding:

$$\dot{m}_F = 4\pi\rho_g \mathcal{D} r_p \ln\left(1 + \mathsf{B_M}\right) \tag{6.29}$$

where $\mathsf{B_M}$ is Spalding mass transfer number given as:

$$\mathsf{B_M} = \frac{Y_{F,\infty} - Y_{F,s}}{Y_{F,s} - 1} \tag{6.30}$$

Assuming phase-change equilibrium at the liquid-gas interface, the fraction of fuel vapour at the interface ($Y_{F,s}$) is calculated from the fuel vapor pressure ($P_{v,F}$) at the droplet temperature (T_p); and this vapor pressure is obtained from the Clausius-Clapeyron relation [59].

The second part of Spalding's model is to quantify the amount of total heat absorbed Q_g by the droplet from the surrounding gas film to complete the droplet evaporation model. It controls the temperature of the droplet (Eq. 6.26), that of gas film T_g, and eventually the vaporization rate $\dot{m}_F$. Conservation of energy (enthalpy) analysis on the gas-film side yields [59]:

$$Q_g = 4\pi r_p \lambda_g \frac{\ln\left(1 + \mathsf{B_T}\right)}{\mathsf{B_T}} \left(T_\infty - T_p\right) \tag{6.31}$$

where, λ_g is the heat conductivity in the gas film, and $\mathsf{B_T}$ is Spalding heat transfer number. Since the mass transfer and heat-transfer process between liquid/gas is coupled, it can be shown that $\mathsf{B_T}$ is related to $\mathsf{B_M}$ as below [59]:

$$\mathsf{B_T} = \left(1 + \mathsf{B_M}\right)^{\beta} - 1 \quad \text{with} \quad \beta = \frac{\mathsf{Sh}\ \mathsf{Pr}}{\mathsf{Nu}\ \mathsf{Sc_F}} \tag{6.32}$$

Nu, Sh, Pr, $\mathsf{Sc_F}$ are Nusselt (ratio of convective to coductive heat transfer rate), Sherwood (ratio of convective to diffusive mass transfer rate), Prandtl (ratio of momentum to thermal diffusivity) and Schmidt (ratio of momentum to mass diffusivity) numbers respectively.

6.2.5.2 Abramzon and Sirignano (AS) Model

Spalding's model above assumed no relative motion between Lagrangian droplets and the gas carrier phase. Abramzon and Sirignano extended this model by accounting for the convective effects due to which both the heat and mass transfer processes are enhanced. However, note that the infinite liquid thermal conductivity assumption still applies so that the temperature of the droplet on the surface and in the interior is the same and uniform (T_p). In other words, transient temperature evolution inside the droplet is not resolved.

The convective effect, i.e., non-zero particle Reynolds number effect, was accounted for by Abramzon and Sirignano [345] (AS) in their model by employing

the Ranz and Marshall [347] correlations that give *modified* Sherwood and Nusselt numbers as follows:

$$\begin{aligned} \mathsf{Sh_0} &= 2 + 0.55\mathsf{Re_p}^{1/2}\mathsf{Sc}^{1/3} \\ \mathsf{Nu_0} &= 2 + 0.55\mathsf{Re_p}^{1/2}\mathsf{Pr}^{1/3} \end{aligned} \tag{6.33}$$

In the AS model [345, 59] an additional *correction factor* was proposed to account for the interaction between the convective boundary layer around the droplet and the Stefan flow, where the latter tends to increase the thickness of mass-transfer and thermal boundary layer in contrast to that around a non-evaporating particle. Effectively, the thickening of the boundary layer augments the mass and heat transfer process between liquid and surrounding gas. The two mass and thermal correction factors F_M and F_T are given in terms of the mass and thermal Spalding numbers:

$$F_x = (1 + \mathsf{B_x})^{0.7} \frac{\ln(1 + \mathsf{B_x})}{\mathsf{B_x}} \tag{6.34}$$

where, $\mathsf{x} = \mathsf{M}$ or T. Furthermore, the above $\mathsf{Sh_0}$ and $\mathsf{Nu_0}$ numbers are corrected with these factors as below:

$$\mathsf{Sh}^* = 2 + \frac{(\mathsf{Sh_0} - 2)}{F_M} \tag{6.35}$$

$$\mathsf{Nu}^* = 2 + \frac{(\mathsf{Nu_0} - 2)}{F_T} \tag{6.36}$$

Finally, the fuel evaporation rate $\dot{m}_F$ and total heat transfer rate to the droplet Q_g can be expressed in terms of Sh^* and Nu^* as:

$$\dot{m}_F = 2\pi\rho_g \mathcal{D} r_p \mathsf{Sh}^* \ln(1 + B_M) \tag{6.37}$$

$$Q_g = 2\pi r_p \lambda_g \mathsf{Nu}^* (T_\infty - T_p) \frac{\ln(1 + B_T)}{B_T} \tag{6.38}$$

This completes the Abramzon-Sirignano evaporation model that is available in the AVBP code and employed in the current work. Note that, since the rate of change of droplet mass is converted into gaseous fuel, the source term in Eqs. (6.10), $\dot{m}_p = -\dot{m}_F$. Also the source of conductive heat transfer from gas to liquid fuel in Eq. (6.11) $\Phi_g^c \equiv Q_g$.

6.2.6 Chemical Kinetics Modeling

Chemistry modeling is another challenging and significant aspect in LES of turbulent reacting flows [348, 349, 350]. Physically, multiple species are consumed and created (or both in the case of intermediate species as per the reaction pathways from reactants to products). These reactions occur over a wide range of (chemical) time scales compared to the (transport/turbulent) flow time scales. As a result, the chemistry problem becomes mathematically stiff from a modeling point of view

when individual species have to be tracked. Besides that, the chemistry is coupled or influenced by other relevant conditions such as flame/wall interaction (heat loss), spray/flame interaction, dilution effects, etc.

Employing the best available description, i.e., detailed chemical kinetics model, which typically for hydrocarbon fuels can contain hundreds of species and thousands of reactions remain prohibitive and unfeasible, and even unnecessary in some situations [13, 108]. In practice, detailed schemes are used only for canonical problems such as: (i) 0D reactors for estimating adiabatic flame temperature and ignition delays; (ii)1D laminar flame simulations for determining fundamental properties such as flame speed, flame-stretch effects; (iii) to analyze pollutant formation reaction pathways, their concentration profiles and (iv) most essentially to extract, develop, optimize and validate simplified/reduced surrogate models from them [351, 352] for LES applications.

Global chemical kinetic schemes that typically have a few species and 2-4 reaction steps have successfully been applied for LES of flame stabilization and dynamics studies for both gaseous and spray flames [353, 321, 323, 60]. However, if the objective is predicting pollutant emissions or near-limit phenomena such as ignition or blow-out transients, or situations where finite-rate chemistry effects are important, in that case, high-fidelity LES requires augmented chemical kinetics. This is where the reduced surrogate mechanisms mentioned above become a valuable tool [354, 355, 356, 357, 358, 359].

In the current work (and in [60]), fuel is considered to be made of single component n-heptane, burning with air under atmospheric conditions. Chemistry is described with a global two-step mechanism (2S_C7H16_DP) based on a fast oxidation reaction, followed by a $CO \leftrightarrow CO_2$ equilibrium, and involving six species ($C_7H_{16}, O_2, CO, H_2O, CO_2$ and N_2) [323, 61].

$$\begin{aligned} 2C_7H_{16} + 15O_2 &\longrightarrow 14CO + 16H_2O \quad (R_1) \\ CO + 0.5O_2 &\longleftrightarrow CO_2 \quad (R_2) \end{aligned} \tag{6.39}$$

Reaction rates for reactions R_1 and R_2 follow an Arrhenius law [13]:

$$q_1 = A_1 f_1(\phi) \left(\frac{\rho Y_{C_7H_{16}}}{W_{C_7H_{16}}}\right)^{0.6} \left(\frac{\rho Y_{O_2}}{W_{O_2}}\right)^{0.9} \exp\left(\frac{-E_{a,1}}{RT}\right) \tag{6.40}$$

$$q_2 = A_2 f_2(\phi) \left[\left(\frac{\rho Y_{CO}}{W_{CO}}\right)^{1.0} \left(\frac{\rho Y_{O_2}}{W_{O_2}}\right)^{0.5} - \frac{1}{K_2}\left(\frac{\rho Y_{CO_2}}{W_{CO_2}}\right)^{1.0}\right] \exp\left(\frac{-E_{a,2}}{RT}\right) \tag{6.41}$$

The pre-exponential constants A_j and the activation energies E_j are: ($A_1 = 1.4 \times 10^{11}$, $A_2 = 5.0 \times 10^9$, $E_1 = 2.9 \times 10^4$, $E_2 = 2.1 \times 10^4$). K_2 is the equilibrium constant of reaction R_2 and ϕ is the local equivalence ratio. The correction function $f_1(\phi)$ and $f_2(\phi)$ allow to recover the correct flame speed $S_L(\phi)$ depending upon local

lean/rich conditions and were caliberated in the work of D. Paulhiac [323, 61]. The mechanism was also cross-verified in 1D-laminar, LES cases of n-heptane two-phase flames computed by Rochette [360, 324], and later by Lo Schiavo [60].

6.2.7 Thickened Flame Turbulent Combustion Model (TFLES)

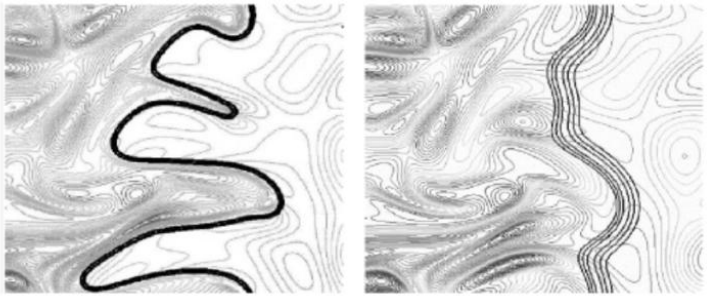

Figure 6.9: Effect of thickening a turbulent flame. Left is the reference DNS and right is the thickened flame with F=5 showing reduced wrinkling [13].

Although LES resolves the majority of spatio-temporal scales of the turbulent flow, the reaction zone of realistic turbulent flames is still very thin (or order ~ 0.1 mm) and falls under the subgrid (SGS) scale for practically affordable LES mesh resolutions. This thin reaction zone is where the majority of the heat release occurs and results in strong gradients of all physical quantities across it. Therefore, it is absolutely essential that the *turbulence-flame-interaction*[2] be appropriately modeled in the LES. The Dynamic Thickened Flame turbulent combustion model (D-TFLES) [13] helps achieves this with a simple yet brilliant solution. There are several other combustion modeling approaches developed and available in the literature - see, for instance, [115, 13, 108, 327, 114] and references therein.

So in the D-TFLES model, the basic idea is to artificially thicken the flame by a thickening factor $\mathcal{F}$ so that the flame can be reasonably resolved on the mesh, as shown in Fig. 6.9, for example. Due to thickening, however, the interaction between turbulence and chemistry (or the flame) is altered as thickening reduces the ability of the vortices to wrinkle the flame front. In order to conserve the flame speed and not underestimate the reaction rate, the diffusivity, and the reaction rate are

[2]Turbulence-chemistry-interaction is a fundamental concept extensively researched and ubiquitous in the turbulent combustion theory and modeling literature [13, 361, 362, 114]. Characterized through non-dimensional numbers such as Da, Ka correlating flame (chemical) and turbulence scales, *regime diagrams* have been drawn. These classify the combustion process in different regimes where distinct physical effects dominate, such as flame wrinkling, stretching, local-quenching, etc. Many commonly made modeling assumptions can stand invalid in some regimes, especially near limit conditions.

corrected by an *efficiency function* $\boldsymbol{\mathcal{E}}$. In the dynamic formulation of the thickened flame model, $\boldsymbol{\mathcal{F}}$ is not constant and is driven by a sensor $\boldsymbol{\mathcal{S}}$ depending on the local temperature and mass fractions. This sensor locates the flame zone so as to not apply the factor $\boldsymbol{\mathcal{F}}$ in non-reactive zones. The efficiency function accounts for the effects of the sub-grid scale wrinkling as a function of the local sub-grid turbulence velocity and spatial filter size. Complete details on D-TFLES can be found in [13]. In this work, the dynamic efficiency function $\boldsymbol{\mathcal{E}}$ proposed by Charlette et al. [363, 13] has been used.

Takeno Index: The TFLES combustion model and its later variants, including D-TFLES, were developed for premixed flames. However, spray combustion gives rise to a complex flame structure where both premixed and diffusion regimes coexist, as discussed earlier. Technically, in this situation, thickening must be applied only to the premixed flame front. Therefore the sensor $\boldsymbol{\mathcal{S}}$ above is further conditioned with Takeno Index [364], which helps distinguish premixed/non-premixed reaction zones so that it selectively applies the thickening only in the premixed reactions zones. Takeno index is defined as:

$$TI = \frac{\nabla Y_F \cdot \nabla Y_{Ox}}{|\nabla Y_F| \cdot |\nabla Y_{Ox}|} \tag{6.42}$$

where Y_F and Y_{Ox} are mass fractions of fuel and oxidizer, respectively. Thickening is only applied to regions with $TI = +1$, signifying a premixed reaction zone. As for the diffusion regions, the flame driven by transport processes adapts to the local mesh resolution. See a recent paper from Cuenot et al. [365] for a complete description of the treatment of non-premixed flames in AVBP, in general.

6.2.7.1 Two-phase Thickened Flame Model for LES (TP-TFLES)

TP-TFLES extends the TFLES combustion model for two-phase spray flames. A consequence of the flame thickening process is that the characteristic chemical time-scale is increased by the factor $\boldsymbol{\mathcal{F}}$. Since the evaporation and combustion (reaction and resulting heat-release) processes are coupled in spray flames, the evaporation rate also needs to be adapted. In order to compensate for the increased chemical time, the characteristic evaporation rate is brought down by the same factor $\boldsymbol{\mathcal{F}}$. Just as the TFLES model conserves the flame speed, the TP-TFLES model analogously preserves the evaporation and chemical time-scales ratio equal to the actual (non-thickened) flame. This was only a brief qualitative description; for detailed formulation and validation of the TP-TFLES model, see - Ch. 8 in the thesis of D. Paulhiac [323].

6.2.8 Numerical Scheme and Boundary Conditions

The fully compressible, explicit, second-order accurate in space and time Lax-Wendroff (LW) [366] numerical scheme is used for all the simulations performed in this thesis. Inlet and outlet flow boundary conditions are treated with Navier-Stokes Characteristic Boundary Conditions (NSCBC) [367, 13], more precisely, its newer formulations [368, 369].

Chapter 7

Combustion Dynamics in SICCA-spray Burner

Contents

7.1 Introduction 191
7.2 SICCA-spray Burner, Mesh and Numerical Setup 193
7.3 Self-sustained thermoacoustic instability LES (Summary of key results) 196
7.3.1 Role of the liquid-wall interaction treatment in spray-acoustic-flame coupling 197
7.3.2 Impact of the Injection Angle 202
7.4 Forced SICCA-spray Flame LES: Results and Discussion . 204
7.4.1 Reference Experimental FDF measurements 204
7.4.2 Inlet Forcing vs. Outlet Forcing 205
7.4.3 Impact of the Injection angle on FTF 209
7.4.4 FTF at other frequencies 213
7.5 Conclusions and Perspectives 214

7.1 Introduction

This chapter reports the acoustically forced Euler-Lagrange (EL) LES results of a turbulent swirling spray flame in the SICCA-spray burner described in the following Sec. 7.2). The overall modeling framework employed is described in the previous Ch. 6. As mentioned in the objectives in Ch. 1, Sec. 1.5, this work builds upon, and complements the work of E. Lo Schiavo et al. [60, 201], who successfully carried out self-sustained, thermoacoustic instability LES in the same configuration and accurately predicted the limit-cycle observed in experiments. The author of this manuscript performed acoustically forced LES, aiming to predict its Flame-Transfer-Function (FTF).

Some of the key results from the work of E. Lo Schiavo et al. [60, 201] are summarized in the following sections of this chapter. The forced LES results are

analyzed in conjunction with these self-sustained instability results, especially using the insight obtained regarding acoustic and liquid-phase coupling.

When it comes to thermoacoustic instability predictions by LES, one method is the brute force approach, where the system is fully simulated to see if a so-called *self-excited regime* appears. In such an approach, the burner, if unstable, indeed resonates, exhibiting instabilities with pressure oscillations increasing in amplitude until they reach a stable limit-cycle for given operating and acoustic boundary conditions. Another commonly adopted method for investigating possible instabilities is to separate the complex flame dynamics from the combustor acoustics [13] as discussed in Ch. 1, Sec. 1.4.1 and 1.4.2. Reduced-ordered acoustic tools, such as Helmholtz solvers [127], network-models [120, 370, 202, 157] are then employed for a more comprehensive system-level stability analysis. A crucial component of such investigations is the flame response model that describes the coupling between the unsteady heat-release and the acoustics, also known as the Flame-Transfer or Describing Functions (FTF/FDFs), usually expressed in the frequency domain [13, 127, 25, 12]. In that case, FTF/FDFs are determined either from analytical expressions, experiments, or LES where acoustic excitation of the flame in a controlled, stable environment allows to measure of the heat release oscillations [25, 12] for different frequencies and perturbation amplitudes.

Numerical (LES) predictions of self-excited thermoacoustic instabilities in gaseous-fuel combustors (from lab-scale to complex industrial configurations) are well established, e.g., see [109, 46, 167, 11, 12], references therein, and citations in the following.

The present work particularly addresses this FTF prediction for turbulent swirling spray flames by employing the classical harmonic forcing at discrete, monotone frequencies. A separate simulation is performed for each frequency in this technique. Other efficient *system identification* approaches exist [371, 372, 178, 233, 230, 232, 12] where the flame is pulsed with broadband (white-noise) acoustic signal. The key advantage of the latter is that a single simulation yields the flame's impulse response (or flame transfer function). However, the LES is typically required to be of much longer duration than in the case of harmonic forcing.

On the other hand, the literature on the LES of combustion dynamics in liquid-fueled combustors [64, 373, 374, 60, 63, 62, 213] has started to appear only in the recent years. Indeed, modeling the liquid-phase physical processes such as primary, secondary, edge atomization, evaporation, liquid-wall interaction, and multi-regime combustion in two-phase flames is still a great challenge in general, and a topic of active research [61]. This work is the first attempt at CERFACS to pulse a two-phase turbulent swirling flame under the EL-LES framework. The objective is to qualify this EL-LES method for such a system identification problem while assessing the uncertainties and sensitivity to the two-phase spray combustion models.

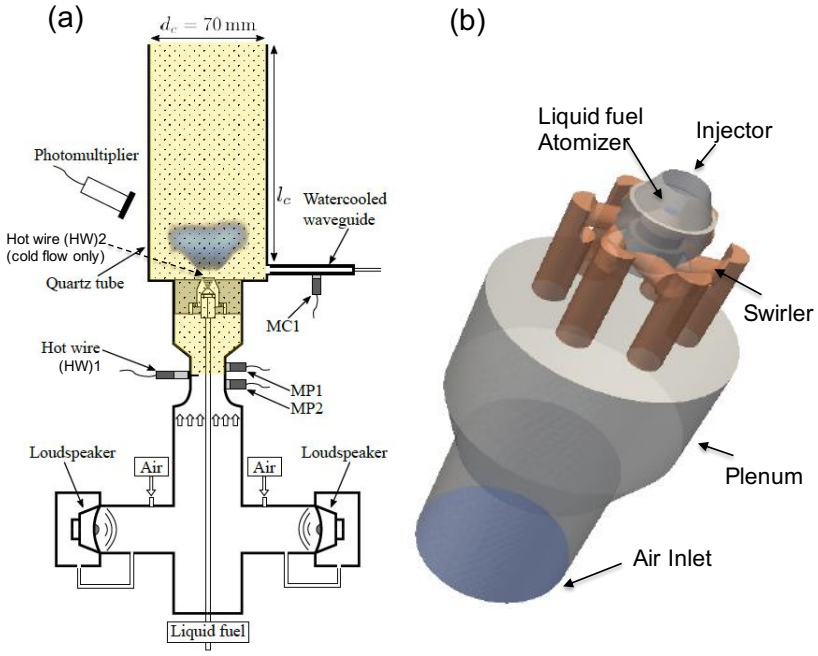

Figure 7.1: (a) Experimental setup of the SICCA-spray rig. The yellow-shaded region denotes the LES computation domain. (b) Close-up of the swirling liquid-fuel injector.

7.2 SICCA-spray Burner, Mesh and Numerical Setup

Figure 7.1 shows the SICCA-spray configuration that is simulated. It is a single-injector burner setup containing a pressure-swirled liquid-fuel atomizer, originally designed and tested in the thesis of K. Prieur [375] at EM2C laboratory in Paris. Later this particular injector was also installed in the lab-scale annular MICCA rig to investigate azimuthal instabilities, and transient phenomena such as ignition (light-around) and blow-out [104, 103, 376]. Next-generation variants of this injector have been designed and tested too - see the subsequent thesis of G. Vignat [377] for a complete survey of these different injectors and their performance evaluation.

This section details the specific numerical setup used for the simulations, including the required input parameters of some of the models described in the previous Chapter 6.

- **Geometry:** Two different computational domains, varying in the combustion chamber length (l_c) are used to mimic the experimental thermo-acoustically stable/unstable operating conditions: (i) $l_c = 165$ mm is stable and thus used for investigating spray flame structure under stable/steady conditions. It is also acoustically forced to compute the FTF. (ii) $l_c = 280$ mm is unstable, and

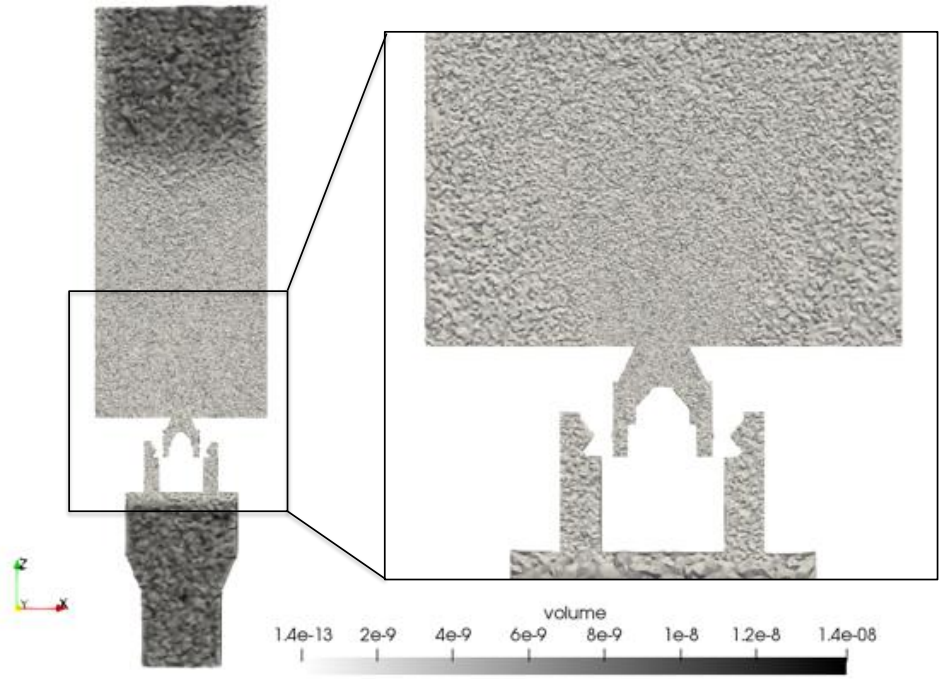

Figure 7.2: Resolution of the unstructured tetrahedral computational mesh. Colormap denotes the volume (m^3) of the mesh elements.

employed for simulating the self-sustained limit cycle. Besides the chamber length, all other parameters remain the same for the stable/unstable operating conditions.

- **Mesh:** Figure 7.2 depicts the computational mesh of the domain. Care has been taken to refine the injection and reaction zones, where the cell size is as fine as $\Delta x = 150$ μm. Downstream near the combustor exit, it is coarser and around $\Delta x = 200$ μm $- 300$ μm. The mesh size is about 20 M cells. The mesh was originally developed, optimized, and validated by E. Lo Schiavo [60] - initially with cold-flow simulations to match the injector pressure-drop Δp (across the swirl injector) from the plenum to the chamber (Exp: 3900 Pa, LES: 4092 Pa, Error: +5%) and swirl number (Exp: 0.55, LES: 0.51, Error: -7%). Later, it was ensured that the mesh resolution was good enough to correctly represent the flame for the reacting flow. This can be verified from the flame-thickening map (Fig. 7.5), where for most of the reaction zone, the thickening factor $\mathcal{F}$ is less than the specified $\mathcal{F}_{max}$.

- **Fuel/Air conditions:** Mass flow rate of air, $\dot{m}_{air} = 2.58$ g/s. Fuel is liquid n-heptane, injection mass flow rate: $\dot{m}_l = 0.144$ g/s. This results into an overall equivalence ratio of 0.85.

- **Chemistry:** Global two-step chemistry (2S_C7H16_DP) - see Sec. 6.2.6.

- **FIM-UR Injection Model:** As described in previous Ch. 6, Sec. 6.2.2, it requires a total of four following input parameters. Two of them are fixed: $\dot{m}_l$, and atomizer orifice discharge diameter $D_0 = 120$ μm.

  The other two input parameters are the *empirical inputs*. Firstly, the droplet size distribution PDF $f(d_p)$. Since the atomization process is not explicitly resolved, it is one of the most important input parameter. This statistical characterization of the spray is achieved by prescribing a *Rosin-Rammler* [300] type of PDF function with *mean* ($d_p^m = 10$ μm) and*Sauter mean diameter* (SMD)($d_p^{SMD} = 18$ μm). An estimate of these mean and SMD diameters is obtained from experimental measurements at a cross-section plane 2.5 mm above the chamber backplane at indicated in Fig. 7.3.

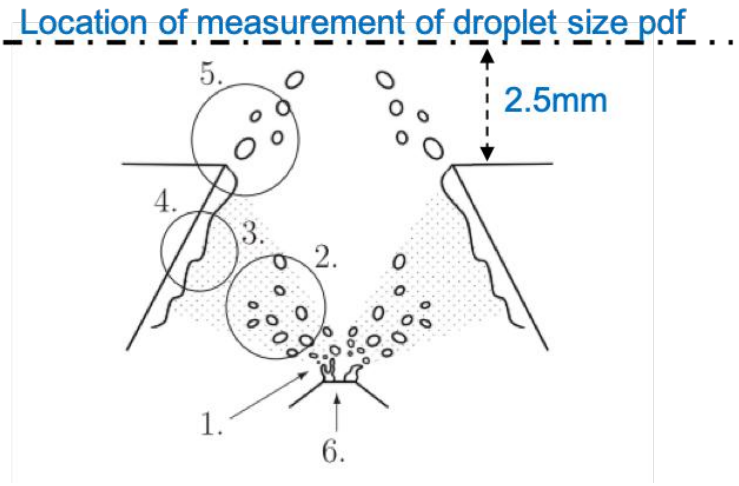

Figure 7.3: A downstream location in the combustor where the mean and SMD statistics of the spray are estimated experimentally. Figure also highlights the pre-filming on the conical injector wall before the fuel film undergoes edge-atomization (or equivalently, in LES, the Lagrangian particles are released from the edge). Adapted from [60].

  The other empirical input is the half-spray angle, θ. A nominal value of $\theta = 45$ is set as a baseline value. Due to lack of optical access inside the injector, it becomes difficult to characterize this value correctly and thus is prone to uncertainty. The impact of this parameter on self-sustained instability (under unstable operating conditions) was investigated by Lo Schiavo et al. [201]. A similar study is also carried out to study the sensitivity of computed FTF in the current work. More discussion to follow in the upcoming sections.

  Also, note that the fuel line is considered stiff since the $\Delta p = 9$ bar is about

three orders-of-magnitude higher than the measured thermoacoustic pressure oscillations ($p' \approx 1 - 2$ kPa). So, the liquid fuel mass flow is presumed to be constant and not modulated due to acoustic oscillations. Besides, variations in the half-spray angle, if any, are neglected too.

Indeed, as such, the above considerations and assumptions of *constant* droplet size distribution, liquid mass flow rate, and spray angle are disputable.

- **Boundary Conditions:** The inflowing air mass flow rate is prescribed with a turbulent mean profile, while the ambient pressure is imposed at outlet boundary condition with the Navier-Stokes Characteristic Boundary Condition (NSCBC) [367, 13] based formulations. The flame forcing, discussed in following Sec. 7.4.2, is performed either from the inlet or from the outlet. In both cases, the acoustic boundary conditions at the inlet (and outlet) were taken to be almost non-reflecting [369, 378] so that all outgoing waves leave the domain and no unwanted resonance is established [173].

  All walls are no-slip and adiabatic except for combustion chamber walls. For the vertical quartz tube wall, experimentally measured external (cold side) temperature profiles were utilized, and based on the quartz wall thickness (3 mm) and conductivity ($\lambda_w = 2.17$ $\mathrm{Wm^{-1}K^{-1}}$), appropriate thermal resistance is specified ($R_w = 1.38\text{e-}03$ $\mathrm{W^{-1}m^2K}$). As a result, the temperature on the inner (hot-side) wall (computational boundary) is not imposed but is rather computed by the solver. This resulting temperature profile was in good agreement with the measured (inner) temperature profile. A constant temperature of 450 K was imposed for the chamber backplane.

In addition to the above parameters, the remaining simulation setup is as per the different models described in the previous Chapter 6.

7.3 Self-sustained thermoacoustic instability LES (Summary of key results)

This section is dedicated to summarizing the key results from the work of the E. Lo Schiavo et al. [60, 201] who performed the EL-LES of the self-sustained instability in the SICCA-spray burner. The authors tested the liquid-wall treatments (SLIP vs. FILM) under both stable and unstable conditions in [60] and pointed out the importance of the FILM model under unstable (dynamic) conditions. This work is briefly recapitulated in the following Sec. 7.3.1. In a subsequent study, the impact of spray injection angle on the instability predictions was examined [201], results of which are outlined in Sec. 7.3.2.

7.3.1 Role of the liquid-wall interaction treatment in spray-acoustic-flame coupling

7.3.1.1 Spray flame under stable condition

The author of this manuscript re-computed the SICCA-spray flame under thermoacoustically stable conditions before forcing the flame. Some qualitative results are briefly presented, which are in line with previous work. A more detailed quantitative analysis of the spray-flame structure under both SLIP/FILM treatments is available in [60].

The outcome of the assessment of SLIP vs. FILM treatments under stable conditions was that there is no significant influence of these models on the flame shape/structure in general, i.e., consistent results are obtained in both cases [60]. Therefore the newer (reproduced) results reported here are obtained with only one - the FILM treatment.

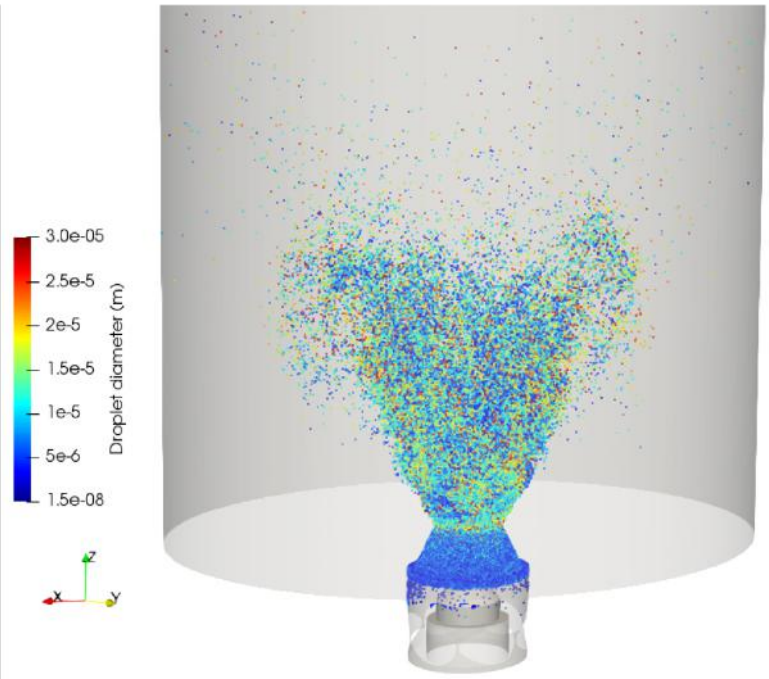

Figure 7.4: An illustration of 3D, instantaneous, fuel spray (Lagrangian particles field) in the combustor issuing from the injector. Colored by droplet diameter.

Figure 7.4 depicts the dispersed Lagrangian phase (spray droplets) in a 3D view, where they are colored by droplet diameter. Qualitatively, the size of the droplets in the combustor is apparently in the range of mean and SMD value of the prescribed Rosin-Rammler distribution. Few larger droplets do penetrate deeper and reach the peripheral regions. A very few droplets cross the reaction zone (where most droplets

are consumed) and travel far downstream.

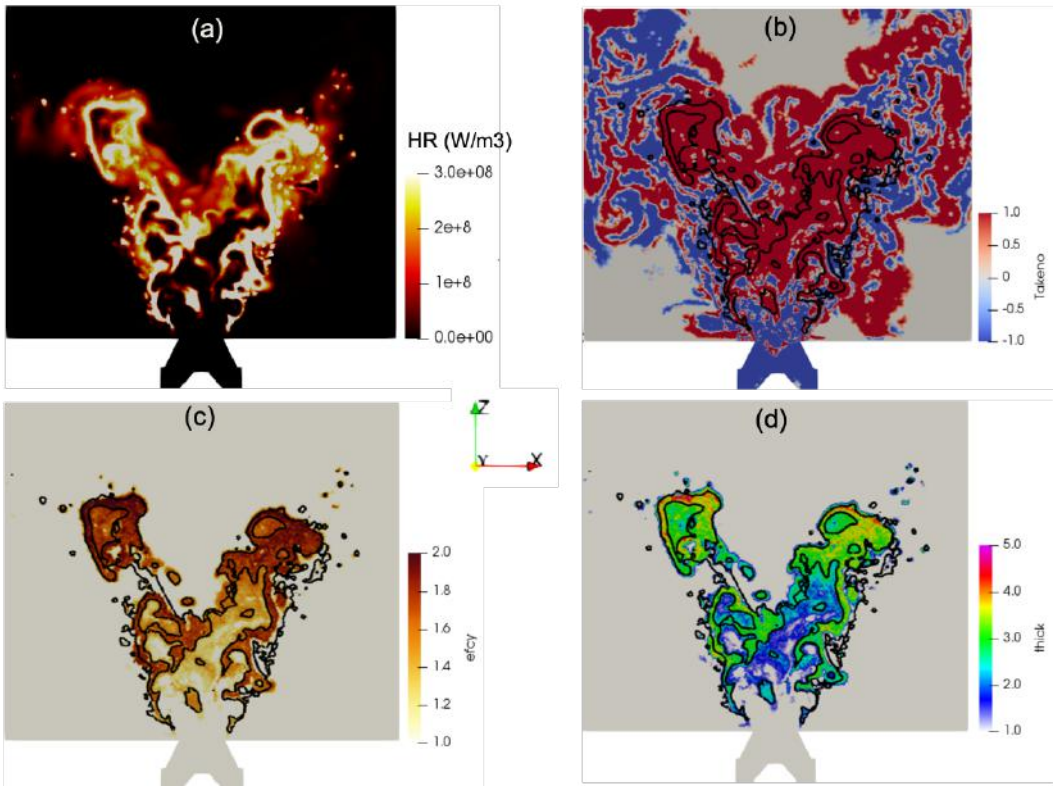

Figure 7.5: Planar, instantaneous contours of: (a) Flame shape (denoted by the heat release rate (HRR) contour), (b) The Takeno Index, (c) Efficieny function ($\mathcal{E}$), and (d) Flame thickening factor ($\mathcal{F}$). The black contour line indicates 10% of the max HRR.

Figure 7.5(a) shows the instantaneous flame shape. Spray flames are a manifestation of a coupled interaction between dispersed liquid phase, gaseous flow/turbulence, evaporation, and chemical processes. As expected and discussed in the previous chapter, a heterogeneous mixture of fuel and air is expected that leads to a complex, multi-regime flame structure. This fact is evident from the Takeno index in Fig. 7.5(b). The flame anchoring region presents both premixed (+1) and diffusion (-1) regimes. However, downstream the premixed regime begins dominating in the center of the swirled jet due to the fuel vapor being trapped by the central recirculation zone (CRZ). On the peripheral side of the flame, combustion occurs mainly in a diffusion regime due to larger droplets reaching these areas and lower gas temperature in the outer recirculation zones (ORZ) on account of heat loss across chamber walls.

As discussed earlier in the *Mesh* bullet point in Sec. 7.2, Fig. 7.5(d,c) confirms that the mesh refinement is good enough. Note that the flame thickening and the

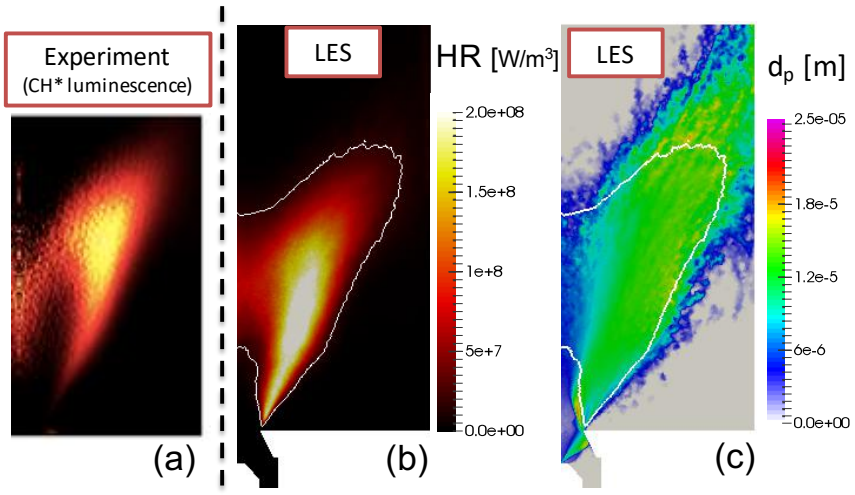

Figure 7.6: (a) Experiment: mean CH* chemiluminescence [103, 375], (b) LES mean heat release rate, and (c) Mean fuel droplet diameter distribution, under stable steady operation. Spray injection angle is $\theta = 45°$. White line is the iso-contour $\dot{q} = 20MW/m^3$, $\sim 10\%$ of the max heat release, denoting the mean flame shape.

efficiency function from the turbulent combustion model (Sec. 6.2.7) are applied only in the premixed regimes, while in the diffusion zones, the flame thickness adapts as per the mesh resolution. The thickening factor field can be seen to be well below the max value, indicating the mesh is able to meet the prescribed criterion of minimum $n = 5$ points in the flame front without having to thicken the flame excessively. The efficiency function is pronounced in the local premixed regions where the flame front undergoes strong wrinkling and roll-up in the turbulent flow, as expected.

Figure 7.6(a,b) compare time-averaged and angle-averaged (azimuthal averaging about the cylindrical axis of the chamber) with Abel transformed CH* chemiluminescence. Overall a good agreement can be observed. Nevertheless, some mismatch in the flame-root or anchoring region can be observed where the numerical heat release is quite strong, contrary to emission in the experiments.

Similarly, adjacent Fig. 7.6(c) depicts contour plot of the mean droplet diameter distribution in the chamber. Some droplets do cross the flame front and even reach up to the chamber wall, but it can be argued from Fig. 7.4 that the number density of those is relatively much low. Note that when large number of droplets cross the flame, they burn in an isolated droplet combustion regime (see Fig. 6.3 and discussion there about two-phase spray combustion regimes). A special type of combustion model [323, 61] is required for such a regime, and this phenomenon is neglected.

7.3.1.2 Spray-Flame dynamics under unstable condition

The SLIP and FILM liquid-wall treatments did not matter or affect the flame under stable conditions. However, its impact under dynamic, thermoacoustically unstable conditions (l_c = 280 mm) was found to be critical as to whether or not the self-excited instability is triggered and sustained to reach a limit-cycle oscillation [60]. Only LES with the FILM model was able to predict the instability, in contrast to the SLIP model.

Figure 7.7 shows how pressure fluctuations p' in the chamber (measured on the back-plane) and heat-release rate fluctuation q' grows towards a self-sustained limit cycle in the case of FILM liquid-wall treatment. While for the SLIP, the heat release signal looks mostly incoherent, and thus pressure remains un-correlated. Here in this figure, only the initial growth of the instability is highlighted. On letting the simulation run for longer, the classical observations of the amplitude of pressure oscillation growing, overshooting, and then stabilizing at a stable oscillating limit-cycle amplitude can be observed in the subsequent Fig. 7.8. The limit-cycle frequency f_{LES} = 500 Hz, and amplitude $p'_{LES} = \pm 2000$ Pa retrieved from the LES are in good agreement with experimentally measured values: f_{EXP} = 530 Hz and $p'_{EXP} = \pm 1700$ Pa [375].

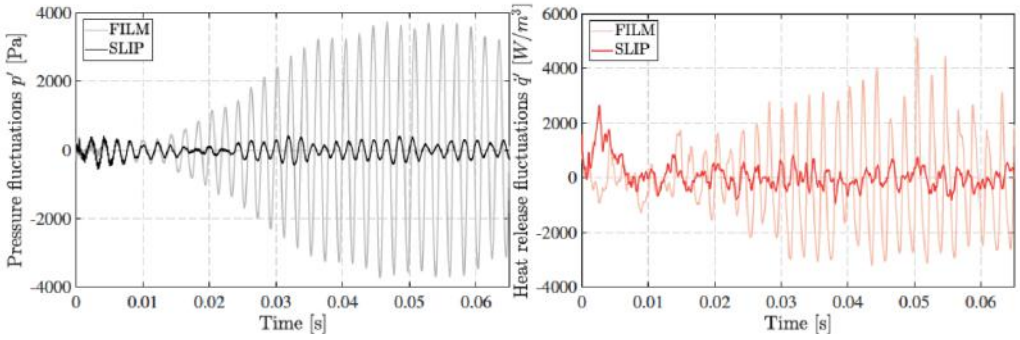

Figure 7.7: Comparison between the FILM and SLIP cases in resonating conditions. (a) Pressure fluctuation of the combustion chamber back-plane as obtained for the two modeling approaches and (b) the temporal evolution of the heat release rate fluctuations. Both quantities are given as a function of time starting from the same initial flame, and only the liquid-wall interaction treatment differs. Reproduced from [60].

As for the flame shape, to remove random oscillations due to turbulence and retrieve only the coherent limit cycle oscillation, LES results are first phase-averaged over 10 cycles (Fig. 7.9). Note that in the following, the phase $\Phi \in [0, 2\pi]$ refers to the pressure signal oscillation for which $\Phi = \pi/2$ corresponds to the positive peak of heat release. Simulation results are finally compared to the experimental CH*

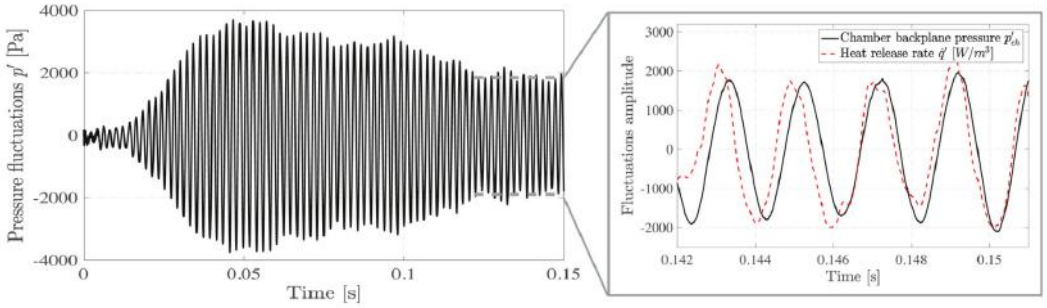

Figure 7.8: Pressure oscillation, measured at the combustion chamber backplane, overshooting and then stabilizing into a limit cycle. Right zoomed image on last few cycles that is in-phase with the global heat-release verifying the Rayleigh criterion. From [60].

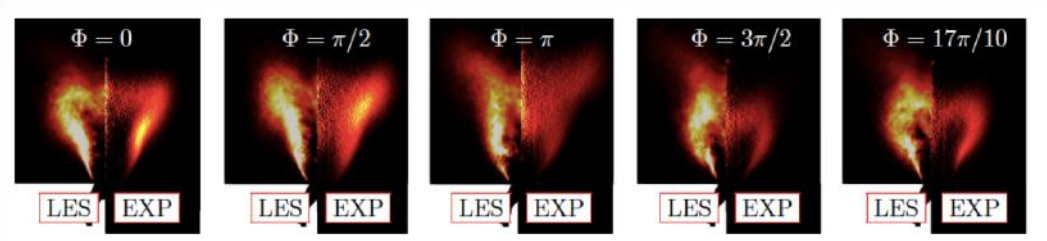

Figure 7.9: Heat release rate phase averaged images in comparison with the experimental CH* chemiluminescence [375]. LES colormap: $\dot{q} \in [0, 250]$ MW/m^3. Figure taken from [60].

images [375] in Fig. 7.9, and a good agreement of the overall flame shape, its extent, as well as its anchoring position is evident.

7.3.1.3 Liquid Film Dynamics

Figure 7.10 illustrates the mechanism on how and why the FILM treatment (see Sec. 6.2.3) is successful in predicting the limit-cycle. It correctly models and captures the essential physical liquid-film and acoustic coupling responsible for the instability. Fig. 7.10(b) displays the non-dimensional film thickness fluctuation $h'/\bar{h}$ as a function of the local spatial coordinate ξ (Fig. 7.10(a)), and obtained at different phases of the limit-cycle period. This film height (or accumulation of liquid droplets in the film) is clearly fluctuating in phase with the acoustic oscillations. As a consequence, the number of particles released and their velocity (which scales with the film height, see Eq. 6.22) at the injector lip is tuned with the acoustic wave.

Figure 7.10(d) depicts how the equivalence ratio at the flame root also oscillates almost in phase corresponding to the film height over an instability cycle, modulating the fuel fed to the flame and thus aiding in sustaining the limit-cycle. In Fig. 7.10(b),

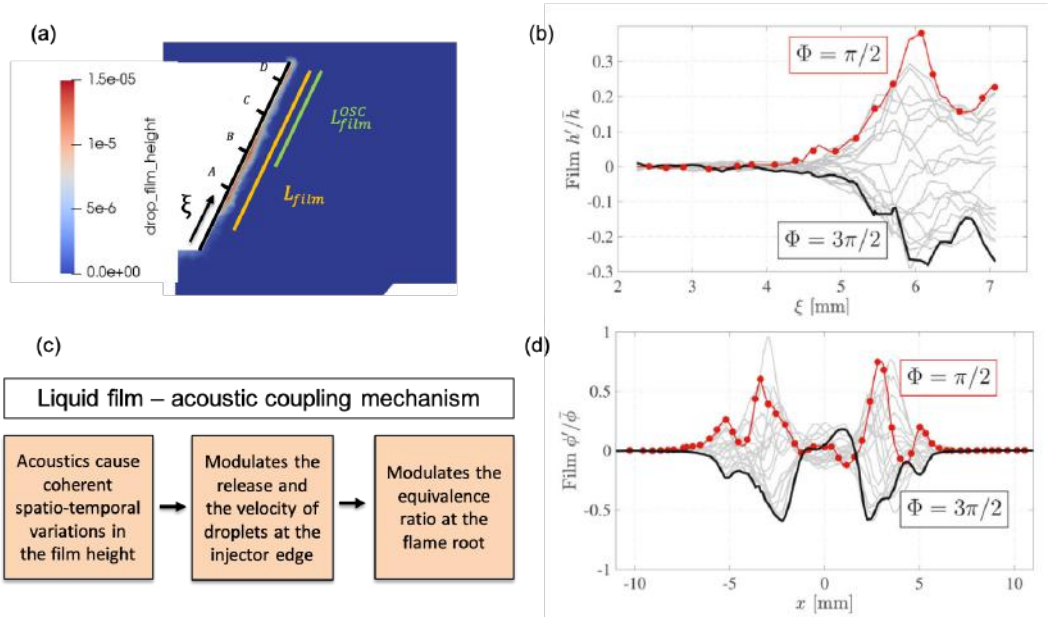

Figure 7.10: Film dynamics on the conical injector pre-filming surface over an acoustic cycle: (a) Instantaneous image of the film height h_f, and the local coordinate ξ along the inclined wall. (b) Coherent film height modulation along ξ. (c) Summary of the liquid-film and acoustic coupling mechanism. (d) Equivalence ratio oscillation at the flame root $z = 2.5$ mm above the back-plane (radial plot along x coordinate).

at $\Phi = \pi/2$ when the fuel accumulation (film height) is maximum, the equivalence ratio is also maximum around that phase and vice-versa at $\Phi = 3\pi/2$.

(Also see Figs. 20, 21 in [60] for the liquid-volume fraction (α_l), and droplet velocity magnitude ($|\vec{v}_p|$) contour plots indicating variations in the fuel injection pattern from the injector lip into the chamber under SLIP and FILM treatments).

7.3.2 Impact of the Injection Angle

Lo Schiavo et al. [201], in a later study, examined the sensitivity of self-excited instability LES results to the spray injection angle - an empirical user-input in the FIM-UR model (Sec. 7.2, 6.2.2) that is difficult to characterize and prone to uncertainties.

To this scope, three values of the half-cone spray angle θ: $\theta = 35°$ (Case-A), $\theta = 45°$ (Case-B) and $\theta = 60°$ (Case-C) are considered. The intermediate angle, $\theta = 45°$, is the baseline case, and was the value also used in the previous work [60] that was summarized in the preceding subsections.

A direct consequence of a small change in the spray angle (by $\pm 10°$ to $15°$ from the baseline value) is its effect on the velocity components of droplets set by the

FIM-UR model. Fig. 7.11, plots the axial (u_z^l) and azimuthal (u_θ^l) velocity determined by the FIM-UR model for given fuel mass-flow-rate and atomizer parameters. FIM-UR keeps the radial component $u_r^l = 0$. The strong impact on velocity components individually and in terms of the relative ratio of their magnitudes is quite evident. Particularly note an almost order of magnitude difference for the azimuthal component for the range of θ values considered.

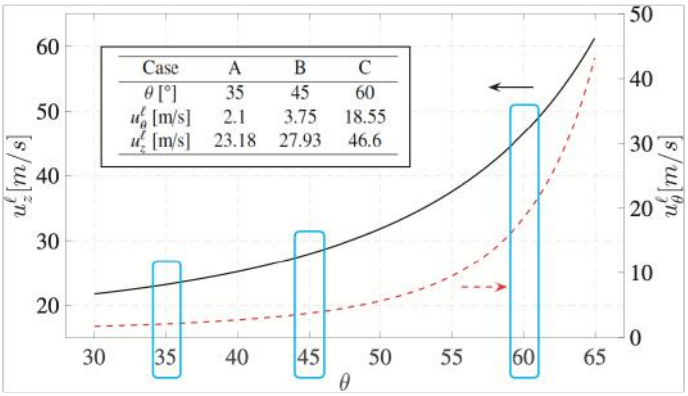

Figure 7.11: Variation in the axial and azimuthal velocity components of the Lagrangian droplets injected by the FIM-UR model with injection angle. Radial component is zero. (See [310] for details of how droplet velocity is determined).

Analogous to SLIP vs. FILM, the impact of injection angle on the spray flame under non-oscillating stable conditions is only minor. However, under unstable operating conditions, the injection angle influences the stability. Compared to baseline case-B, decreasing the angle to $\theta = 35°$ actually stabilizes the system, while increasing it to $\theta = 60°$ sustains the instability with slight modification in the frequency and amplitude of the limit-cycle.

Another important impact of change in the injection angle (θ) is that it actually modifies the film dynamics on the conical wall considerably by moving the point of impingement, as could be imagined from the illustration in Fig. 7.10. In fact, in the case of the $\theta = 35°$, it is observed that droplets hardly interact with the wall, and most droplets directly enter into the chamber. It breaks the synchronization between acoustics and the liquid film, which could explain the stabilization of the combustor (for this configuration and operating conditions). On the other hand, for the $\theta = 60°$ case, the point where the fuel jet impinges on the injector wall could be visualized moving upstream (than in Fig. 7.10(b)) as the spray angle widens. Coherent spatio-temporal oscillation of the film is still observed as it continues to synchronize with the acoustics. Just that, the phase of oscillating film height (and thus the phase of release of droplets) at the edge is now different from the baseline

case. See [201] for more details.

7.4 Forced SICCA-spray Flame LES: Results and Discussion

This section will discuss the results of forced SICCA-spray flame in an attempt to predict its FTF. K. Prieur [375] in his thesis at EM2C, experimentally measured the FDF of this flame and also attempted to compute it back then with AVBP using Euler-Euler (EE) [379, 312] LES formalism. The FTF computed and reported for a few discrete forcing frequencies, and amplitudes were not satisfactory in comparison to experimental values, to say the least. While the phase was more or less predicted correctly, the gain was largely underpredicted by more than 50%. This was also one of the motivations to revisit the problem of forcing the spray flame in LES and try to predict its FTF (here, however, using the Euler-Lagrange (EL) framework).

7.4.1 Reference Experimental FDF measurements

The only experimental reference available for validating forced Euler-Lagrange LES of SICCA-spray flame when this work was initiated was the FDF measurements reported in the thesis of K. Prieur [375]. Recently, new measurements of the FDF were made as part of the works of Soundararajan et al. [94], Vignat [377], and this data was made available from the EM2C lab[1]. This newer data is used for validation and is briefly described next.

To obtain the FTF/FDF, the experimental rig in Fig. 7.1 is acoustically excited utilizing two loudspeaker driving units mounted in the plenum [94, 377]. For FDF measurements, the driver units are operated at six different voltage levels $V_{0,pp}$ (500 mV to 1300 mV in increments of 200 mV), and a linear frequency sweep is performed from 300 Hz to 800 Hz, at each level. It is important to note that, for a given voltage across the driver loudspeakers, the hot wire probe (HW1) in Fig. 7.1 measures different velocity fluctuations $u'/\bar{u}$ levels for different forcing frequencies. Initial FDF measurements by Prieur [375] was defined with respect to the velocity perturbations at HW1. Therefore it actually represented the *Injector+Flame* describing function ($\mathcal{F}_{IF}$), i.e., it inherently included the dynamic acoustic response of the swirl injector. However, in these new measurements [94], the response of the flame ($\mathcal{F}_F$) was isolated from the swirl injector response ($\mathcal{F}_I$). It was achieved with the help of the burner transfer function ($\mathcal{F}_I$) characterized under *cold flow* conditions by correlating the velocity fluctuations measured at a location (HW2) near the flame root just above the injector lip with velocity fluctuations registered at HW1

[1]Courtesy Preethi R. Soundararajan (also ANNULIGhT ESR), G. Vignat, D. Durox, A. Renaud and S. Candel for useful discussions and sharing SICCA-spray experimental data.

upstream in the plenum. Subsequently, the injector+flame describing function is rescaled (or corrected) to obtain the flame only describing function as below. See [94] for more details on this.

$$\mathcal{F}_F = \mathcal{F}_{IF}/\mathcal{F}_I \tag{7.1}$$

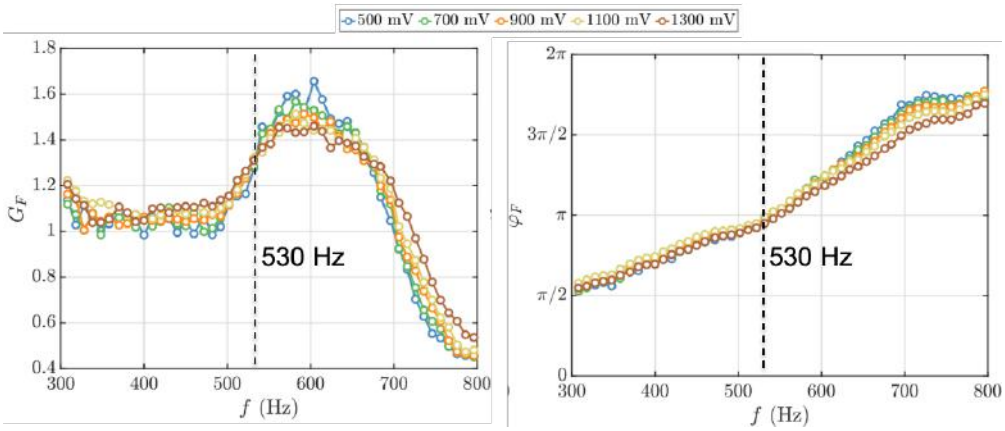

Figure 7.12: The experimental gain and phase plots of the FDF ($\mathcal{F}_F$) defined with respect to the velocity fluctuations at HW2 near the flame root (Fig. 7.1) for different loudspeaker driving unit voltages. Note that the phase is unwrapped, and the Fourier convention used is not the same as in STORM. Data generated as a part of the works [94, 377].

Figure 7.12 shows the extracted gain and phase of the scaled describing function ($\mathcal{F}_F$) as a function of the excitation frequency and voltages. Note that the HW2 hot-wire is the reference location for $\mathcal{F}_F$, and it is 2.5 mm above the backplane and 3 mm away from the central axis (Fig. 7.1).

This exercise of characterizing ($\mathcal{F}_F$) is also supported by the conclusions of Truffin and Poinsot [371] who recommended using a reference location close to the flame in such system response identification (irrespective of the approach viz., experiments or LES).

7.4.2 Inlet Forcing vs. Outlet Forcing

Both inlet and outlet forcing were explored to calculate the flame response with LES, and the equivalence of these two approaches is touched upon here in this subsection. The flame is acoustically forced by pulsing either the velocity at the inlet boundary or the outlet pressure at a specific frequency. Its amplitude is adjusted to reach the desired velocity fluctuation level at the FTF reference location (HW2 for $\mathcal{F}_F$ in the current context).

In LES, FTF ($\mathcal{F}_F$) is determined with reference to velocity signal at HW2 location, in the presence of flame (hot conditions). In other words, the HW2 location

Method , (Forcing)	$\mathcal{F}_F$, Gain [-]	$\mathcal{F}_F$, Delay [ms]	$\mathcal{F}_F$, Phase [rad]	Ref. HW2 $u'_{rms}/\bar{u}$	Ref. HW1 $u'_{rms}/\bar{u}$
LES, (inlet)	0.98	0.64	0.68π	0.13	0.54
LES, (outlet)	1.03	0.69	0.70π	0.13	-
EXP, (inlet)	1.27	0.90	0.96π	0.13	0.40

Table 7.1: FTF ($\mathcal{F}_F$) obtained by forcing the flame in LES from the inlet and the outlet at 530 Hz, along with available experimental data for forcing corresponding to (530 Hz , 500 mV).

velocity signal in LES with flame (in hot conditions) is assumed to be equivalent to the HW2 signal in experiments under cold conditions that helps extract flame only transfer function $\mathcal{F}_F$.

For the analysis, low-amplitude forcing (corresponding to the 500 mV case) at **530 Hz** frequency is considered at first. This frequency coincides with the frequency of the self-sustained limit-cycle observed in the unstable configuration ($l_c = 280$ mm) both in experiments and LES, as discussed in the previous Sec. 7.3.

In experiments [94] forcing is done only from the inlet side. When the flame in stable configuration ($l_c = 165$ mm) was forced at this operating point (500 mV, 530 Hz), $\mathcal{F}_{IF}$ transfer function is obtained (w.r.t HW1). The velocity fluctuation levels recorded in the plenum by HW1 $u'_{1,rms}/\bar{u}_1 = 0.40$. Now for $\mathcal{F}_I$, the burner is also forced under cold condition and velocity fluctuations recorded at HW2 is of amplitude $u'_{2,rms}/\bar{u}_2 = 0.13$, while maintaining $u'_{1,rms}/\bar{u}_1 = 0.40$ at HW1. The last row of Table. 7.1 gives the scaled flame response finally obtained as per Eq. (7.1). Mentioned are the gain, phase (and delay) of $\mathcal{F}_F$ flame transfer function, and the recorded $u'_{rms}/\bar{u}$ amplitudes at HW1 and HW2 (cold) reference locations.

The first row in Table. 7.1 lists the FTF ($\mathcal{F}_F$) obtained from LES by pulsing the system from *inlet boundary*. It must be noted that the velocity pulsation amplitude at the inlet boundary is tuned so as to reach the velocity fluctuation level at the flame root (HW2 location) equal to that in experiments, i.e., $u'_{2,rms}/\bar{u}_2 = 0.13$. Under this condition, and after ensuring statistical convergence is reached, velocity amplitude recorded in plenum at HW1 is $u'_{1,rms}/\bar{u}_1 = 0.54$, much higher than experimental value of 0.40 as mentioned in Tab. 7.1. In fact, the experience has been such that the velocity amplitude at the inlet had to be raised to higher and higher values to reach desired velocity amplitude at HW2. This indicates a probable non-perfect representation by the computational model, particularly the acoustics resolution in plenum and swirler/injector domains. Two points in this regard: (i) The impedance at the inlet boundary is indeed imprecise, considering the fact that the upstream part

of the rig is not modeled. The acoustic environment inside the plenum in LES might not be fully identical to that in the experiment. (ii) This result also suggests that the discretization level chosen for the swirler vanes could be probably insufficient to correctly capture the transmission/reflection of acoustic waves through the swirled injector.

It should, however, be stressed that the above inaccuracies did not influence the prediction of self-sustained limit-cycle in the work of Lo Schiavo et al. [60, 201, 62]; most likely because it is a *decoupled* chamber thermoacoustic mode where the flame couples with the first (quarter-wave) chamber acoustic eigenmode and is weakly influenced by the plenum acoustics.

The second row in Tab. 7.1 gives the FTF computed via outlet forcing, and the result is fairly consistent with that from inlet excitation. This outcome is in line with the results of Gaudron et. al. [380], who experimentally investigated inlet and outlet forcing for a turbulent swirling gaseous flame. They concluded that the two approaches are equivalent as long the FTF reference location is close to the flame, which is indeed true in the current case.

Signal processing for computing the FTF:

As discussed earlier in Ch. 1, Sec. 1.4.2, FTF is defined as:

$$\mathcal{F}(\omega) = \frac{\dot{Q}'(\omega)/\bar{\dot{Q}}}{u'/\bar{u}} = G(\omega)\, e^{-j\varphi(\omega)} \tag{7.2}$$

The FTF above is the ratio of global (volume integrated) heat release and velocity fluctuation at some reference location, *in the frequency domain*. Therefore, for both inlet/outlet forced cases, the FTF is computed by transforming the temporal signals into frequency-space and taking the ratio of Fourier coefficients of heat release and velocity signals for the single target frequency - here 530 Hz. In other words, the FTF computation reduces to the analysis of time discrete signals recovered from the LES. Due to computational cost, the LES signals typically have very short durations. Therefore, care has to be taken to ensure the quality of the signals and their processing:

1. Foremost, by verifying that the *initial transients* are removed from the signals used to compute FTF and confirming that statistical convergence is reached. Besides, the signal length should be such that it contains enough number of cycles of the target frequency. The longer the signal, the better the quality of the Fast Fourier Transform (FFT) and subsequent spectral analysis.

2. Instead of using velocity signal at just one probe point in the computational domain, *multiple acoustically equivalent probes* are defined and ensemble-averaged to get the reference velocity signal. This ensures that the impact of noise or

turbulent non-coherent fluctuations on acoustic signal and the FTF computation is minimized. It yields an FTF that is more robust and reliable.

The above fundamental signal processing considerations and more are taken into account in this study to ensure signal quality, with the help of a dedicated *spectral analysis tool*[2] developed by the COOP team at CERFACS.

This work considers 8 acoustically equivalent reference probes placed circumferentially (at HW2 location) near the flame root. The following shows the signals used for computing the FTF for one case (530 Hz, outlet forcing).

Figure 7.13 shows the temporal signal of global heat release ($Q'/\bar{Q}$) oscillation and the raw fluctuating velocity signal from probe1 out of 8 equivalent probes mentioned above. The velocity signal above the injector lip (or at the flame root) is noisy owing to high-frequency non-coherent turbulent fluctuations. For the sake of visualization, overlaid on it is the plot of the same signal after low-pass filtering around the target frequency of 530 Hz highlighting the coherent acoustic oscillation.

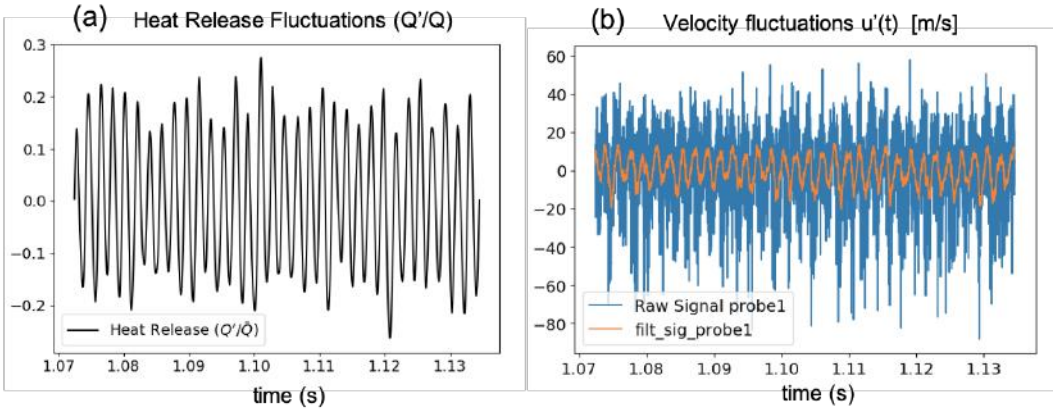

Figure 7.13: Outlet forcing at 530 Hz case from Table 7.1. (a) Global heat release signal from the LES and, (b) Raw and low-pass-filtered velocity fluctuation signal from probe-1 for example.

Figure 7.14(a) shows the FFT of the heat release and velocity signals - the latter being an ensembled-averaged signal over 8 equivalent reference probes. A clear monotone peak at 530 Hz forcing frequency of normalized Fourier coefficients magnitude (amplitude) can be observed. The adjacent Fig. 7.14(b) plots the Fourier coefficients of *individual* fluctuating velocity signals from 8 reference probes (the colored dots) along with that of global heat release signal (black square) on a complex plane. The purple circle and the green line indicate the amplitude and phase of the Fourier coefficient of the velocity signal averaged over all the probes. Since all the individual probes fall together near their average value, it highlights their

[2]SATIS: A tool for Spectral Analysis of Time Signals (https://cerfacs.fr/coop/satis)

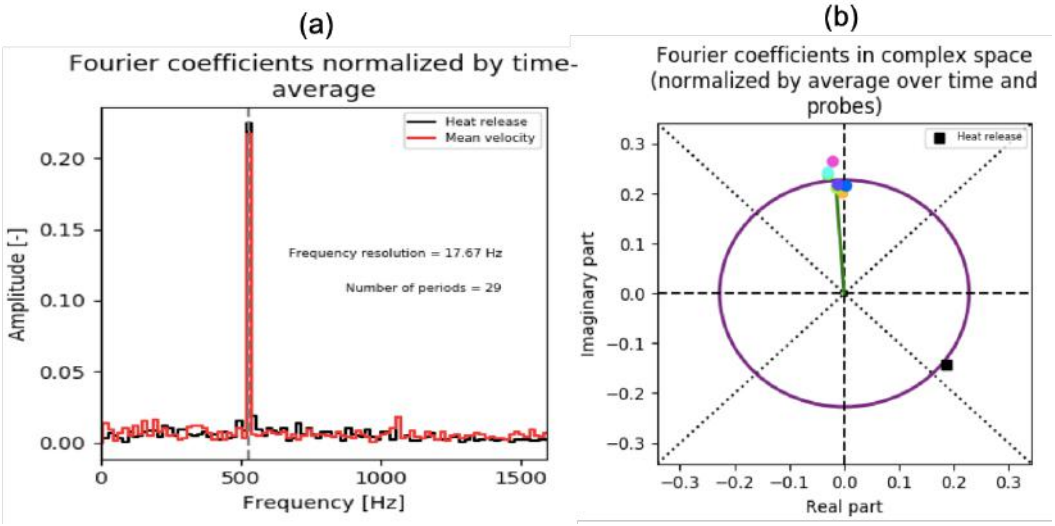

Figure 7.14: (a) Fast Fourier Transform (FFT) of the signals in Fig. 7.13 (velocity is ensemble-averaged over 8 equivalent reference probes before FFT). (b) Fourier coefficients (at 530 Hz) of the heat release and velocity signals from individual probes on a complex plane.

invariability (or their equivalence). This diagnostic can help identify and remove "bad" probes (whatsoever the reason) and helps improve the confidence in reference signals and eventually the computed FTF.

Finally, in closing this subsection, the computed FTF after exciting the flame at 530 Hz (from inlet and outlet) is compared with the reference experimental FTF given in Tab. 7.1. While the numerical FTF from inlet/outlet forcing is more or less consistent, verifying the equivalence between the two approaches when the reference location is close to the flame [371, 380], the FTF gain and phase (or delay) both are underpredicted by about 20-30 %. The following subsection will try to investigate this discrepancy by analyzing the sensitivity of the FTF to spray injection angle input parameter.

7.4.3 Impact of the Injection angle on FTF

Analyzing the sensitivity of FTF to the injection angle is motivated by previous work of Lo Schiavo et al. [201] where the impact of the spray injection angle on the self-sustained LES limit cycle predictions was investigated (briefly discussed in Sec. 7.3.2).

As mentioned earlier, this empirical input of the FIM-UR model [310] is not easy to characterize and prone to many uncertainties. Correlations exist in the literature [58], and they could be used to prescribe this angle in FIM-UR; however, such correlations are not universal. In reality, the fuel spray angle and subsequent

atomization process strongly depend on (or are sensitive to) many operating conditions. For example, fuel line pressure drop, physical properties of the fuel [381, 382] and, as recently observed in the SICCA-spray experiments at EM2C lab [377, 213], also to the interaction of the liquid spray with the surrounding strong swirling flow causing the explosive breakup of the fuel [377, 213, 383, 384]. Besides, it is also expected that the spray angle and atomization respond dynamically to acoustic oscillations based on these recent works [63, 65, 385]. The spray angle and atomization hence remain quite susceptible to variations. Therefore, it would be worthwhile to investigate the influence of this parameter in the current numerical framework.

In a relevant study by Cunha Caldeira Mesquita et al. [386, 387] at EM2C, the authors demonstrated how the injection angle parameter influenced the spatial distribution of droplet size statistics (pdf) in the combustor, and the liquid velocity field in the configuration simulated. The study highlighted how the angle parameter had to be calibrated for correct reproduction of the numerical spray consistent with experimental measurements.

Spray injection angles in the range: $\theta = 35°$, to $60°$ are considered, where the $\theta = 45°$ is the baseline case discussed in previous Sec. 7.4.2. For this analysis, flame transfer functions are computed by adopting outlet-forcing at 530 Hz.

Figure 7.15 plots the variation of computed global FTF gain and delay as a function of θ. In reference to the baseline case of $45°$, reducing or increasing the spray angle yields a peculiar opposing trend of the gain and phase. At $\theta = 35°$, the FTF gain is reasonably close to the experimental value, while the agreement between the time-delay (or phase) is the worst. For $\theta = 60°$, a contrary situation appears. Although time-delay matches well, the discrepancy in the gain is maxed for the range of θ values considered.

To further analyze these results, the LES data are post-processed using three-dimensional Dynamic Mode Decomposition (DMD) [388] to reconstruct the dynamics of the system at the forcing frequency and get a detailed view into the coherent oscillation patterns of the flame heat release. The DMD is performed using about 280 3D solution snapshots, covering about ≈ 30 acoustic cycles.

For discerning the variations in the local flame response due to different injection angles, a *local FTF* is constructed as:

$$FTF_{local}(\omega, \vec{x}) = \frac{\hat{q}(\omega, \vec{x})/\bar{q}(\vec{x})}{\hat{u}(\omega, x_{ref})/\bar{u}(x_{ref})} \tag{7.3}$$

where ($\hat{}$) and ($\bar{}$) denote the oscillating, frequency-domain DMD variables (mode shape) and its mean respectively. Local FTF in Eq. 7.3 is correlating the oscillating heat-release mode $\hat{q}(\omega, \vec{x})$ mode (at 530 Hz forcing frequency) to local fluctuating velocity $\hat{u}(\omega, x_{ref})$ at HW2 reference location.

Figure 7.16 shows the field of magnitude and phase of the local FTF defined above. Considerable differences in the oscillating HR patterns can be observed due

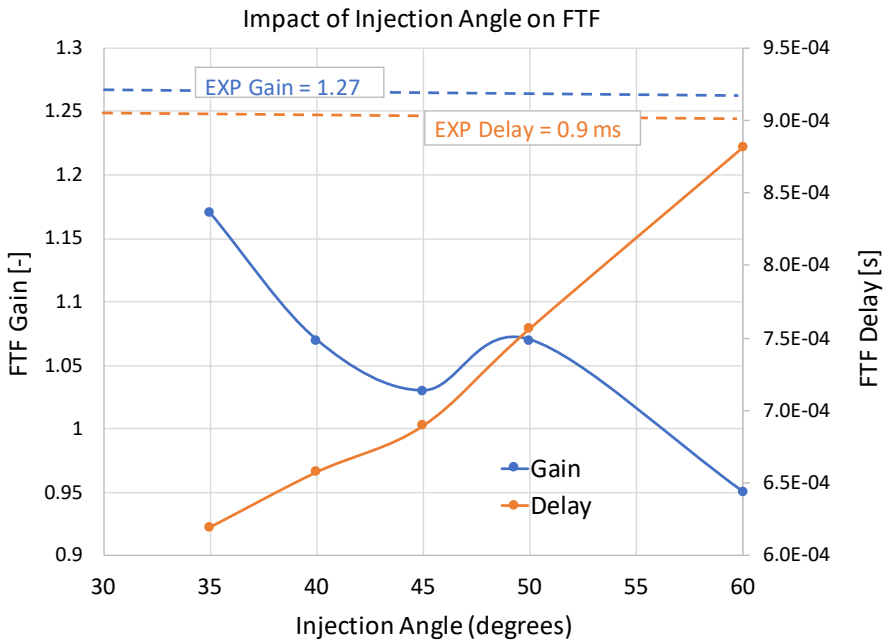

Figure 7.15: Opposing trend of the global FTF Gain and Delay (or phase) with injection angle in reference to experimental values.

to the variations in the prescribed injection angle. Thanks to this local FTF view, a possible link between the global FTF trend (Fig. 7.15) and the fuel droplet dynamics is qualitatively discussed in the following. The arguments presented are supported by Fig. 7.17 which depict instantaneous fuel liquid volume fraction (α_l) contours at different phases of pressure oscillation (at injector outlet or chamber backplane) for two extreme injection angles.

In general, the Lagrangian droplets impinging on the conical injector wall lose their initial momentum due to the film treatment and also couple with the acoustic oscillations as demonstrated by Lo Schiavo et al. [60, 201] and discussed in previous Sec. (7.3.1, 7.3.2). Droplets are then released at a slower speed and in modulated manner into the chamber as per the synchronization between the film and acoustic waves. It was discussed how injection angle modifies the impingement point on the conical wall and, in turn, alters the length of the film and its properties (height and speed). This change in film dynamics directly influences the speed and the phase at which the droplets are released from the injector lip and, consequently, the fuel supplied to the flame root. Similar behavior is expected in the current forced conditions as well.

$\theta = 35°$ case: In this case, from Figure 7.17 one can observe that the liquid fuel droplets hardly interact with the wall and are injected almost directly into the chamber, penetrating deeper due to their high speed. As a result, the liquid

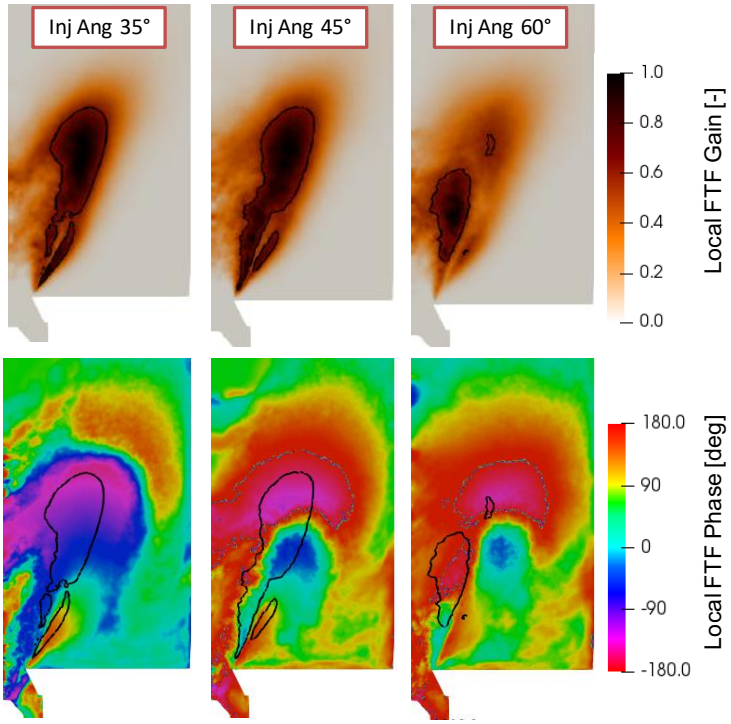

Figure 7.16: Local FTF gain and phase-delay (Eq. 7.3) and its variation with spray injection angle. Gain is normalized by its max value. Black contour line is the 60% of max value thus enclosing region of most intense heat release fluctuations.

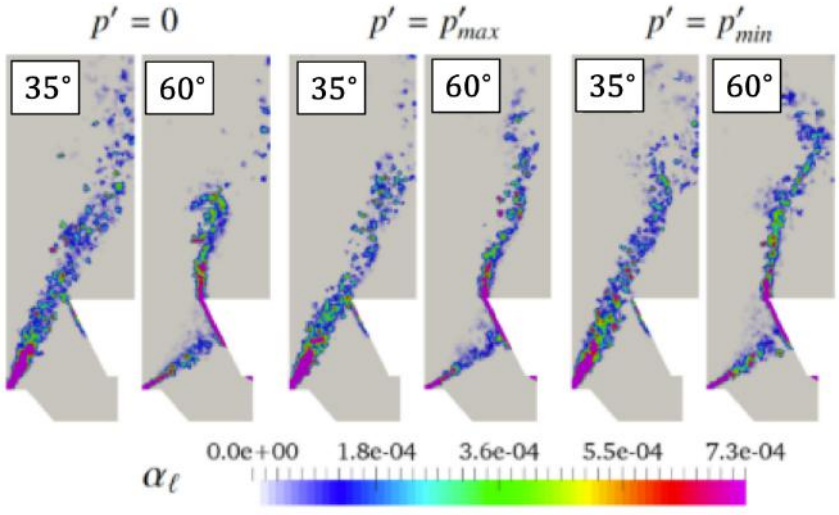

Figure 7.17: Liquid volume fraction α_l at three different phases of pressure oscillation for injection angles: $\theta = 35°$ and $\theta = 60°$.

fuel post evaporation and mixing burn largely in the downstream flame tip region: evident from the intense heat release rate (HRR) fluctuation in that region in Fig. 7.16. Furthermore, the fuel burns rapidly in this region, as indicated by the high-intensity heat-release perturbations being almost in-phase (Fig. 7.16). Though this phase value is smaller than the expected global phase delay (Fig. 7.15), it still results in an overall constructive phase interference of the local flame response, thus explaining the high global FTF gain than other injection angles.

$\theta = 60°$ case: For this other extreme case all the fuel droplets (true for $\theta = 45°$ also) hit the injector wall, and form a film before they are released into the chamber (see Fig. 7.17). The HRR fluctuations are overall moderate in strength and radially more spread out than $\theta = 35°$. Note that the small region of intense perturbations highlighted in Fig. 7.16, even though closer to the injector, the global FTF time-delay that is yielded in this case is longer than for $\theta = 35°$ and in better agreement with experimental value as noted in Fig. 7.15. The global FTF time-delay computed in this case is 8.86 ms, which corresponds to a global phase $\varphi = 0.94\pi$ rad $= 170°$ ($\varphi = 2\pi f\tau$, for $f = 530$ Hz). It is confirmed from the phase plot in Fig. 7.16 that the high-intensity region enclosed by the black contour and a significant downstream part of the flame is indeed oscillating at this phase value, which matches with measured phase value (0.96π rad for a time-delay of 0.90 ms.) As for the global gain, in this case, it is the outer branch of the flame and the flame root region, which are in phase opposition (green color in the phase plot in Fig. 7.16) that brings down the predicted global gain to a low value.

$\theta = 45°$ case: From $\theta = 35°$ to $\theta = 45°$, the slow, modulated release of droplets from the injector lip, explains the enhanced intensity of HRR oscillation in the flame root and increase in global time-delay. In general, for the local flame responses, intermediate observations can be made in this case compared to previously discussed ($\theta = 35°$ and $\theta = 60°$) cases. Overall, different parts of the high-intensity region oscillate in distinct phases.

In closing, the above local FTF analysis substantiates the peculiar opposing trend (Fig. 7.15) of the global FTF determined from the standard signal processing described earlier. Even if it may not thoroughly and clearly explain the observations, the analysis does provide some insight into the behavior of the flame response and its sensitivity to injection angle.

7.4.4 FTF at other frequencies

All the FTF results discussed so far were obtained by forcing the flame at the frequency of 530 Hz. A couple of other frequencies were checked as well: 360 Hz and 644 Hz. Similar results are obtained at these frequencies too. Inlet/outlet forcing yields approximately the same FTF; however, a discrepancy of about 20-30%

(underprediction of both global gain and time-delay) against experimental values prevails. An analogous study of the sensitivity to injection angle was not performed at these frequencies.

7.5 Conclusions and Perspectives

Previous numerical work of Lo Schiavo et al. [60, 201] at CERFACS on SICCA-spray burner revealed that the coupling and synchronization of the liquid film forming on the conical injector wall with acoustic waves were at the core of triggering and sustaining self-excited thermoacoustic limit cycle. It was successfully predicted in the LES with a good agreement of frequency and amplitude with experiments, thanks to the FILM model [294] for Lagrangian droplets and boundary wall interaction.

This work simulates the acoustic forcing of the turbulent swirling SICCA-spray flame using the Euler-Lagrange (EL) LES modeling framework. The objective was to compute the Flame-Transfer-Function (FTF) and assess the suitability of the EL approach and other two-phase combustion models for such a system identification problem.

The FIM-UR liquid fuel injection model [310] employed has a mean spray injection angle as an input parameter. It was discussed that this angle is prone to several physical uncertainties. The sensitivity of FTF predictions to this parameter was evaluated. The computed global FTF showed this peculiar opposing trend of gain and time delay. A DMD-based analysis of local flame response provided some insight into the observed behavior.

Despite the encouraging results obtained in self-sustained limit-cycle instability simulations, the forced mode of operation is certainly exhibiting difficulties. FTF obtained for (baseline) 45° injection angle deviates from experimental value by about 20-30%.

Another related point, although not discussed in this chapter but is probably worth a mention, is that the FTF predictions are even more sensitive to the prescribed droplet size distribution PDF in the FIM-UR model than injection angle. So much so that it even brings noticeable changes in mean flame under thermoacoustically stable conditions. Similar sensitivity was observed by E. Lo Schiavo [60, 201], where an unstable simulation was stabilized by somewhat changing the injection droplet size distribution.

The flame response numerically retrieved remains sensitive in general to the two-phase combustion modeling. Further investigations and model developments are required to improve prediction fidelity. In reality, the liquid-phase processes such as injection, atomization, and evaporation all dynamically respond to pressure and velocity variations due to dynamic conditions prevailing in the combustor (self-excited or forced). Therefore, one potential direction for future work could be to

develop a dynamic injection model that would suitably vary the injection angle or the droplet size PDF, or both. Another potential option could be, though at a significantly higher cost, is to use brute force and explicitly resolve the atomization process.

Chapter 8

Thesis Conclusions and Perspectives

There are broadly two parts to the Ph.D. work accomplished by the author of this manuscript. The first major part dealt with development of STORM (**St**ate-Space **R**educed-**O**rder-**M**odeling) - a low-order thermoacoustic network modeling tool under development at CERFACS. The author has been a co-developer of the tool along with the preceding Ph.D. student Dr. C. Laurent [197, 157, 198]. While the second minor part reports results from the first assessment at CERFACS of acoustically forcing Euler-Lagrange (EL) LES of turbulent swirling spray flame.

PART-1: Development of STORM

STORM is a low-order acoustic-network modeling (LOM) tool developed for studying thermoacoustic combustion instabilities in complex, realistic configurations. It is based on the *state-space* (SS) framework and *generalized modal expansions*. This work falls under the work-package *WP2: Passive control methods and tools* of the EU ITN ANNULIGhT project, with the relevant objective of improving existing network models used in the industry.

One of the main goals behind initiating the development of STORM was to make faster and computationally cheaper thermoacoustic stability analysis of industrially relevant configurations possible. Most low-order network models available in the literature involve drastic simplifications to geometry and are limited to 1D wave-based longitudinal networks and or idealized annulus-like geometries. Real engine combustors, on the contrary, include intricate geometrical complexities, multiple cavities, and components such as the chamber, casing, plenum, swirlers, dilution holes, multiperforated liners, upstream compressor diffuser, and downstream turbine stages, all of them interacting acoustically and thus playing a role in the stability of the engine.

The classical modal expansion (Galerkin projection) method, although known for a while and having the advantage of being capable of handling arbitrarily complex geometries, has not really been a go-to choice for building full-fledged, extensive acoustic networks. A core impediment has been the reliance on an orthogonal rigid-wall (OB) basis. This shortcoming was resolved with the overcomplete (OC) frame

modal expansion technique proposed in the thesis of C. Laurent [157, 197].

OC-frame modal expansion method, a generalization of the classical approach, significantly improves the convergence of the modal expansion. It yields the correct representation of acoustic variables at the interfaces of subdomains in the network, eliminating issues of Gibbs oscillations/fringes arising while using rigid-wall OB bases for the subdomains.

The capability of the tool was illustrated through several examples. The most significant of them was the successful application of STORM to carry out thermoacoustic stability analysis of the SAFRAN engine combustor [199]. The substantial gain in CPU-time requirements (approximately by a factor of 1000) in comparison to Helmholtz solver AVSP in solving the non-linear eigenvalue problem (NLEVP) for thermoacoustic modes is worth noting. The network approach's modularity, flexibility, and low computational cost suggest the feasibility of conducting extensive parametric studies directly on industry-relevant configurations.

The *surface spectral connections* methodology developed [198], allows seamless interconnections between multi-dimensional 3D subdomains over topologically elaborate, curved interfaces (thanks to OC-frame method). In addition, it also presents the opportunity to impose Rayleigh conductivity (or impedance) to model the interface between subdomains as a multi-perforated liner wall (or as a global system impedance boundary).

The flame transfer functions (FTFs), boundary acoustic impedances (Z), the conductivity (K) of acoustic liners, and external damping devices such as Helmholtz resonators all play a critical role in determining the thermoacoustic stability of engines. All of these physical quantities are typically defined in the frequency domain. However, all the network objects in STORM are represented in the time-domain as state-space (SS) sub-models.

It was discussed how the *rational approximation techniques* (Padé approximation or Pole-Residue (Multi-pole) expansion) are indispensable ways for generating time-domain state-space models from frequency response data. Few important physical constraints of reality, BIBO stability, causality, and passivity (if relevant) must be respected when extracting such data-driven low-order dynamical (SS) models (for them to be physically consistent). These constraints are usually enforced in well-established fitting algorithms reviewed from the literature. The algorithms work perfectly fine; however, occasionally, the process may fail, as shown in the example in Chapter 4. It turns out that if data violates one of the above physical constraints, the fitting process fails. Most commonly, it is the causality in frequency response data that is violated. The concept of causality is well interpreted in the time domain. However, causality in the frequency domain implies that the real and imaginary parts of the frequency response function/data are not independent but related through the Kramers-Krönig (KK) dispersion relations. A robust, practical method for detecting

any causality violation in data was identified from the literature and described. Its implementation in STORM is a work-in-progress.

Modal expansion technique in STORM, just like FEM Helmholtz solvers, inherently involves *zero-Mach number* mean flow assumption. DECBC (Delayed Entropy Coupled Boundary Condition), a special network impedance element and its state-space model, was developed within the STORM framework that indirectly models the mean-flow effects, the convected entropy-waves and helps predict the mixed entropy-acoustic instability. DECBC was validated for an analytical 1D case and will be extended to 3D using the surface-spectral-connections methodology in the near future.

For future work, to improve the tool's overall robustness and accuracy, the author believes that it will be worthwhile to investigate and further develop numerical techniques for mitigating problems arising due to system ill-conditioning and the spurious components (because of overcomplete nature of frames). Besides that, one direction that could be undertaken is developing methods and capabilities for state-space representation of Flame Describing Functions (FDFs) and other types of non-linear flame response models. This will facilitate non-linear stability analysis, limit-cycle amplitude predictions, and time-domain simulations with STORM. There is also a potential scope to develop STORM into a comprehensive tool for thermoacoustic analysis of combustors. For instance, by including adjoint methods [389] and exploiting the tool for systematic sensitivity analysis and optimization problems, and Uncertainty Quantification (UQ) [390] studies.

PART-2: Euler-Lagrange (EL) LES of SICCA-spray Flame

Key results from the recent work of a colleague (also an ANNULIGhT ESR) E. Lo Schiavo et al. [60, 201] were reviewed. It demonstrated the importance of the FILM liquid-wall interaction model [294] in predicting self-excited thermoacoustic instability in SICCA-spray burner with Euler-Lagrange (EL) LES. The coupling and synchronization of the liquid-film forming on the conical injector wall with acoustic oscillations was fundamental in triggering and sustaining the limit-cycle instability.

Complementing this work, the author of this manuscript performed forced turbulent swirling spray flame simulations. The objective was to compute the Flame-Transfer-Function (FTF) and assess the suitability of the same EL-LES two-phase combustion modeling framework for such a system identification problem. The sensitivity of the results to the FIM-UR model's injection angle empirical input parameter was closely analyzed, revealing this peculiar opposing trend of the global FTF gain and phase(or time delay).

One of the primary outcomes of the study was that the turbulent swirling SICCA-spray flame is, as such robust to the EL-LES, two-phase combustion modeling parameters under stable operating conditions. However, they exhibit con-

siderable sensitivity, in general, under dynamic (self-excited instability or acoustic forcing). Despite the encouraging results obtained in self-sustained limit-cycle instability simulations, the forced mode of operation is certainly exhibiting difficulties. FTF obtained for the (baseline) 45-degree injection angle deviates from the experimental value by about 20-25%.

Further investigations and model developments are required to improve prediction fidelity. In reality, the liquid-phase processes such as injection, atomization, and evaporation all dynamically respond to pressure and velocity variations due to dynamic conditions prevailing in the combustor (self-excited or forced). Therefore, one potential direction for future work could be to develop a dynamic injection model that would suitably vary the injection angle or the droplet size PDF, or both. Another potential option could be, though at a significantly higher cost, is to use brute force and explicitly resolve the atomization process.

Publications

This Ph.D. work has led to following journal and conference publications:

1. C. Laurent, A. Badhe, and F. Nicoud, "Representing geometrically complex liners and boundaries in low-order modeling of thermoacoustic instabilities," *Journal of Computational Physics*, vol. 428, 2021.

2. A. Badhe, C. Laurent, C. Lapeyre, and F. Nicoud, "Low-Order Thermoacoustic Analysis of Real Engines," in *Symposium on Thermoacoustics in Combustion (SoTiC): Industry meets Academia, (Munich, Germany)*, 2021.

3. A. Badhe, D. Laera, and L. Gicquel, "High-fidelity Large Eddy Simulations of the Flame Transfer Function of a turbulent swirling spray flame," in *10th European Combustion Meeting, (Napoli, Italy)*, 2021.

Bibliography

[1] T. C. Lieuwen and V. Yang, *Combustion Instabilities in Gas Turbine Engines: Operational Experience, Fundamental Mechanisms, and Modeling (Progress in Astronautics and Aeronautics)*. American Institute of Aeronautics and Astronautics, 2005. (Cited on pages 4, 5, 8, 9, 10, 11, 15, 24, 94, 95 and 173.)

[2] A. H. Lefebvre and D. R. Ballal, *Gas Turbine Combustion : Alternative Fuels and Emissions*. Taylor & Francis, 3rd ed., 2010. (Cited on pages 4, 8, 169, 170 and 179.)

[3] D. Dunn-Rankin and P. Therkelsen, eds., *Lean Combustion*. Elsevier Inc., 2nd ed., 2016. (Cited on page 4.)

[4] G. A. Richards, M. M. McMillian, R. S. Gemmen, W. A. Rogers, and S. R. Cully, "Issues for low-emission, fuel-flexible power systems," *Progress in Energy and Combustion Science*, vol. 27, no. 2, pp. 141–169, 2001. (Cited on page 4.)

[5] F. E. C. Culick, "Unsteady Motions in Combustion Chambers for Propulsion Systems," Tech. Rep. December, NATO Research and Technology Organization, 2006. (Cited on pages 5 and 22.)

[6] S. Candel, "Combustion dynamics and control: Progress and challenges," *Proceedings of the Combustion Institute*, vol. 29, pp. 1–28, jan 2002. (Cited on pages 5 and 9.)

[7] T. C. Lieuwen, *Unsteady Combustor Physics*. Cambridge University Press, 2009. (Cited on pages 5, 6, 8, 11, 12, 15, 17, 19, 24 and 173.)

[8] Y. Huang and V. Yang, "Dynamics and stability of lean-premixed swirl-stabilized combustion," *Progress in Energy and Combustion Science*, vol. 35, no. 4, 2009. (Cited on page 5.)

[9] J. O'Connor, V. Acharya, and T. Lieuwen, "Transverse combustion instabilities: Acoustic, fluid mechanic, and flame processes," *Progress in Energy and Combustion Science*, vol. 49, pp. 1–39, 2015. (Cited on pages 5, 10, 13, 24 and 26.)

[10] A. P. Dowling and Y. Mahmoudi, "Combustion Noise," *Proceedings of the Combustion Institute*, vol. 35, pp. 65–100, jan 2015. (Cited on pages 5, 7, 18 and 132.)

[11] T. Poinsot, "Prediction and control of combustion instabilities in real engines," *Proceedings of the Combustion Institute*, vol. 36, no. 1, pp. 1–28, 2017. (Cited on pages 5, 9, 10, 15, 174 and 192.)

[12] W. Polifke, "Modeling and Analysis of Premixed Flame Dynamics by Means of Distributed Time Delays," *Progress in Energy and Combustion Science*, vol. 79, 2020. (Cited on pages 5, 15, 24, 25, 94, 95, 99, 100, 101, 128 and 192.)

[13] T. Poinsot and D. Veynante, *Theoretical and Numerical Combustion*. 3rd ed., 2012. (Cited on pages 5, 6, 10, 12, 13, 14, 15, 16, 17, 19, 21, 37, 38, 141, 174, 175, 187, 188, 189, 190, 192 and 196.)

[14] F. Nicoud and T. Poinsot, "Thermoacoustic instabilities: Should the Rayleigh criterion be extended to include entropy changes?," *Combustion and Flame*, vol. 142, no. 1-2, pp. 153–159, 2005. (Cited on pages 6 and 141.)

[15] L. Magri, M. P. Juniper, and J. P. Moeck, "Sensitivity of the Rayleigh criterion in thermoacoustics," *Journal of Fluid Mechanics*, vol. 882, 2020. (Cited on pages 6 and 141.)

[16] T. Lieuwen and B. T. Zinn, "The role of equivalence ratio oscillations in driving combustion instabilities in low NOx gas turbines," *Symposium (International) on Combustion*, vol. 27, pp. 1809–1816, jan 1998. (Cited on page 6.)

[17] S. Hemchandra, "Premixed flame response to equivalence ratio fluctuations: Comparison between reduced order modeling and detailed computations," *Combustion and Flame*, vol. 159, pp. 3530–3543, dec 2012. (Cited on page 6.)

[18] A. Albayrak and W. Polifke, "An analytical model based on the G-equation for the response of technically premixed flames to perturbations of equivalence ratio," *International journal of spray and combustion dynamics*, vol. 10, no. 2, pp. 103–110, 2018. (Cited on pages 6, 25 and 94.)

[19] T. Schuller, D. Durox, and S. Candel, "A unified model for the prediction of laminar flame transfer functions: comparisons between conical and V-flame dynamics," *Combustion and Flame*, vol. 134, pp. 21–34, 2003. (Cited on pages 6, 25 and 94.)

[20] P. Palies, T. Schuller, D. Durox, and S. Candel, "Modeling of premixed swirling flames transfer functions," *Proceedings of the Combustion Institute*, vol. 33, no. 2, pp. 2967–2974, 2011. (Cited on pages 6, 25, 94, 114, 115 and 116.)

[21] S. Hemchandra, N. Peters, and T. Lieuwen, "Heat release response of acoustically forced turbulent premixed flames - Role of kinematic restoration," *Proceedings of the Combustion Institute*, vol. 33, no. 1, pp. 1609–1617, 2011. (Cited on page 6.)

[22] R. S. Blumenthal, P. Subramanian, R. I. Sujith, and W. Polifke, "Novel perspectives on the dynamics of premixed flames," *Combustion and Flame*, vol. 160, no. 7, pp. 1215–1224, 2013. (Cited on pages 6 and 100.)

[23] T. Steinbacher, A. Albayrak, A. Ghani, and W. Polifke, "Response of premixed flames to irrotational and vortical velocity fields generated by acoustic perturbations," *Proceedings of the Combustion Institute*, vol. 37, pp. 5367–5375, jan 2019. (Cited on page 6.)

[24] V. Acharya and T. Lieuwen, "Nonlinear response of swirling premixed flames to helical flow disturbances," *Journal of Fluid Mechanics*, vol. 896, no. A6, 2020. (Cited on page 6.)

[25] S. Candel, D. Durox, T. Schuller, J.-F. Bourgouin, and J. P. Moeck, "Dynamics of Swirling Flames," *Annual Review of Fluid Mechanics*, vol. 46, pp. 147–173, jan 2014. (Cited on pages 6, 7, 15, 24, 94, 95, 98 and 192.)

[26] P. Palies, D. Durox, T. Schuller, and S. Candel, "The combined dynamics of swirler and turbulent premixed swirling flames," *Combustion and Flame*, vol. 157, no. 9, pp. 1698–1717, 2010. (Cited on pages 7 and 98.)

[27] P. Palies, D. Durox, T. Schuller, and S. Candel, "Acoustic–convective mode conversion in an aerofoil cascade," *Journal of Fluid Mechanics*, vol. 672, pp. 545–569, apr 2011. (Cited on page 7.)

[28] A. Albayrak, D. A. Bezgin, and W. Polifke, "Response of a swirl flame to inertial waves," *International Journal of Spray and Combustion Dynamics*, vol. 10, no. 4, pp. 277–286, 2018. (Cited on page 7.)

[29] T. J. Poinsot, A. C. Trouve, D. P. Veynante, S. M. Candel, and E. J. Esposito, "Vortex-driven acoustically coupled combustion instabilities," *Journal of Fluid Mechanics*, vol. 177, pp. 265–292, 1987. (Cited on page 7.)

[30] B. Emerson, J. O'connor, M. Juniper, and T. Lieuwen, "Density ratio effects on reacting bluffbody flow field characteristics," *Journal of Fluid Mechanics*, vol. 706, pp. 219–250, 2012. (Cited on page 7.)

[31] S. Ducruix, T. Schuller, D. Durox, and S. Candel, "Combustion Dynamics and Instabilities: Elementary Coupling and Driving Mechanisms," *Journal of Propulsion and Power*, vol. 19, pp. 722–734, may 2003. (Cited on page 7.)

[32] K. I. Matveev and F. E. Culick, "A model for combustion instability involving vortex shedding," *Combustion Science and Technology*, vol. 175, pp. 1059–1083, jun 2003. (Cited on page 7.)

[33] S. K. Dhanuka, J. E. Temme, J. F. Driscoll, and H. C. Mongia, "Vortex-shedding and mixing layer effects on periodic flashback in a lean premixed prevaporized gas turbine combustor," *Proceedings of the Combustion Institute*, vol. 32, pp. 2901–2908, jan 2009. (Cited on page 7.)

[34] C. J. Lawn and W. Polifke, "A MODEL FOR THE THERMOACOUSTIC RESPONSE OF A PREMIXED SWIRL BURNER, PART II: THE FLAME RESPONSE," *Combustion Science and Technology*, vol. 176, pp. 1359–1390, aug 2010. (Cited on page 7.)

[35] A. M. Steinberg, I. Boxx, M. Stöhr, C. D. Carter, and W. Meier, "Flow-flame interactions causing acoustically coupled heat release fluctuations in a thermo-acoustically unstable gas turbine model combustor," *Combustion and Flame*, vol. 157, no. 12, pp. 2250–2266, 2010. (Cited on page 7.)

[36] M. Stöhr, R. R. Sadanandan, and W. W. Meier, "Phase-resolved characterization of vortex-flame interaction in a turbulent swirl flame," *Experiments in Fluids*, vol. 51, pp. 1153–1167, 2011. (Cited on page 7.)

[37] M. Stöhr, I. Boxx, C. D. Carter, and W. Meier, "Experimental study of vortex-flame interaction in a gas turbine model combustor," *Combustion and Flame*, vol. 159, no. 8, pp. 2636–2649, 2012. (Cited on page 7.)

[38] J. P. Moeck, J. F. Bourgouin, D. Durox, T. Schuller, and S. Candel, "Nonlinear interaction between a precessing vortex core and acoustic oscillations in a turbulent swirling flame," *Combustion and Flame*, vol. 159, pp. 2650–2668, aug 2012. (Cited on page 7.)

[39] K. Oberleithner, M. Stöhr, S. H. Im, C. M. Arndt, and A. M. Steinberg, "Formation and flame-induced suppression of the precessing vortex core in a swirl combustor: Experiments and linear stability analysis," *Combustion and Flame*, vol. 162, pp. 3100–3114, aug 2015. (Cited on page 7.)

[40] S. Taamallah, Y. Dagan, N. Chakroun, S. J. Shanbhogue, K. Vogiatzaki, and A. F. Ghoniem, "Helical vortex core dynamics and flame interaction in turbulent premixed swirl combustion: A combined experimental and large eddy simulation investigation," *Physics of Fluids*, vol. 31, p. 25108, 2019. (Cited on page 7.)

[41] S. Terhaar, K. Oberleithner, and C. O. Paschereit, "Key parameters governing the precessing vortex core in reacting flows: An experimental and analytical study," *Proceedings of the Combustion Institute*, vol. 35, no. 3, pp. 3347–3354, 2015. (Cited on page 7.)

[42] S. Terhaar, B. Ćosić, C. O. Paschereit, and K. Oberleithner, "Suppression and excitation of the precessing vortex core by acoustic velocity fluctuations: An experimental and analytical study," *Combustion and Flame*, vol. 172, pp. 234–251, 2016. (Cited on page 7.)

[43] F. Lückoff and K. Oberleithner, "Excitation of the precessing vortex core by active flow control to suppress thermoacoustic instabilities in swirl flames," *International Journal of Spray and Combustion Dynamics*, vol. 11, 2019. (Cited on page 7.)

[44] F. E. Marble and S. M. Candel, "Acoustic disturbance from gas non-uniformities convected through a nozzle," *Journal of Sound and Vibration*, vol. 55, no. 2, pp. 225–243, 1977. (Cited on pages 7, 132, 137, 147 and 156.)

[45] E. Motheau, L. Selle, and F. Nicoud, "Accounting for convective effects in zero-Mach-number thermoacoustic models," *Journal of Sound and Vibration*, vol. 333, no. 1, pp. 246–262, 2014. (Cited on pages 7, 18, 19, 20, 23, 29, 131, 132, 135, 137, 138, 140, 142, 144, 146, 147, 154, 161 and 168.)

[46] E. Motheau, F. Nicoud, and T. Poinsot, "Mixed acoustic-entropy combustion instabilities in gas turbines," *Journal of Fluid Mechanics*, vol. 749, pp. 542–576, 2014. (Cited on pages 7, 19, 20, 23, 29, 131, 132, 133, 134, 135, 140, 142, 143, 168 and 192.)

[47] A. S. Morgans and I. Duran, "Entropy noise: A review of theory, progress and challenges," *International Journal of Spray and Combustion Dynamics*, vol. 8, no. 4, pp. 285–298, 2016. (Cited on pages 7, 18 and 132.)

[48] T. F. Guiberti, D. Durox, L. Zimmer, and T. Schuller, "Analysis of topology transitions of swirl flames interacting with the combustor side wall," *Combustion and Flame*, vol. 162, no. 11, pp. 4342–4357, 2014. (Cited on page 8.)

[49] R. Mercier, T. F. Guiberti, A. Chatelier, D. Durox, O. Gicquel, N. Darabiha, T. Schuller, and B. Fiorina, "Experimental and numerical investigation of the influence of thermal boundary conditions on premixed swirling flame stabilization.," *Combustion and Flame*, vol. 171, pp. 42–58, 2016. (Cited on page 8.)

[50] A. Chatelier, T. Guiberti, R. Mercier, N. Bertier, B. Fiorina, and T. Schuller, "Experimental and Numerical Investigation of the Response of a Swirled Flame to Flow Modulations in a Non-Adiabatic Combustor," *Flow, Turbulence and Combustion*, vol. 102, no. 4, pp. 995–1023, 2019. (Cited on page 8.)

[51] A. Ghani and T. Poinsot, "Flame Quenching at Walls: A Source of Sound Generation," *Flow, Turbulence and Combustion*, vol. 99, pp. 173–184, mar 2017. (Cited on pages 8 and 14.)

[52] L. Tay-Wo-Chong, A. Scarpato, and W. Polifke, "LES Combustion Model with Stretch and Heat Loss Effects for Prediction of Premix Flame Characteristics and Dynamics.," in *Proceedings of ASME Turbo Expo*, 2017. (Cited on page 8.)

[53] S. Hong, S. J. Shanbhogue, K. S. Kedia, and A. F. Ghoniem, "Impact of the Flame-Holder Heat-Transfer Characteristics on the Onset of Combustion Instability," *Combustion Science and Technology*, vol. 185, no. 10, pp. 1541–1567, 2013. (Cited on page 8.)

[54] D. Mejia, L. Selle, R. Bazile, and T. Poinsot, "Wall-temperature effects on flame response to acoustic oscillations," *Proceedings of the Combustion Institute*, vol. 35, no. 3, pp. 3201–3208, 2015. (Cited on page 8.)

[55] M. Miguel-Brebion, D. Mejia, P. Xavier, F. Duchaine, B. Bédat, L. Selle, and T. Poinsot, "Joint experimental and numerical study of the influence of flame holder temperature on the stabilization of a laminar methane flame on a cylinder," *Combustion and Flame*, vol. 172, pp. 153–161, 2016. (Cited on page 8.)

[56] D. Mejia, M. Brebion, A. Ghani, T. Kaiser, F. Duchaine, L. Selle, T. Poinsot, and M. Miguel-Brebion, "Influence of flame-holder temperature on the acoustic flame transfer functions of a laminar flame," *Combustion and Flame*, vol. 188, pp. 5–12, 2018. (Cited on page 8.)

[57] P. Agostinelli, D. Laera, I. Boxx, L. Gicquel, and T. Poinsot, "Impact of wall heat transfer in Large Eddy Simulation of flame dynamics in a swirled combustion chamber," *Combustion and Flame*, vol. 234, p. 111728, dec 2021. (Cited on pages 8 and 14.)

[58] A. H. Lefebvre and V. G. Mcdonell, *Atomization and Sprays*. Taylor & Francis, CRC Press, 2nd ed., 2017. (Cited on pages 8, 169, 170, 179 and 209.)

[59] W. A. Sirignano, *Fluid Dynamics and Transport of Droplets and Sprays*. Cambridge University Press, 2010. (Cited on pages 8, 169, 183, 184, 185 and 186.)

[60] E. Lo Schiavo, D. Laera, E. Riber, L. Gicquel, and T. Poinsot, "Effects of liquid fuel / wall interaction on thermoacoustic instabilities in swirling spray flames," *Combustion and Flame*, vol. 219, pp. 86–101, 2020. (Cited on pages 8, 29, 30, 80, 171, 175, 176, 178, 179, 180, 187, 188, 191, 192, 194, 195, 196, 197, 200, 201, 202, 207, 211, 214 and 219.)

[61] D. Paulhiac, B. Cuenot, E. Riber, L. Esclapez, and S. Richard, "Analysis of the spray flame structure in a lab-scale burner using Large Eddy Simulation and Discrete Particle Simulation," *Combustion and Flame*, vol. 212, pp. 25–38, 2020. (Cited on pages 8, 172, 187, 188, 192 and 199.)

[62] G. Vignat, E. Lo Schiavo, D. Laera, A. Renaud, L. Gicquel, D. Durox, and S. Candel, "Dynamics of spray and swirling flame under acoustic oscillations: A joint experimental and LES investigation," *Proceedings of the Combustion Institute*, vol. 38, no. 4, pp. 6015–6024, 2021. (Cited on pages 8, 80, 192 and 207.)

[63] A. L. Pillai, J. Nagao, R. Awane, and R. Kurose, "Influences of liquid fuel atomization and flow rate fluctuations on spray combustion instabilities in a backward-facing step combustor," *Combustion and Flame*, vol. 220, pp. 337–356, 2020. (Cited on pages 8, 178, 192 and 210.)

[64] S. Tachibana, K. Saito, T. Yamamoto, M. Makida, T. Kitano, and R. Kurose, "Experimental and numerical investigation of thermo-acoustic instability in a liquid-fuel aero-engine combustor at elevated pressure: Validity of large-eddy simulation of spray combustion," *Combustion and Flame*, vol. 162, no. 6, pp. 2621–2637, 2015. (Cited on pages 8 and 192.)

[65] J. M. Apeloig, F. X. D'Herbigny, F. Simon, P. Gajan, M. Orain, and S. Roux, "Liquid-fuel behavior in an aeronautical injector submitted to thermoacoustic instabilities," *Journal of Propulsion and Power*, vol. 31, no. 1, pp. 309–319, 2015. (Cited on pages 8 and 210.)

[66] A. Innocenti, A. Andreini, B. Facchini, and A. Peschiulli, "Numerical analysis of the dynamic flame response of a spray flame for aero-engine applications," *International journal of spray and combustion dynamics*, vol. 9, no. 4, pp. 310–329, 2017. (Cited on page 8.)

[67] J. Reveillon and L. Vervisch, "Analysis of weakly turbulent dilute-spray flames and spray combustion regimes," *Journal of Fluid Mechanics*, vol. 537, pp. 317–347, 2005. (Cited on pages 8 and 173.)

[68] M. Hoeijmakers, V. Kornilov, I. Lopez Arteaga, P. de Goey, and H. Nijmeijer, "Intrinsic instability of flame-acoustic coupling," *Combustion and Flame*, vol. 161, no. 11, pp. 2860–2867, 2014. (Cited on page 8.)

[69] T. Emmert, S. Bomberg, and W. Polifke, "Intrinsic thermoacoustic instability of premixed flames," *Combustion and Flame*, vol. 162, pp. 75–85, jan 2015. (Cited on page 8.)

[70] E. Courtine, L. Selle, and T. Poinsot, "DNS of Intrinsic ThermoAcoustic modes in laminar premixed flames," *Combustion and Flame*, vol. 162, no. 11, pp. 4331–4341, 2015. (Cited on page 8.)

[71] A. Ghani, T. Steinbacher, A. Albayrak, and W. Polifke, "Intrinsic thermoacoustic feedback loop in turbulent spray flames," *Combustion and Flame*, vol. 205, pp. 22–32, 2019. (Cited on page 8.)

[72] A. Orchini, C. F. Silva, G. A. Mensah, and J. P. Moeck, "Thermoacoustic modes of intrinsic and acoustic origin and their interplay with exceptional points," *Combustion and Flame*, vol. 211, pp. 83–95, 2020. (Cited on page 8.)

[73] P. E. Buschmann, G. A. Mensah, and J. P. Moeck, "Intrinsic thermoacoustic modes in an annular combustion chamber," *Combustion and Flame*, vol. 214, pp. 251–262, 2020. (Cited on page 8.)

[74] C. F. Silva, M. Merk, T. Komarek, and W. Polifke, "The contribution of intrinsic thermoacoustic feedback to combustion noise and resonances of a confined turbulent premixed flame," *Combustion and Flame*, vol. 182, no. April, pp. 269–278, 2017. (Cited on page 8.)

[75] M. Haeringer, M. Merk, and W. Polifke, "Inclusion of higher harmonics in the flame describing function for predicting limit cycles of self-excited combustion instabilities," *Proceedings of the Combustion Institute*, vol. 37, no. 4, pp. 5255–5262, 2019. (Cited on pages 9 and 26.)

[76] K. T. Kim, "Nonlinear Interactions Between the Fundamental and Higher Harmonics of Self-Excited Combustion Instabilities," *Combustion Science and Technology*, vol. 189, pp. 1091–1106, jul 2017. (Cited on page 9.)

[77] J. M. Wicker, M. W. Yoon, and V. Yang, "Linear and non-linear pressure oscillations in baffled combustion chambers," *Journal of Sound and Vibration*, vol. 184, pp. 141–171, jul 1995. (Cited on page 9.)

[78] K. J. Lee, H. J. Kim, S. Seo, and H. S. Choi, "Experimental Verification for Acoustic Damping Enhancement by Gaps in Injector-Formed Baffles," *Journal of Propulsion and Power*, vol. 25, pp. 435–442, may 2009. (Cited on page 9.)

[79] B. Cosic, T. G. Reichel, and C. O. Paschereit, "Acoustic Response of a Helmholtz Resonator Exposed to Hot-Gas Penetration and High Amplitude Oscillations," *Journal of Engineering for Gas Turbines and Power*, vol. 134, 2012. (Cited on page 9.)

[80] N. Noiray and B. Schuermans, "Theoretical and experimental investigations on damper performance for suppression of thermoacoustic oscillations," *Journal of Sound and Vibration*, vol. 331, pp. 2753–2763, jun 2012. (Cited on page 9.)

[81] M. R. Bothien, N. Noiray, and B. Schuermans, "A novel damping device for broadband attenuation of low-frequency combustion pulsations in gas turbines," *Journal of Engineering for Gas Turbines and Power*, vol. 136, no. 4, pp. 1–10, 2014. (Cited on page 9.)

[82] M. S. Howe, "The dissipation of sound at an edge," *Journal of Sound and Vibration*, vol. 70, pp. 407–411, jun 1980. (Cited on pages 9, 54 and 57.)

[83] A. Scarpato, N. Tran, S. Ducruix, and T. Schuller, "Modeling the damping properties of perforated screens traversed by a bias flow and backed by a cavity at low Strouhal number," *Journal of Sound and Vibration*, vol. 331, no. 2, pp. 276–290, 2012. (Cited on pages 9 and 54.)

[84] Y. Dong and A. S. Morgans, "The acoustics of short circular holes opening to confined and unconfined spaces," *Journal of Sound and Vibration*, vol. 393, pp. 41–61, 2017. (Cited on page 9.)

[85] S. Mendez and J. D. Eldredge, "Acoustic modeling of perforated plates with bias flow for Large-Eddy Simulations," *Journal of Computational Physics*, vol. 228, pp. 4757–4772, 2009. (Cited on page 9.)

[86] M. Bauerheim, P. Salas, F. Nicoud, and T. Poinsot, "Symmetry breaking of azimuthal thermo-acoustic modes in annular cavities: a theoretical study," *Journal of Fluid Mechanics*, vol. 760, pp. 431–465, 2014. (Cited on page 10.)

[87] M. Bauerheim, M. Cazalens, and T. Poinsot, "A theoretical study of mean azimuthal flow and asymmetry effects on thermo-acoustic modes in annular combustors," *Proceedings of the Combustion Institute*, vol. 35, no. 3, pp. 3219–3227, 2015. (Cited on pages 10 and 22.)

[88] G. A. Mensah, L. Magri, A. Orchini, and J. P. Moeck, "Effects of Asymmetry on Thermoacoustic Modes in Annular Combustors: A Higher-Order Perturbation Study," *Journal of Engineering for Gas Turbines and Power*, vol. 141, no. 4, 2019. (Cited on pages 10, 102 and 106.)

[89] G. Ghirardo, H. T. Nygård, A. Cuquel, and N. A. Worth, "Symmetry breaking modelling for azimuthal combustion dynamics," *Proceedings of the Combustion Institute*, vol. 38, pp. 5953–5962, jan 2021. (Cited on page 10.)

[90] M. P. Juniper and R. Sujith, "Sensitivity and Nonlinearity of Thermoacoustic Oscillations," *Annual Review of Fluid Mechanics*, vol. 50, no. 1, 2018. (Cited on pages 10, 11 and 15.)

[91] R. I. Sujith, M. P. Juniper, and P. J. Schmid, "Non-normality and nonlinearity in thermoacoustic instabilities," *International Journal of Spray and Combustion Dynamics*, vol. 8, no. 2, pp. 119–146, 2016. (Cited on pages 10, 11, 12 and 164.)

[92] M. P. Juniper, "Triggering in thermoacoustics," *International Journal of Spray and Combustion Dynamics*, vol. 4, no. 3, pp. 217–238, 2012. (Cited on page 12.)

[93] G. Staffelbach, L. Y. Gicquel, G. Boudier, and T. Poinsot, "Large Eddy Simulation of self excited azimuthal modes in annular combustors," *Proceedings of the Combustion Institute*, vol. 32 II, no. 2, pp. 2909–2916, 2009. (Cited on pages 12, 14 and 26.)

[94] P. Rajendram Soundararajan, G. Vignat, D. Durox, A. Renaud, and S. Candel, "Effect of Different Fuels on Combustion Instabilities in an Annular Combustor," *Journal of Engineering for Gas Turbines and Power*, vol. 143, mar 2021. (Cited on pages 12, 14, 80, 81, 204, 205 and 206.)

[95] G. Vignat, D. Durox, T. Schuller, and S. Candel, "Combustion Dynamics of Annular Systems," *Combustion Science and Technology*, pp. 1–31, mar 2020. (Cited on pages 13 and 80.)

[96] N. A. Worth and J. R. Dawson, "Modal dynamics of self-excited azimuthal instabilities in an annular combustion chamber," *Combustion and Flame*, vol. 160, no. 11, pp. 2476–2489, 2013. (Cited on page 13.)

[97] N. A. Worth and J. R. Dawson, "Self-excited circumferential instabilities in a model annular gas turbine combustor: Global flame dynamics," *Proceedings of the Combustion Institute*, vol. 34, no. 2, pp. 3127–3134, 2013. (Cited on page 13.)

[98] J. R. Dawson and N. A. Worth, "Flame dynamics and unsteady heat release rate of self-excited azimuthal modes in an annular combustor," *Combustion and Flame*, vol. 161, no. 10, pp. 2565–2578, 2014. (Cited on pages 13 and 26.)

[99] J. F. Bourgouin, D. Durox, J. P. Moeck, T. Schuller, and S. Candel, "Self-sustained instabilities in an annular combustor coupled by azimuthal and longitudinal acoustic modes," *Proceedings of the ASME Turbo Expo*, vol. 1 B, pp. 1–13, 2013. (Cited on page 14.)

[100] J.-F. Bourgouin, D. Durox, J. P. Moeck, T. Schuller, and S. Candel, "Characterization and Modeling of a Spinning Thermoacoustic Instability in an Annular Combustor Equipped With Multiple Matrix Injectors," *Proceedings of the ASME Turbo Expo 2014: Turbine Technical Conference and Exposition - GT2014-25067*, pp. 1–15, 2014. (Cited on page 14.)

[101] J. F. Bourgouin, D. Durox, J. P. Moeck, T. Schuller, and S. Candel, "A new pattern of instability observed in an annular combustor: The slanted mode," *Proceedings of the Combustion Institute*, vol. 35, no. 3, pp. 3237–3244, 2015. (Cited on page 14.)

[102] M. Mazur, H. T. Nygård, J. R. Dawson, and N. A. Worth, "Characteristics of self-excited spinning azimuthal modes in an annular combustor with turbulent premixed bluff-body flames," *Proceedings of the Combustion Institute*, vol. 37, no. 4, pp. 5129–5136, 2019. (Cited on page 14.)

[103] K. Prieur, D. Durox, T. Schuller, and S. Candel, "Combustion Instabilities in a Spray Annular Chamber With Intermittent Partial Blow-Off," *Journal of Engineering for Gas Turbines and Power*, vol. 140, no. 3, p. 31503, 2017. (Cited on pages 14, 193 and 199.)

[104] K. Prieur, D. Durox, T. Schuller, and S. Candel, "A hysteresis phenomenon leading to spinning or standing azimuthal instabilities in an annular combustor," *Combustion and Flame*, vol. 175, pp. 283–291, 2017. (Cited on pages 14, 80 and 193.)

[105] S. C. Humbert, J. Moeck, A. Orchini, and C. O. Paschereit, "Effect of an Azimuthal Mean Flow On the Structure and Stability of Thermoacoustic Modes in an Annular Combustor Model with Electroacoustic Feedback (GTP-20-1401)," *Journal of Engineering for Gas Turbines and Power*, 2020. (Cited on page 14.)

[106] J. Kim, T. John, S. Adhikari, D. Wu, B. Emerson, V. Acharya, M. Isono, T. Saito, and T. Lieuwen, "Nonlinear dynamics of combustor azimuthal modes: Experiments and modeling," *Combustion and Flame*, vol. 238, p. 111931, apr 2022. (Cited on page 14.)

[107] M. Mazur, Y. H. Kwah, T. Indlekofer, J. R. Dawson, and N. A. Worth, "Self-excited longitudinal and azimuthal modes in a pressurised annular combustor," *Proceedings of the Combustion Institute*, vol. 38, pp. 5997–6004, jan 2021. (Cited on page 14.)

[108] L. Y. M. Gicquel, G. Staffelbach, and T. Poinsot, "Large Eddy Simulations of gaseous flames in gas turbine combustion chambers," *Progress in Energy and Combustion Science*, vol. 38, no. 6, pp. 782–817, 2012. (Cited on pages 14, 16, 174, 187 and 188.)

[109] P. Wolf, G. Staffelbach, L. Y. Gicquel, J. D. Müller, and T. Poinsot, "Acoustic and Large Eddy Simulation studies of azimuthal modes in annular combustion chambers," *Combustion and Flame*, vol. 159, no. 11, pp. 3398–3413, 2012. (Cited on pages 14, 20, 26 and 192.)

[110] M. Bauerheim, T. Jaravel, L. Esclapez, E. Riber, L. Y. Gicquel, B. Cuenot, M. Cazalens, S. Bourgois, and M. Rullaud, "Multiphase flow LES study of the fuel split effects on combustion instabilities in an ultra low-NOx annular combustor," *Journal of Engineering for Gas Turbines and Power*, vol. 138, no. 6, 2015. (Cited on page 14.)

[111] M. Bauerheim, F. Nicoud, and T. Poinsot, "Progress in analytical methods to predict and control azimuthal combustion instability modes in annular chambers," *Physics of Fluids*, vol. 28, feb 2016. (Cited on pages 15, 21 and 26.)

[112] F. Nicoud and K. Wieczorek, "About the zero Mach number assumption in the calculation of thermoacoustic instabilities," *International Journal of Spray and Combustion Dynamics*, vol. 1, no. 1, p. 67, 2009. (Cited on pages 15, 17, 18, 19, 22, 47, 134, 137 and 141.)

[113] N. Noiray, D. Durox, T. Schuller, and S. Candel, "A unified framework for nonlinear combustion instability analysis based on the describing function.," *Journal of Fluid Mechanics*, vol. 615, pp. 139–167, 2008. (Cited on pages 15, 26, 94, 95 and 98.)

[114] R. S. Cant and E. Mastorakos, *An Introduction to Turbulent Reacting Flows.* Imperial College Press, 2008. (Cited on pages 16, 174 and 188.)

[115] H. Pitsch, "Large-Eddy Simulation of Turbulent Combustion," *Annual Review of Fluid Mechanics*, vol. 38, no. 1, pp. 453–482, 2006. (Cited on pages 16, 174 and 188.)

[116] A. Urbano, L. Selle, G. Staffelbach, B. Cuenot, T. Schmitt, S. Ducruix, and S. Candel, "Exploration of combustion instability triggering using Large Eddy Simulation of a multiple injector Liquid Rocket Engine," *Combustion and Flame*, vol. 169, pp. pp. 129–140, jul 2016. (Cited on page 17.)

[117] C. Laurent, G. Staffelbach, F. Nicoud, and T. Poinsot, "Heat-release dynamics in a doubly-transcritical LO_2 /LCH_4 cryogenic coaxial jet flame subjected to fuel inflow acoustic modulation," *Proceedings of the Combustion Institute*, vol. 38, no. 4, pp. 6375–6383, 2021. (Cited on page 17.)

[118] C. K. Tam, "Computational aeroacoustics: An overview of computational challenges and applications," *International Journal of Computational Fluid Dynamics*, vol. 18, no. 6, pp. 547–567, 2004. (Cited on page 18.)

[119] I. Duran and S. Moreau, "Solution of the quasi-one-dimensional linearized Euler equations using flow invariants and the Magnus expansion," *Journal of Fluid Mechanics*, vol. 723, pp. 190–231, 2013. (Cited on pages 18, 132 and 137.)

[120] M. Bauerheim, I. Duran, T. Livebardon, G. Wang, S. Moreau, and T. Poinsot, "Transmission and reflection of acoustic and entropy waves through a stator-rotor stage," *Journal of Sound and Vibration*, vol. 374, pp. 260–278, 2016. (Cited on pages 18, 132, 137, 143 and 192.)

[121] K. Wieczorek, C. Sensiau, W. Polifke, and F. Nicoud, "Assessing non-normal effects in thermoacoustic systems with mean flow," *Physics of Fluids*, vol. 23, no. 10, pp. 1–15, 2011. (Cited on page 18.)

[122] T. Hummel, C. Temmler, B. Schuermans, and T. Sattelmayer, "Reduced-order modeling of aeroacoustic systems for stability analyses of thermoacoustically noncompact gas turbine combustors," *Journal of Engineering for Gas Turbines and Power*, vol. 138, no. 5, pp. 1–11, 2016. (Cited on page 18.)

[123] M. Schulze, T. Hummel, N. Klarmann, F. Berger, B. Schuermans, and T. Sattelmayer, "Linearized Euler Equations for the Prediction of Linear High-Frequency Stability in Gas Turbine Combustors," *Journal of Engineering for Gas Turbines and Power*, vol. 139, mar 2017. (Cited on page 18.)

[124] T. Hofmeister, T. Hummel, B. Schuermans, and T. Sattelmayer, "Modeling and Quantification of Acoustic Damping Induced by Vortex Shedding in Noncompact Thermoacoustic Systems," *Journal of Engineering for Gas Turbines and Power*, vol. 142, mar 2020. (Cited on page 18.)

[125] T. Hofmeister, T. Hummel, F. Berger, N. Klarmann, and T. Sattelmayer, "Elimination of Numerical Damping in the Stability Analysis of Noncompact Thermoacoustic Systems with Linearized Euler Equations," *Journal of Engineering for Gas Turbines and Power*, vol. 143, mar 2021. (Cited on page 18.)

[126] A. Avdonin, M. Meindl, and W. Polifke, "Thermoacoustic analysis of a laminar premixed flame using a linearized reactive flow solver," *Proceedings of the Combustion Institute*, vol. 37, no. 4, pp. 5307–5314, 2019. (Cited on page 19.)

[127] F. Nicoud, L. Benoit, C. Sensiau, and T. Poinsot, "Acoustic modes in combustors with complex impedances and multidimensional active flames," *AIAA Journal*, vol. 45, no. 2, 2007. (Cited on pages 19, 20, 23, 25, 37, 42, 43, 50, 51, 54, 61, 80, 83, 84, 86, 89, 90, 131, 135, 140, 141 and 192.)

[128] C. Pankiewitz and T. Sattelmayer, "Time domain simulation of combustion instabilities in annular combustors," *Journal of Engineering for Gas Turbines and Power*, vol. 125, no. 3, pp. 677–685, 2003. (Cited on pages 19 and 25.)

[129] S. M. Camporeale, B. Fortunato, and G. Campa, "A finite element method for three-dimensional analysis of thermo-acoustic combustion instability," *Journal of Engineering for Gas Turbines and Power*, vol. 133, no. 1, pp. 1–13, 2011. (Cited on pages 19 and 42.)

[130] C. F. Silva, F. Nicoud, T. Schuller, D. Durox, and S. Candel, "Combining a Helmholtz solver with the flame describing function to assess combustion instability in a premixed swirled combustor," *Combustion and Flame*, vol. 160, no. 9, pp. 1743–1754, 2013. (Cited on pages 20, 26 and 98.)

[131] D. Laera and S. M. Camporeale, "A weakly nonlinear approach based on a distributed flame describing function to study the combustion dynamics of a full-scale lean-premixed swirled burner," *Journal of Engineering for Gas Turbines and Power*, vol. 139, no. 9, 2017. (Cited on page 20.)

[132] E. Gullaud and F. Nicoud, "Effect of Perforated Plates on the Acoustics of Annular Combustors," *AIAA Journal*, vol. 50, no. 12, pp. 2629–2642, 2012. (Cited on pages 20, 54, 57 and 61.)

[133] F. Ni, M. Miguel-Brebion, F. Nicoud, and T. Poinsot, "Accounting for acoustic damping in a helmholtz solver," *AIAA Journal*, vol. 55, no. 4, pp. 1205–1220, 2017. (Cited on page 20.)

[134] F. Ni, F. Nicoud, Y. Méry, and G. Staffelbach, "Including flow-acoustic interactions in the Helmholtz computations of industrial combustors," *AIAA Journal*, vol. 56, no. 12, pp. 4815–4829, 2018. (Cited on page 20.)

[135] T. Schuller, D. Durox, P. Palies, and S. Candel, "Acoustic decoupling of longitudinal modes in generic combustion systems," *Combustion and Flame*, vol. 159, no. 5, pp. 1921–1931, 2012. (Cited on pages 21, 22, 37 and 38.)

[136] M. Bauerheim, J. F. Parmentier, P. Salas, F. Nicoud, and T. Poinsot, "An analytical model for azimuthal thermoacoustic modes in an annular chamber fed by an annular plenum," *Combustion and Flame*, vol. 161, no. 5, pp. 1374–1389, 2014. (Cited on pages 21, 22, 28, 73, 74, 75, 76 and 77.)

[137] M. Bauerheim, F. Nicoud, and T. Poinsot, "Theoretical analysis of the mass balance equation through a flame at zero and non-zero mach numbers," *Combustion and Flame*, vol. 162, no. 1, pp. 60–67, 2015. (Cited on pages 21 and 141.)

[138] L. Strobio Chen, S. Bomberg, and W. Polifke, "Propagation and generation of acoustic and entropy waves across a moving flame front," *Combustion and Flame*, vol. 166, pp. 170–180, 2016. (Cited on pages 21 and 141.)

[139] S. R. Stow and A. P. Dowling, "Thermoacoustic Oscillations in an Annular Combustor," in *ASME TURBO EXPO*, ASME, jun 2001. (Cited on page 22.)

[140] A. P. Dowling and S. R. Stow, "Acoustic Analysis of Gas Turbine Combustors," *Journal of Propulsion and Power*, vol. 19, pp. 751–764, sep 2003. (Cited on pages 22, 141 and 163.)

[141] J. Kopitz, A. Huber, T. Sattelmayer, and W. Polifke, "Thermoacoustic stability analysis of an annular combustion chamber with acoustic low order modeling and validation against experiment," in *Proceedings of the ASME Turbo Expo*, vol. 2, pp. 583–593, 2005. (Cited on page 22.)

[142] X. Han, J. Li, and A. S. Morgans, "Prediction of combustion instability limit cycle oscillations by combining flame describing function simulations with a thermoacoustic network model," *Combustion and Flame*, vol. 162, pp. 3632–3647, 2015. (Cited on page 22.)

[143] J. Li and A. S. Morgans, "Time domain simulations of nonlinear thermoacoustic behaviour in a simple combustor using a wave-based approach," *Journal of Sound and Vibration*, vol. 346, 2015. (Cited on pages 22, 26 and 98.)

[144] A. Orchini, S. J. Illingworth, and M. P. Juniper, "Frequency domain and time domain analysis of thermoacoustic oscillations with wave-based acoustics," *Journal of Fluid Mechanics*, vol. 775, pp. 387–414, jun 2015. (Cited on pages 22 and 32.)

[145] J. Li, Y. Xia, A. S. Morgans, and X. Han, "Numerical prediction of combustion instability limit cycle oscillations for a combustor with a long flame," *Combustion and Flame*, vol. 185, pp. 28–43, 2017. (Cited on pages 22 and 24.)

[146] B. T. Zinn and M. E. Lores, "Application of the Galerkin Method in the Solution of Nonlinear Axial Combustion Instability Problems in Liquid Rockets," *Combustion Science and Technology*, vol. 4, pp. 269–278, sep 1971. (Cited on page 22.)

[147] K. Balasubramanian, "Non-normality and nonlinearity in combustion-acoustic interaction in diffusion flames," *Journal of Fluid Mechanics*, vol. 594, pp. 29–57, 2008. (Cited on page 22.)

[148] M. Juniper, "Triggering in the horizontal Rijke tube: non-normality, transient growth and bypass transition," *J. Fluid Mech*, vol. 667, pp. 272–308, 2011. (Cited on page 22.)

[149] N. Noiray, M. Bothien, and B. Schuermans, "Investigation of azimuthal staging concepts in annular gas turbines," *Combustion Theory and Modelling*, vol. 15, no. 5, pp. 585–606, 2011. (Cited on pages 22 and 23.)

[150] N. Noiray and B. Schuermans, "On the dynamic nature of azimuthal thermoacoustic modes in annular gas turbine combustion chambers," in *Proceedings of the Royal Society A*, 2013. (Cited on page 22.)

[151] G. Ghirardo, M. P. Juniper, and J. P. Moeck, "Weakly nonlinear analysis of thermoacoustic instabilities in annular combustors," *Journal of Fluid Mechanics*, vol. 805, pp. 52–87, 2016. (Cited on page 22.)

[152] B. Schuermans, V. Bellucci, and C. O. Paschereit, "Thermoacoustic modeling and control of multi burner combustion systems," *American Society of Mechanical Engineers, International Gas Turbine Institute, Turbo Expo (Publication) IGTI*, vol. 2, pp. 509–519, 2003. (Cited on pages 22, 23, 32, 35, 36 and 86.)

[153] S. R. Stow and A. P. Dowling, "Low-Order Modelling of Thermoacoustic Limit Cycles," in *ASME Turbo Expo*, pp. 775–786, ASME, jan 2004. (Cited on page 22.)

[154] V. Bellucci, B. Schuermans, D. Nowak, P. Flohr, and C. O. Paschereit, "Thermoacoustic modeling of a gas turbine combustor equipped with acoustic dampers," *Journal of Turbomachinery*, vol. 127, no. 2, pp. 372–379, 2005. (Cited on pages 22, 32 and 86.)

[155] S. R. Stow and A. P. Dowling, "A Time-Domain Network Model for Nonlinear Thermoacoustic Oscillations," *Journal of Engineering for Gas Turbines and Power*, vol. 131, no. 3, p. 031502, 2009. (Cited on page 22.)

[156] S. Bethke, U. Wever, and W. Krebs, "Stability analysis of gas-turbine combustion chamber," in *11th AIAA/CEAS Aeroacoustics Conference*, vol. 1, pp. 407–422, 2005. (Cited on pages 23 and 86.)

[157] C. Laurent, M. Bauerheim, T. Poinsot, and F. Nicoud, "A novel modal expansion method for low-order modeling of thermoacoustic instabilities in complex geometries," *Combustion and Flame*, vol. 206, pp. 334–348, 2019. (Cited on pages 23, 28, 32, 37, 39, 40, 45, 68, 70, 73, 109, 192, 217 and 218.)

[158] Y. Méry, *Mécanismes d'instabilités de combustion haute-fréquence et application aux moteurs-fusées*. PhD thesis, Ecole Centrale Paris, 2010. (Cited on page 23.)

[159] M. Gonzalez-Flesca, P. Scouflaire, S. Thomas, S. Ducruix, and S. Candel, "Reduced Order Modeling Approach to Combustion Instabilities of Liquid Rocket Engines," *AIAA Journal*, 2018. (Cited on page 23.)

[160] D. Marchal, A. Fougnie, S. Thomas, and S. Ducruix, "Study of the acoustic damping in a nonreactive pressurized chamber combining experiments, simulations and modeling," in *INitiative en Combustion Avancée (INCA)*, 2021. (Cited on page 23.)

[161] A. Fougnie, S. Thomas, and S. Ducruix, "Low Order Modeling of High Frequency Combustion Instabilities in Liquid Rocket Engines," in *Space Propulsion*, (Portugal), 2021. (Cited on page 23.)

[162] B. Schuermans, C. O. Paschereit, and P. Monkewitz, "Non-linear combustion instabilities in annular gas-turbine combustors," in *44th AIAA Aerospace Sciences Meeting*, vol. 9, pp. 6634–6645, 2006. (Cited on page 23.)

[163] B. Schuermans, F. Guethe, D. Pennell, D. Guyot, and C. O. Paschereit, "Thermoacoustic modeling of a gas turbine using transfer functions measured under full engine pressure," *Journal of Engineering for Gas Turbines and Power*, vol. 132, no. 11, 2010. (Cited on pages 23, 32, 86, 102 and 106.)

[164] M. Bothien, N. Noiray, and B. Schuermans, "Analysis of azimuthal thermoacoustic modes in annular gas turbine combustion chambers," *Journal of Engineering for Gas Turbines and Power*, vol. 137, no. June 2015, pp. 1–8, 2015. (Cited on page 23.)

[165] D. Yang, D. Laera, and A. S. Morgans, "A systematic study of nonlinear coupling of thermoacoustic modes in annular combustors," *Journal of Sound and Vibration*, vol. 456, pp. 137–161, 2019. (Cited on page 23.)

[166] A. Orchini, G. A. Mensah, and J. P. Moeck, "Effects of nonlinear modal interactions on the thermoacoustic stability of annular combustors," *Journal of Engineering for Gas Turbines and Power*, vol. 141, no. 2, 2019. (Cited on page 23.)

[167] A. Ghani, T. Poinsot, L. Gicquel, G. Staffelbach, G. Staffelbach LES, and G. Les, "LES of longitudinal and transverse self-excited combustion instabilities in a bluff-body stabilized turbulent premixed flame," *Combustion and Flame*, vol. 162, no. 11, pp. 4075–4083, 2015. (Cited on pages 24 and 192.)

[168] M. Zellhuber, J. Schwing, B. Schuermans, T. Sattelmayer, and W. Polifke, "Experimental and Numerical Investigation of Thermoacoustic Sources Related to High-Frequency Instabilities," *International Journal of Spray and Combustion Dynamics*, vol. 6, pp. 1–34, mar 2014. (Cited on page 24.)

[169] F. Baillot and F. Lespinasse, "Response of a laminar premixed V-flame to a high-frequency transverse acoustic field," *Combustion and Flame*, vol. 161, no. 5, pp. 1247–1267, 2014. (Cited on pages 24 and 26.)

[170] V. Acharya, M. Aguilar, M. Malanosk, and T. Lieuwen, "Dynamics of a transversely excited swirling, lifted flame: Flame response modeling and comparison with experiments," *Journal of Engineering for Gas Turbines and Power*, vol. 136, no. 5, 2014. (Cited on page 24.)

[171] D. Laera, K. Prieur, D. Durox, T. Schuller, S. M. Camporeale, and S. Candel, "Impact of heat release distribution on the spinning modes of an annular combustor with multiple matrix burners," *Journal of Engineering for Gas Turbines and Power*, vol. 139, no. 5, pp. 1–10, 2017. (Cited on page 24.)

[172] L. Crocco, "Research on combustion instability in liquid propellant rockets," *Symposium (International) on Combustion*, vol. 12, pp. 85–99, jan 1969. (Cited on page 25.)

[173] F. Dupuy, M. Gatti, C. Mirat, L. Gicquel, F. Nicoud, and T. Schuller, "Combining analytical models and LES data to determine the transfer function from swirled premixed flames," *Combustion and Flame*, vol. 217, pp. 222–236, 2020. (Cited on pages 25, 114, 115, 128 and 196.)

[174] A. Huber and W. Polifke, "Dynamics of Practical Premixed Flames, Part I: Model Structure and Identification:," *International Journal of Spray and Combustion Dynamics*, vol. 1, pp. 199–228, jun 2009. (Cited on page 25.)

[175] A. Huber and W. Polifke, "Dynamics of Practical Premixed Flames, Part II: Identification and Interpretation of CFD Data:," *International Journal of Spray and Combustion Dynamics*, vol. 1, pp. 229–249, jun 2009. (Cited on page 25.)

[176] S. Bade, M. Wagner, C. Hirsch, T. Sattelmayer, and B. Schuermans, "Design for thermoacoustic stability: Modeling of burner and flame dynamics," *Journal of Engineering for Gas Turbines and Power*, vol. 135, nov 2013. (Cited on pages 25 and 100.)

[177] B. Schuermans, V. Bellucci, F. Guethe, F. Meili, P. Flohr, and C. O. Paschereit, "A Detailed Analysis of Thermoacoustic Interaction Mechanisms in a Turbulent Premixed Flame," in *ASME Turbo Expo*, 2004. (Cited on page 25.)

[178] T. Komarek and W. Polifke, "Impact of swirl fluctuations on the flame response of a perfectly premixed swirl burner," *Journal of Engineering for Gas Turbines and Power*, vol. 132, pp. 1–7, jun 2010. (Cited on pages 25, 100 and 192.)

[179] P. Subramanian, R. S. Blumenthal, W. Polifke, and R. I. Sujith, "Distributed time lag response functions for the modelling of combustion dynamics," *Combustion Theory and Modelling*, vol. 19, no. 2, pp. 223–237, 2015. (Cited on pages 25, 100, 102 and 106.)

[180] K. T. Kim, J. G. Lee, B. D. Quay, and D. A. Santavicca, "Spatially distributed flame transfer functions for predicting combustion dynamics in lean premixed gas turbine combustors," *Combustion and Flame*, vol. 157, no. 9, pp. 1718–1730, 2010. (Cited on page 25.)

[181] M. Zhu, A. P. Dowling, and K. N. Bray, "Transfer function calculations for aeroengine combustion oscillations," *Journal of Engineering for Gas Turbines and Power*, vol. 127, no. 1, pp. 18–26, 2005. (Cited on page 25.)

[182] P. Palies, D. Durox, T. Schuller, and S. Candel, "Nonlinear combustion instability analysis based on the flame describing function applied to turbulent premixed swirling flames," *Combustion and Flame*, vol. 158, pp. 1980–1991, oct 2011. (Cited on pages 26 and 98.)

[183] D. Laera, T. Schuller, K. Prieur, D. Durox, S. M. Camporeale, and S. Candel, "Flame Describing Function analysis of spinning and standing modes in an annular combustor and comparison with experiments," *Combustion and Flame*, vol. 184, pp. 136–152, 2017. (Cited on pages 26 and 98.)

[184] A. Orchini and M. P. Juniper, "Flame Double Input Describing Function analysis," *Combustion and Flame*, vol. 171, pp. 87–102, 2016. (Cited on page 26.)

[185] K. Kashinath, I. C. Waugh, and M. P. Juniper, "Nonlinear self-excited thermoacoustic oscillations of a ducted premixed flame: Bifurcations and routes to chaos," *Journal of Fluid Mechanics*, vol. 761, pp. 399–430, 2014. (Cited on page 26.)

[186] A. Orchini, G. Rigas, and M. P. Juniper, "Weakly nonlinear analysis of thermoacoustic bifurcations in the Rijke tube," *Journal of Fluid Mechanics*, vol. 805, no. 2016, pp. 523–550, 2016. (Cited on pages 26, 102 and 106.)

[187] C. Sensiau, F. Nicoud, and T. Poinsot, "A tool to study azimuthal standing and spinning modes in annular combustors," *International Journal of Aeroacoustics*, vol. 8, p. 57, 2009. (Cited on page 26.)

[188] M. Bauerheim, G. Staffelbach, N. A. Worth, J. Dawson, L. Y. M. Gicquel, and T. Poinsot, "Sensitivity of LES-based harmonic flame response model for turbulent swirled flames and impact on the stability of azimuthal modes.," *Proceedings of the Combustion Institute*, vol. 35, no. 3, pp. 3219–3227, 2015. (Cited on page 26.)

[189] A. Saurabh and C. O. Paschereit, "Dynamics of premixed swirl flames under the influence of transverse acoustic fluctuations," *Combustion and Flame*, vol. 182, pp. 298–312, aug 2017. (Cited on page 26.)

[190] A. Saurabh and C. O. Paschereit, "Premixed Flame Dynamics in Response to Two-Dimensional Acoustic Forcing," *Combustion Science and Technology*, vol. 191, pp. 1184–1200, jul 2018. (Cited on page 26.)

[191] F. Baillot, C. Patat, M. Cáceres, J.-B. Blaisot, and E. Domingues, "Saturation phenomenon of swirling spray flames at pressure antinodes of a transverse acoustic field," *Proceedings of the Combustion Institute*, vol. 38, pp. 5987–5995, oct 2021. (Cited on page 26.)

[192] N. Purwar, M. Haeringer, B. Schuermans, and W. Polifke, "Flame response to transverse velocity excitation leading to frequency doubling and modal coupling," *Combustion and Flame*, vol. 230, 2021. (Cited on page 27.)

[193] V. S. Acharya and T. C. Lieuwen, "Significance of the direct excitation mechanism for high-frequency response of premixed flames to flow oscillations," *Journal of Engineering for Gas Turbines and Power*, vol. 143, jan 2021. (Cited on page 27.)

[194] V. Sharifi, A. M. Kempf, and C. Beck, "Large-eddy simulation of acoustic flame response to high-frequency transverse excitations," *AIAA Journal*, vol. 57, no. 1, pp. 327–340, 2019. (Cited on page 27.)

[195] H. T. Nygård, M. Mazur, J. R. Dawson, and N. A. Worth, "Flame dynamics of azimuthal forced spinning and standing modes in an annular combustor," *Proceedings of the Combustion Institute*, vol. 37, no. 4, pp. 5113–5120, 2019. (Cited on page 27.)

[196] H. T. Nygård, G. Ghirardo, and N. A. Worth, "Azimuthal flame response and symmetry breaking in a forced annular combustor," *Combustion and Flame*, vol. 233, p. 111565, nov 2021. (Cited on page 27.)

[197] C. Laurent, *Low-Order Modeling and High-Fidelity Simulations for the Prediction of Combustion Instabilities in Liquid Rocket Engines and Gas Turbines*. Dissertation, Institut National Polytechnique de Toulouse (INPT), 2020. (Cited on pages 27, 28, 32, 34, 35, 37, 39, 40, 41, 42, 43, 45, 47, 52, 53, 55, 57, 59, 61, 65, 66, 68, 69, 70, 71, 73, 79, 93, 109, 158, 166, 217 and 218.)

[198] C. Laurent, A. Badhe, and F. Nicoud, "Representing geometrically complex liners and boundaries in low-order modeling of thermoacoustic instabilities.," *Journal of Computational Physics*, vol. 428, 2021. (Cited on pages 28, 32, 41, 52, 53, 55, 57, 59, 61, 70, 71, 73, 217 and 218.)

[199] A. Badhe, C. Laurent, C. Lapeyre, and F. Nicoud, "Low-Order Thermoacoustic Analysis of Real Engines," in *Symposium on Thermoacoustics in Combustion (SoTiC): Industry meets Academia*, (Munich), 2021. (Cited on pages 28, 32, 52, 70, 73 and 218.)

[200] A. Badhe, D. Laera, and L. Gicquel, "High-fidelity Large Eddy Simulations of the Flame Transfer Function of a turbulent swirling spray flame," in *10th European Combustion Meeting*, (Napoli, Italy), 2021. (Cited on page 29.)

[201] E. Lo Schiavo, D. Laera, E. Riber, L. Gicquel, and T. Poinsot, "On the impact of fuel injection angle in Euler–Lagrange large eddy simulations of swirling spray flames exhibiting thermoacoustic instabilities," *Combustion and Flame*, vol. 227, pp. 359–370, may 2021. (Cited on pages 29, 30, 80, 178, 191, 195, 196, 202, 204, 207, 209, 211, 214 and 219.)

[202] T. Emmert, M. Meindl, S. Jaensch, and W. Polifke, "Linear state space interconnect modeling of acoustic systems," *Acta Acustica united with Acustica*, vol. 102, no. 5, pp. 824–833, 2016. (Cited on pages 32, 102 and 192.)

[203] M. Meindl, A. Albayrak, and W. Polifke, "A state-space formulation of a discontinuous Galerkin method for thermoacoustic stability analysis," *Journal of Sound and Vibration*, vol. 481, pp. 1–21, 2020. (Cited on page 32.)

[204] B. Friedland, *Control System Design: An Introduction To State-Space Methods*. Dover Publications, Inc. Mineola, New York., 2005. (Cited on pages 33 and 95.)

[205] K. Ogata, *Modern Control Engineering*. Pearson, 5th ed., 2010. (Cited on pages 33, 95 and 112.)

[206] K. Zhou, J. C. Doyle, and K. Glover, *Robust And Optimal Control*. Prentice Hall, 1996. (Cited on page 35.)

[207] A. Kaufmann, F. Nicoud, and T. Poinsot, "Flow forcing techniques for numerical simulation of combustion instabilities," *Combustion and Flame*, vol. 131, no. 4, pp. 371–385, 2002. (Cited on page 38.)

[208] C. Lawn, "The acoustic impedance of perforated plates under various flow conditions relating to combustion chamber liners," *Applied Acoustics*, vol. 106, pp. 144–154, 2016. (Cited on page 54.)

[209] A. D. Pierce, *Acoustics*. Springer International, 2019. (Cited on page 73.)

[210] G. Vignat, D. Durox, A. Renaud, and S. Candel, "High Amplitude Combustion Instabilities in an Annular Combustor Inducing Pressure Field Deformation and Flame Blow Off," *Journal of Engineering for Gas Turbines and Power*, vol. 142, no. 1, 2020. (Cited on page 80.)

[211] K. Prieur, D. Durox, G. Vignat, T. Schuller, S. Candel, and S. C. Experimental, "Experimental determinations of Flame Describing Functions of swirling spray flames," in *Colloque INCA*, 2017. (Cited on page 80.)

[212] G. Vignat, D. Durox, K. Prieur, and S. Candel, "An experimental study into the effect of injector pressure loss on self-sustained combustion instabilities in a swirled spray burner," *Proceedings of the Combustion Institute*, vol. 37, no. 4, pp. 5205–5213, 2019. (Cited on page 80.)

[213] G. Vignat, P. Rajendram Soundararajan, D. Durox, A. Vié, A. Renaud, and S. Candel, "A Joint Experimental and Large Eddy Simulation Characterization of the Liquid Fuel Spray in a Swirl Injector," *Journal of Engineering for Gas Turbines and Power*, vol. 143, aug 2021. (Cited on pages 80, 192 and 210.)

[214] P. R. Soundararajan, D. Durox, A. Renaud, G. Vignat, and S. Candel, "Swirler effects on combustion instabilities analyzed with measured FDFs, injector impedances and damping rates," *Combustion and Flame*, vol. 238, p. 111947, apr 2022. (Cited on pages 80 and 81.)

[215] F. Dupuy, *Reduced Order Models and Large Eddy Simulation for Combustion Instabilities in aeronautical Gas Turbines*. PhD thesis, Institut National Polytechnique de Toulouse, Toulouse, 2020. (Cited on pages 89, 117 and 128.)

[216] P. Salas, *Physical and numerical aspects of thermoacoustic instabilities in annular combustion chambers*. PhD thesis, Université Sciences et Technologies - Bordeaux I, 2013. (Cited on pages 89 and 90.)

[217] Y. Saad, *Numerical Methods for Large Eigenvalue Problems*. Society for Industrial and Applied Mathematics (SIAM), jan 2011. (Cited on page 90.)

[218] S. Güttel and F. Tisseur, "The nonlinear eigenvalue problem," *Acta Numerica*, vol. 26, pp. 1–94, may 2017. (Cited on page 90.)

[219] P. E. Buschmann, G. A. Mensah, F. Nicoud, and J. P. Moeck, "Solution of Thermoacoustic Eigenvalue Problems With a Noniterative Method," *Journal of Engineering for Gas Turbines and Power*, vol. 142, mar 2020. (Cited on page 91.)

[220] G. A. Mensah, G. Campa, and J. P. Moeck, "Efficient Computation of Thermoacoustic Modes in Industrial Annular Combustion Chambers Based on Bloch-Wave Theory," *Journal of Engineering for Gas Turbines and Power*, vol. 138, no. 8, 2016. (Cited on page 91.)

[221] G. A. Mensah, A. Orchini, P. E. Buschmann, and L. Grubišić, "A subspace-accelerated method for solving nonlinear thermoacoustic eigenvalue problems," *Journal of Sound and Vibration*, vol. 520, pp. 22–460, mar 2022. (Cited on page 91.)

[222] Y. Saad, M. El-Guide, and A. Międlar, "A rational approximation method for the nonlinear eigenvalue problem," *arXiv:1901.01188v2[math.NA]*, jan 2019. (Cited on page 91.)

[223] T. Kailath, *Linear Systems*. Prentice-Hall, 1980. (Cited on page 95.)

[224] G. F. Franklin, D. J. Powell, and A. F. Emami-Naeini, *Feedback Control of Dynamic Systems*. Pearson, 8th ed., 2019. (Cited on pages 95, 121, 122, 123 and 124.)

[225] K. J. Åström and R. M. Murray, *Feedback systems : An Introduction for Scientists and Engineers*. Princeton University Press, 2nd ed., 2021. (Cited on pages 95, 121, 122, 123 and 124.)

[226] L. Ljung, *System Identification*. Birkhäuser, Boston, MA, 1998. (Cited on pages 95 and 97.)

[227] A. K. Tangirala, *Principles of System Identification : Theory and Practice*. CRC Press, 1st ed., 2015. (Cited on pages 95 and 97.)

[228] T. Schuller, T. Poinsot, and S. Candel, "Dynamics and control of premixed combustion systems based on flame transfer and describing functions," *Journal of Fluid Mechanics*, vol. 894, p. 1, 2020. (Cited on page 95.)

[229] M. Schmid, R. S. Blumenthal, M. Schulze, W. Polifke, and T. Sattelmayer, "Quantitative stability analysis using real-valued frequency response data," *Journal of Engineering for Gas Turbines and Power*, vol. 135, no. 12, pp. 1–8, 2013. (Cited on pages 97 and 99.)

[230] L. Tay-Wo-Chong, S. Bomberg, A. Ulhaq, T. Komarek, and W. Polifke, "Comparative Validation Study on Identification of Premixed Flame Transfer Function," *Journal of Engineering for Gas Turbines and Power*, vol. 134, no. 2, 2012. (Cited on pages 99 and 192.)

[231] M. A. Macquisten, M. Whiteman, S. R. Stow, and A. J. Moran, "Exploitation of measured flame transfer functions for a two phase lean fuel injector to predict thermoacoustic modes in full annular combustors," *Proceedings of the ASME Turbo Expo*, vol. 4A, pp. 1–10, 2014. (Cited on page 99.)

[232] W. Polifke, "Black-box system identification for reduced order model construction," *Annals of Nuclear Energy*, vol. 67, pp. 109–128, 2014. (Cited on pages 99, 113, 128 and 192.)

[233] L. Tay Wo Chong, T. Komarek, R. Kaess, F. Stephan, and W. Polifke, "Identification of Flame Transfer Functions From LES of a Premixed Swirl Burner," in *Proceedings of ASME Turbo Expo 2010*, 2010. (Cited on pages 100 and 192.)

[234] H. A. Kramers, "La diffusion de la lumière par les atomes," in *Atti del Congresso Internationale dei Fisici (Transactions of Volta Centenary Congress), Como*, (Como), pp. 545–557, 1927. (Cited on pages 101, 112 and 121.)

[235] R. d. L. Krönig, "On the Theory of Dispersion of X-Rays," *Journal of the Optical Society of America*, vol. 12, pp. 547–557, jun 1926. (Cited on pages 101, 112 and 121.)

[236] E. C. Titchmarsh, *Introduction to the Theory of Fourier Integrals*. Clarendon Press, 1937. (Cited on pages 101, 112 and 121.)

[237] J. S. Toll, "Causality and the Dispersion Relation: Logical foundations," *Physical Review*, vol. 104, no. 6, pp. 1760–1770, 1956. (Cited on pages 101, 112 and 120.)

[238] H. M. Nussenzveig, *Causality and Dispersion Relations*. Academic Press, 1972. (Cited on pages 101, 112 and 120.)

[239] P. Triverio, S. Grivet-Talocia, M. S. Nakhla, F. G. Canavero, and R. Achar, "Stability, causality, and passivity in electrical interconnect models," *IEEE Transactions on Advanced Packaging*, vol. 30, no. 4, pp. 795–808, 2007. (Cited on pages 101, 109, 110, 111, 112, 113, 120 and 121.)

[240] P. Triverio and S. Grivet-Talocia, "Robust Causality Characterization via Generalized Dispersion Relations," *IEEE Transactions on Advanced Packaging*, vol. 31, no. 3, p. 579, 2008. (Cited on pages 101, 112, 120, 121 and 125.)

[241] J. Bechhoefer, "Kramers–Krönig, Bode, and the meaning of zero.," *American Journal of Physics*, vol. 79, no. 10, pp. 1053–1059, 2011. (Cited on pages 101, 112, 121, 122, 123 and 124.)

[242] Q. Douasbin, C. Scalo, L. Selle, and T. Poinsot, "Delayed-time domain impedance boundary conditions (D-TDIBC)," *Journal of Computational Physics*, vol. 371, pp. 50–66, oct 2018. (Cited on pages 102, 104, 105, 107, 108, 110, 112, 113, 114, 117, 127 and 149.)

[243] S. Jaensch, C. Sovardi, and W. Polifke, "On the robust, flexible and consistent implementation of time domain impedance boundary conditions for compressible flow simulations," *Journal of Computational Physics*, vol. 314, no. March, pp. 145–159, 2016. (Cited on pages 102, 104 and 106.)

[244] K. Y. Fung and H. Ju, "Time-domain Impedance Boundary Conditions for Computational Acoustics and Aeroacoustics," *International Journal of Computational Fluid Dynamics*, vol. 18, pp. 503–511, aug 2004. (Cited on pages 102 and 104.)

[245] C. Tam and L. Auriault, "Time-domain impedance boundary conditions for computational aeroacoustics," *AIAA Journal*, vol. 34, pp. 917–923, may 1996. (Cited on pages 102 and 104.)

[246] M. R. Bothien, J. P. Moeck, A. Lacarelle, and C. O. Paschereit, "Time domain modelling and stability analysis of complex thermoacoustic systems," *Proceedings of the Institution of Mechanical Engineers, Part A: Journal of Power and Energy*, vol. 221, no. 5, pp. 657–668, 2007. (Cited on pages 102, 105 and 106.)

[247] B. Gustavsen and A. Semlyen, "Rational approximation of frequency domain responses by vector fitting," *IEEE Transactions on Power Delivery*, vol. 14, no. 3, 1999. (Cited on pages 103 and 106.)

[248] P. Triverio, "Vector Fitting," in *Handbook on Model Order Reduction, Volume 1: System- and Data-Driven Methods and Algorithms* (P. Benner, W. Schilders, S. Grivet-Talocia, A. Quarteroni, G. Rozza, and L. Miguel Silveira, eds.), De Gruyter, 2021. (Cited on pages 103, 104, 106, 107, 109, 112, 113, 114, 120 and 127.)

[249] Q. Douasbin, *Acoustic waves in combustion devices: interactions with flames and boundary conditions*. PhD thesis, Institut National Polytechnique de Toulouse (Toulouse INP), 2018. (Cited on pages 104, 105, 107, 112 and 114.)

[250] S. Jaensch, M. Merk, E. A. Gopalakrishnan, S. Bomberg, T. Emmert, R. I. Sujith, and W. Polifke, "Hybrid CFD/low-order modeling of nonlinear thermoacoustic oscillations," *Proceedings of the Combustion Institute*, vol. 36, no. 3, 2017. (Cited on page 105.)

[251] X. Y. Li, X. D. Li, and C. K. Tam, "Improved Multipole Broadband Time-Domain Impedance Boundary Condition," *AIAA Journal*, vol. 50, pp. 980–984, apr 2012. (Cited on page 106.)

[252] B. Cotté, P. Blanc-Benon, C. Bogey, and F. Poisson, "Time-Domain Impedance Boundary Conditions for Simulations of Outdoor Sound Propagation," *AIAA Journal*, vol. 47, no. 10, 2009. (Cited on page 106.)

[253] E. C. Levy, "Complex-curve fitting," *IRE Transactions on Automatic Control*, vol. AC-4, pp. 37–43, jul 1959. (Cited on page 106.)

[254] C. K. Sanathanan and J. Koerner, "Transfer Function Synthesis as a Ratio of Two Complex Polynomials," *IEEE Transactions on Automatic Control*, vol. 8, no. 1, pp. 56–58, 1963. (Cited on page 106.)

[255] S. Grivet-Talocia and B. Gustavsen, *Passive Macromodeling: Theory and Applications*. Wiley, 2015. (Cited on pages 107, 109, 112, 113 and 125.)

[256] S. W. Rienstra and A. Hirschberg, *An Introduction to Acoustics*. 2021. (Cited on pages 110 and 113.)

[257] P. Triverio, "Robust Causality Check for Sampled Scattering Parameters via a Filtered Fourier Transform," *IEEE Microwave and Wireless Components Letters*, vol. 24, no. 2, pp. 72–74, 2014. (Cited on pages 112, 125, 126 and 127.)

[258] P. Triverio, "An Accurate, Robust and Intuitive Technique to Detect Causality Violations in Broadband Frequency Measurements," in *IEEE International Symposium on Electromagnetic Compatibility (EMC)*, (Raleigh, NC, USA), IEEE, 2014. (Cited on pages 112, 125 and 126.)

[259] M. Merk, C. Silva, W. Polifke, R. Gaudron, M. Gatti, C. Mirat, and T. Schuller, "Direct Assessment of the Acoustic Scattering Matrix of a Turbulent Swirl Combustor by Combining System Identification, Large Eddy Simulation and Analytical Approaches," *Journal of Engineering for Gas Turbines and Power*, vol. 141, no. 2, 2019. (Cited on pages 113 and 114.)

[260] M. Merk, R. Gaudron, C. Silva, M. Gatti, C. Mirat, T. Schuller, and W. Polifke, "Prediction of combustion noise of an enclosed flame by simultaneous identification of noise source and flame dynamics," *Proceedings of the Combustion Institute*, vol. 37, no. 4, pp. 5263–5270, 2019. (Cited on pages 113 and 114.)

[261] M. Gatti, R. Gaudron, C. Mirat, L. Zimmer, and T. Schuller, "Impact of swirl and bluff-body on the transfer function of premixed flames," *Proceedings of the Combustion Institute*, vol. 37, no. 4, pp. 5197–5204, 2019. (Cited on page 114.)

[262] G. Ghirardo, B. Ćosić, M. P. Juniper, and J. P. Moeck, "State-space realization of a describing function," *Nonlinear Dynamics*, vol. 82, pp. 9–28, oct 2015. (Cited on page 120.)

[263] H. W. Bode, "Relations Between Attenuation and Phase in Feedback Amplifier Design," *Bell Systems Technical Journal*, vol. 19, no. 3, pp. 421–454, 1940. (Cited on page 121.)

[264] X. Chen, H. Fathy, and J. O'connor, "Impact of Sensor Placement on Mode Observability and LQG Control of a Thermoacoustic System," *International Federation of Automatic Control (IFAC)-PapersOnLine*, vol. 53, no. 2, pp. 4214–4221, 2020. (Cited on page 124.)

[265] X. Chen, J. O'Connor, and H. Fathy, "Heat Release Rate Estimation Using Multiple Non-Minimum Phase Sensor Measurements in a One-dimensional Combustor," *International Federation of Automatic Control (IFAC)-PapersOnLine*, vol. 54, pp. 723–728, jan 2021. (Cited on page 124.)

[266] X. Chen, J. O'Connor, and H. Fathy, "Optimizing Thermoacoustic Characterization Experiments for Identifiability Improves Both Parameter Estimation Accuracy and Closed-Loop Controller Robustness Guarantees," *Combustion Science and Technology*, 2021. (Cited on page 124.)

[267] X. Chen, S. Hemchandra, H. Fathy, and J. O'Connor, "Linear control of thermoacoustic oscillations with flame dynamics modeled by a level-set method," *Combustion and Flame*, vol. 237, p. 111686, mar 2022. (Cited on page 124.)

[268] E. Motheau, *Accounting for mean flow effects in a zero-Mach number thermo-acoustic solver: Application to entropy induced combustion instabilities.* PhD thesis, Institut National Polytechnique de Toulouse (INP Toulouse), 2013. (Cited on pages 131, 135 and 136.)

[269] N. A. Cumpsty and F. E. Marble, "Core noise from gas turbine exhausts," *Journal of Sound and Vibration*, vol. 54, pp. 297–309, sep 1977. (Cited on page 132.)

[270] A. Dowling, "The calculation of thermoacoustic oscillations," *Journal of Sound and Vibration*, vol. 180, pp. 557–581, mar 1995. (Cited on pages 132, 141 and 146.)

[271] W. Polifke, C. O. Paschereit, and K. Paschereit, "Constructive and Destructive Interference of Acoustic and Entropy Waves in a Premixed Combustor with a Choked Exit," *The International Journal of Acoustics and Vibration*, vol. 6, no. 3, 2001. (Cited on page 132.)

[272] N. Kings and F. Bake, "Indirect combustion noise: noise generation by accelerated vorticity in a nozzle flow," *International Journal of Spray and Combustion Dynamics*, vol. 2, no. 3, pp. 253–266, 2010. (Cited on pages 132 and 143.)

[273] L. Li and X. Sun, "Effect of vorticity waves on azimuthal instabilities in annular chambers," *Combustion and Flame*, vol. 162, pp. 628–641, 2015. (Cited on pages 132 and 143.)

[274] I. Duran and A. S. Morgans, "On the reflection and transmission of circumferential waves through nozzles," *Journal of Fluid Mechanics*, vol. 773, pp. 137–153, 2015. (Cited on pages 132, 137 and 143.)

[275] L. Magri, "On indirect noise in multicomponent nozzle flows," *Journal of Fluid Mechanics*, vol. 828, p. 2, 2017. (Cited on pages 132 and 143.)

[276] M. Weilenmann and N. Noiray, "Experiments on sound reflection and production by choked nozzle flows subject to acoustic and entropy waves," *Journal of Sound and Vibration*, vol. 492, p. 115799, feb 2021. (Cited on pages 132 and 143.)

[277] M. S. Howe, "Indirect combustion noise," *Journal of Fluid Mechanics*, vol. 659, pp. 267–288, 2010. (Cited on page 132.)

[278] M. Ihme, "Combustion and Engine-Core Noise," *Annu. Rev. Fluid Mech.*, vol. 49, pp. 277–310, 2017. (Cited on page 132.)

[279] C. K. W. Tam, F. Bake, L. S. Hultgren, and T. Poinsot, "Combustion noise: modeling and prediction," *CEAS Aeronautical Journal*, vol. 10, no. 1, pp. 101–122, 2019. (Cited on page 132.)

[280] M. Weilenmann, U. Doll, R. Bombach, A. Blondé, D. Ebi, Y. Xiong, and N. Noiray, "Linear and nonlinear entropy-wave response of technically-premixed jet-flames-array and swirled flame to acoustic forcing," *Proceedings of the Combustion Institute*, vol. 38, pp. 6135–6143, sep 2021. (Cited on pages 132 and 143.)

[281] I. Durán, S. Moreau, and T. Poinsot, "Analytical and numerical study of combustion noise through a subsonic nozzle," *AIAA Journal*, vol. 51, no. 1, pp. 42–52, 2013. (Cited on page 137.)

[282] P. E. Doak, "Fluctuating Total Enthalpy as the Basic Generalized Acoustic Field," *Theoretical and Computational Fluid Dynamics 1998 10:1*, vol. 10, no. 1, pp. 115–133, 1998. (Cited on page 138.)

[283] B. T. Chu, "On the energy transfer to small disturbances in fluid flow (Part I)," *Acta Mechanica 1965 1:3*, vol. 1, pp. 215–234, sep 1965. (Cited on page 141.)

[284] M. K. Myers, "Transport of energy by disturbances in arbitrary steady flows," *Journal of Fluid Mechanics*, vol. 226, pp. 383–400, 1991. (Cited on page 141.)

[285] M. Brear, F. Nicoud, M. Talei, A. Giauque, E. Hawkes, B. M. I C H A E L J B R E A R, M. J. Brear, F. Nicoud, M. Talei, A. Giauque, and E. Hawkes, "Disturbance energy transport and sound production in gaseous combustion," *Journal of Fluid Mechanics*, vol. 707, pp. 53–73, 2012. (Cited on page 141.)

[286] K. Joseph George and R. I. Sujith, "On Chu's disturbance energy," *Journal of Sound and Vibration*, vol. 330, no. 22, pp. 5280–5291, 2011. (Cited on page 141.)

[287] K. J. George and R. I. Sujith, "Disturbance energy norms: A critical analysis," *Journal of Sound and Vibration*, vol. 331, no. 7, pp. 1552–1566, 2012. (Cited on page 141.)

[288] L. Magri, J. O'Brien, and M. Ihme, "Compositional inhomogeneities as a source of indirect combustion noise," *Journal of Fluid Mechanics*, vol. 799, pp. 1–12, 2016. (Cited on page 143.)

[289] F. De Domenico, E. O. Rolland, J. Rodrigues, L. Magri, and S. Hochgreb, "Compositional and entropy indirect noise generated in subsonic non-isentropic nozzles," *Journal of Fluid Mechanics*, vol. 910, p. 5, 2021. (Cited on page 143.)

[290] J. Eckstein, E. Freitag, C. Hirsch, and T. Sattelmayer, "Experimental Study on the Role of Entropy Waves in Low-Frequency Oscillations in a RQL Combustor," *Journal of Engineering for Gas Turbines and Power*, vol. 128, pp. 264–270, apr 2006. (Cited on page 146.)

[291] A. S. Morgans, C. S. Goh, and J. A. Dahan, "The dissipation and shear dispersion of entropy waves in combustor thermoacoustics," *Journal of Fluid Mechanics*, vol. 733, p. R2, 2013. (Cited on page 146.)

[292] C. S. Goh and A. S. Morgans, "The influence of entropy waves on the thermoacoustic stability of a model combustor," *Combustion Science and Technology*, vol. 185, no. 2, pp. 249–268, 2013. (Cited on pages 146 and 163.)

[293] L. N. Trefethen and M. Embree, *SPECTRA AND PSEUDOSPECTRA: The Behavior of NonnormaI Matrices and Operators*. Princeton University Press, 2005. (Cited on pages 164 and 165.)

[294] G. Chaussonnet, *Modeling of liquid film and breakup phenomena in Large-Eddy Simulations of aeroengines fueled by airblast atomizers*. PhD thesis, Institut National Polytechnique de Toulouse (INPT), 2014. (Cited on pages 170, 171, 180, 181, 182, 214 and 219.)

[295] W. A. Sirignano, "Advances in droplet array combustion theory and modeling," *Progress in Energy and Combustion Science*, vol. 42, pp. 54–86, 2014. (Cited on page 169.)

[296] S. K. Aggarwal, "A review of spray ignition phenomena: Present status and future research," *Progress in Energy and Combustion Science*, vol. 24, pp. 565–600, jan 1998. (Cited on page 169.)

[297] S. K. Aggarwal, "Single droplet ignition: Theoretical analyses and experimental findings," *Progress in Energy and Combustion Science*, vol. 45, pp. 79–107, dec 2014. (Cited on page 169.)

[298] P. Jenny, D. Roekaerts, and N. Beishuizen, "Modeling of turbulent dilute spray combustion," *Progress in Energy and Combustion Science*, vol. 38, pp. 846–887, dec 2012. (Cited on page 169.)

[299] A. R. Masri, "Turbulent Combustion of Sprays: From Dilute to Dense," *Combustion Science and Technology*, vol. 188, pp. 1619–1639, oct 2016. (Cited on page 169.)

[300] C. T. Crowe, J. D. Schwarzkopf, M. Sommerfeld, and Y. Tsuji, *Multiphase Flows with Droplets and Particles*. CRC Press, 2nd ed., 2011. (Cited on pages 169, 176, 183 and 195.)

[301] R. O. Fox, "Large-Eddy-Simulation Tools for Multiphase Flows," *Annual Review of Fluid Mechanics*, vol. 44, pp. 47–76, dec 2012. (Cited on page 169.)

[302] M. Gorokhovski and M. Herrmann, "Modeling Primary Atomization," *Annual Review of Fluid Mechanics*, vol. 40, pp. 343–366, jan 2008. (Cited on page 169.)

[303] S. Subramaniam, "Lagrangian-Eulerian methods for multiphase flows," *Progress in Energy and Combustion Science*, vol. 39, no. 2-3, pp. 215–245, 2013. (Cited on page 169.)

[304] O. Desjardins and H. Pitsch, "Detailed numerical investigation of turbulent atomization of liquid jets," *Atomization and Sprays*, vol. 20, no. 4, pp. 311–336, 2010. (Cited on page 169.)

[305] K. Luo, H. Pitsch, M. G. Pai, and O. Desjardins, "Direct numerical simulations and analysis of three-dimensional n-heptane spray flames in a model swirl combustor," *Proceedings of the Combustion Institute*, vol. 33, no. 2, pp. 2143–2152, 2011. (Cited on page 169.)

[306] O. Desjardins, J. O. McCaslin, M. Owkes, and P. Brady, "Direct numerical and large-eddy simulation of primary atomization in complex geometries," *Atomization and Sprays*, vol. 23, no. 11, pp. 1001–1048, 2013. (Cited on page 169.)

[307] V. Le Chenadec and H. Pitsch, "A conservative framework for primary atomization computation and application to the study of nozzle and density ratio effects," *Atomization and Sprays*, vol. 23, no. 12, pp. 1139–1165, 2013. (Cited on page 169.)

[308] J. Capecelatro and O. Desjardins, "An Euler–Lagrange strategy for simulating particle-laden flows," *Journal of Computational Physics*, vol. 238, pp. 1–31, apr 2013. (Cited on page 169.)

[309] E. Knudsen, Shashank, and H. Pitsch, "Modeling partially premixed combustion behavior in multiphase LES," *Combustion and Flame*, vol. 162, no. 1, pp. 159–180, 2015. (Cited on page 169.)

[310] M. Sanjosé, J. M. Senoner, F. Jaegle, B. Cuenot, S. Moreau, and T. Poinsot, "Fuel injection model for Euler-Euler and Euler-Lagrange large-eddy simulations of an evaporating spray inside an aeronautical combustor," *International Journal of Multiphase Flow*, vol. 37, no. 5, pp. 514–529, 2011. (Cited on pages 170, 178, 179, 203, 209 and 214.)

[311] J. Senoner, *Large-Eddy Simulation of the two-phase flow in an aeronautical combustor using an Euler-Lagrange approach*. PhD thesis, Institut National Polytechnique de Toulouse (INPT), 2010. (Cited on pages 170, 172 and 176.)

[312] M. Sanjosé, *Evaluation de la méthode Euler-Euler pour la simulation aux grandes échelles des chambres à carburant liquide*. PhD thesis, Institut National Polytechnique de Toulouse (INPT), 2009. (Cited on pages 170 and 204.)

[313] N. Lafrate, *Simulation aux grandes échelles diphasique dans les moteurs downsizes à allumage commande*. PhD thesis, Institut National Polytechnique de Toulouse (INPT), 2016. (Cited on page 171.)

[314] G. Chaussonnet, O. Vermorel, E. Riber, and B. Cuenot, "A new phenomenological model to predict drop size distribution in Large-Eddy Simulations of airblast atomizers," *International Journal of Multiphase Flow*, vol. 80, no. January 2019, pp. 29–42, 2016. (Cited on pages 171, 177 and 180.)

[315] J. Carmona, *Modélisation des phénomènes diphasiques dans des injecteurs aéronautiques de type Airblast*. PhD thesis, Institut National Polytechnique de Toulouse (INPT), 2021. (Cited on pages 171 and 177.)

[316] S. Balachandar and J. K. Eaton, "Turbulent dispersed multiphase flow," *Annual Review of Fluid Mechanics*, vol. 42, pp. 111–133, 2010. (Cited on page 171.)

[317] F. Jaegle, *Large eddy simulation of evaporating sprays in complex geometries using Eulerian and Lagrangian methods*. PhD thesis, Institut National Polytechnique de Toulouse (INPT), 2009. (Cited on page 172.)

[318] P. Sierra Sànchez, *Modeling the dispersion and evaporation of sprays in aeronautical combustion chambers*. PhD thesis, Institut National Polytechnique de Toulouse (INPT), 2012. (Cited on page 172.)

[319] V. Shastry, *Simulation of multicomponent spray combustion in gas turbine engines*. PhD thesis, Institut National Polytechnique de Toulouse (INPT), 2022. (Cited on page 172.)

[320] Q. Cazeres, *Analysis and reduction of chemical kinetics for combustion applications*. PhD thesis, Institut National Polytechnique de Toulouse (INPT), 2021. (Cited on page 172.)

[321] B. Rochette, F. Collin-Bastiani, L. Gicquel, O. Vermorel, D. Veynante, and T. Poinsot, "Influence of chemical schemes, numerical method and dynamic turbulent combustion modeling

on LES of premixed turbulent flames," *Combustion and Flame*, vol. 191, pp. 417–430, 2018. (Cited on pages 172 and 187.)

[322] B. Rochette, E. Riber, B. Cuenot, and O. Vermorel, "A generic and self-adapting method for flame detection and thickening in the thickened flame model," *Combustion and Flame*, vol. 212, pp. 448–458, 2020. (Cited on page 172.)

[323] D. Paulhiac, *Modélisation de la combustion d'un spray dans un brûleur aéronautique*. PhD thesis, Institut National Polytechnique de Toulouse (INPT), 2015. (Cited on pages 173, 187, 188, 189 and 199.)

[324] B. Rochette, *Modeling and simulation of two-phase flow turbulent combustion in aeronautical engines*. PhD thesis, Institut National Polytechnique de Toulouse (INPT), 2019. (Cited on pages 173, 174, 177 and 188.)

[325] E. Mastorakos, "Forced ignition of turbulent spray flames," *Proceedings of the Combustion Institute*, vol. 36, pp. 2367–2383, jan 2017. (Cited on page 173.)

[326] F. Collin-Bastiani, *Modeling and numerical simulations of two-phase ignition in gas turbine*. PhD thesis, Institut National Polytechnique de Toulouse (INPT), 2019. (Cited on page 174.)

[327] T. Echekki and E. Mastorakos, eds., *Turbulent Combustion Modeling: Advances, New Trends and Perspectives.*, vol. 95 of *Fluid Mechanics and Its Applications*. Springer, 2011. (Cited on pages 174 and 188.)

[328] V. Raman and M. Hassanaly, "Emerging trends in numerical simulations of combustion systems," *Proceedings of the Combustion Institute*, vol. 37, pp. 2073–2089, jan 2019. (Cited on page 174.)

[329] S. B. Pope, *Turbulent flows*. Cambridge University Press, 2000. (Cited on page 174.)

[330] P. Sagaut, S. Deck, and M. Terracol, *Multiscale and Multiresolution Approaches in Turbulence*. Imperial College Press, 2nd ed., 2013. (Cited on page 174.)

[331] F. Nicoud and F. Ducros, "Subgrid-Scale Stress Modelling Based on the Square of the Velocity Gradient Tensor," *Flow, Turbulence and Combustion 1999 62:3*, vol. 62, no. 3, pp. 183–200, 1999. (Cited on page 175.)

[332] J. Carmona, N. Odier, O. Desjardins, B. Cuenot, A. Misdariis, and A. Cayre, "A comparative study of direct numerical simulation and experimental results on a prefilming airblast atomization configuration," *Atomization and Sprays*, vol. 31, no. 8, pp. 9–32, 2021. (Cited on page 177.)

[333] G. Chaussonnet, T. Dauch, M. Keller, M. Okraschevski, C. Ates, C. Schwitzke, R. Koch, and H. J. Bauer, "Progress in the Smoothed Particle Hydrodynamics Method to Simulate and Post-process Numerical Simulations of Annular Airblast Atomizers," *Flow, Turbulence and Combustion*, vol. 105, pp. 1119–1147, nov 2020. (Cited on page 177.)

[334] R. Janodet, C. Guillamón, V. Moureau, R. Mercier, G. Lartigue, P. Benard, T. Ménard, A. Berlemont, and P. Bénard, "A massively parallel accurate conservative level set algorithm for simulating turbulent atomization on adaptive unstructured grids," *Journal Computational Physics*, vol. 458, 2022. (Cited on page 178.)

[335] A. A. Mukundan, T. Ménard, J. C. Brändle de Motta, and A. Berlemont, "Detailed numerical simulations of primary atomization of airblasted liquid sheet," *International Journal of Multiphase Flow*, vol. 147, p. 103848, feb 2022. (Cited on page 178.)

[336] L. Palanti, S. Puggelli, L. Langone, A. Andreini, J. Reveillon, B. Duret, and F. X. Demoulin, "An attempt to predict spray characteristics at early stage of the atomization process by using surface density and curvature distribution," *International Journal of Multiphase Flow*, vol. 147, p. 103879, feb 2022. (Cited on page 178.)

[337] A. Ahmed, G. Tretola, S. Navarro-Martinez, K. Vogiatzaki, B. Duret, J. Reveillon, and F. X. Demoulin1, "Atomization modeling using surface density and stochastic fields," *Atomization and Sprays*, vol. 30, no. 4, pp. 239–266, 2020. (Cited on page 178.)

[338] J. Anez, A. Ahmed, N. Hecht, B. Duret, J. Reveillon, and F. X. Demoulin, "Eulerian–Lagrangian spray atomization model coupled with interface capturing method for diesel injectors," *International Journal of Multiphase Flow*, vol. 113, pp. 325–342, apr 2019. (Cited on page 178.)

[339] J. Wen, Y. Hu, and R. Kurose, "Numerical simulation of kerosene jet in crossflow atomization and evaporation under the elevated pressure and oscillating air-flow condition," *Atomization and Sprays*, vol. 31, no. 7, pp. 73–87, 2021. (Cited on page 178.)

[340] J. Wen, Y. Hu, T. Nishiie, J. Iino, A. Masri, and R. Kurose, "A flamelet LES of turbulent dense spray flame using a detailed high-resolution VOF simulation of liquid fuel atomization," *Combustion and Flame*, vol. 237, p. 111742, mar 2022. (Cited on page 178.)

[341] J. Shinjo and A. Umemura, "Fluid dynamic and autoignition characteristics of early fuel sprays using hybrid atomization LES," *Combustion and Flame*, vol. 203, pp. 313–333, may 2019. (Cited on page 178.)

[342] B. de Saint-Venant, "Théorie du Mouvement Non Permanent des Eaux, avec Application aux Crues de Rivières et à l'Introduction des Marées dans leur Lit.," *Comptes Rendus des séances de l'Académie des Sciences*, pp. 147–154, 1871. (Cited on page 180.)

[343] O. Thual, *Hydrodynamique de l'environnement.* Ecole Polytechnique, 2010. (Cited on page 180.)

[344] L. Schiller and Z. Naumann, "A Drag Coefficient Correlation," *VDI Zeritung*, vol. 77, pp. 318–320, 1935. (Cited on page 183.)

[345] B. Abramzon and W. A. Sirignano, "Droplet vaporization model for spray combustion calculations," *International Journal of Heat and Mass Transfer*, vol. 32, no. 9, pp. 1605–1618, 1989. (Cited on pages 183, 185 and 186.)

[346] D. B. Spalding, "The Combustion of Liquid Fuels," *Symposium (International) on Combustion*, vol. 4, no. 1, pp. 847–864, 1953. (Cited on page 183.)

[347] W. E. Ranz and M. W. R., "Evaporation from drops, parts I & II.," *Chem Eng Prog.*, vol. 48, no. 4, 1952. (Cited on page 186.)

[348] T. Lu and C. K. Law, "Toward accommodating realistic fuel chemistry in large-scale computations," *Progress in Energy and Combustion Science*, vol. 35, pp. 192–215, apr 2009. (Cited on page 186.)

[349] H. Wang, R. Xu, K. Wang, C. T. Bowman, R. K. Hanson, D. F. Davidson, K. Brezinsky, and F. N. Egolfopoulos, "A physics-based approach to modeling real-fuel combustion chemistry - I. Evidence from experiments, and thermodynamic, chemical kinetic and statistical considerations," *Combustion and Flame*, vol. 193, pp. 502–519, jul 2018. (Cited on page 186.)

[350] R. Xu, K. Wang, S. Banerjee, J. Shao, T. Parise, Y. Zhu, S. Wang, A. Movaghar, D. J. Lee, R. Zhao, X. Han, Y. Gao, T. Lu, K. Brezinsky, F. N. Egolfopoulos, D. F. Davidson, R. K. Hanson, C. T. Bowman, and H. Wang, "A physics-based approach to modeling real-fuel combustion chemistry – II. Reaction kinetic models of jet and rocket fuels," *Combustion and Flame*, vol. 193, pp. 520–537, jul 2018. (Cited on page 186.)

[351] A. Felden, L. Esclapez, E. Riber, B. Cuenot, and H. Wang, "Including real fuel chemistry in LES of turbulent spray combustion," *Combustion and Flame*, vol. 193, pp. 397–416, 2018. (Cited on page 187.)

[352] Q. Cazères, P. Pepiot, E. Riber, and B. Cuenot, "A fully automatic procedure for the analytical reduction of chemical kinetics mechanisms for Computational Fluid Dynamics applications," *Fuel*, vol. 303, p. 121247, nov 2021. (Cited on page 187.)

[353] B. Franzelli, E. Riber, L. Y. Gicquel, and T. Poinsot, "Large Eddy Simulation of combustion instabilities in a lean partially premixed swirled flame," *Combustion and Flame*, vol. 159, no. 2, pp. 621–637, 2012. (Cited on page 187.)

[354] T. Jaravel, E. Riber, B. Cuenot, and G. Bulat, "Large Eddy Simulation of an industrial gas turbine combustor using reduced chemistry with accurate pollutant prediction," *Proceedings of the Combustion Institute*, vol. 36, pp. 3817–3825, 2017. (Cited on page 187.)

[355] F. Collin-Bastiani, J. Marrero-Santiago, E. Riber, G. Cabot, B. Renou, and B. Cuenot, "A joint experimental and numerical study of ignition in a spray burner," *Proceedings of the Combustion Institute*, vol. 37, no. 4, pp. 5047–5055, 2019. (Cited on page 187.)

[356] D. Barré, L. Esclapez, M. Cordier, E. Riber, B. Cuenot, G. Staffelbach, B. Renou, A. Vandel, L. Y. Gicquel, and G. Cabot, "Flame propagation in aeronautical swirled multi-burners: Experimental and numerical investigation," *Combustion and Flame*, vol. 161, pp. 2387–2405, sep 2014. (Cited on page 187.)

[357] K. Töpperwien, F. Collin-Bastiani, E. Riber, B. Cuenot, G. Vignat, K. Prieur, D. Durox, S. Candel, and R. Vicquelin, "Large-Eddy Simulation of Flame Dynamics during the Ignition of a Swirling Injector Unit and Comparison with Experiments," *Journal of Engineering for Gas Turbines and Power*, vol. 143, feb 2021. (Cited on page 187.)

[358] L. Esclapez, P. C. Ma, E. Mayhew, R. Xu, S. Stouffer, T. Lee, H. Wang, and M. Ihme, "Fuel effects on lean blow-out in a realistic gas turbine combustor," *Combustion and Flame*, vol. 181, pp. 82–99, jul 2017. (Cited on page 187.)

[359] P. C. Ma, H. Wu, J. W. Labahn, T. Jaravel, and M. Ihme, "Analysis of transient blow-out dynamics in a swirl-stabilized combustor using large-eddy simulations," *Proceedings of the Combustion Institute*, vol. 37, pp. 5073–5082, jan 2019. (Cited on page 187.)

[360] B. Rochette, E. Riber, and B. Cuenot, "Effect of non-zero relative velocity on the flame speed of two-phase laminar flames," *Proceedings of the Combustion Institute*, vol. 37, no. 3, pp. 3393–3400, 2019. (Cited on page 188.)

[361] N. Peters, *Turbulent combustion*. Cambridge University Press, 2000. (Cited on page 188.)

[362] C. K. Law, *Combustion physics*. Cambridge University Press, 2010. (Cited on page 188.)

[363] F. Charlette, C. Meneveau, and D. Veynante, "A power-law flame wrinkling model for LES of premixed turbulent combustion Part II: dynamic formulation," *Combustion and Flame*, vol. 131, pp. 181–197, oct 2002. (Cited on page 189.)

[364] T. Takeno, M. Murayama, and Y. Tanida, "Fractal analysis of turbulent premixed flame surface," *Experiments in Fluids 1990 10:2*, vol. 10, pp. 61–70, dec 1990. (Cited on page 189.)

[365] B. Cuenot, F. Shum-Kivan, and S. Blanchard, "The thickened flame approach for non-premixed combustion: Principles and implications for turbulent combustion modeling," *Combustion and Flame*, p. 111702, sep 2021. (Cited on page 189.)

[366] P. D. Lax and B. Wendroff, "Difference schemes for hyperbolic equations with high order of accuracy," *Communications on Pure and Applied Mathematics*, vol. 17, pp. 381–398, aug 1964. (Cited on page 190.)

[367] T. J. Poinsot and S. K. Lele, "Boundary Conditions for Direct Simulations of Compressible Viscous Flows," *Journal of Computational Physics*, vol. 101, pp. 104–129, 1992. (Cited on pages 190 and 196.)

[368] L. Selle, F. Nicoucd, and T. Poinsot, "Actual impedance of nonreflecting boundary conditions: Implications for computation of resonators," *AIAA Journal*, vol. 42, no. 5, pp. 958–964, 2004. (Cited on page 190.)

[369] G. Daviller, G. Oztarlik, and T. Poinsot, "A generalized non-reflecting inlet boundary condition for steady and forced compressible flows with injection of vortical and acoustic waves," *Computers and Fluids*, vol. 190, pp. 503–513, 2019. (Cited on pages 190 and 196.)

[370] J. Li, D. Yang, C. Luzzato, and A. S. Morgans, "Open Source Combustion Instability Low Order Simulator (OSCILOS-Long) Technical report," tech. rep., Department of Mechanical Engineering, Imperial College London, UK, 2017. (Cited on page 192.)

[371] K. Truffin and T. Poinsot, "Comparison and extension of methods for acoustic identification of burners," *Combustion and Flame*, vol. 142, no. 4, pp. 388–400, 2005. (Cited on pages 192, 205 and 209.)

[372] A. Giauque, L. Selle, L. Gicquel, T. Poinsot, H. Buechner, P. Kaufmann, and W. Krebs, "System identification of a large-scale swirled partially premixed combustor using LES and measurements," *Journal of Turbulence*, vol. 6, 2005. (Cited on page 192.)

[373] T. Kitano, K. Kaneko, R. Kurose, and S. Komori, "Large-eddy simulations of gas- and liquid-fueled combustion instabilities in back-step flows," *Combustion and Flame*, vol. 170, pp. 63–78, 2016. (Cited on page 192.)

[374] A. Tyliszczak, D. E. Cavaliere, and E. Mastorakos, "LES/CMC of blow-off in a liquid fueled swirl burner," *Flow, Turbulence and Combustion*, vol. 92, no. 1-2, pp. 237–267, 2014. (Cited on page 192.)

[375] K. Prieur, *Dynamique de la combustion dans un foyer annulaire multi-injecteurs diphasique.* PhD thesis, Université Paris-Saclay, 2017. (Cited on pages 193, 199, 200, 201 and 204.)

[376] K. Prieur, G. Vignat, D. Durox, and T. Schuller, "Flame and spray dynamics during the light-round process in an annular system equipped with multiple swirl spray injectors," *Journal Of Engineering For Gas Turbines And Power*, vol. 141, no. 6, 2019. (Cited on page 193.)

[377] G. Vignat, *Injection and combustion dynamics in swirled spray flames and azimuthal coupling in annular combustors.* PhD thesis, Université Paris-Saclay, 2020. (Cited on pages 193, 204, 205 and 210.)

[378] L. Selle, G. Lartigue, T. Poinsot, R. Koch, K. U. Schildmacher, W. Krebs, B. Prade, P. Kaufmann, and D. Veynante, "Compressible large eddy simulation of turbulent combustion in complex geometry on unstructured meshes," *Combustion and Flame*, vol. 137, no. 4, pp. 489–505, 2004. (Cited on page 196.)

[379] M. Boileau, S. Pascaud, E. Riber, B. Cuenot, L. Y. Gicquel, T. J. Poinsot, and M. Cazalens, "Investigation of Two-Fluid Methods for Large Eddy Simulation of Spray Combustion in Gas Turbines," *Flow, Turbulence and Combustion*, vol. 80, pp. 291–321, dec 2008. (Cited on page 204.)

[380] R. Gaudron, M. Gatti, C. Mirat, and T. Schuller, "Flame Describing Functions of a Confined Premixed Swirled Combustor With Upstream and Downstream Forcing," *Journal Of Engineering For Gas Turbines And Power*, vol. 141, no. 5, p. 051016, 2019. (Cited on pages 207 and 209.)

[381] S. K. Chen, A. H. Lefebvre, and J. Rollbuhler, "Factors Influencing the Effective Spray Cone Angle of Pressure-Swirl Atomizers," *Journal of Engineering for Gas Turbines and Power*, vol. 114, pp. 97–103, jan 1992. (Cited on page 210.)

[382] J. Ballester and C. Dopazo, "Discharge coefficient and spray angle measurements for small pressure-swirl nozzles," *Atomization and Sprays*, vol. 4, no. 3, pp. 351–367, 1994. (Cited on page 210.)

[383] M. Govindaraj, K. D. Ghate, M. S. Rao, V. S. Iyengar, S. Thirumalachari, and S. Kothandaraman, "Experimental study of spray breakup phenomena in small-scale simplex atomizers with and without air swirl," *Atomization and Sprays*, vol. 28, no. 4, pp. 299–320, 2018. (Cited on page 210.)

[384] E. J. Hopfinger and J. C. Lasheras, "Explosive breakup of a liquid jet by a swirling coaxial gas jet," *Physics of Fluids*, vol. 8, p. 1696, jun 1998. (Cited on page 210.)

[385] T. Yi and D. A. Santavicca, "Forced Flame Response of Turbulent Liquid-Fueled Lean-Direct-Injection Combustion to Fuel Modulations," *Journal of Propulsion and Power*, vol. 25, no. 6, 2009. (Cited on page 210.)

[386] L. Cunha Caldeira Mesquita, A. Vié, and S. Ducruix, "Large Eddy Simulation of a Two-Phase Staged Swirling Burner Using an Euler-Lagrange Approach: Validation of the Injection Strategy," in *Proceedings of the ASME Turbo Expo*, vol. 4B, American Society of Mechanical Engineers Digital Collection, aug 2018. (Cited on page 210.)

[387] L. C. Mesquita, A. Vié, L. Zimmer, and S. Ducruix, "Numerical analysis of flame shape bifurcation in a two-stage swirled liquid burner using Large Eddy Simulation," *Proceedings of the Combustion Institute*, vol. 38, pp. 5971–5978, jan 2021. (Cited on page 210.)

[388] P. Schmid, "Dynamic mode decomposition of numerical and experimental data," *J. Fluid Mech*, vol. 656, pp. 5–28, 2010. (Cited on page 210.)

[389] L. Magri, "Adjoint Methods as Design Tools in Thermoacoustics," *Applied Mechanics Reviews*, vol. 71, no. 2, 2019. (Cited on page 219.)

[390] S. Richard, J. Lamouroux, A. Ndiaye, and F. Nicoud, "Application of UQ to Combustor Design," in *Notes on Numerical Fluid Mechanics and Multidisciplinary Design* (C. Hirsch, D. Wunsch, Szumbarski, Ł.-W. J., and J. Ł., Pons-Prats, eds.), vol. 140, pp. 399–414, Springer, 2019. (Cited on page 219.)